

”Investigations of the inverse model catalysts  
 $CeO_x$ /Rh(111) and  $MnO_x$ /Pd(111)  
with photoemission spectroscopy  
and scanning tunnelling microscopy”

## **Dissertation**

von

Mag. rer. nat. Sven ECK

eingereicht am

Institut für Experimentalphysik

der Karl Franzens Universität Graz

(Oktober 2003)

Und auch ich, ich sang beim Scheiden: Vale universitas!  
Vale Burschenlust und Freuden! Ex! Und dann zerschellt das Glas.  
Graz, du traute Stadt der Lieder, bleibst mir in der Ferne nah!  
Kehrt die Jugend auch nicht wieder, die Erinnerung ist da.

*Student sein in Graz, wenn der Flieder blüht,  
Student sein in Graz, wenn das Weinlaub glüht,  
Wenn im Herzen die feurige Jugendlust brennt,  
Student sein in Graz, Student sein, Student!*

### **Grazer Studentenlied**

(Gerold Walzel, 1925)

# Contents

<b>1</b>	<b>Introduction</b>	<b>5</b>
1.1	Acknowledgements . . . . .	9
<b>2</b>	<b>Experimental</b>	<b>11</b>
2.1	The Scienta UHV system . . . . .	12
2.2	Alignment of the Scienta system at a beamline . . . . .	16
2.3	Testing the resolution of the SES 200 analyser with the Helium lamp . . . . .	19
2.4	Definition of monolayer-equivalent . . . . .	23
<b>3</b>	<b>The Ceria-Rhodium(111) interface</b>	<b>25</b>
3.1	Introduction . . . . .	26
3.1.1	Determining the cerium oxidation state with XPS . . . . .	30
3.1.2	$CeO_x$ - resonant photoemission of the 4f state . . . . .	38
3.1.3	Characterisation of CO adsorption sites with HR-XPS . . . . .	43
3.2	Growth and thermal properties of ultrathin cerium oxide layers on Rh(111) . . . . .	49
3.2.1	The surface phase diagram of cerium oxide on Rh(111) . . . . .	49
3.2.2	The growth of ceria on Rh(111) at 250°C . . . . .	53
3.2.3	Partial reduction of ceria on Rh(111) at $T \leq 800^\circ\text{C}$ . . . . .	57
3.2.4	Decomposition of ceria on Rh(111) - surface alloy formation . . . . .	64
3.3	Adsorption and reaction of CO on a ceria-Rh(111) "inverse model catalyst" surface . . . . .	67
3.3.1	Introduction . . . . .	67
3.3.2	Adsorption of CO on oxygen-precovered Rh(111) 2x1-O . . . . .	68
3.3.3	Adsorption of CO on ceria-Rh(111) surfaces . . . . .	74
3.3.4	Adsorption of CO on (partially) reduced ceria-Rh(111) surfaces . . . . .	78

3.4	Summary . . . . .	85
<b>4</b>	<b>The Manganese-oxide-Palladium(111) interface</b>	<b>87</b>
4.1	Introduction . . . . .	87
4.1.1	Preparation of thin oxidised manganese films . . . . .	91
4.2	Thick films (>3 MLE) of MnO on Pd(111): XPS, UPS and LEED . . . . .	92
4.2.1	Mn 2p XPS . . . . .	92
4.2.2	Mn 3s XPS . . . . .	95
4.2.3	Mn metal deposition as studied with XPS . . . . .	99
4.2.4	Oxidation of thick manganese films on Pd(111) . . . . .	104
4.2.5	UPS of manganese oxide films . . . . .	108
4.2.6	MnO uptake - XPS . . . . .	112
4.2.7	MnO uptake - UPS . . . . .	117
4.2.8	CO adsorption experiments with UPS . . . . .	120
4.2.9	MnO/Pd(111) LEED phase diagram . . . . .	123
4.2.10	Annealing thick MnO layers in UHV . . . . .	128
4.3	Thin films ( $\leq 3$ MLE) of MnO on Pd(111): XPS, UPS and LEED . . . . .	134
4.3.1	1 MLE MnO on Pd(111) - different preparations . . . . .	134
4.3.2	Annealing thin MnO films in UHV - XPS and LEED . . . . .	136
4.3.3	Annealing thin MnO films in UHV - UPS and LEED . . . . .	142
4.3.4	UPS and XPS of 1 MLE MnO post-oxidised and annealed in UHV .	150
4.3.5	Re-oxidation of the $Pd_xMn_y$ alloy surfaces after annealing in UHV	155
4.3.6	Summary of MnO/Pd(111) photo-emission experiments . . . . .	158
4.4	STM of manganese oxide on Pd(111) . . . . .	161
4.4.1	STM characterisation of the ordered MnO phase . . . . .	161
4.4.2	STM of sub-mono-layer MnO/Pd(111) surfaces . . . . .	164
4.4.3	STM of annealed MnO/Pd(111) surfaces . . . . .	169
4.4.4	STM on MnO/Pd(111): summary and outline . . . . .	174
<b>A</b>	<b>Curriculum vitae</b>	<b>185</b>
<b>B</b>	<b>List of Publications:</b>	<b>191</b>
<b>C</b>	<b>Manual for SCIENTA SES-200 analyser and ESCA 300 software</b>	<b>193</b>



# Chapter 1

## Introduction

The interfaces between metal surfaces and oxide overlayers or substrates are of crucial importance for the macroscopic behaviour of a variety of modern technological devices, such as gas sensors, solid state electronic devices, metal-ceramic composites, magnetic tunnelling diodes, and a wide range of metal-oxide catalysts [1]. Epitaxially grown thin films of oxides on dissimilar metals or on other oxide substrates are relevant to the development of novel applications in the technology for the coming decades, for example in heterostructure-based nanodevices, but they are also of fundamental scientific interest as models for oxide surfaces in general [2].

Thin films of oxides on metals, for example, retain many of their chemical bulk properties and yet remain conductive, which is advantageous for the application of modern surface analysis techniques. Epitaxial oxide films on metal substrates may be used as supports with atomically ordered surface structure for the controlled deposition of metal particles, thus creating excellent model systems for supported metal catalysts [3, 4]. These model catalyst systems have been used successfully to investigate the relationship between surface structure and catalytic activity, such as particle size effects and metal-support interaction [5].

One class of model systems, the so-called planar model catalysts,[6] i.e. metal particles deposited on flat oxide single crystalline surfaces, are particularly useful in the quest for novel catalysts with tailored selectivities, since they allow the preparation and characterisation of well-defined metal-oxide interfaces, which have been demonstrated to play a decisive role in the performance of oxide-supported metal catalysts [7]

The application of thin film oxide phases in electronic device technology requires the

precise control of the stoichiometry of the oxide, which is not trivial if the films are very thin and close to a metal surface. In ultrathin oxide films on metals with the oxide thickness of the order of one to several atomic layers, the stoichiometry and the oxidation state may not be identical to those of known bulk phases, because the proximity to the metal surface perturbs the electronic structure of the oxide. Interfacial oxide layers particular to and stabilised by the interface may thus be formed, and these are the subject of a recent publication of F.P. Netzer [8].

There are incidental reports in the literature that oxide phases in the vicinity of a metal surface occur in a lower oxidation state than in the thermodynamically most stable oxide phase. This is conspicuous in the case of transition metal oxides, which can form oxides with different oxidation states. Intuitively, this preference for "lower oxides" (this term is used by Netzer to designate a low oxidation state or substoichiometric oxide phases) at the metal- oxide interface may be ascribed to the electron donor properties or the "reducing character" of a metallic surface. In his review Netzer examined the published evidence and showed that there indeed appears to be a general trend [8].

An interesting effect in the context of reduced oxides near metallic phases has been reported in the field of heterogeneous catalysis: the so-called strong metal-support interaction (SMSI) effect [9, 10]. It has been observed that the high temperature reduction of an oxide-supported metal catalyst leads to a catalyst surface with significantly altered chemical properties, namely reduced capabilities of  $H_2$  and CO chemisorption but increased reactivity for some catalytic reactions. This striking phenomenon has prompted a great number of studies over the last 20 years, and the SMSI effect has been found in a number of catalyst systems, where the oxide support consists of a reducible transition metal oxide. There is now converging opinion in favour of the so-called encapsulation or decoration model of SMSI [11, 12]: the metal particles of the catalyst in the SMSI state are (partially) covered by a reduced oxide phase.

Accordingly, the oxide support in the proximity of the metal particles is reduced to a lower oxide, which tends to spread over the metal surface, thus encapsulating the metal particles. This different wetting behaviour towards metals of lower transition metal oxides, as compared to the higher oxidation state oxides, has been associated with an altered interfacial energy balance[13]. Also, the possible role of the metal phase in catalyzing the reduction of the oxide support at the metal-oxide-phase boundary has been suggested

[14]. Clearly, interfacial oxide phases must play a critical role in this oxide migration effect, and an intermediate  $TiO_{1.1}$  type oxide double layer has recently been proposed to encapsulate the Pt particles, as observed in a scanning tunnelling microscopy (STM) study of Pt on  $TiO_2(110)$  [12].

The essential characteristics of a metal-oxide interface are the geometry (structure and morphology), the electronics (electronic energy level structure), the chemistry (stoichiometry) and the adhesion strength. The last includes physical as well as chemical interactions, which sometimes lead to a distinction between reactive and nonreactive interfaces [15]. A suitable approach to studying the basic aspects of interfaces at the atomic level is to use model systems, created by growing ultrathin films on single crystal substrates. With regard to the purpose of this thesis, namely to identify oxide phases at the metal-oxide-phase boundary, the controlled growth of thin layers of oxides on metal single crystal surfaces appears to be the most promising approach. Indeed, the most of the published work which addressed the question of structure and stoichiometry of interfacial oxide layers involved the growth of ultrathin films of oxides on metal single crystal surfaces.

In this work two inverse model catalyst surfaces will be presented, which have been fabricated and investigated under ultra high vacuum conditions. As the work represents results from experimental research work, chapter 2 gives a detailed description of the experimental setup used to obtain these results. The major part of the presented results was obtained on a transportable ultra high vacuum system (called the "Scienta UHV system") which is equipped with a high resolution electron analyser and was designed for experiments involving synchrotron radiation. One of the first aims of the experimental work was the setup of this transportable machine as an end-station at the Materials Science Beamline of the synchrotron facility ELETTRA in Trieste, Italy. Due to the lack of a detailed manual and the insufficient support by the manufacturing company Scienta, the properties of this special analyser had to be explored before reproducible results could be expected. As a result of the measurements on the high resolution electron analyser a home-made manual has been written by the author (appendix C). Since the technical details of tuning and maintenance of the Scienta UHV system are of minor interest for those who are not working with this system, chapter 2 only contains the most important results concerning the alignment and resolution test results for the Scienta UHV system. Furthermore, chapter 2 contains a coverage definition for an oxide film on a metal substrate

which is frequently used throughout the work, the "monolayer-equivalent".

Chapter 3 contains the results and discussion obtained on a Cerium-oxide/Rh(111) inverse model catalyst. Ultrathin layers of cerium oxide have been deposited on a Rh(111) surface and their growth morphology, structure, and thermal stability have been investigated by LEED, STM, XPS, and valence band resonant photoemission. Furthermore, the adsorption of CO and the reaction of CO with preadsorbed oxygen has been investigated by comparing the Rh(111)2x1-O surface and ceria decorated Rh(111) inverse model catalyst surfaces using C 1s and O 1s core level and valence band photoelectron spectroscopy with synchrotron radiation. The CO exposures in this work have been performed at 300-320K to restrict the adsorption of CO to the Rh sites of the catalyst surface. In Chapter 4, another metal-oxide/metal interface is presented. Here, ultrathin layers of manganese oxide have been deposited on a Pd(111) surface and their oxidation state, growth mode and thermal stability have been investigated by LEED, STM, XPS, and valence band photoemission. Both chapters represent results obtained separately on the  $CeO_x/Rh(111)$  and the MnO/Pd(111) interface, thus each chapter includes its own introduction and summary.

## 1.1 Acknowledgements

First of all I want to express my gratitude to the supervisor of my PhD, Prof. Dr. F.P. Netzer, who gave me the opportunity to learn scientific work on an interesting topic and simultaneously supported my employment by the Austrian Science Funds. Next, I am very grateful to Prof. Dr. Mike Ramsey and Dr. Kevin C. Prince for the personal and scientific help I got during my work in Triest. I would like to thank Carla Castellarin Cudia for her support with the CO adsorption experiments on the cerium oxide/Rh(111) inverse model catalyst and the kindly permission to use some of her STM-results on the same interface in my thesis. Furthermore I want to thank Hannes Schoiswohl and "Zarko" Surnev for letting me join some of the experiments and publications on the vanadium oxide/Rh(111) interface. Due to a lack of time and space I decided to cut these experiments out of my thesis, but I am looking forward to their publication in Hannes' PhD thesis.

Furthermore, I would like to thank all members of the Surface Science group of the Karl Franzens University in Graz - those who have not been mentioned explicitly in the previous paragraph - for a nice cooperative time with a lot of fruitful discussions and personal help in the last three years.

*Mein besonderer Dank gilt meiner Ehefrau Katharina, die in den ersten Jahren unsere Ehe besonders wegen meiner häufigen Abwesenheit im Zuge der Forschungsarbeiten in Triest sehr viel Verständnis aufbringen mußte.*



**Figure 1.1:** Photograph of the Surface science group taken in jan., 2003; from left to right: Hannes Schoiswohl, "Mike" G. Ramsey, Carla Castellarin-Cudia, Günter Frömmel, Svetlozar "Zarko" Surnev, Falko P. Netzer, Georg Koller, Sven Eck, Barbara Winter, Michael Sock, Jan Ivanco and Georgi Tzvetkov

## Chapter 2

## Experimental

## 2.1 The Scienta UHV system

All photoemission spectra presented in this work have been obtained with a Scienta SES-200 electron analyser mounted on a three-chamber ultra high vacuum system designed by *M.G. Ramsey*. In the following sections, the entire UHV system will be called the "Scienta system". Figure 2.1 shows a picture of the Scienta system during the photoemission and -absorption measurements at the Materials Science Beamline (MSB) of the third generation synchrotron ELETTRA in Triest, Italy.

The SCIENTA UHV system attached to the  
Materials Science Beamline (MSB) at ELETTRA

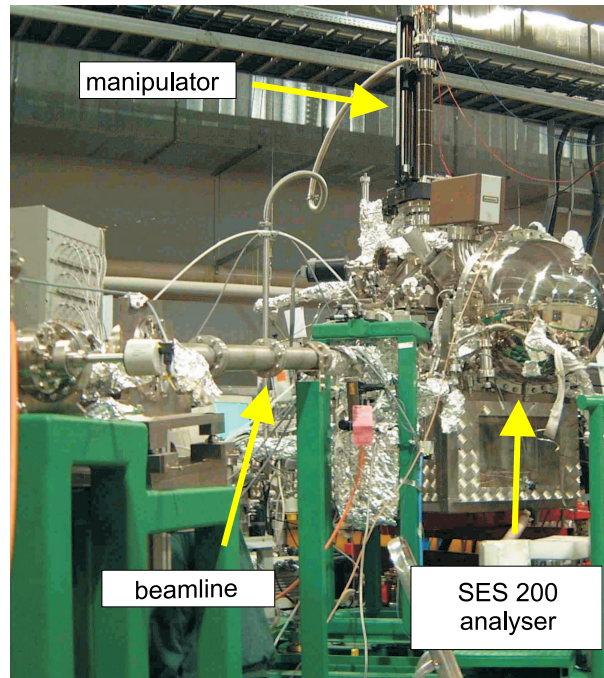


**Figure 2.1:** Picture of the SCIENTA UHV system taken in the period when it was used as end-station for the Materials Science Beamline at ELETTRA (Aug., 2000 to Dec., 2002)

In this system ultra high vacuum (UHV) conditions during experiments are obtained by an array of pumps, as shown in figure 2.2. Furthermore, the image shows the arrangements of the three chambers, which can be separated from each other by valves holding pressure differences up to  $10^{-10}$  mbar versus atmospheric pressure.

The fast entry chamber (FE) has a storage facility for 5 sample plates which can be transferred to the preparation chamber with a magnetically coupled transfer mechanism. A turbomolecular pump attached to the fast entry chamber ensures UHV conditions within



10 hours (including a bake-out of the FE) after replacing the samples in the sample storage facility and starting the pump.

During the measurement period 2000-2003, the preparation chamber (PCH) was equipped with a LEED apparatus for low energy electron diffraction analysis, a gas-inlet system ("gas-handling-line") for  $O_2$  and CO dosing, a mass-spectrometer to monitor residual gas and dosing gas purity, an  $Ar^+$  ion-gun for sample cleaning, an ionisation gauge ("ion-gauge") to measure the system pressure, an electron beam evaporator for metal evaporation, a getter pump ("NEG" stands for Non Evaporating Getter) to improve the  $H_2$  background pressure and a manipulator for the sample transfer.

### The Scienta UHV System (2000-2003)

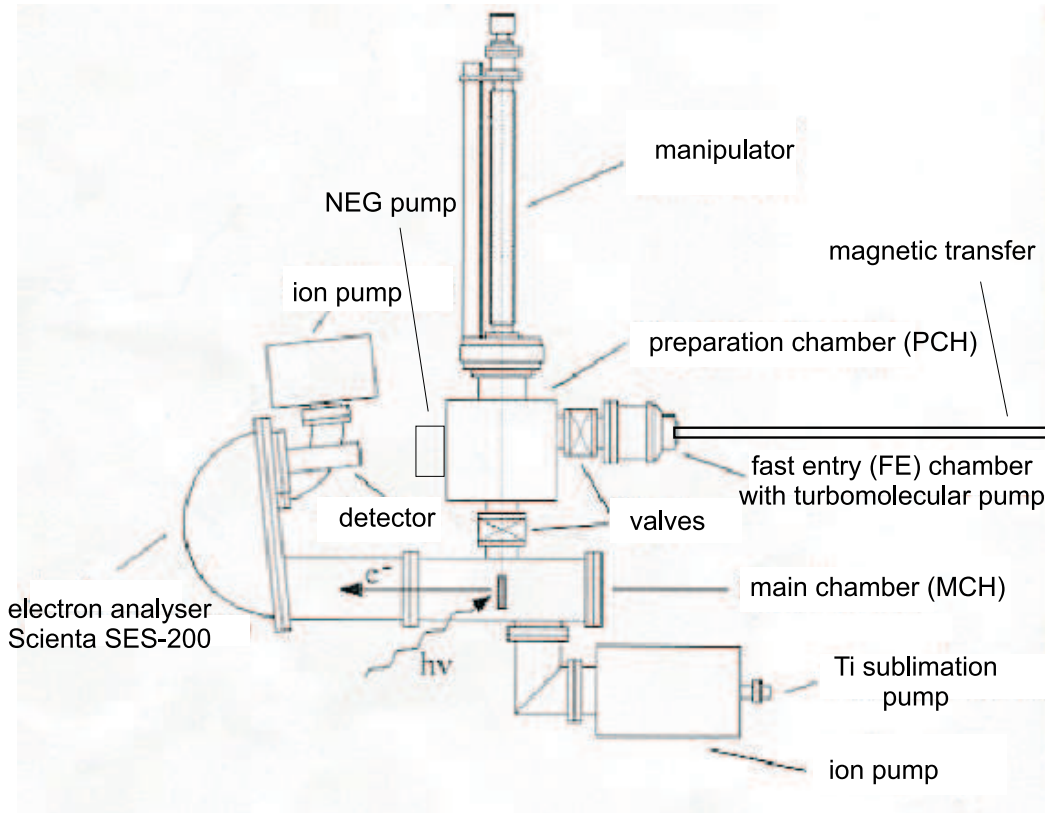


**Figure 2.2:** Illustration of the arrangement of chambers, pumps, manipulator and electron analyser in the SCIENTA UHV system in the period of the measurements presented in this work

The manipulator (Omniac 600) is combined with a sample holder designed by *K. Ansperger* and *M. G. Ramsey* and allows sample transfers (from the fast entry chamber to the preparation chamber and from the preparation chamber to the main chamber)

with samples spot-welded onto standard Omicron-type sample plates. A sapphire between sample holder and manipulator head ensures that the sample is thermally connected to the manipulator rod (which is in turn coolable to temperatures  $\leq 100\text{K}$  by the use of liquid nitrogen), rotatable in azimuthal directions and at the same time electrically isolated to enable indirect heating. The indirect heating of the sample is achieved by applying positive voltages (relative to ground) up to  $1000\text{V}$  to the sample to accelerate the electrons emitted from a tungsten filament (grounded on one side) right behind the sample plate. Due to the high annealing temperatures needed for the rhodium single crystal ( $\geq 1000^\circ\text{C}$ ), the sample plate was made of molybdenum. To fix the rhodium crystal on the plate, a  $0.5\text{ mm}$  thick tantalum wire was spot-welded first around the sides of the  $\text{Rh}(111)$  crystal and then onto four tantalum studs that had been embedded into the molybdenum plate. For the mounting of the palladium crystal a tantalum plate was used. To minimise field effects in the photoemission experiments all materials used for the sample head have to be non-magnetic. Since UHV conditions are required during the measurements to maintain defined clean surface conditions, only high vapour pressure materials are commonly used in UHV systems. For the presented measurements the manipulator was also equipped with a chromel-alumel thermocouple. The thermocouple was spot welded directly to the sides of the  $\text{Rh}(111)$  and  $\text{Pd}(111)$  single crystals, which allows exact temperature measurements during the experiments. (Knowing the exact temperature was considered more important than the ability to transfer the sample to the FE chamber which is inhibited when the thermocouple is attached directly to the crystal.)

The third chamber, the main chamber (MCH), is equipped with a titanium sublimation pump and two ion pumps, an ionisation gauge to monitor the pressure, a discharge lamp, a twin anode x-ray source and the high resolution SES 200 electron analyser. During the  $\text{CeO}_x/\text{Rh}(111)$  experiments, the Scienta system was attached to the Materials Science Beamline (MSB) at ELETTRA as discussed in detail in section 2.2. During the  $\text{MnO}/\text{Pd}(111)$  experiments, the discharge lamp and the x-ray source were mounted symmetrically on both sides of the electron analyser lenses, with incident angles of  $\sim 45^\circ$  when the sample was positioned for normal emission. The discharge lamp is used for He I and He II-excited ultraviolet photoemission spectroscopy (UPS). He I and He II excitation can be obtained by controlling the He partial pressure inside the discharge lamp. Stable discharge conditions with reasonable countrates in UPS have been routinely obtained for

partial pressures of  $2 \times 10^{-1}$  mbar for He I and  $4 \times 10^{-2}$  mbar for He II, as measured with a Pirani gauge; the pressure rise in the main chamber due to the flow of He through the lamp aperture was  $\sim 5 \times 10^{-8}$  mbar in case of He I and  $\sim 5 \times 10^{-9}$  mbar in case of He II. The He I spot diameter on the sample was  $\sim 1$  mm as measured with the countrate on the multi-channel plate of the SES 200 analyser.

The twin anode water-cooled x-ray source was mounted on a linear motion facility that allowed the x-ray source aperture to approach the sample up to a distance of  $\sim 2$  cm for XPS measurements. At this distance the spot diameter of the x-rays on the sample is  $\sim 10$  mm, as measured with the SES electron analyser. The source was commonly operated with 15 kV and an emission current of 10 mA. After proper outgassing of both filaments and anodes, no pressure rise was detected in the main chamber during XPS measurements. For UPS measurements keeping the x-ray source close to the sample influenced the secondary electrons (especially the low kinetic electrons around the secondary electron cut-off) due to field effects created by the stainless steel capping of the x-ray source, thus the x-ray source was retracted by  $\sim 10$  cm for measurements where the secondary electrons had to be monitored, i.e. for workfunction measurements. The inside of the measurement chamber (MCH) was shielded with a special alloy, called  $m\mu$ -metal, in order to reduce the influence of magnetic fields on high resolution photoemission spectroscopy. After the UHV system had been attached to the Materials Science beamline (MSB) the magnetic fields inside the main chamber were measured and found to be two orders of magnitude less than the terrestrial magnetic field.

## 2.2 Alignment of the Scienta system at a beamline

For part of the presented measurements the Scienta end-station was attached to a newly built beamline at the 3<sup>rd</sup> generation synchrotron ELETTRA in Trieste, Italy. The Materials Science beamline (MSB) was designed and built by the Czech Academy of Sciences and was still in the commissioning phase when the SCIENTA UHV chamber was mounted as the end-station. Figure 2.3 shows a simplified sketch of end-station and beamline at ELETTRA.

Insufficient alignment of end-station and beamline may cause severe problems in getting acceptable results with the Scienta analyser both in terms of resolution and intensity, therefore the proper alignment procedure will be described briefly.

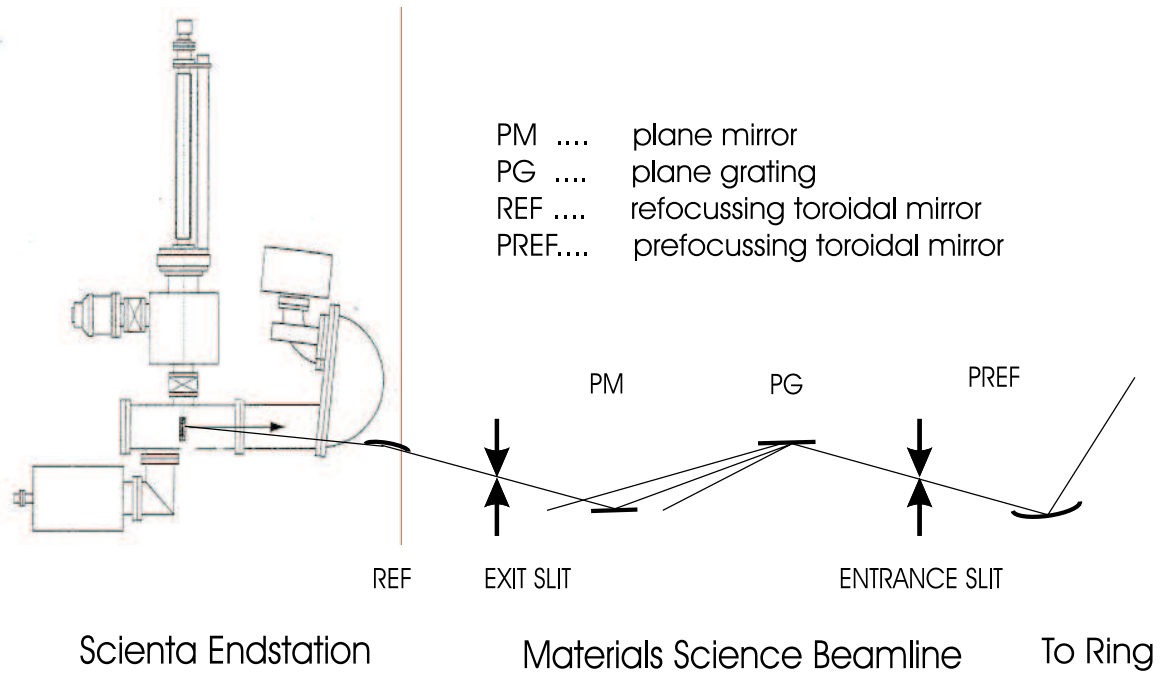


**Figure 2.3:** Sketch of beamline and end-station at ELETTRA

Figure 2.4 shows the angular orientation of the ports on the Scienta main chamber and the various mounted sources when the Scienta system was attached to the Materials Science Beamline at ELETTRA. For the chamber alignment on a beamline the ports for the synchrotron light and for the Helium lamp should be used in the same way as shown in this sketch because only this arrangement enables the observation of light from the beamline on a window directly opposite to the beamline entrance port. Both He-lamp

and beamline ports provide the same photon incidence angle for the sample in normal emission, which is crucial for resolution tests.

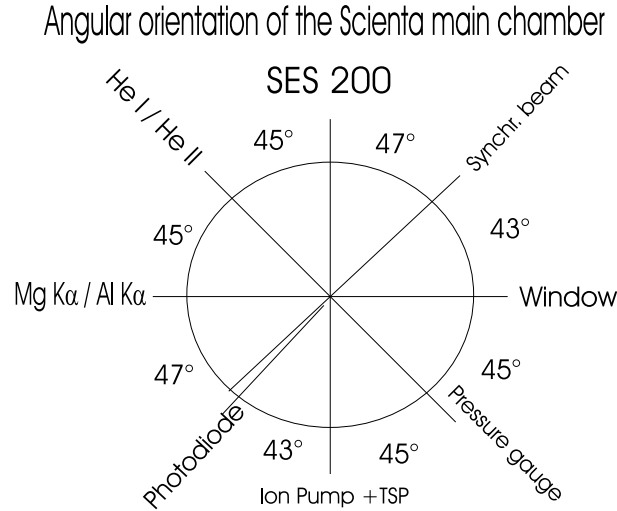


**Figure 2.4:** Angular orientation of the Scienta main chamber ports

The rough chamber alignment relative to the beamline can be checked by putting zero order light through the main chamber while the manipulator is retracted to the preparation chamber.

*Note: Never switch on the channel plate voltage (on the Scienta Supplies rack) when the beamline monochromator is set to zero order light! Zero order light reflected into the electron analyser will seriously damage (if not ruin) the fragile multi-channel-plate (mcp)!* At ELETTRA, a photo diode was mounted on a linear motion adapter on the port opposite to the photon beam. The photodiode could be retracted vertically and the zero order light could be observed on a window behind it. For better observation of the beam position this window was covered with fluorescent material. Since the two ports of beamline entrance and opposite window do not align exactly (due to a fabrication mistake), the zero order light was observed slightly to the left of and above the centre of the window (the misalignment is  $\sim 2$  degrees, as sketched in figure 2.4) after the best alignment of chamber and beamline had been found .

*Note: Before starting the fine adjustment of the chamber set all lens deflection voltages (P5, P6/P7, K4/K5) in the ESCA300 software to zero; this has to be repeated for all pass energies (for details see Scienta manual in appendix A).*

As soon as the zero order light has been observed on the right position on the window, the

monochromator should be set to first order light at a photon energy where the beamline gives a high flux, i.e. below the big loss of photon flux around 280eV due to carbon-induced absorption on the optical elements. Subsequently, the sample is moved to a vertical position (z-direction) where a good countrate had previously been obtained on the channelplate with He I and x-ray excitations. This position should show the sample vertically aligned with the He lamp and analyser aperture and centred in the direction perpendicular to the lens of the analyser.

Using the synchrotron light, the fine adjustment of the chamber position can be obtained by watching the counts on a sample-derived photoemission feature (e.g. for most metals the valence band with the characteristic Fermi edge) in the Scienta *interactive mode*. This mode allows the simultaneous monitoring of the counts on the mcp-camera while carefully changing the chamber position (for description of the "Scienta Interactive mode see the manual given in appendix A). At ELETTRA, the photon beam was vertically centred on the sample by adjusting the refocus mirror of the Materials Science beamline. If there is no such facility to adjust the height of the light exiting the beamline, the chamber height must be adjusted in such a way that the light in the centre of the sample produces counts in the centre of the mcp. Depending on the spot size the photoelectrons will show a more or less narrow vertical stripe on the channel plate along the "energy direction". After the vertical adjustment, the angle of the chamber relative to the beamline has to be fine adjusted.

*Note: The best alignment is reached if moving the sample towards the analyser lenses moves the counts evenly (no severe intensity loss) from left to right across the multi channel plate (mcp) as observed on the monitor (i.e. perpendicular to the kinetic energy direction on the mcp)*

The correct focus position of the sample - which is crucial for a good resolution obtained with the SES 200 analyser - is defined by the photoelectron stripe being horizontally centred on the multi-channel plate (with all deflection voltages set to zero). At ELETTRA the resolution of the beamline and the Scienta analyser were measured with both He I and beamline excited photoelectrons generating counts in the centre of the channelplate. Before testing the resolution obtained with the beamline, the Helium lamp position was adjusted. After that adjustment, both Helium lamp and synchrotron beam resulted in counts on the same region of the detector window without moving the sample.

## 2.3 Testing the resolution of the SES 200 analyser with the Helium lamp

Before testing the resolution of the Materials Science beamline the resolution of the electron analyser had to be measured. The line width of any photoemission line measured is a contribution of several energy widths. Equation 2.1 is a simplification assuming that there is only two contributions to the total line width: thermal line width and instrument (analyser) resolution.

$$total\ line\ width = \sqrt{(thermal\ line\ width)^2 + (analyser\ resolution)^2} \quad (2.1)$$

To measure the resolution of the analyser a sample of polycrystalline gold was used. The thermal contribution is  $thermal\ line\ width = 4kT$  where  $k$  is the Boltzmann constant ( $k = 8.6 \times 10^{-5}$  eV/K) and  $T$  is the sample temperature in Kelvin. To obtain a sharper line the gold was cooled with liquid nitrogen to a temperature of  $\sim 100$ K. Although there was no thermocouple directly attached to the gold, a thermocouple attached to the sample-holder proved that the temperature was stable. The thermal line width of the Fermi edge at 100 K is  $4kT = 400k = 34.4$  meV.

The theoretical resolution of the SES-200 hemispherical analyser is given by

$$(SES - resolution\ in\ eV) = \frac{PE \times (slit\ width\ in\ mm)}{2 \times 200\ mm} \quad (2.2)$$

where PE is the pass energy and 200 mm is the radius of the analyser hemisphere. This equation leads to a theoretical resolution table (Table 2.1) for the SES-200 analyser which can also be found in Leisenberger's thesis [16].

The total resolution of analyser and Helium lamp was measured using the line width of the gold Fermi level at 120 K as described above. The line width was taken from the spectra in two different ways. The first method is shown in figure 2.5

In this method the experimenter draws a line through the assumed Fermi cut-off, next he determines the height of the cut-off. 16 percent are subtracted from the height on both sides. The width of the resulting cut-off is the measured line-width  $\Delta E$  that has to be converted into eV on the energy scale of the spectrum. Since the drawing of the first line might already lead to an experimental error, a second method was used to determine the line-width of a measured Fermi level.

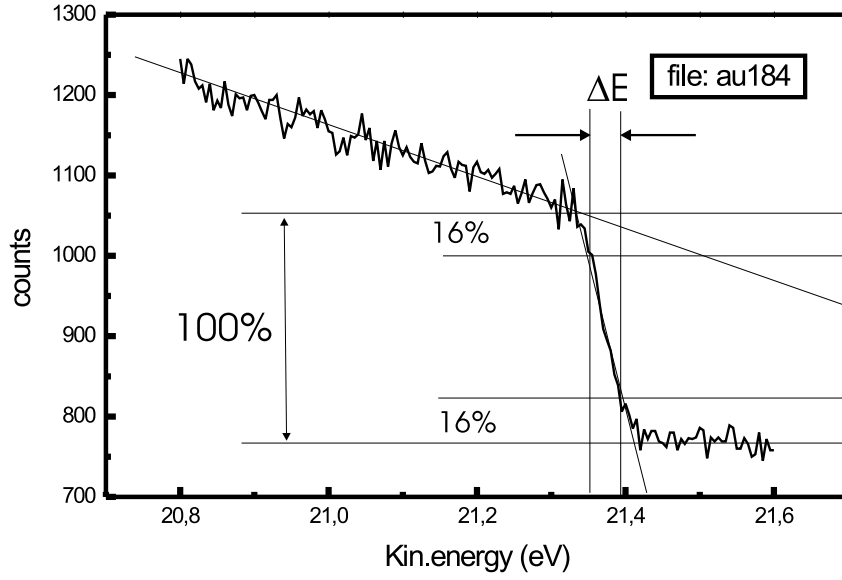


**Figure 2.5:** Taking the line-width  $\Delta E$  from a Fermi level spectrum

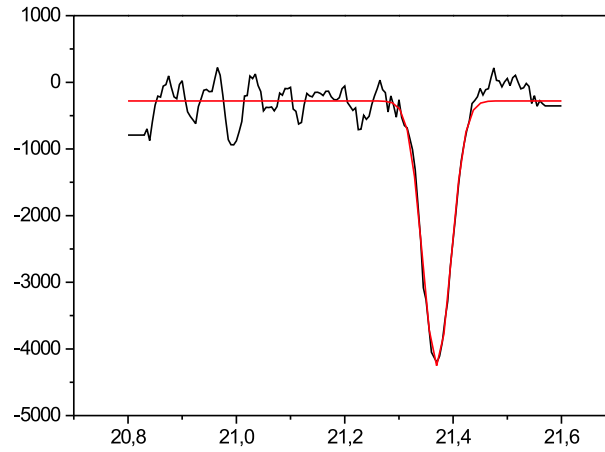


**Figure 2.6:** Fermi level differentiated and fit with a Gaussian

In this second method the spectrum was exported into a data analysis program. With this program the spectrum was differentiated and then a Gaussian peak was fit into the resulting spectrum. Figure 2.6 shows the differentiated spectrum and the Gauss-fit corresponding to the spectrum in figure 2.5. The full width at half maximum (FWHM) of that Gauss-fit can be considered as a good approximation for the width of the Fermi level cut-off. Both ways to determine the line-width showed the same results within the experimental error of  $\pm 5\%$ . With the help of standard data analysis software (such as



Microcal Origin used here) the second method was found to be more convenient.

The experimental restrictions of measuring the complete resolution table were given by the fact that too low pass energies and slits lead to very poor statistics and too high counts might have damaged the multi channel plate (mcp) of the detector. For that reason the measured resolution table presented in table 2.2 is not complete. In that table the numbers in brackets give the values obtained by differentiating and Gauss-fitting, the other numbers were obtained on the same spectra using the 16-percent-method.

In the given resolution tables the diagonals correspond to constant spectral intensity and resolution because the intensity scales linearly with the pass energy and reciprocally with the slit width. Halved pass energy and doubled slit width therefore leads to the same intensity and resolution. Best statistics were obtained in the diagonal that joins (PE 20 / slit 1.5) and (PE 75 / slit 0.5).

Assuming that the thermal line width is 30 to 40 meV and correlating the measured resolution to the total resolution in equation 2.1 on page 19, the measured resolution table matches the theoretical values given in table 2.1 for the pass energies 5, 10, 20 and 40. Interestingly, pass energy 75 with a 0.8 mm wide slit showed a better resolution than equation 2.2 predicted. This result might be explained with a source (spot on the sample) that is smaller than the 0.8 mm slit width of the Scienta entrance slit. The combination of pass energy 75 and slit width 0.8 mm has been taken as a standard for most of the achieved "high resolution" spectra because it provides a resolution reasonable for solid state photoemission features and a good count rate and therefore good statistics. Furthermore pass energy 75 can be used with both high energy (HiEp) and low energy (LoEp) high voltage supplies of the Scienta end-station and showed the same count-rate and resolution for both supplies.

Slit/PE	5	10	20	40	75	150	300	500	1000
2.5	31	62	125	250	469	938	1875	3125	6350
1.5	19	38	75	150	281	562	1125	1875	3750
0.8	10	20	40	80	150	300	600	1000	2000
0.5	6	13	25	50	94	188	375	625	1250
0.3	4	8	15	30	57	113	225	375	750
0.2	3	5	10	20	38	75	150	250	500

**Table 2.1:** SES-200 theoretical resolution table (slit width in mm, resolution in meV)

Slit/PE	5	10	20	40	75
1.5	52(45)	64(61)	95(90)	-	-
0.8	-	-	66(61)	78(75)	99(100)
0.5	-	-	60(61)	68(75)	76(83)
0.3	-	-	-	60(61)	59(68)
0.2	-	-	-	-	59(60)

**Table 2.2:** SES-200 measured resolution in meV, explanation in the text

## 2.4 Definition of monolayer-equivalent

In the current work all coverages are either given in monolayers (ML)-for CO adsorption and metal deposition on metal surfaces- or in monolayer-equivalents (MLE)- for metal-oxides on metal surfaces.

A monolayer coverage of a (gas-)molecule on a single crystal surface is defined by the number of molecules that is needed to adsorb one molecule on each surface atom.

The adsorption of molecules from the gas phase onto a given metal surface is determined by the amount of molecules provided by the gas pressure and the amount of adsorbed molecules. This correlation is described by the sticking coefficient  $S$ . Simplified, a sticking coefficient of one means that every molecule that hits the surface stays there. For the deposition of a metal on another metal that is not an unreasonable assumption.

The growth mode of metal oxides on metal single crystal surfaces varies depending on the materials and surfaces chosen. Without knowing the stoichiometry and the unit cell of the growing film, the coverage of a full monolayer cannot be determined. To have a relative coverage measure of the deposited material, the so-called monolayer equivalent has been created. A monolayer (ML) of V on Pd(111) is one vanadium atom per Pd(111) surface atom. A monolayer equivalent of V evaporated in an oxygen atmosphere onto Pd(111) is the same amount of vanadium, but the actual oxide coverage of the Pd(111) surface will depend on the structure and stoichiometry of the oxide on the surface. The deposition rate of the various metal evaporators used in the presented experiments were measured with a quartz micro-balance in the UHV.

The quartz micro-balance measures a change in the quartz frequency related to adsorbed/deposited mass per square cm.

With a given density of  $1\text{g/cm}^3$  the control unit of the micro balance shows a height in cm :

$$1_{unit} = \frac{\text{weight of adsorbed mass per area (g/cm}^2\text{)}}{\text{density (1 g/cm}^3\text{)}} = \text{height(cm)} = 10^{-8}\text{height(Angstrom)}$$

### 1 MLE $\text{CeO}_x$ on Rh(111)

The Rh (111) surface has  $1.59 \times 10^{15}$  atoms per  $\text{cm}^2$

1 MLE Ce on Rh(111)= 1 Ce atom per Rh(111) surface atom

$$1 \text{ mol } Ce = 140.1 [g] \dots 6.022 \times 10^{23} [atoms] (\text{Avogadro})$$

$$x [g] \dots 1.59 \times 10^{15} [atoms]$$

$$x = \frac{1.59 \times 10^{15} \times 140.1}{6.022 \times 10^{23}}$$

$$x = 10.56 \times 10^{-8} [g/cm^2]$$

That means 10.56 units measured with the micro-balance refer to 1 MLE  $CeO_x$  on Rh(111).

### **1 MLE $MnO_x$ on Pd(111)**

The Pd(111) surface has  $1.526 \times 10^{15} [atoms/cm^2]$ .

1 MLE Mn on Pd(111) = 1 Mn atom per Pd(111) surface atom.

$$1 \text{ mol } Mn = 54.94 [g] \dots 6.022 \times 10^{23} [atoms] (\text{Avogadro})$$

$$x [g] \dots 1.526 \times 10^{15} [atoms]$$

$$x = \frac{1.526 \times 10^{15} \times 54.94}{6.022 \times 10^{23}}$$

$$x = 13.9 \times 10^{-8} g/cm^2$$

That means 13.9 units measured with the micro-balance refer to 1 MLE  $MnO_x$  on Pd(111).

## **Chapter 3**

### **The Ceria-Rhodium(111) interface**

### 3.1 Introduction

Cerium is a group III metal of the lanthanides, with the atomic number 58 and a hexagonal close packed (hcp) crystal structure. Metallic cerium is prepared by reduction techniques, such as by reducing cerous fluoride with calcium, or by electrolysis of molten cerous chloride or other cerous halides. Cerium is an iron-grey lustrous metal. It is malleable, and oxidises very readily at room temperature, especially in moist air. Except for europium, cerium is the most reactive of the rare-earth metals. It slowly decomposes in cold water, and rapidly in hot water. Alkali solutions and dilute and concentrated acids attack the metal rapidly. The pure metal may ignite when scratched with a knife. It is the most abundant of the rare earth metals and is found in minerals including allanite, monazite, cerite, and bastnaesite. Cerium and its oxides are used in a variety of fields ranging from cosmetics over the manufacturing of rechargeable batteries and gas sensors to various catalytic applications, where the most important application is probably in the field of heterogeneous catalysis.

#### Cerium oxidation states

The stable cerium oxidation states at room temperature are given in table 3.1. Furthermore, this table gives the electronic ground state configuration for cerium and its bulk oxides and the melting / decomposition temperatures to indicate their thermal stability.

#### The Cerium-oxide/ Rhodium interface

Rhodium (Rh) and cerium oxides are critical components of current automotive three-way exhaust catalysts (TWCs), particularly with regard to NO and CO conversion at

	formal oxidation state	ground state configuration	melting /decomp. temp.
Ce		$[Xe]4f^1(5d6s)^3$	795°C
$Ce_2O_3$	$Ce^{3+}$	$[Xe]4f^1$	2230°C
$CeO_2$	$Ce^{4+}$	$[Xe]4f^0$	2400°C

**Table 3.1:** Cerium and cerium-oxide ground state configuration and melting/decomposition points

rich and stoichiometric air-fuel ratios. Rh supported on  $CeO_2$  is active for  $NO_x$  and CO conversions.  $ZrO_2$  incorporation into  $CeO_2$  is reported to lead to high thermal durability in terms of oxygen storage capacity. In a very recent publication the design of advanced automotive exhaust catalysts involving ceria, zirconia and rhodium has been presented and tested towards catalytic reactivity [17]. In this paper, the Rh- $CeO_2$  interaction contributing to  $NO_x$  reduction and the catalytic behaviour of Rh-loaded  $CeO_2$ - $ZrO_2$  mixed oxide is addressed.

Thus, cerium oxide and Rh are important components of the three-way catalyst used in commercial catalytic converters for automotive emission control. The addition of ceria improves the performance of the group VIII metals of the catalyst and a combination of various favourable factors has been ascribed to the promoting role of ceria [18]. One outstanding property of ceria is certainly its reversible oxygen storage capacity, which provides oxygen to the gas mixture during fuel-rich cycles and absorbs oxygen in the fuel-lean cycles. The key factor for the latter property is the  $Ce^{4+} \rightleftharpoons Ce^{3+}$  redox pair, which allows for an easy release or uptake of oxygen by providing a source or sink of electrons. Also, the interactions at the interface between the ceria and the noble metal may add to the promoting role of ceria by enhancing the catalytic activity for CO oxidation [18], perhaps via the creation of active sites at the oxide-metal boundary [19].

In a previous work the oxygen pressure and substrate temperature parameters for reactive evaporation of cerium have been investigated in order to obtain ordered Ce oxide films on Rh(111) at their highest possible oxidation state [20]. In these investigations a Rh(111)- $(1.4 \times 1.4)CeO_x$  LEED pattern has been reported for thin cerium oxide films, which have been prepared by reactive evaporation in  $2 \times 10^{-7}$  mbar  $O_2$  onto Rh(111) at 250°C. Furthermore, other oxide overlayer preparation methods, such as evaporation of Ce metal and post-oxidation by  $O_2$  exposure at various temperatures or oxidation of Ce-Rh alloy phases, formed by annealing of metallic Ce overlayers, have also been tested. Qualitatively similar results, i.e. epitaxially ordered Ce oxide films have been obtained. However, carbon free metallic Ce overlayers are difficult to prepare and the oxide films prepared by the latter methods are more prone to contamination and less completely oxidised than by using the single step reactive evaporation process.

After the determination of the chemical state of these films by laboratory source XPS and UPS more detailed investigations of the ceria films have been performed by

two collaborating PhD students. The author of this work concentrated on photo-emission studies of the growth and reaction behaviour of the ceria/Rh(111) films using synchrotron and laboratory source excited photo-emission techniques in combination with low energy electron diffraction (LEED). Contemporaneously Carla Castellarin-Cudia concentrated on the growth and reduction behaviour of the same metal-oxide/metal interface using combined LEED and STM techniques. Consequently, a more detailed description of the STM and LEED results can be found in C. Castellarin's thesis [21].

The experiments of this study have been performed in two different ultrahigh vacuum (UHV) systems, with base pressures  $\sim 1 \times 10^{-10}$  mbar in both systems. The STM experiments were carried out in a custom-designed three-chamber UHV system equipped with a room temperature STM (Omicron micro-STM), sample preparation and LEED/AES facilities as described by C. Castellarin Cudia [21]. The STM was operated in the constant-current mode, with sample biases between -2 and +2 V and tunnelling currents between 1 and 1.5 nA. Typically, higher biases were used for imaging thicker oxide films, whereas biases  $< 1$  V were employed for high-resolution imaging of the thin ceria layers. The Rh crystal was mounted on a Mo sample plate and was heated indirectly by electron bombardment from the back side. The crystal temperatures were determined by thermocouple readings in separate calibration experiments and preset heating powers were used subsequently. The temperatures given in the STM experiments are accurate to  $\pm 20^\circ\text{C}$ .

The photoemission spectra were measured in a multi-chamber custom-designed high-resolution electron spectrometer, with a Scienta SES 200 analyser and a preparation chamber containing sample cleaning, evaporation and LEED facilities as reported in section 2.1. For the CO adsorption experiments the system was pumped by turbomolecular and ion pumps and, in addition, it contained a NEG pump (SAES Getters SpA) to minimise the partial pressure of hydrogen in the background gas; the base pressure during these experiments was  $\leq 1 \times 10^{-10}$  mbar. The CO and  $\text{O}_2$  gases were dosed from the system ambient via leak valves.

For the resonant photoemission and high resolution XPS experiments the Scienta spectrometer was attached to the Materials Science beamline, operated by the Czech Academy of Sciences in cooperation with ELETTRA. The photoelectron spectra were taken in normal-emission geometry with photons incident at  $47^\circ$  with respect to the surface normal.



The C 1s core level spectra have been recorded with a photon energy of 400 eV and a combined energy resolution (SX 700-type monochromator plus spectrometer) of 0.3-0.4 eV, whereas the valence band spectra have been taken with photon energies between 108 and 125 eV, i.e. off and on the Ce 4d-4f giant resonance, with a total energy resolution of 0.1 eV (details concerning the Ce 4d-4f resonance are given in section 3.1.2). Both on-resonance and off-resonance spectra are in the broad Cooper minimum region of the Rh 4d emission cross section.

The O 1s and Ce 3d core level spectra have been excited with a conventional laboratory ( $MgK\alpha$ ) x-ray source because of monochromator limitations at higher photon energies. The laboratory X-ray source was attached in a symmetric position to the inlet of the synchrotron radiation, with photons incident at  $45^\circ$  in normal emission geometry.

The Rh sample in this system was also heated by electron bombardment from the back side. However, the crystal temperatures were measured directly with a chromel-alumel thermocouple spot-welded to the edge of the crystal. The temperatures given in the XPS experiments are therefore accurate to  $\pm 5^\circ\text{C}$ .

The clean Rh(111) substrate surface was prepared by  $Ar^+$  ion bombardment and annealing at  $1000^\circ\text{C}$ , and heating cycles in  $O_2$  followed by a final anneal at  $1100^\circ\text{C}$ . The cleanliness of the Rh(111) surface was checked by XPS, AES and LEED. Cerium oxide overlayers were deposited by reactive evaporation of cerium metal in  $2 \times 10^{-7}$  mbar  $O_2$  onto the Rh(111) surface at a temperature of  $250^\circ\text{C}$ . The cerium evaporation rate was monitored by a quartz crystal micro balance and a typical evaporation rate was 0.5 monolayer  $\text{min}^{-1}$ . Since the actual oxide coverage depends on the morphology and oxidation state of the oxide overlayer, which in turn varies as a function of coverage, only relative cerium oxide coverages will be given in this chapter in terms of monolayer equivalents (MLE). As mentioned before, this corresponds to the evaporated amount of Ce as referred to the density of Rh(111) surface atoms, as discussed in section 2.4. Note that a single monolayer of  $CeO_2(111)$  on the Rh(111) surface corresponds to  $\sim 0.5$  MLE. After careful outgassing of the cerium evaporator contamination-free Ce-oxide/Rh(111) surfaces have been routinely obtained. In the annealing experiments the surfaces were kept for 10 minutes at the indicated temperatures.

### 3.1.1 Determining the cerium oxidation state with XPS

#### Chemical shifts in XPS

One of the most valuable diagnostic properties of the core level photoelectron spectroscopy is the *chemical shift*. The chemical shift implies that the detailed core-level binding energy of an atom of a certain element depends on the chemical surroundings of the probed atom. Chemical shifts were unambiguously observed for the first time by Hagström and co-workers [22, and ref. therein]. Since then the shifts have developed into a routine technique to identify and distinguish between different chemical species in a system. The chemical shift is the basis of many of the most powerful applications of core level spectroscopy, however, the understanding of the chemical shift is still developing and regularly discussed also in rather general terms, as proved by a recent publication by Martensson and Nilsson [22].

The core level binding energy is defined as the total energy difference between the ionised (N-1 electron) final state system and the initial (N electron system). In this way one can express the chemical shift between two systems A and B as

$$\Delta E_B = E_{ion,A}(N-1) - E_{G,A}(N) - (E_{ion,B}(N-1) - (E_{G,B}(N))) \quad (3.1)$$

$$= E_{ion,A}(N-1) - E_{ion,B}(N-1) - (E_{G,A}(N) - (E_{G,B}(N))) \quad (3.2)$$

The shift is thus determined by two total energy differences, one relating to the initial states and one relating to the final states. The chemical shift may be dominated by either the initial or final state terms in equation 3.2.

Often chemical shifts are treated in a different way which leads to a different meaning of the terms *initial* and *final state effects*. This is related to the often used separation of the core level binding energy into a set of contributions which correspond to different levels of approximations. The ionization energy is then given by a sum of two terms.

$$E_B = E_{Koopman} + E_{relaxation} \quad (3.3)$$

The first term is the orbital energy or the frozen orbital approximation energy. This would be the ionization energy given by Hartree-Fock calculations, if all other electrons were unaffected by the ionization (Koopman's theorem). The second term, the relaxation energy, is due to the relaxation or screening by the other electrons in the system as the

core electron is removed. There is first of all an atomic contribution to the relaxation energy due to the contraction of the atomic orbitals. In a molecular or solid system there is in addition a flow of charge towards the core hole site. In fact, in extended systems the ionization often leads to a final state in which the core hole site is more or less completely neutralised by a valence electron. (A third energy contribution to the chemical shifts, the correlation energy contribution, which partly covers the insufficiency of the assumptions of Hartree Fock eigenvalues, is on good grounds often neglected.)

It has been common to refer to the two terms in equation 3.3 as the initial and final state shifts, respectively. This nomenclature has been adopted in section 3.1.1. However, this separation is completely different from the one in equation 3.2 which is based on the total energy terms. There are several reasons why the expression in equation 3.3 has been quite commonly used. Often it is simply assumed that the relaxation energy is the same for the ionization of different atoms in a system or that it is nearly the same for core ionisations in similar systems. The experimental shifts are then compared directly to calculated Koopman's shifts. This is a great simplification because no total energies have to be calculated. This constancy of relaxation energies occurs rather often although it is most difficult to know when this approximation really applies. Another reason for sticking to this type of approach originates from the earlier use of potential models for interpreting chemical shifts, i.e. the notion that the chemical shifts are due to the charge state of the ionised atom [22, and ref. therein]. The calculated orbital energies are sensitive to the charge state in much the same way as they are in these potential models. The original potential model worked well in certain classes of carbon systems but failed completely in other cases owing to the neglect of screening or relaxation effects. In spite of this, the general idea has continuously directed the thinking of the field.

## Ce 3d XPS

Photoelectron spectra are final state spectra which reflect the initial states to a greater or lesser extent, depending on the localisation of the states themselves. The striking properties observed in many solids containing lanthanide elements originate always from the presence of an open 4f shell keeping largely its atomic character. The localisation of the 4f charge inside the mean orbit of the 5s, 5p, 5d and 6s shells introduces strong final states effects in XPS [23].

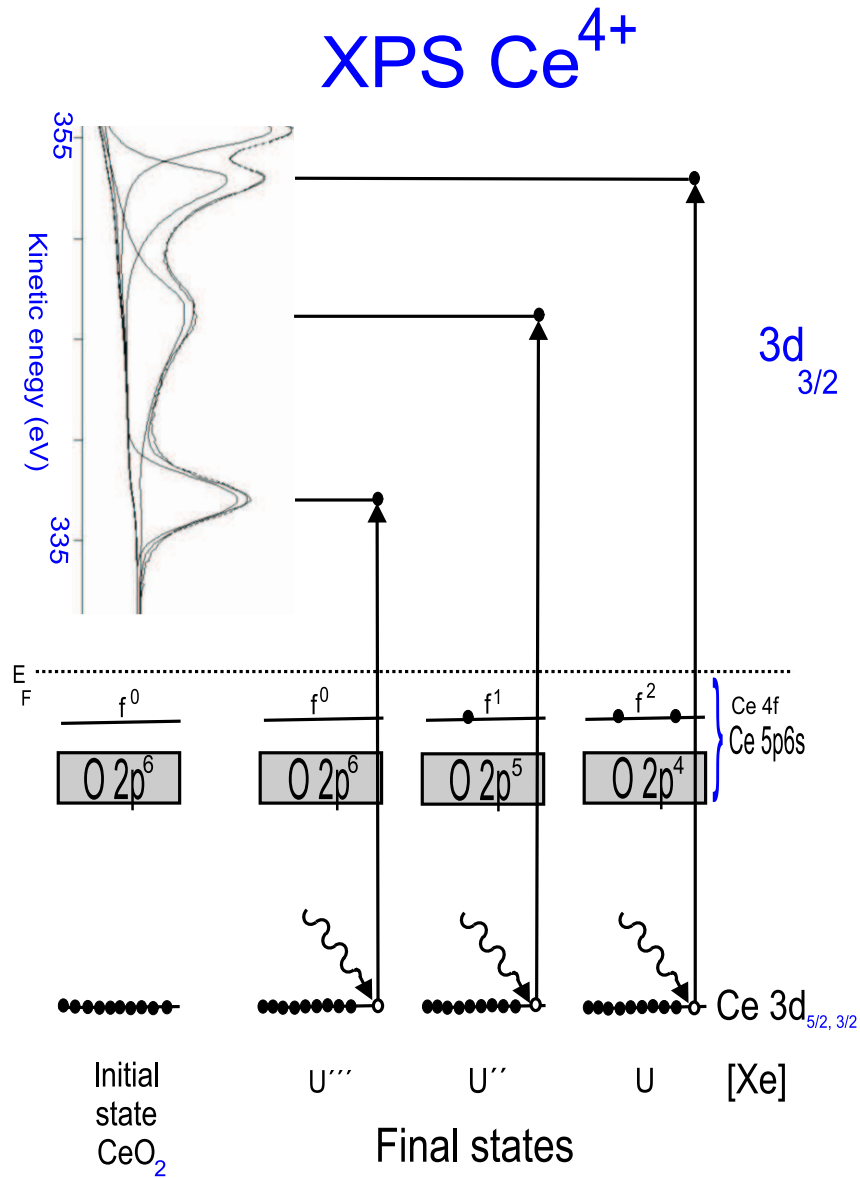
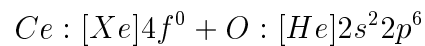


**Figure 3.1:** Sketch to explain the  $\text{Ce}$  3d photoemission spectrum

Figure 3.1 sketches the initial and final states for  $\text{Ce}3d_{3/2}$  photoemission in the case of  $\text{CeO}_2$ . As table 3.1 shows, the ground state of  $\text{CeO}_2$  is:



Thus, the valence band of  $\text{CeO}_2$  is dominated by the filled O 2p states. The generation of a hole in the 3d shell by the photoemission process induces a reaction of the valence band electrons. The valence band reaction to the hole can be explained as electrostatic screening, which leads to an energetically more favourable configuration. The strongly

localised 4f electrons are more suitable to screen the hole in the Ce 3d state than the neighbouring O 2p electrons, thus the O 2p electrons start to populate the Ce 4f states. This leads to three different final states originating from the  $Ce : [Xe]4f^0$  initial state:

$$Ce\ 3d^9\ (4f\ 5d\ 6s)^0 + O\ 2p^6$$

$$Ce\ 3d^9\ (4f\ 5d\ 6s)^1 + O\ 2p^5$$

$$Ce\ 3d^9\ (4f\ 5d\ 6s)^2 + O\ 2p^4$$

The final state with the twofold occupied 4f state is the energetically most favourable because it screens the Ce 3d hole best. Therefore this is the final state with the lowest measured binding energy. The maxima in the XPS Ce 3d spectra are assigned as  $f^0$ ,  $f^1$  and  $f^2$  due to the 4f final state occupation.

In a similar way the Ce 3d maxima of  $Ce_2O_3$  can be assigned. Cerium in  $Ce_2O_3$  is threefold ionised ( $Ce^{3+}$ ) and has a remaining 4f electron in the ground state. Thus the possible final state configurations are restricted to  $4f^1$  and  $4f^2$ . The *chemical shift* between the two oxidation states of Ce is  $\approx 1$  eV. Here, the *chemical shift* is the difference in measured XPS binding energies between two atoms of the same element but with different chemical surroundings. Taking the definition of Eqn. 3.3, it is an initial state effect which can be explained by the chemical surrounding influencing the atomic potential, thus the binding energy. Knowing the chemical shift, the spin-orbit split and the possible final states one can unambiguously assign the Ce 3d photoemission maxima of the cerium oxides.

Figure 3.2 shows the total Ce 3d spectra of  $Ce^{4+}$  and  $Ce^{3+}$  measured on a thick film of reactively evaporated Cerium oxide on Rh(111). Table 3.2 proves that the values obtained for thick  $CeO_x$  films on Rh(111) after reactive evaporation and after subsequent annealing in UHV coincide with the ones obtained on  $CeO_2$  and  $CeO_{1.5}$  films on Pt(111) as published by Hardacre et al. [24].

In a study of ordered ultra thin cerium oxide films on Pt(111) Schierbaum undertook strong efforts to deconvolute the Ce 3d spectra of a mixed cerium oxide surface in order to evaluate the percentages of each oxidation state on the surface [25]. Figure 3.3 shows a deconvolution of the Ce 3d spectrum obtained on 0.67 MLE  $CeO_x/Rh(111)$  after reactive evaporation. The deconvolution was performed with the WinESCA software using Voigt functions keeping all parameters (Gaussian/Lorentzian mix, asymmetry and FWHM)

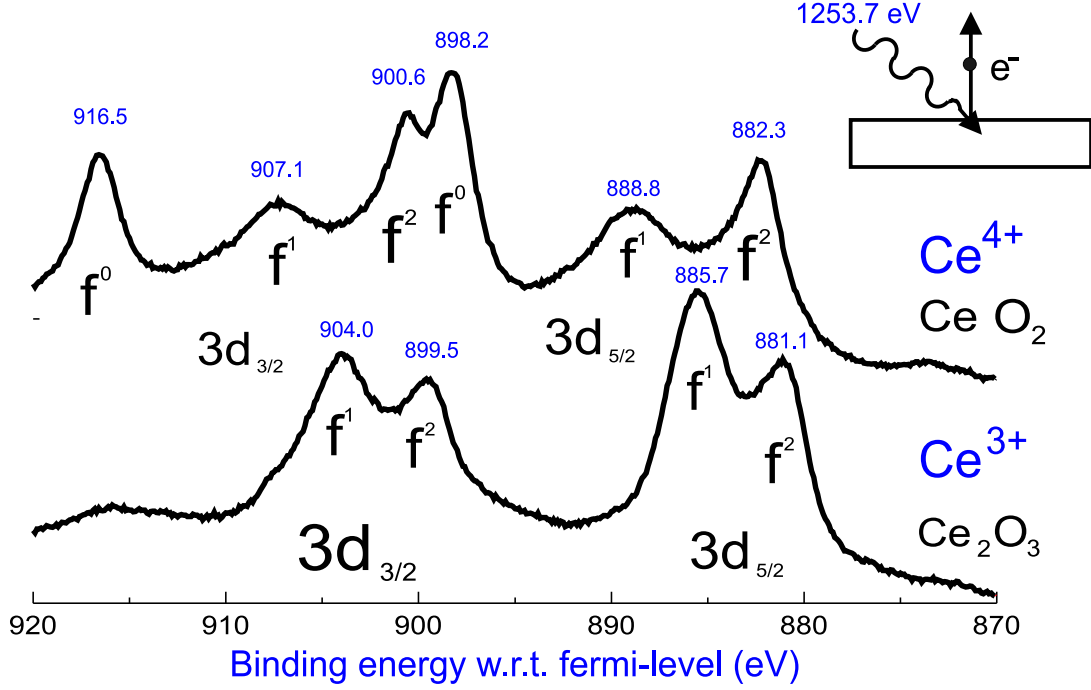


**Figure 3.2:**  $\text{MgK}\alpha$  - excited Ce 3d spectra of the two cerium oxidation states; top: 12 MLE  $\text{Ce}^{4+}$  obtained after reactively evaporating 12 ML Ce onto Rh(111) at  $250^\circ\text{C}$ ; bottom:  $\text{Ce}^{3+}$  obtained after annealing the same surface to  $850^\circ\text{C}$  in UHV for 5 minutes

equal within 20% for each spin-orbit splitting pair (e.g.  $\text{Ce}3d_{5/2} - f^1$  and  $\text{Ce}3d_{3/2} - f^1$ ). Furthermore the spin orbit splitting energy was fixed to 18.3 eV and the ratio between 5/2 and 3/2 area of the same final state was fixed to 1.5. As described partly in previous publications [20, 8] and discussed in detail later (section 3.2.2), the Cerium oxide /Rh(111) surfaces with coverages below 1 MLE showed an overlap of  $\text{Ce}^{4+}$  and  $\text{Ce}^{3+}$  derived maxima in their Ce 3d spectra.

Due to the *chemical shift* of the 2 different initial states, the *spin-orbit splitting* and the different *final states* 10 different photoemission maxima have to be taken into account in the deconvolution of the Ce 3d spectra. The different unknown lifetimes of the final states further complicate a reasonable deconvolution. However, the relative percentages of  $\text{Ce}^{3+}$  and  $\text{Ce}^{4+}$  can be evaluated in a simpler way using the stand-alone  $3d_{5/2} - f^0$  final state maximum, which only appears in the Ce 3d spectra of  $\text{Ce}^{4+}$ . For a 15 MLE thick cerium oxide film reactively evaporated in  $2 \times 10^{-7}$  mbar  $\text{O}_2$  on Rh(111) at  $250^\circ\text{C}$  the Ce 3d spectrum is equivalent to the ones obtained for bulk  $\text{CeO}_2$  [26, 25, 24] and can

Binding energies of the Ce 3d maxima				
[24]	maxima in this work	BE(eV)	FWHM	BE(eV)[24]
$Ce^{4+}$				
u'''	$f^0 3d_{3/2}$	916.5	2.3	916.7
u''	$f^1 3d_{3/2}$	907.1	4.6	907.4
u	$f^2 3d_{3/2}$	900.6	2.6	901.0
v'''	$f^0 3d_{5/2}$	898.2	2.3	898.2
v''	$f^1 3d_{5/2}$	888.8	4.8	888.8
v	$f^2 3d_{5/2}$	882.3	2.6	882.3
$Ce^{3+}$				
u'	$f^1 3d_{3/2}$	904.0	4.4	903.5
u <sup>0</sup>	$f^2 3d_{3/2}$	899.5	3.1	898.8
v'	$f^1 3d_{5/2}$	885.7	3.4	884.8
v <sup>0</sup>	$f^2 3d_{5/2}$	881.1	3.3	880.1

**Table 3.2:** *MgK $\alpha$  excited Ce 3d maxima measured on a 12 MLE thick CeO<sub>x</sub> film reactively evaporated on Rh(111) ( $Ce^{4+}$ ) and annealed to 850°C in UHV ( $Ce^{3+}$ ) compared to the values published by Hardacre et al.*

therefore be taken as a reference for  $Ce^{4+}$ .

The area of the  $f^0$ - derived maximum in the Ce 3d spectrum divided by the area of the total Ce 3d spectrum gives a dimension free number (and is thus independent from the amount of Ce on the surface) which can be attributed to 100%  $Ce^{4+}$

$$\frac{A(f^0, 15 MLE)}{A(total, 15 ML)} = \delta \text{ (.....100\% } Ce^{4+}) \quad (3.4)$$

In the same way, the area of the  $f^0$ -derived maximum in the Ce 3d spectrum can be evaluated for an arbitrary  $CeO_x$  surface.

$$\frac{A(f^0, arb.coverage)}{A(total, arb.coverage)} = \alpha \text{ (.....x\% } Ce^{4+}) \quad (3.5)$$

This number ( $\alpha$  in equation 3.5) represents the amount of  $Ce^{4+}$  in the  $CeO_x$  surface layer and has to be referenced to the number obtained for 100%  $Ce^{4+}$ :

$$\frac{\alpha}{\delta} = x \text{ (.....\% } Ce^{4+}) \quad (3.6)$$

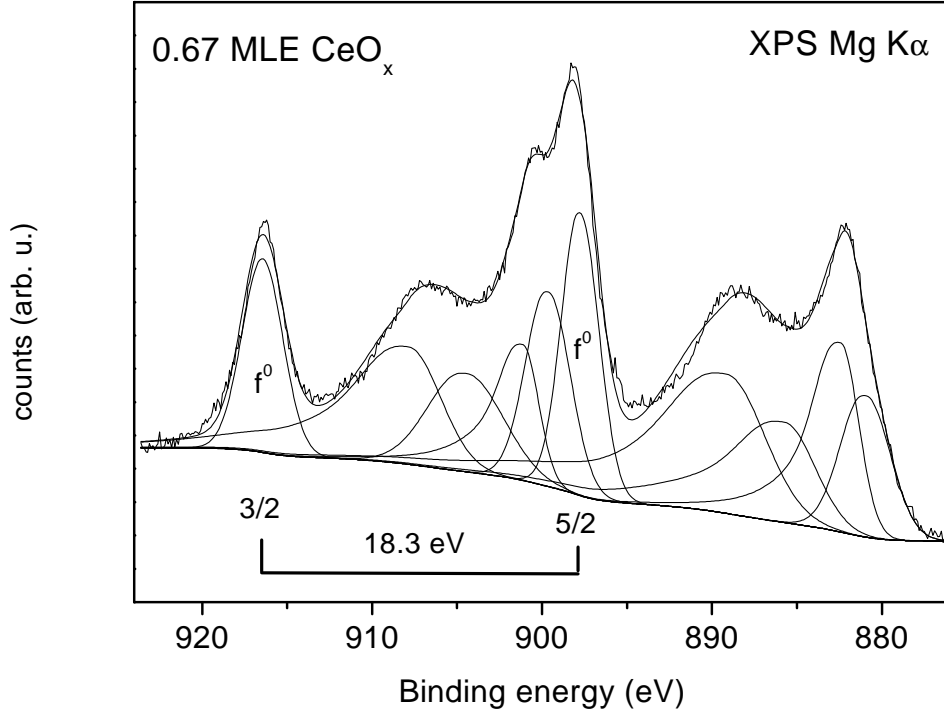


**Figure 3.3:** *MgK $\alpha$ -excited Ce 3d spectrum of 0.67 MLE reactively evaporated cerium oxide; the Ce 3d shows maxima which can be attributed to a mixture of  $Ce^{4+}$  and  $Ce^{3+}$ -derived final states*

In section 3.2.2- figure 3.14, this value is plotted for reactively evaporated cerium on Rh(111) as a function of the cerium oxide coverage.

Considering only two possible oxidation states in the cerium oxide films the amount of  $Ce^{3+}$  (called  $\beta$ ) can be determined as

$$\beta (\%Ce^{3+}) = 1 - x \quad (3.7)$$

Or, using the equations 3.4 to 3.7:

$$\beta = 1 - \frac{A(f^0, \text{arb.coverage}) \cdot A(\text{total}, 15 \text{ MLE})}{A(\text{total}, \text{arb.coverage}) \cdot A(f^0, 15 \text{ MLE})} \quad (3.8)$$

Examples for the evaluation of the cerium oxidation state with this method are given in [20]. For cerium oxide films on Rh(111), which have been reduced by annealing in UHV, this determination of the oxidation state holds as long as no alloying overlaps



the reduction behaviour. The formation of a Ce-Rh surface alloy renders the simplified method inaccurate because a Ce3d- $f^0$  final state has been reported for the cerium-rhodium surface alloy [27]. In fact, a close look at the bottom spectrum in figure 3.2 reveals a small component at 915.5 eV, that can be attributed to  $f^0$  final states arising from a Ce-Rh surface alloy. Presumably the cerium at the interface between the thick  $CeO_x$ -film and the substrate starts alloying with rhodium at the employed annealing temperature, as suggested by XPS measurements including photoemission spectra in the O1s, Rh 3d and Ce 3d regions. However, the difference in the binding energy between the oxides and the Ce-Rh surface alloy allows to distinguish between the  $f^0$  component of  $CeO_2$  and the one of the Ce-Rh surface alloy.

### 3.1.2 $CeO_x$ - resonant photoemission of the 4f state

Apart from the indirect measurement of the Ce 4f states in Ce 3d photoemission spectra, they can also be excited directly. The Ce 4f emission can be amplified relative to the rest of the valence band features by changing the exciting photon energy and using cross section effects as well as with resonance effects. Table 3.3 summarises the calculated atomic subshell photoionization cross sections for cerium, oxygen and rhodium subshells that contribute to the  $CeO_x$ /Rh(111) valence band as a function of photon energy ; the numbers have been taken from [28]. The table illustrates that by going from He II excitation to photon energies around 130 eV, the photoemission from the Rh 4d band strongly loses intensity with respect to the O 2p and Ce 4f valence band features; The cross section for Rh 4d drops by 99 %, whereas the ones for O2p and Ce 4f only drop by 90 and 30%, respectively. This suppression of the substrate valence band features in the photoemission spectra originates from the Cooper minimum of the Rh 4d band centred at  $\sim 120$  eV.

Two different valence band photo emission spectra of 0.7 MLE  $CeO_{2-x}$  on Rh(111) are presented in figure 3.4. Both spectra were taken with synchrotron radiation at the synchrotron facility ELETTRA (for details see experimental section). The photon energies delivered by the monochromator were measured by evaluating the kinetic energy position of the Fermi edge. The top spectrum in figure 3.4 was taken with a photon energy of 124 eV, the bottom one with 108 eV.

The valence band spectrum excited with 108 eV is dominated by electrons emitted from the O 2p band (at binding energies between -3 and -7 eV). Furthermore a small contribution of the Rh 4d band is visible at binding energies ranging from the Fermi level

Atomic photoionization cross sections for the  $CeO_{2-x}$ /Rh(111) valence band

subshell	Excitation source and/or photon energy					
	$AlK\alpha$	$MgK\alpha$	200eV	132.3eV	He II	He I
Ce 4f	$0.22 \times 10^{-2}$	$0.39 \times 10^{-2}$	0.7365	1.394	2.033	0.6255
O 2p	$0.24 \times 10^{-3}$	$0.50 \times 10^{-3}$	0.1836	0.5795	6.816	10.67
Rh 4d	$0.12 \times 10^{-1}$	$0.20 \times 10^{-1}$	0.3817	0.2930	27.83	22.75

**Table 3.3:** Atomic Subshell Photoionization cross sections for Ce 4f and O2p and Rh 4d

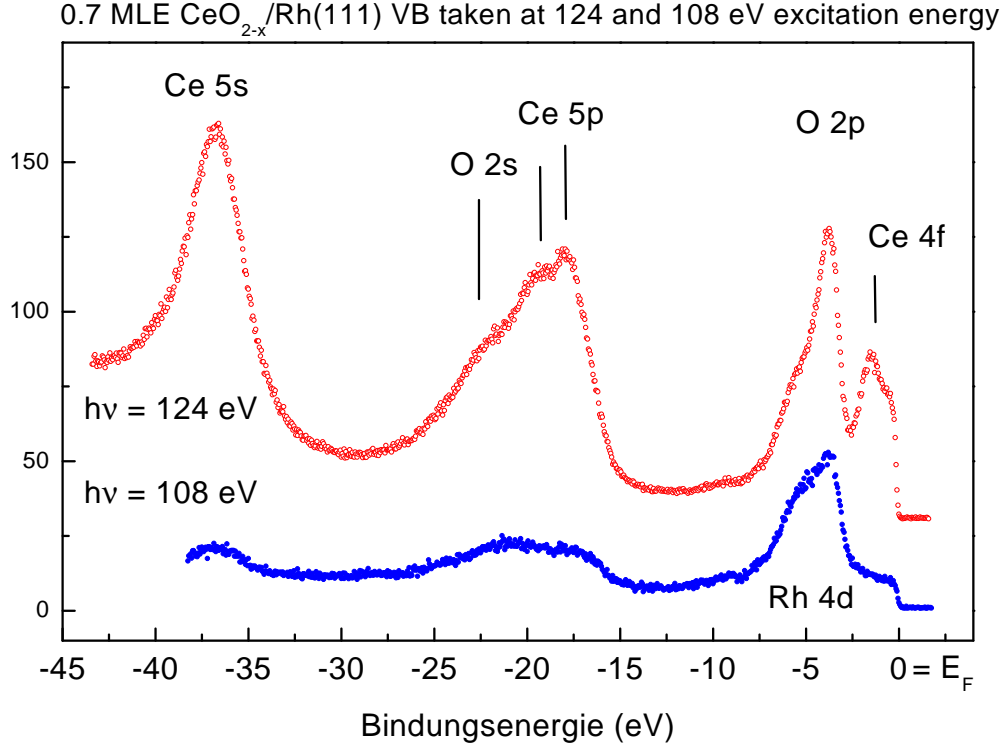


**Figure 3.4:** VB-photoemission spectra of 0.7 MLE  $\text{CeO}_x$  on  $\text{Rh}(111)$ , taken with two different excitation energies; top: photon energy 124 eV, bottom: photon energy 108 eV

to  $\sim 3$  eV. Apart from the low contribution of the Rh 4d band (due to the Rh 4d Cooper minimum around this photon energy), the valence band resembles very much the one obtained for excitation with He II published in previous work [20, chapter 4].

Increasing the photoexcitation energy by 16 eV drastically changes the photoemission spectrum, (top spectrum in figure 3.4). At  $\sim 1.5$  eV below the Fermi level a new photoemission peak appears, which can be attributed to the excitation from the Ce 4f states. The strong enhancement of the Ce 4f derived emission at excitation energies around 125 eV is attributed to a resonance involving Ce 4d and Ce 4f valence band states. A similar resonance - observed in photoabsorption spectra - is known as the *giant 4d-4f resonance* of Ce [29]. The sketch in figure 3.5 is drawn to illustrate this resonance behaviour in the photoemission spectra in a strongly simplified picture. The diagram shows the valence band and the shallow core levels of a cerium and a neighbouring oxygen atom. The inci-

## Ce 4d-4f resonance

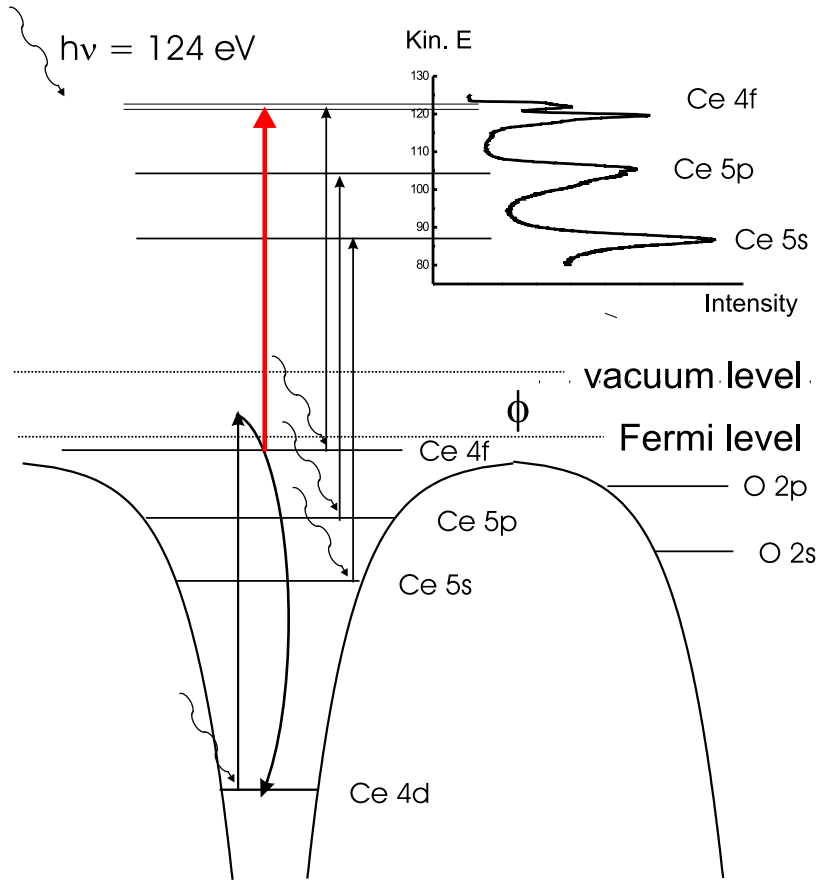


**Figure 3.5:** Sketch illustrating the giant 4d to 4f photoemission resonance in cerium and its oxides

dent photons are sketched as wavy arrows. Direct excitations from the Ce 4f, 5p and 5s levels are sketched as vertical arrows, where the arrow length should reflect the photon energy. On the top right of the graph the resulting spectrum is drawn (intensity versus kinetic energy of the emitted photoelectrons). At photon energies just above the binding energy of the Ce 4d electrons ( $\sim 118$  eV), electrons from this level get excited into unoccupied states just above the Fermi level. Their kinetic energy is not high enough to overcome the workfunction barrier. They re-decay into their stable Ce 4d configuration transmitting their energy to the 4f electrons. The electrons excited by this autoionization process have the same final state as the electrons emitted by the direct transition. This creates an interference between the direct and autoionization emission channels leading to the strongly enhanced emission from the 4f states at this particular photon energy. The

4d-4f excited electrons can interfere also with electrons in the Ce 5p and 5s shells, which leads to a resonance enhancement also for emissions from these levels, as can be seen in figure 3.4. However, the 4f intensity is amplified most, because the probability of energy transfer between electrons is higher if they have the same principal quantum number.

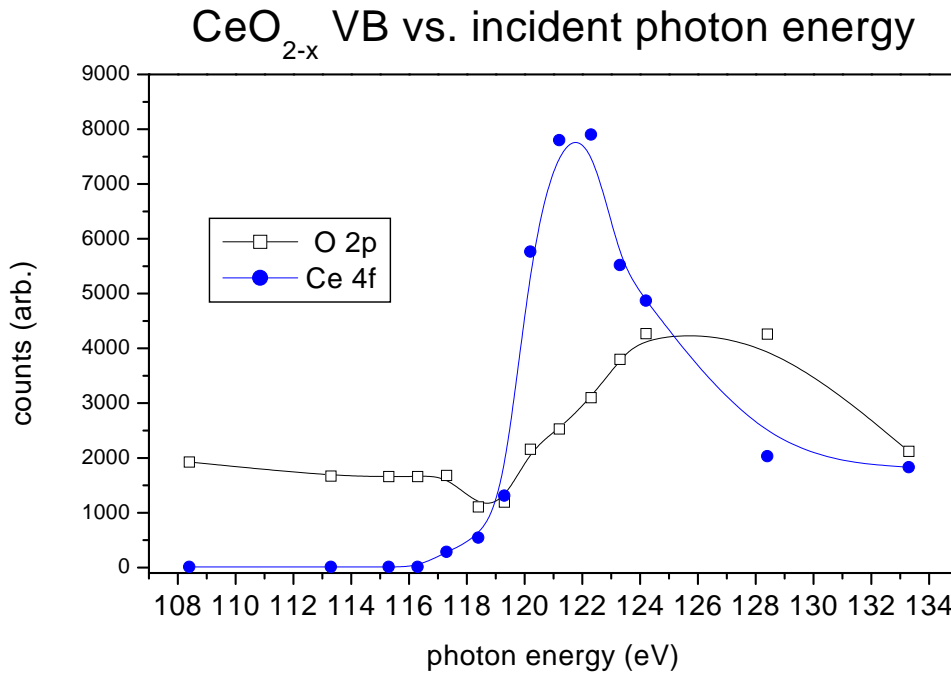


**Figure 3.6:** *O2p and Ce 4f signal area versus exciting photon energy measured on 1 MLE  $CeO_{1.5}/Rh(111)$*

The resonance effect is localised on the cerium atom. Thus, the oxygen valence band electrons should not profit from the 4d resonance. The intensity of the O 2p and the Ce 4f photoelectrons have been measured with different photon energies. Valence band spectra with photon energies from 108 to 134 eV have been measured on a 1 MLE cerium oxide / Rh(111) surface which had previously been reduced to  $CeO_{1.5}$  by annealing in UHV; the resulting VB spectrum at 125 eV was similar to the one presented in figure 3.15d on page 58. The results for the O2p and Ce 4f area are plotted in figure 3.6 versus the exciting photon energy. The intensities have not been normalised to the photon flux of the beamline, which showed a linear increase between 50 and 150 eV due to the monochromator characteristics. All the involved valence band spectra were taken within

one hour, therefore the drop of the intensity due to energy losses within the storage ring can be neglected.

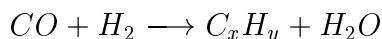
The Ce 4d-4f resonance reveals a  $\sim 4$  eV broad peak with a maximum around 122 eV. Surprisingly, the O 2p intensity shows a resonance behaviour as well, albeit weaker. The O 2p intensity reveals a  $\sim 6$  eV broad resonance centred at  $\sim 126$  eV excitation energy. This enhancement of the O 2p intensity can be explained by the O 2p electrons that are involved in the bonding with the cerium. As mentioned in the introduction cerium contributes to the bonding by providing its (5d6s) electrons for the filling of the O 2p shell. These electrons can be judged as de-localised between the oxygen and the cerium atom. Via this hybridisation with the cerium valence band, the oxygen 2p intensity can profit from the cerium 4d-4f autoionization process.

One of the approximations used by Yeh and co-workers to calculate the atomic photoionization cross-sections given in table 3.3 on page 38 is the *frozen core approximation* which reduces many electron wavefunctions to one-electron wavefunctions. Thus the corrections to core relaxations or other multichannel processes were neglected in these calculations. The calculated values are therefore not applicable to photoionization processes that are known to be many-electron processes, such as the Ce 4d-4f resonance discussed above. This explains why the resonance behaviour illustrated in figure 3.6 is not reflected in the numbers given in table 3.3.

### 3.1.3 Characterisation of CO adsorption sites with HR-XPS

#### CO adsorption on metal surfaces

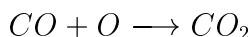
Carbon monoxide investigations appear very frequently in surface science publications due to the catalytic relevance on one side and the relative simplicity of this diatomic molecule on the other side. The catalytic relevance of the CO interaction with metal surfaces is provided by its role in the Fischer-Tropsch synthesis [30],



in the water-gas shift reaction



and in the automotive exhaust gas conversion. In this work, investigations will be presented on the *CO-oxidation reaction*



on our cerium oxide / Rh(111) inverse model catalyst system (section 3.3).

Adsorption experiments of CO on various metal single crystal surfaces have been performed since the very start of surface science studies. The CO adsorption on most of the transition metals has been investigated with every standard surface science technique such as low energy electron diffraction (LEED), vibrational techniques (HREELS, IRAS), inverse- and direct photoemission (IPES, UPS). The development of synchrotrons and monochromatising facilities have made it possible to directly distinguish between different CO adsorption sites not only by means of vibrational spectroscopy, but also with high resolution core level photoemission spectroscopy (HR-XPS). With third generation synchrotron radiation sources (such as BESSY II, MAX II and ELETTRA) and adequate monochromators and electron analysers it is now possible to measure the C 1s core level binding energy with a resolution of 100 meV or better.

On a closed packed surface three different high-symmetry CO adsorption sites can be distinguished, as sketched in figure 3.7. The chemical shift in the C 1s spectra between CO adsorbed in different sites on metal single crystals is typically  $\leq 0.5$  eV. The C 1s binding energies that have been obtained on the three surfaces Pt(111), Rh(111) and

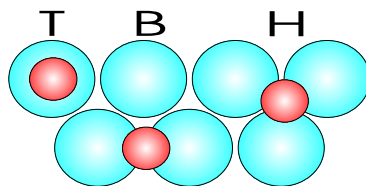


**Figure 3.7:** Schematic diagram displaying the CO adsorption sites on closed packed metal surfaces; T....on-top, B....bridge, H...(3-fold) hollow.

C 1s BE (eV)	Pt(111)	Rh(111)	Pd(111)
3-fold hollow	-	285.4	285.7
bridge	-	-	285.9
on-top	286.7	286.0	286.3
reference	[31]	[32]	[33]

**Table 3.4:** C1s Binding energies of CO adsorbed in different sites on the closed packed (111) surfaces of Pt, Rh and Pd

Pd(111) are given in table 3.4. All these values refer to CO saturation coverages at room temperature. A combination of the XPS results with LEED, STM and vibrational spectroscopy (HREELS) resulted in the attribution of the C 1s binding energies to on-top, bridge and three-fold hollow sites, respectively.

### CO on Rh(111)

The influence of coverage and substrate temperature on the adsorption sites of CO on Rh(111) has been the subject of a recent publication by Beutler et.al. [32]. The low temperature saturation coverage of CO on Rh(111) shows a  $(2 \times 2)$  LEED pattern associated with the  $(2 \times 2)$ -3CO structure which is sketched on the left hand side in figure 3.8. In the same figure on the right hand side two C 1s spectra are displayed together with curve fits for the two major components.

The spectra have been taken at the Materials Science beamline (MSB) at ELETTRA. The raw photoemission spectra have been corrected for photon energy (= kinetic energy of the Fermi edge) and normalised at 284eV binding energy. The resulting C 1s spectra clearly show two different carbon 1s components with binding energies close to the ones



published for CO adsorbed in on-top and in three-fold hollow sites, respectively [32, 34]. Both low and room temperature spectra in figure 3.8 have been fit with two components using by Donjiac-Sunjic convoluted with Gaussian lineshapes. Recently bridge sites have been detected for CO adsorbed on Rh(111) at room temperature [35]. However, treating the two-fold (bridge) and three-fold hollow sites as one "hollow site" component (as compared to "on-top" sites) is sensible considering the 0.35 eV total resolution (induced by the MSB monochromator). The best fit results have been obtained with binding energies of  $286.1 \text{ eV} \pm 0.05 \text{ eV}$  and  $285.6 \text{ eV} \pm 0.05 \text{ eV}$  for on-top and hollow adsorption, respectively. These values are - within the experimental error - identical with the ones given by Beutler [32] and Jaworowski [34].

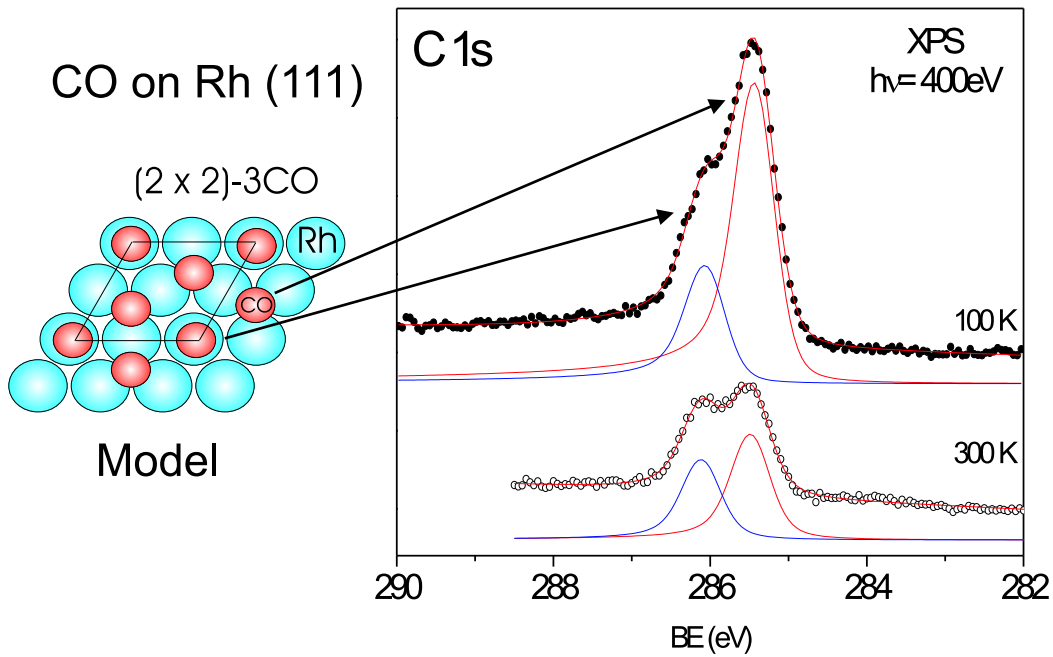


**Figure 3.8:** CO on Rh(111): left hand side: model of the  $(2 \times 2) - 3\text{CO}$  saturation coverage at 100K; right hand side: C1s spectra (circles) and fits (lines) for CO saturation at 100K (filled circles) and at 300K (open circles).

The low temperature saturation structure model for CO on Rh(111) has one CO molecule per unit cell adsorbed in on-top and two molecules per unit cell adsorbed in 3-fold hollow sites. Quantification of XPS spectra is usually complicated due to the un-

known exact number for the photoionization cross-section and the effect of photoelectron diffraction on the measured photoemission signal. However, keeping the measurement geometry and the excitation energy of the incident photons fixed for a set of experiments makes them quantitatively comparable. Under these conditions and relying on Beutlers low temperature saturation model, we can quantify the amount of CO in on-top and hollow sites by taking the 100K-CO saturation spectrum as a reference. In detail, all C 1s spectra have been fit by two components with fixed lineshape parameters and the binding energies given above. Thus, the area of the 100K-286.0eV BE-component refers to a coverage of 0.25 ML CO in on-top sites and the area of the 100K-285.5eV one refers to 0.5 ML CO in hollow sites on Rh(111). (Remember for adsorbates a coverage of 1 monolayer corresponds to 1 adsorbate species per substrate surface atom). All CO coverages given in this work have been determined in this way, for instance, the room temperature saturation for CO on Rh(111) (open circled spectrum in figure 3.8) shows a total CO coverage of 0.45 ML with  $\sim 60\%$  CO in on-top and  $\sim 40\%$  in hollow sites.

### **Oxygen and CO coadsorption on Rh(111)**

The same group which published the CO HR-XPS results on CO adsorbed on Rh(111) [32], investigated also the adsorption sites in O and CO coadsorption phases on Rh(111) by high-resolution core-level photoemission [34]. In this latter work high-resolution core-level spectroscopy was used in combination with low-energy electron diffraction (LEED) and photoelectron diffraction to identify the adsorption sites for three different coadsorbed phases consisting of ordered overlayers of oxygen coadsorbed with CO on the Rh(111) single-crystal surface. The three ordered overlayer structures, which were denoted as 2O+CO/Rh(111), O+CO/Rh(111) and O+2CO/Rh(111), all showed  $(2 \times 2)$  LEED patterns. The different coadsorption phases found by Jaworowski and co-workers are illustrated in figure 3.9.

These coadsorption phases were prepared by dosing  $O_2$  at 550 K (which is similar to the reactive evaporation conditions for  $CeO_x$  films on Rh(111)), and subsequent CO dosing between 200 and 250K ; the photoemission spectroscopy was performed at 120 K [34].

For oxygen on Rh(111) the saturation coverage (obtained by dosing  $O_2$  between 500K and RT) shows a  $(2 \times 2)$  LEED pattern which has been - associated with three equivalent

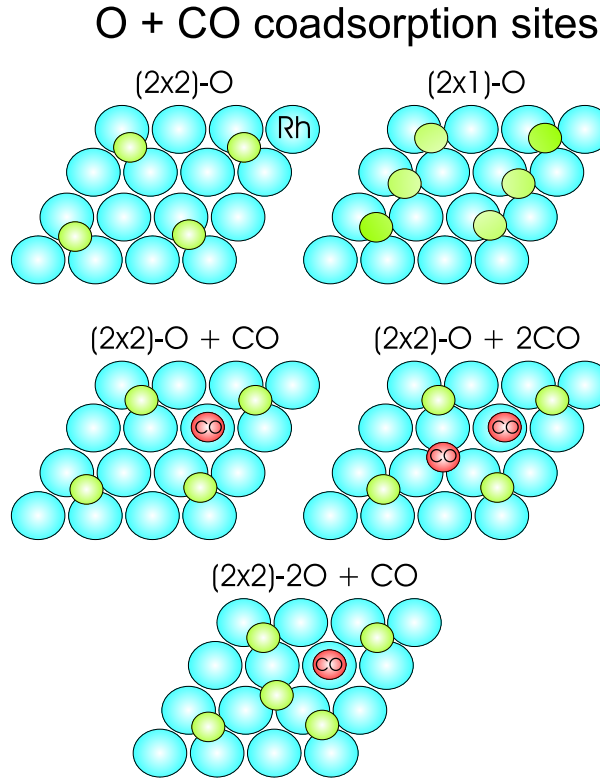


**Figure 3.9:** Model for oxygen and carbon monoxide coadsorption phases on  $Rh(111)$ , as given in reference [34]

domains of a  $(2 \times 1)$ -O overlayer with an oxygen coverage of 0.5 ML [36]. A model of the  $(2 \times 1)$ -O overlayer is shown in the top right drawing in figure 3.9.

In the  $2O+CO$  and  $O+CO$  phases the CO molecules were found to occupy only on-top sites while the  $O+2CO$  phase showed CO molecules in both on-top and three-fold hollow sites. In all cases the oxygen atoms were found in three-fold hollow sites. For the  $O+CO$  and  $O+2CO$  phases the results confirmed previous determinations by LEED, while the  $2O+CO$  phase had not been observed before on  $Rh(111)$ . The core-level binding energies of the C 1s and O 1s core levels for both adsorbates are characteristic of the adsorption site and are very close to the binding energies found for the pure cases of only oxygen or CO adsorbed on  $Rh(111)$ . In the coadsorption phases the interaction between the adsorbates has only a minor influence on the core-level binding energies. For the  $O+2CO/Rh(111)$  coadsorption phase a full CO coverage was not obtained; less than 80% of the unit cells contain two CO molecules.

These coadsorption sites are of interest for the CO oxidation reaction on the cerium

oxide-rhodium inverse model catalyst because they may be precursor states for the O+CO clean-off reaction presented in section 3.3.

## 3.2 Growth and thermal properties of ultrathin cerium oxide layers on Rh(111)

### 3.2.1 The surface phase diagram of cerium oxide on Rh(111)

The Ce-oxide/Rh(111) surface phase diagram is shown in Fig. 3.10 as a plot of the regions of stability of the various overlayer phases as observed by LEED and STM. It gives an overview of the stability of various surfaces and oxide structures as a function of oxide coverage and annealing temperature. At the deposition temperature of 250°C and low oxide coverages ( $<0.6$  MLE) the Ce oxide is disordered and the  $(2 \times 2)$  structure of chemisorbed oxygen is the only ordered LEED pattern. The Ce oxide remains poorly ordered after evaporation at 250°C in the coverage range  $\theta_{oxide} = 0.6 - 1.5$  MLE, but improvement of order is detected for  $T > 300 - 350^\circ\text{C}$ , where a so-called  $(1.4 \times 1.4)$  pattern is appearing in LEED. A representative LEED pattern is reproduced in Fig. 3.11, image A.

In the region  $\theta_{oxide} \sim 0.6 - 1.9$  MLE,  $T \approx 300 - 550^\circ\text{C}$ , the  $(1.4 \times 1.4)$  pattern is accompanied by satellite reflexes, which are interpreted in terms of double scattering between the thin Ce oxide islands and the Rh substrate. For  $T > 550 - 750^\circ\text{C}$ ,  $\theta_{oxide} \sim 0.6 - 2.5$  MLE, the satellites of the  $(1.4 \times 1.4)$  pattern disappear, which may be understood by the increasing Ce oxide island thickness, as a result of ripening processes at the elevated temperatures as observed by STM.

The  $(1.4 \times 1.4)$  pattern (Fig. 3.11 A) consists of the Rh(111)- $1 \times 1$  reflexes (the outer hexagon) and of the reflections from the ordered Ce oxide island surfaces (the inner hexagon). Obviously, the scattering from the Rh(111) and from the Ce oxide surfaces are superimposed incoherently at this growth stage. The lattice constant of the Ce oxide is measured to  $3.85 \pm 0.05$  Å from the LEED image, which is consistent with both the  $CeO_2(111)$  surface lattice (3.89 Å) and the  $Ce_2O_3(0001)$  surface (3.82 Å). Thus, the measurement of the surface lattice constant does not allow to distinguish between the two possible  $CeO_2$  and  $Ce_2O_3$  oxide surfaces. However, the combined experimental evidence of LEED, STM and XPS is in favour of the formation of  $CeO_2(111)$  surfaces, and we attribute the hexagonal array of the Ce oxide derived  $(1.4 \times 1.4)$  LEED reflexes therefore to scattering from  $CeO_2(111)$ -type island surfaces. The sharp  $(1.4 \times 1.4)$  pattern

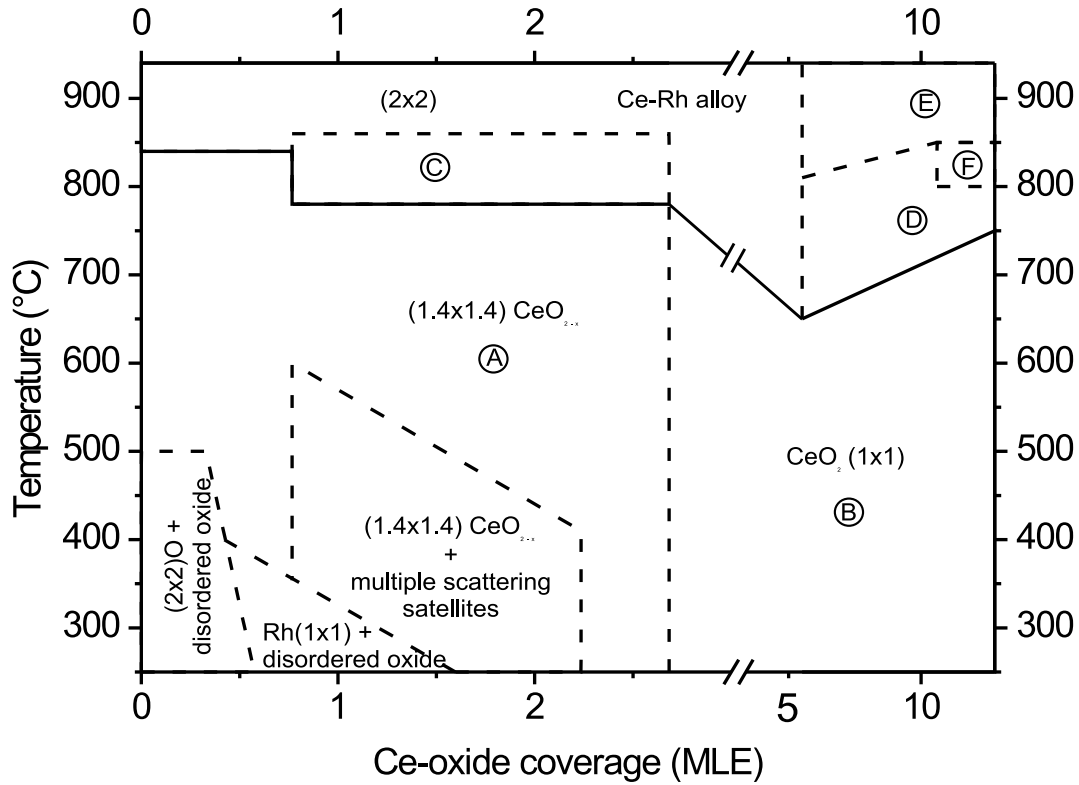


**Figure 3.10:** Surface phase diagram of cerium oxide on Rh(111), showing the stability regions of overlayer phases as a function of oxide coverage and annealing temperature. A-F mark regions where corresponding LEED photographs are given in the following image

indicates clearly that the  $CeO_2$  crystallites are well ordered and rotationally aligned with the principal azimuth directions of the substrate. For oxide coverages  $\geq 3.2 - 3.8$  MLE the  $CeO_2(111)1 \times 1$  spots are observed exclusively (see Fig. 3.11 B), indicating that the Ce oxide islands have reached the coalescence stage.

For  $T > 700 - 750^\circ\text{C}$  the Ce oxide decomposes and Ce-Rh surface alloy structures are formed. The decomposition temperature is a function of the oxide coverage, and oxide islands and surface alloy phases can coexist up to  $T \approx 850^\circ\text{C}$ . For low  $\theta_{oxide} \leq 2.5$  MLE and  $T > 850^\circ\text{C}$  a  $(2 \times 2)$  alloy LEED pattern is observed (not shown), but in the region C of the phase diagram of Fig. 3.10 the LEED pattern contains the  $(1.4 \times 1.4)$  pattern with

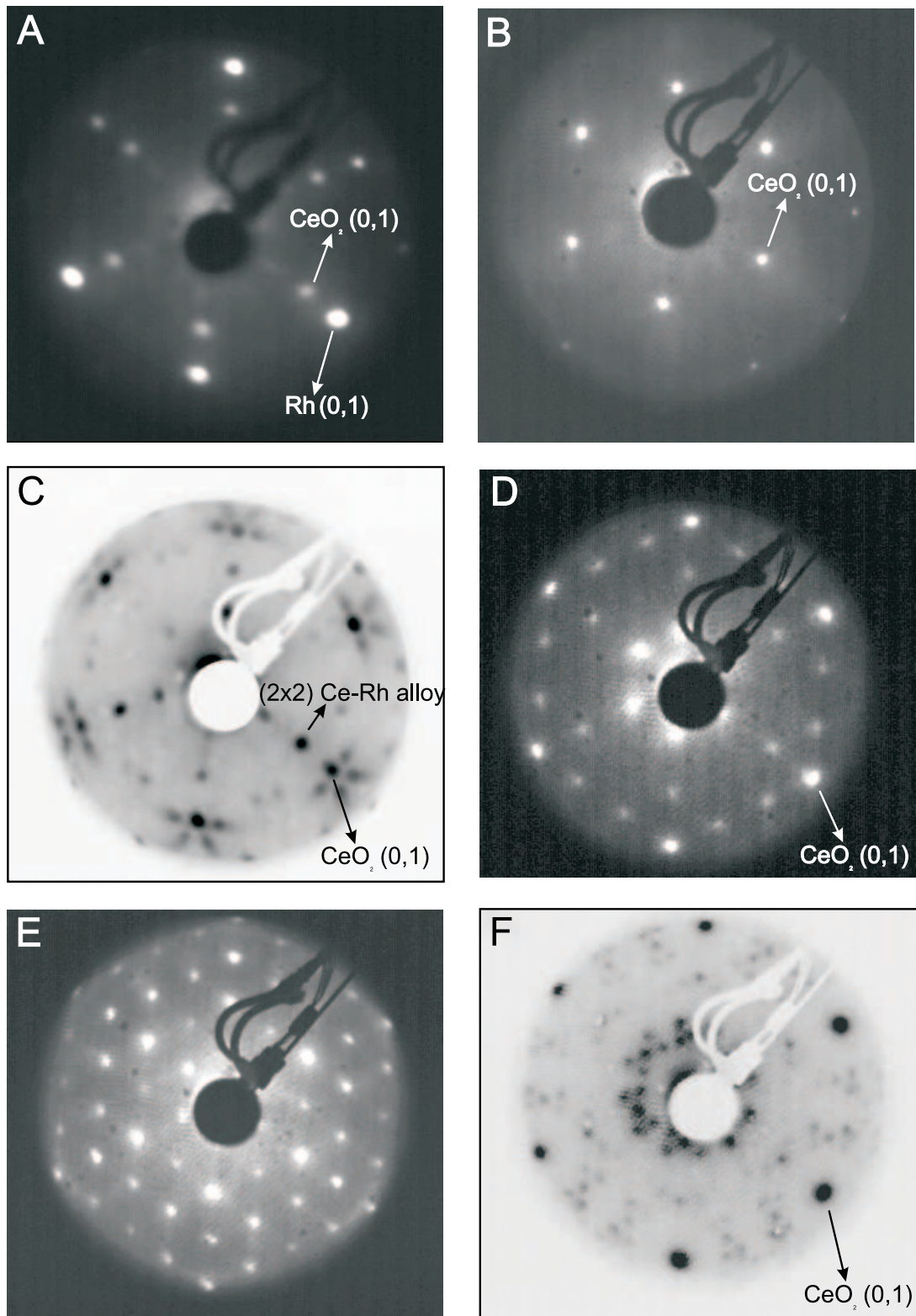


**Figure 3.11:** LEED photographs of: (A)  $(1.4 \times 1.4)$  pattern, electron energy  $E = 84$  eV; (B)  $\text{CeO}_2(111)1 \times 1$  pattern,  $E = 84$  eV; (C)  $\text{CeO}_2(111)1 \times 1$  + satellites plus  $(2 \times 2)$  pattern,  $E = 44.6$  eV; (D)  $\text{CeO}_2(111)1 \times 1$  plus  $(4 \times 4)$  pattern,  $E = 33$  eV; (E)  $(4 \times 4)$  pattern,  $E = 45.3$  eV; (F)  $\text{CeO}_2(111)1 \times 1$  plus  $(4 \times 4)$  + satellites pattern,  $E = 32.6$  eV

a complex satellite structure plus the  $(2 \times 2)$  pattern (see Fig. 3.11 C), which is indicative of the coexistence of Ce oxide, Rh(111), and alloy areas.

For higher oxide coverages ( $\theta_{oxide} > 2.5$  MLE) and  $T = 650 - 800^\circ\text{C}$  a  $(4 \times 4)$  Ce-Rh surface alloy structure coexists with the  $CeO_2(1 \times 1)$  pattern (see Fig. 3.11, D; note that the  $CeO_2$  1<sup>st</sup> order spots coincide with the  $(4 \times 4)$  3/4<sup>th</sup> order spots), whereas for  $T > 850^\circ\text{C}$  the oxide is decomposed completely and the  $(4 \times 4)$  alloy pattern solely remains (Fig. 3.11 E). Fig. 3.11, image F, displays a LEED pattern which has been recorded for a 13 MLE oxide coverage at  $\sim 800 - 850^\circ\text{C}$ , showing both  $CeO_2$  (1x1) spots and  $(4 \times 4)$  alloy spots with a complicated satellite structure; this again indicates the coexistence of oxide (albeit in a reduced state) and alloy phases.



### 3.2.2 The growth of ceria on Rh(111) at 250°C

The growth conditions of ceria employed in this study have been determined with the objective of obtaining ordered overlayers, which are as fully oxidised as possible. A Rh substrate temperature of 250°C and an oxygen pressure of  $2 \times 10^{-7}$  mbar provided the best compromise for achieving the desired overlayers, although fully oxidised  $CeO_2$  has not been obtained for the first few monolayers (see below).

#### STM results

Fig. 3.12 shows large-scale STM images of Ce oxide on Rh(111) at various growth stages. In Figs. 3.12(a) and (b) areas of the Rh crystal surface have been imaged where many mono-atomic steps separate terraces of  $\sim 200 - 400$  Å width. Many small Ce oxide islands of  $\sim 20 - 50$  Å average diameter are observed on the terraces for  $\theta_{oxide} = 0.32$  MLE (fig. 3.12a), no preferential step edge decoration is seen.

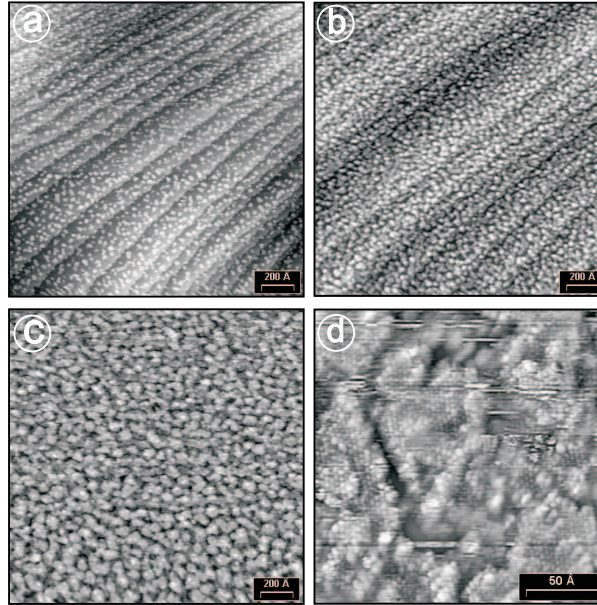


**Figure 3.12:** STM images of cerium oxide on Rh(111) deposited at 250°C. (a)  $\theta_{oxide} = 0.32$  MLE, sample bias  $V = 1.99V$ , tunnelling current  $I = 0.81nA$ ; (b)  $\theta_{oxide} = 1.3$  MLE,  $V = 2.03V$ ,  $I = 1.27nA$ ; (c)  $\theta_{oxide} = 2.5$  MLE,  $V = 1.3V$ ,  $I = 1.05nA$ ; (d) same as (c),  $\theta_{oxide} = 2.5$  MLE,  $V = 0.8V$ ,  $I = 1.53nA$ .

For  $\theta_{oxide} = 1.3$  MLE (fig. 3.12b) the islands have percolated and the Rh surface is

essentially covered by the oxide phase. At higher coverage,  $\theta_{oxide} = 2.5$  MLE (fig. 3.12c), the islands grow three-dimensionally and their irregular shapes are clearly apparent. The magnified view of this surface in fig. 3.12(d) confirms the irregular island boundaries, but also indicates the existence of some crystalline order within the island structures, in agreement with the observation of the  $(1.4 \times 1.4)$  LEED pattern (see Fig. 3.10). The STM images of Fig. 3.12 in conjunction with the LEED data thus establish a kind of polycrystalline epitaxial growth [37] of the ceria on Rh(111). The adsorption of CO at room temperature on ceria/Rh(111) has been used to titrate the free Rh metal sites (see [20] and section 3.3). These experiments have established that the Rh surface is completely covered by the oxide at  $\theta_{oxide} \approx 1$  MLE, which is consistent with the STM observations in fig. 3.12(b). Using the areas of the  $CeO_2(111)$  and Rh(111) unit cells a full monolayer of  $CeO_2(111)$  on Rh(111) should correspond to  $\theta_{oxide} \approx 0.5$  MLE. The fact that 1 MLE of ceria is necessary to completely cover the Rh(111) surface indicates that the ceria grows initially in form of a double layer oxide.

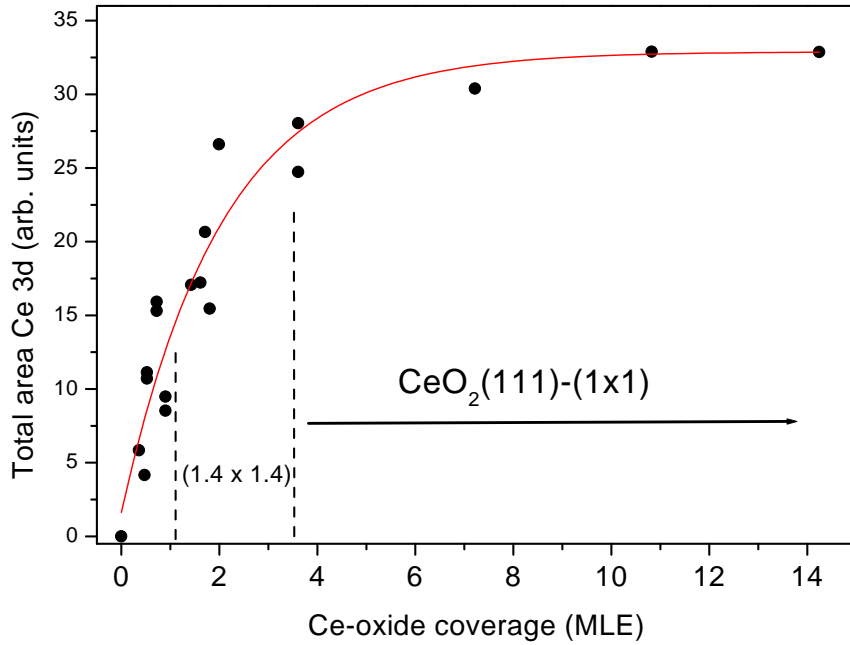


**Figure 3.13:** Cerium oxide uptake curve: total area of Ce 3d XPS peaks versus the coverage, as evaluated from the deposition parameters. The range of observed LEED patterns is indicated.

### XPS results

Fig.3.13 presents the analysis of the Ce 3d XPS spectra recorded during the oxide growth process: the total Ce 3d XPS area is plotted versus the oxide coverage as derived from the evaporation rate and this represents the oxide uptake curve of the surface; the coverage regions, where the  $(1.4 \times 1.4)$  and  $CeO_2(1 \times 1)$  LEED patterns are observed, are also indicated.

The uptake curve is consistent with the island growth mode, and the appearance of the  $CeO_2(1 \times 1)$  LEED structure at  $\sim 3.5$  MLE coincides with a marked decrease of the gradient of the uptake curve, indicating the point of coalescence of the oxide overlayer.

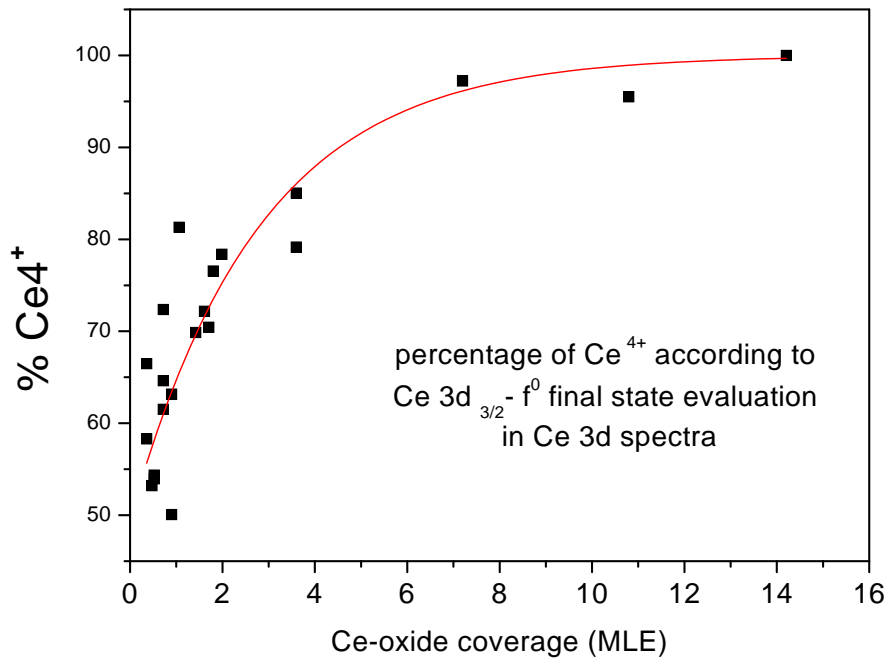


**Figure 3.14:** Plot of the percentage of  $Ce^{4+}$  in the Ce 3d signal as a function of oxide coverage

Fig.3.14 gives a plot of the percentage of  $Ce^{4+}$  in the Ce 3d signal as a function of oxide coverage. The  $Ce^{4+}$  percentage portion in the Ce oxide layer has been evaluated using the intensity (area) of the  $f^0$  final state peak of the  $3d_{3/2}$  spin-orbit component [23] at 916.5 eV binding energy, with the fully oxidised 13 MLE Ce oxide layer as a calibration point for  $CeO_2$ . The latter spectrum [20] is very similar to the corresponding published

spectra for  $CeO_2$  in the literature [38],[39].

The data of Fig.3.14 indicate that for oxide coverages up to 2.5 MLE significant amounts of reduced  $Ce^{3+}$  species are present in the oxide overlayer. Similar observations, i.e. more reduced oxide phases in the proximity of a metal-oxide interface, have been frequently reported in the literature and have been ascribed to, amongst other effects, strong metal-metal bonding at the interface [8]. As an indication for strong metal-metal bonding the affinity to surface alloy formation may be taken, which is clearly strong in the case of the Ce-Rh system [40]. Ce 3d spectra characteristic of fully oxidised  $CeO_2$  films are obtained for  $\theta_{oxide} \geq 6$  MLE.

The fact that the oxide derived reflections of the  $(1.4 \times 1.4)$  LEED pattern transform continuously into the  $CeO_2(1 \times 1)$  LEED pattern with increasing oxide coverage suggests that the Ce oxide overlayer grows from the beginning in the  $CeO_2$  fluorite structure with the (111) orientation parallel to Rh(111). The  $Ce^{3+}$  species may then be associated with oxygen defects, as indeed observed in the STM on the well-ordered Ce oxide islands formed at elevated temperature [21], or with a Ce termination of the oxide phase at the Ce-oxide/Rh interface. Support for the presence of reduced  $Ce^{3+}$  atomic species at the interface is obtained from the resonant photoemission measurements as discussed below.

### 3.2.3 Partial reduction of ceria on Rh(111) at $T \leq 800^\circ\text{C}$

Photoemission spectra of the valence band region of 1.3 MLE Ce oxide as deposited on Rh(111) at  $250^\circ\text{C}$  (curves a and b, "as-laid") and after annealing at  $600^\circ\text{C}$  (curves c and d) are displayed in Fig. 3.15. Spectra (b) and (d) have been excited with a photon energy of  $h\nu = 125$  eV, i.e. at the giant 4d-4f resonance of Ce [29], whereas spectra (a) and (c) are the corresponding off-resonance spectra ( $h\nu = 110$  eV). The spectra have been normalised at  $\sim 12.5$  eV binding energy, where the secondary electron background is structureless. The as-laid oxide surface spectra show photoemission intensity from the Fermi energy to a binding energy of 2.5 eV, which is derived from the Rh substrate 4d band.

The O 2p valence band extends from 2.5 to  $\sim 7.5$  eV, whereas the spectral intensity between 15-25 eV is due to emission from the Ce 5p and O 2s shallow core states. The O 2p valence band shows different structure in the on-resonance (b) and off-resonance spectra (a): it appears that the peak at  $\sim 3.3$  eV is enhanced in the on-resonance spectrum. Intensity enhancement is also observed in the Ce 5p region due to the resonance interference process. The O 2p valence band two-peak structure is consistent with the valence band of a bulk sample of  $\text{CeO}_2$  as reported by Mullins et al. [39]. This supports our conjecture that the cerium oxide as deposited at  $250^\circ\text{C}$  grows in a  $\text{CeO}_2$  stoichiometry.

Applying reducing conditions to the Ce-oxide/Rh(111) surface by annealing to  $600^\circ\text{C}$  in vacuum (curves c and d) introduces little changes in the O 2p valence band apart from an overall small shift to higher binding energy ( $\sim 0.2$  eV), however the appearance of the 4f derived emission at 1 eV below  $E_F$  indicates reduction of some  $\text{Ce}^{4+}(4f^0)$  to  $\text{Ce}^{3+}(4f^1)$  species in the oxide. Note that the Ce 4f emission intensity in spectrum (d) is greatly enhanced at  $h\nu = 125$  eV by the Ce 4d-4f resonance process as compared to the emission of the Rh substrate 4d valence band. This is clearly demonstrated by the off-resonance spectrum (c) from the same surface, where the 4f emission is not visible and only weak Rh 4d emission is observed between  $E_F$  and 2.5 eV. The modifications of the spectral profile of the O 2p band between off-resonance and on-resonance spectra indicate that states in the lower binding energy part of the O 2p band are coupled to Ce derived states with resonating behaviour at the Ce 4d-4f resonance. We propose that the photoemission peak at  $\sim 3.2$ - $3.5$  eV is due to O 2p states hybridised with Ce valence states. Indeed, Ce derived states have been identified in this energy range of the O 2p band in the first-principles electronic structure calculations of Skorodumova et al. [41] for  $\text{CeO}_2$ .

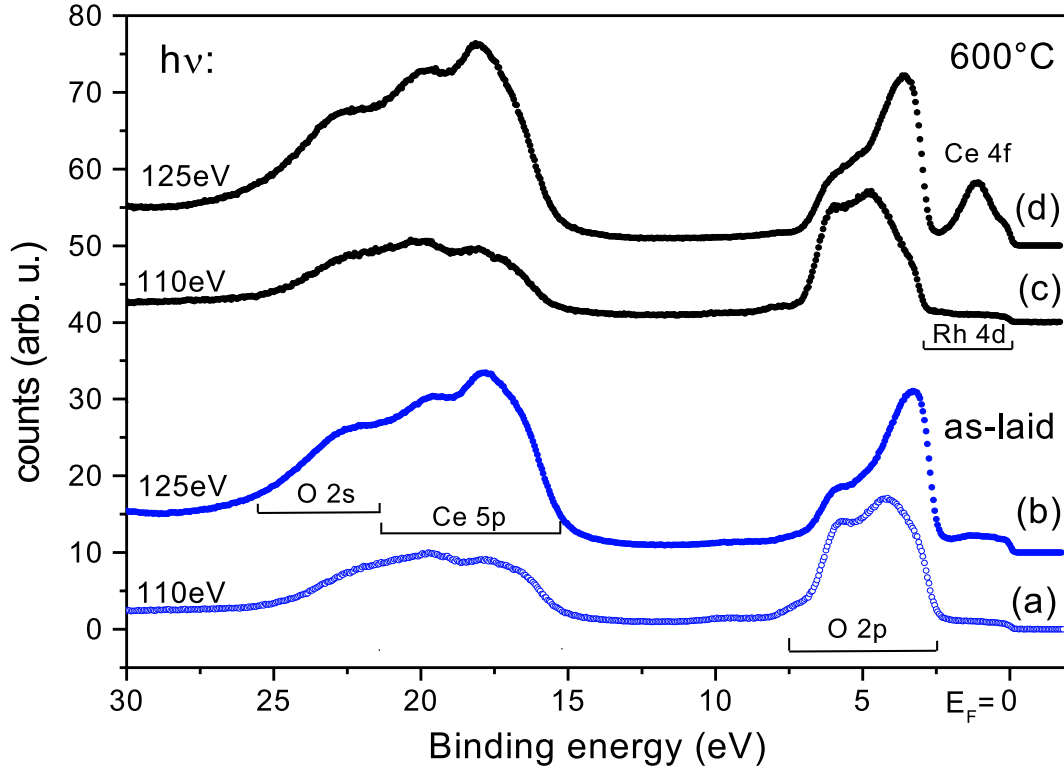


**Figure 3.15:** Valence band photoemission spectra of the as-laid 1.3 MLE Ce-oxide/Rh(111) surface (a, b) and after annealing at 600°C (c, d). Spectra (b) and (d) have been excited by a photon energy  $h\nu = 125$  eV corresponding to the maximum of the Ce 4d - 4f giant resonance (on-resonance), while spectra (a) and (c) have been excited with a photon energy in the pre-resonance region  $h\nu = 110$  eV (off-resonance). The Rh valence band emissions are weak in all spectra, as these photon energies are at the Rh 4d Cooper minimum.

The absence of 4f photoemission from  $Ce^{3+}$  species in the as-laid 1.3 MLE ceria spectrum of Fig. 3.15(a) and (b) is at variance with the Ce 3d XPS results in Fig. 3, where a  $Ce^{3+}$  contribution is clearly identified at this coverage. The role of the X-ray beam in reducing the ceria films has been investigated explicitly, but no photon induced reduction effects have been detected. We presume therefore that the different surface sensitivities in the two photoemission experiments are responsible for the different results. In the resonant photoemission experiment the photoelectron escape depth at  $\sim 125$  eV kinetic

energy should be minimal and the probing depth should be confined to the surface layers of the oxide islands. Conversely, using  $MgK\alpha$  radiation the Ce 3d photoelectrons have kinetic energies of the order of 350 eV with correspondingly larger escape depths: they can thus originate from both the outer surface of the Ce oxide islands and also from the interface to the Rh. This supports the conjecture that the contribution of reduced  $Ce^{3+}$  species in the as-laid Ce oxide overlayers originates from the ceria-Rh interface, as proposed previously [8]. The appearance of the 4f emission on the heated surface in Fig. 3.15(d) then testifies that  $Ce^{3+}$  species are formed at the surface of the ceria islands under the reducing conditions of the vacuum annealing process. Indeed, the formation of oxygen surface vacancies upon annealing is observed in the STM (see Fig. 3.17d).

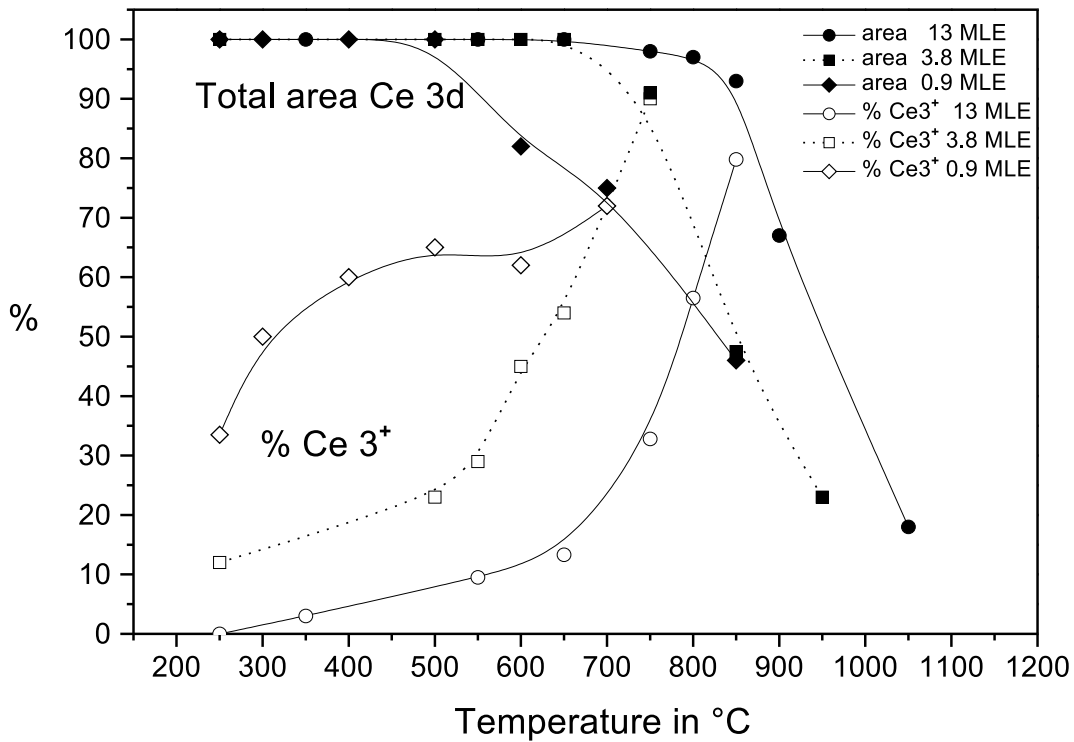


**Figure 3.16:** Analysis of Ce 3d XPS spectra of ceria overlayers of different thickness (13 MLE, 3.8 MLE, 0.9 MLE) as a function of the annealing temperature. Solid symbols designate the total Ce 3d peak area (normalised to 100), open symbols refer to the percentage of  $Ce^{3+}$  in the Ce 3d signal.

The reduction by vacuum annealing of ceria overlayers on Rh(111) as followed by Ce 3d XPS spectra is summarised in Fig. 3.16. Here, the total Ce 3d XPS peak areas and the percentage of reduced  $Ce^{3+}$  are given as a function of annealing temperature for different Ce oxide coverages. The thick 13 MLE ceria film is essentially stable up to  $\sim 800^\circ\text{C}$  (see total Ce 3d area), but reduction of  $Ce^{4+}$  to  $Ce^{3+}$  becomes significant beyond  $650^\circ\text{C}$ . At  $T > 800^\circ\text{C}$  the Ce 3d signal decreases rapidly indicating oxide decomposition, and the formation of Ce-Rh alloy phases and the loss of Ce from surface-near regions due to diffusion into the Rh bulk reduces the Ce content of the surface. The thermal stability of ceria on Rh(111) is a function of film thickness: the 3.8 MLE film starts to decompose at  $\sim 650^\circ\text{C}$ , whereas for submonolayer coverages (0.9 MLE in Fig. 3.16)  $T \approx 550^\circ\text{C}$  marks the decomposition onset temperature. The reduction of  $Ce^{4+}$  to  $Ce^{3+}$  in the ceria follows the same trend, with the 0.9 MLE submonolayer film being most sensitive to moderate vacuum annealing temperatures. This coverage dependence reflects the influence of the Rh substrate, which enhances the tendency for reduction of the oxide in the proximity of the interface. Similar results have been reported in a previous investigation of ceria particles on Rh(111) [38]. The present STM observations support the XPS results of Fig. 3.16: on a 6.5 MLE ceria film no defects at the surface have been observed after annealing to  $700^\circ\text{C}$ . This confirms the dominant influence of the ceria-Rh interface in the reduction process, and indicates that kinetic effects play a less important role in the thickness dependent stability of the cerium oxide overlayers.

The evolution of the morphology of ceria overlayers upon annealing in UHV is illustrated by the STM images of Fig. 3.17, by way of example for  $\theta_{oxide} = 0.9$  MLE. Fig. 3.17 (a) shows the surface after annealing at  $\sim 475^\circ\text{C}$ . In comparison to the STM image from the as-laid surface (not shown) the  $475^\circ\text{C}$  annealed surface shows first signs of agglomeration. The agglomeration is enhanced on further annealing to  $\sim 585^\circ\text{C}$  (Fig. 3.17b), where larger oxide islands with defined boundaries are formed. After annealing at  $680\text{--}700^\circ\text{C}$  well-ordered hexagonal crystallite structures have developed (Fig. 3.17 c) with diameters of up to  $200 \text{ \AA}$ . The high-resolution STM images of Fig. 3.17(d), taken from the top surface of a ceria island prepared similarly as in Fig. 3.17(c), confirm the crystalline order with a hexagonal lattice constant of  $3.85 \pm 0.05 \text{ \AA}$  and reveal a number of dark spots and patches due to oxygen vacancy defects. The latter are partly ordered and the result of reduction as discussed in Fig. 3.16. The formation of defects and their



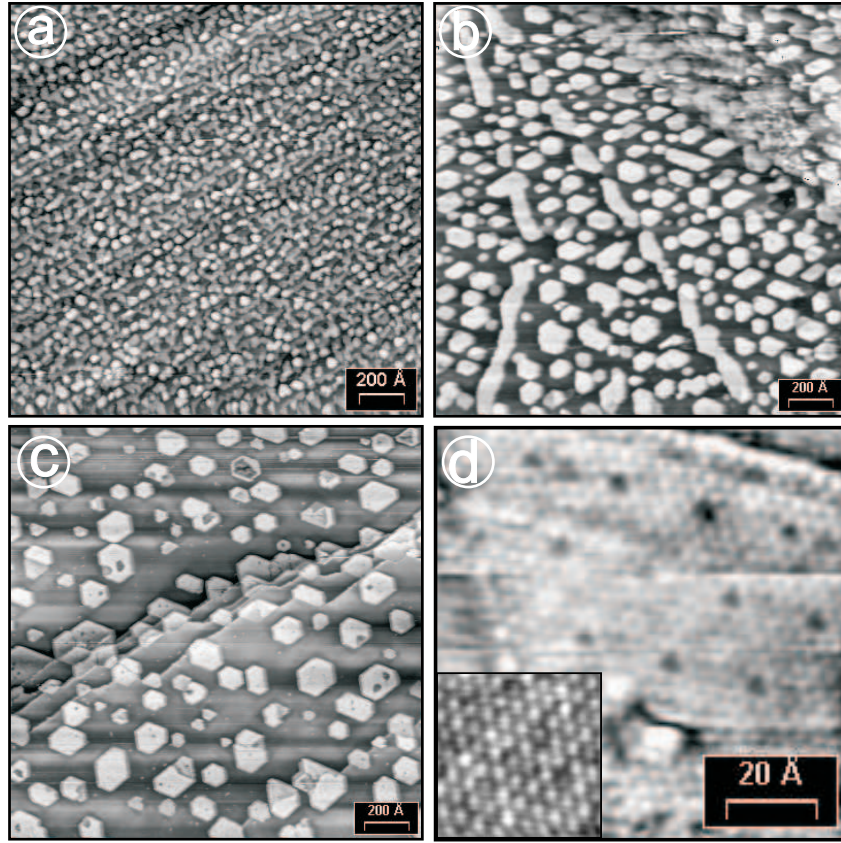


**Figure 3.17:** STM images of 0.9 MLE ceria/Rh(111) after annealing to: (a) 475 °C,  $U = 2V$ ,  $I = 0.96nA$  ; (b) 585 °C,  $U = 1.98V$ ,  $I = 1.03nA$  ; (c) 700 °C,  $U = 0.73V$ ,  $I = 1.18nA$ ; (d) 700 °C,  $U = 0.98V$ ,  $I = 1.02nA$  ; high-resolution image of the surface of a ceria island as in (c). Note the dark patches due to oxygen vacancy defects. The insert in (d) is a magnified atomic-resolution image (0.75V, 1.07nA) of the ceria surface.

apparent long-range ordering are presented in detail in C. Castellarin-Cudia's thesis [21]. STM images showing surface defects as in Fig. 3.17(d), though not ordered, have been reported recently by Berner and Schierbaum for heated  $CeO_2$  island surfaces on Pt(111) [42].

Summarising briefly this section, vacuum annealing of ceria overlayers on Rh(111) leads to a ripening of the oxide islands and to the formation of well-ordered hexagonal crystallite structures. Partial reduction of the oxide surfaces occurs and the concomitant creation of oxygen surface vacancies is confirmed by STM. The amount of reduction and the decomposition temperature of the Ce oxide is a function of the oxide layer thickness, indicating that the Rh(111) surface stimulates the reduction process.

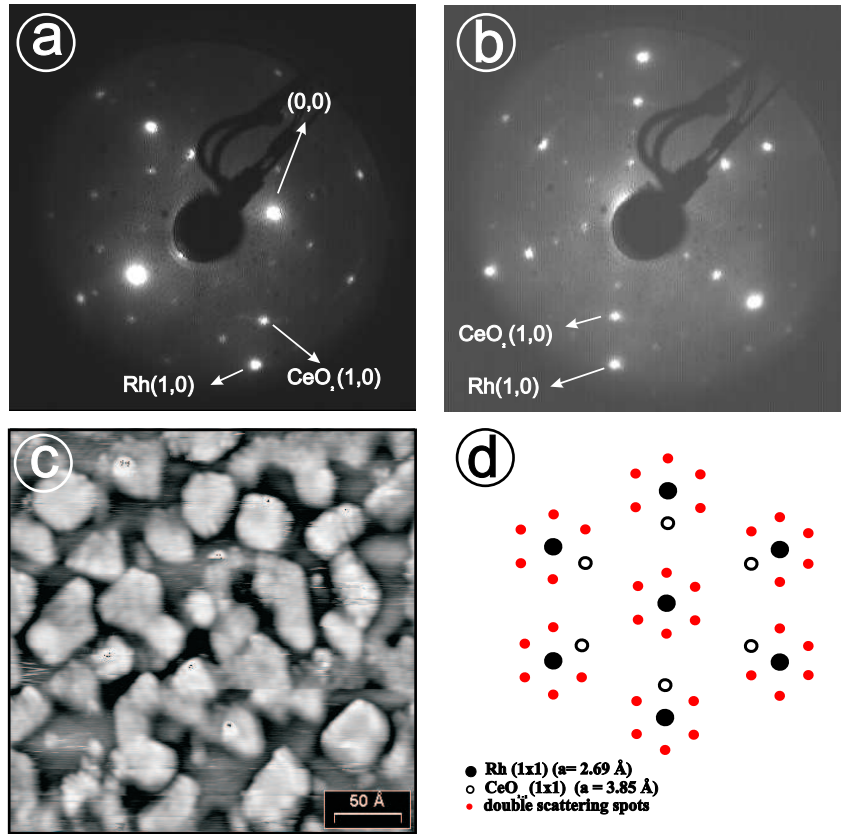


**Figure 3.18:** (a) LEED photograph of the 0.9 MLE ceria/Rh(111) surface annealed to  $\sim 470^\circ\text{C}$ , displaying the  $(1.4 \times 1.4)$  pattern with satellites;  $E = 81\text{ eV}$ , off-normal incidence. (b) LEED photograph of the surface in (a),  $E = 84\text{ eV}$ , normal incidence. (c) STM image of the surface in (a),  $U = 2.13\text{ V}$ ,  $I = 1\text{ nA}$ . (d) Simulated LEED pattern including double scattering between the Rh(111) substrate and the CeO<sub>2</sub> overlayer.

### LEED pattern induced by double scattering

At this point we would like to digress shortly and comment on a region in the phase diagram, between 0.6-1.9 MLE oxide coverage after moderate annealing, where a  $(1.4 \times 1.4)$  LEED pattern with satellite spots is observed (see Fig. 3.10). Corresponding LEED photographs are reproduced in Figs. 3.18(a) and (b) along with an STM image of the 0.9 MLE Ce-oxide/Rh(111) surface heated to  $470^\circ\text{C}$  in Fig. 3.18(c). The STM measurement shows that the Ce oxide island shapes are still mainly random, but STM line profiles across the islands indicate that many islands are bilayer structures.

The LEED pattern may then be interpreted in terms of multiple scattering effects

between the oxide and the substrate structure, with the double scattering vector  $\mathbf{g} = \mathbf{g}_{CeO_2} + \mathbf{g}_{Rh}$  generating the satellite spots. The schematic simulation of the LEED pattern in Fig. 3.18(d) illustrates the  $Rh(1 \times 1)$  (solid circles) and the  $CeO_2(1 \times 1)$  (open circles) reflections and the double scattering spots (grey circles). The LEED pattern thus reflects the internal order of the Ce oxide islands, which is difficult to recognise in the STM because stable tunnelling conditions with atomic resolution were difficult to obtain from these surfaces.

### 3.2.4 Decomposition of ceria on Rh(111) - surface alloy formation

Ordered Ce-Rh surface alloy phases are formed by decomposition of ceria at  $T \geq 700-800^\circ\text{C}$ . At lower oxide coverages a  $(2 \times 2)$ , at higher oxide coverages a  $(4 \times 4)$  LEED pattern is observed. LEED and O 1s XPS measurements indicate that below  $\sim 800^\circ\text{C}$  the surface alloys coexist with reduced  $\text{CeO}_{2-x}$  island structures, see e.g. the LEED pictures of Figs. 3.11 C, D, and F, where the  $\text{CeO}_2(1 \times 1)$  reflections have still high intensity. Resonance valence band photoemission spectra of 1.3 MLE Ce-oxide/Rh(111) in the as-laid state (a) and after annealing to  $\sim 850^\circ\text{C}$  (b and c) are displayed in Fig. 3.19.

The as-laid surface spectrum is identical to Fig. 3.15 (b) and shows Rh 4d, O 2p, Ce 5p, and O 2s emission bands. The on-resonance spectrum (c) of the annealed surface is significantly different from the as-laid surface spectrum, with an intense Ce  $4f^1$  emission at 2 eV below EF and a sharp peak at the Fermi level. The O 2p band of ceria is replaced by a feature centred at 5 eV, which shows no resonance coupling indicating oxygen chemisorbed on Rh sites of the alloy. The presence of oxygen at the surface after this treatment is confirmed by the O 2s emission observed in figure 3.19 a and c at  $\sim 23\text{eV}$  BE. The validity of resonance photoemission to probe surface processes becomes apparent by comparing the on-resonance (curve c) and off-resonance (curve b) spectra. In the latter the Ce 4f emission is barely visible and the Rh 4d emission is unaltered with respect to the unannealed surface. The O 2p emission is dominant in the off-resonance spectrum, but it indicates also that the oxide oxygen of ceria is replaced by a different oxygen species.

The interpretation of the on-resonance spectrum of Fig. 3.19 (c) is straightforward. The formation of the Ce-Rh alloy phase with reduced trivalent  $\text{Ce}^{3+}$  species is confirmed by the Ce  $4f^1$  peak and the behaviour of the Rh 4d emission at the Fermi level. The resonance enhancement near  $E_F$  is the result of the hybridisation of Rh 4d states with Ce 5d states, and the concomitant coupling to the Ce 4d-4f resonance process. The presence of the O 2p emission indicates that oxygen is still present at the surface at this temperature (see also the O 2s feature at  $\sim 22.5\text{ eV}$ ), presumably in form of chemisorbed oxygen on Rh sites.

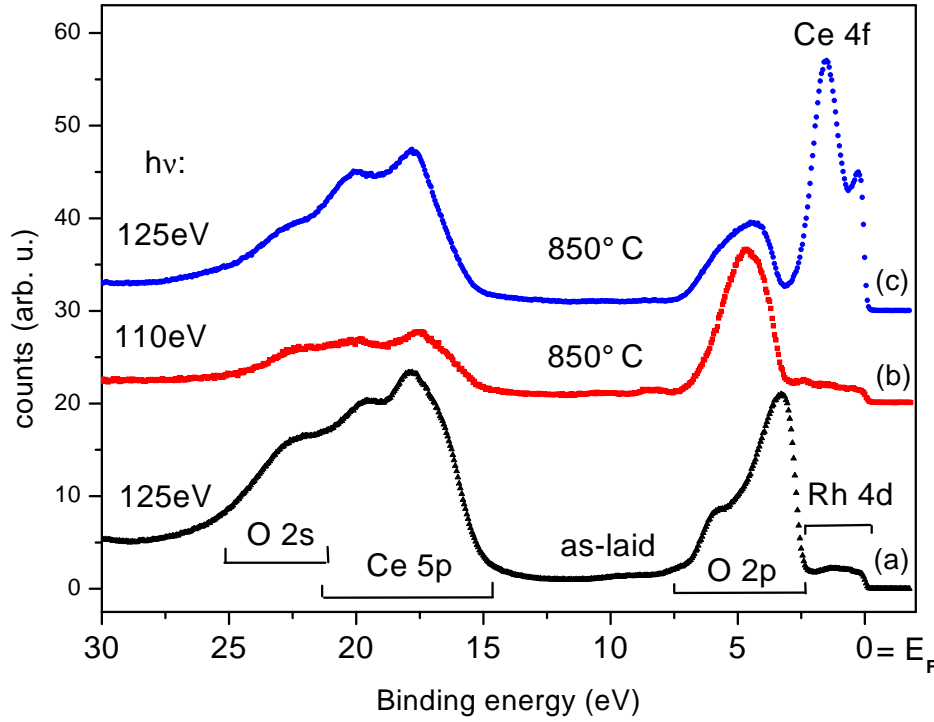


**Figure 3.19:** Resonant valence band photoemission spectra of the as-laid 1.3 MLE ceria/Rh(111) surface (a, on-resonance) and after annealing to 850 °C (b: off-resonance; c: on-resonance).

### Summary: reduction and decomposition of $CeO_{2-x}$ on Rh(111)

The growth morphology and structure and the thermal reduction of ultrathin ceria overlayers on Rh(111) have been investigated by LEED, STM, XPS, and valence band resonant photoemission with use of synchrotron radiation. The ceria grows in form of ordered  $CeO_2$  crystallites following a Vollmer-Weber island growth mode, with (111) faces parallel and orientationally aligned to the Rh(111) substrate. Ultrathin ceria layers (<6 MLE) contain significant amounts of  $Ce^{3+}$  species, which appear to be dominantly located at the ceria-Rh interface. For ceria films thicker than 6 MLE stoichiometric  $CeO_2$  is detected in XPS. Annealing in vacuum leads to the formation of well-defined hexagonal island structures, accompanied by partial reduction and the formation of  $Ce^{3+}$  species at the surface with concomitant surface O vacancies. The degree of reduction depends on the oxide

layer thickness, suggesting a promoting role of the ceria-Rh interface for the reduction process. At high temperature ( $>800^{\circ}\text{C}$ ) the ceria decomposes and Ce-Rh surface alloy phases are detected. The surface alloying process is clearly identified in valence band resonance photoemission spectra.

### 3.3 Adsorption and reaction of CO on a ceria-Rh(111) "inverse model catalyst" surface

#### 3.3.1 Introduction

Rhodium and cerium oxide (ceria) constitute important components of the commercial three-way catalyst for automotive emission control. The addition of ceria to this multicomponent supported metal catalyst improves the performance of the different group VIII metals and several mechanisms have been proposed to explain the promoting role of ceria [18]: amongst others, a stabilising role against sintering of the metal particles and an enhancement of the activity for the water gas shift reaction has been discussed.

The strong interaction of noble metal atoms with ceria surfaces in general and the ability of oxygen to migrate from  $CeO_2$  to Rh has been invoked to rationalise the increase of the CO oxidation activity of the metal. Several papers in the literature have shown that ceria promoted Rh surfaces can exhibit enhanced reaction rates for CO oxidation, along with very different kinetic rate expressions when compared to Rh or ceria individually ([43], [44], [45], [46]). Also, the dissociative adsorption of CO on Rh particles deposited on ceria surfaces has been reported [47], while intact molecular adsorption is generally found on Rh low-index single crystal surfaces [48], [32]. Mullins and Overbury [47] have associated the degree of CO dissociation on ceria supported Rh with the degree of reduction of the ceria, but have suggested that the morphology of the Rh particles does not affect the dissociation activity, although this latter proposition was based on indirect evidence.

In the following sections, we present resonance valence band spectra and X-ray photoemission spectra (XPS) of C and O 1s core levels, recorded with synchrotron radiation, to follow the CO uptake and the distribution of adsorption sites in a quantitative way on oxygen-precovered and ceria decorated Rh(111) surfaces. The clean-off reaction of CO with oxygen preadsorbed on the Rh surface yielding  $CO_2$ , that desorbs into the gas phase, and the reduction of ceria during this process is also addressed. Moreover, the influence of annealing of the inverse catalyst surfaces in vacuum, inducing reduction of the ceria and eventually the formation of a surface alloy, on the CO adsorption properties has also been investigated.

We find as an important result that ceria decorated Rh(111) surfaces do not dissociate

CO, this suggests that low-coordinated Rh atoms as present abundantly on small metal particles are likely to be the active centres for CO dissociation. However, a small amount of CO dissociation is identified on the Ce-Rh surface alloy. The effect of the ceria observed is a different balance of CO adsorption sites on the ceria promoted Rh(111) surfaces and an enhanced rate of the O+CO clean-off reaction, as compared on pure Rh(111).

### 3.3.2 Adsorption of CO on oxygen-precovered Rh(111) 2x1-O

Figure 3.20 illustrates a typical ceria-Rh(111) inverse catalyst surface, as obtained after deposition of  $\sim 0.5$  monolayers (MLE) of ceria at 520 K and cooled down to room temperature in an oxygen atmosphere. The large scale constant-current topographic STM image reveals irregularly shaped cerium oxide nano-particles, which are randomly distributed over the Rh surface. The majority of the oxide particles consists of a double layer of (111) oriented fluorite-type  $CeO_2$ , as indicated by LEED and XPS and established previously (sections 3.2.1 and 3.2.2). In between the oxide islands the Rh(111) metal areas are covered by a chemisorbed  $(2 \times 1)$  oxygen adlayer, as a result of the oxygen ambient during the cerium oxide preparation.

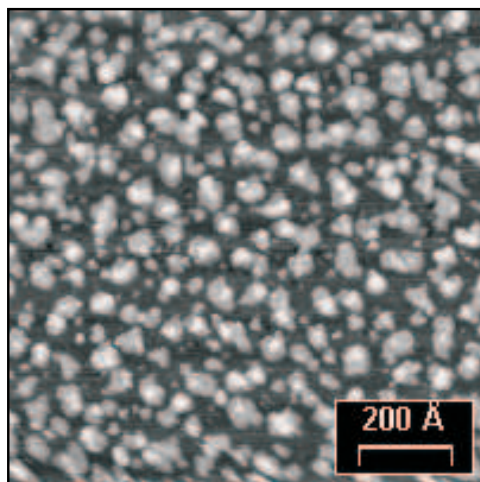


**Figure 3.20:** Constant current topographic STM image of  $\sim 0.5$  MLE of cerium oxide island structures on Rh(111). Tunneling conditions: 0.92 V sample bias; 1.02 nA tunneling current.

Since the bare Rh areas of our inverse catalyst surfaces are covered by chemisorbed oxygen after preparation, it is necessary to establish the adsorption properties of CO on a corresponding Rh(111)2x1-O surface. The  $(2 \times 1)$  oxygen surface was created by exposing



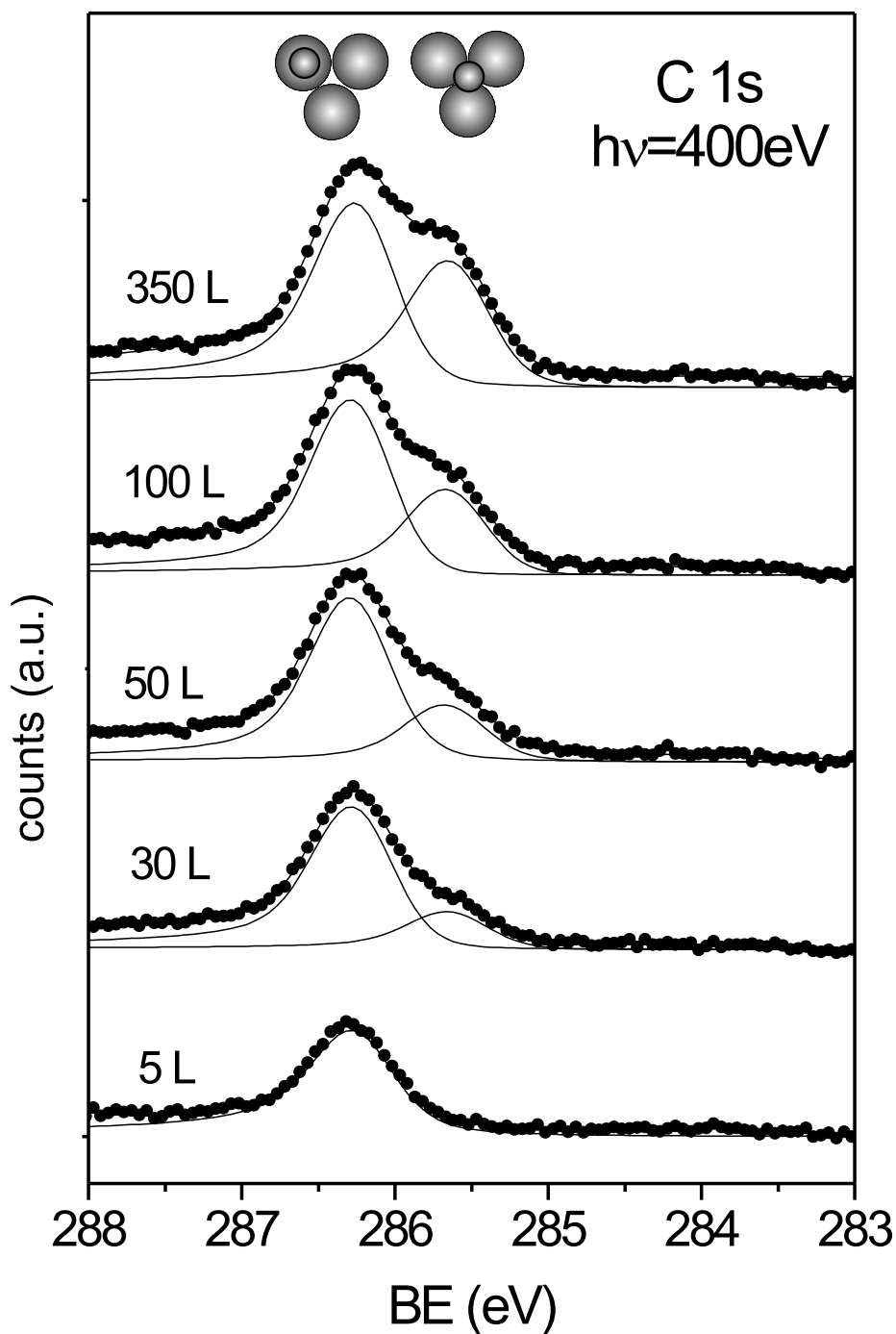
the clean Rh(111) surface to 60 L  $O_2$  (1 Langmuir (L) =  $1 \times 10^{-6}$  torr · sec) at 520 K and to an additional 60 L  $O_2$  during cooling down to room temperature. This corresponds closely to the conditions during preparation of the ceria decorated Rh(111) surfaces. In accordance with Jaworowski et al. [34] the  $(2 \times 2)$  LEED pattern observed from this surface is associated with the three equivalent domains of a  $(2 \times 1)$ -O overlayer with an oxygen coverage of 0.5 ML.

The adsorption of CO on the ceria decorated Rh surfaces has been studied here at room temperature, in order to restrict the adsorption to the metal sites of the inverse catalyst. Note that "room temperature" is meant to correspond to a temperature of  $\sim 300$ -320 K. Since the saturation coverage of CO on clean Rh(111) at room temperature is a sensitive function of the exact adsorption temperature [32], we have used the  $(2 \times 2)$ -3CO structure obtained at 120K with a coverage of 0.75 ML [49] as calibration point for our oxygen coverage evaluation (for details see section 3.1.3).

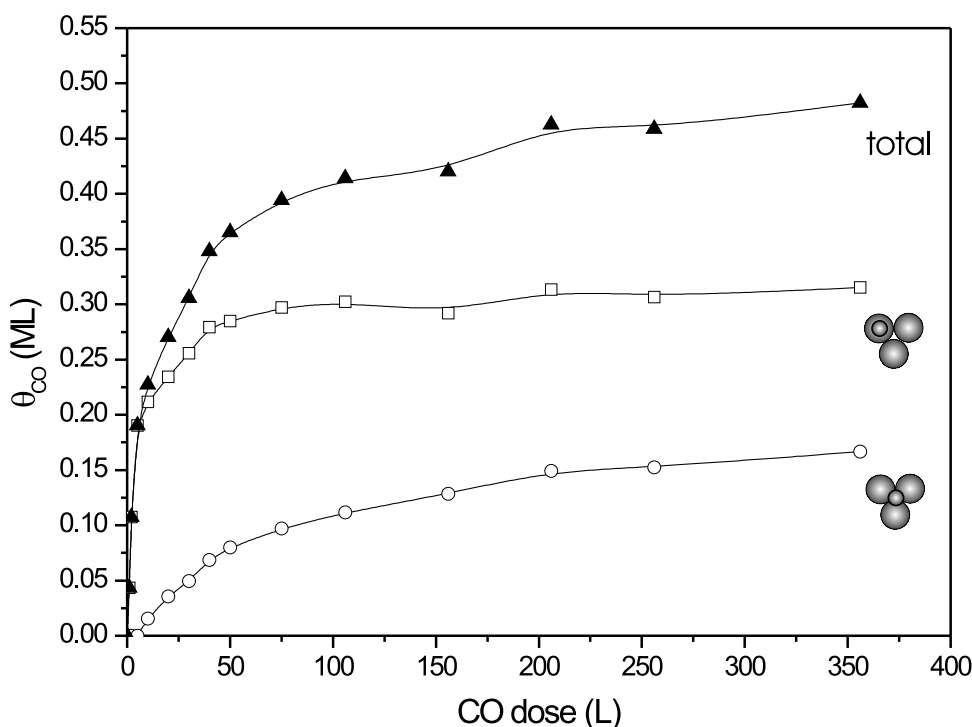
Figure 3.21 shows a series of C 1s XPS spectra of CO adsorbed on Rh(111)2x1-O at room temperature as a function of CO exposure. For low exposures a single peak at a binding energy of 286.2 eV is observed, whereas a second structure grows in at 285.7 eV at higher exposures. These C 1s binding energy values, derived from a decomposition of the spectra into the individual components using Donjiac-Sunjic convoluted with Gaussian lineshapes as model functions, are associated, in agreement with Jaworowski et al. [34], with CO adsorbed in on-top and three-fold hollow sites, respectively. Clearly, the on-top adsorption sites are populated first and then the hollow sites become occupied, as also observed on the clean Rh(111) surface [49].

Figure 3.22 gives the CO coverage on Rh(111)2x1-O as a function of CO exposure, i.e. the uptake curves for the total CO coverage and for the CO coverage in on-top and hollow adsorption positions, as derived from the areas of the respective C 1s peak components. As seen, the saturation of the surface with CO is only slowly established: after 350L the total CO coverage amounts to  $\sim 0.47$  ML, which is divided into 0.31 ML in on-top and 0.16 ML in hollow sites, i.e.  $CO_{on-top}/CO_{hollow} \approx 2$ .

Figure 3.23 shows a comparison of the uptake curves for the total CO coverage on clean Rh(111) and on Rh(111)2x1-O. The slower CO uptake on the O-precovered surface is clearly indicated and can also be quantified by calculating the initial sticking coefficient  $S_0$  from the initial slope of the curves. Accordingly,  $S_0$  on clean Rh(111) is close to 1,



**Figure 3.21:** C 1s core level spectra of CO adsorbed on the Rh(111)2x1-O surface at room temperature for various exposures. The spectra have been normalised to the background intensity at 283 eV. The curves below the data points are the result of the decomposition analysis, the lines through the data points are the resulting fits. The sketches at the top of the figure indicate the CO components in on-top and three-fold hollow adsorption sites.



**Figure 3.22:** CO uptake curves in the form of coverage versus dose for the total CO coverage and for the CO coverage in on-top and hollow adsorption positions, as derived from the areas of the respective C 1s components.

whereas it is reduced to 0.25 on the  $(2 \times 1)$ -O surface.

The slower CO uptake on the O-precovered surface, as compared to the clean Rh surface, can be associated with a site blocking effect of the preadsorbed oxygen or with a reaction induced kinetic effect. Figure 3.24 and 3.25 reveal that the latter is the case. In figure 3.24 O 1s XPS spectra of the Rh(111)2x1-O surface (bottom curve), of a Rh(111) surface saturated with a room temperature CO adlayer (middle curve), and of the Rh(111)2x1-O surface exposed to 350 L CO at room temperature (top curve) are displayed.

The chemisorbed oxygen occurs with a O 1s binding energy of 529.4 eV, while the  $CO_{on-top}$  and  $CO_{hollow}$  are characterised by O 1s binding energies of 531.9 eV and 530.6 eV, respectively. Most importantly, however, the top spectrum of figure 3.24 shows that the oxygen precoverage has been reduced from 0.5 ML to 0.08 ML by the clean-off reaction

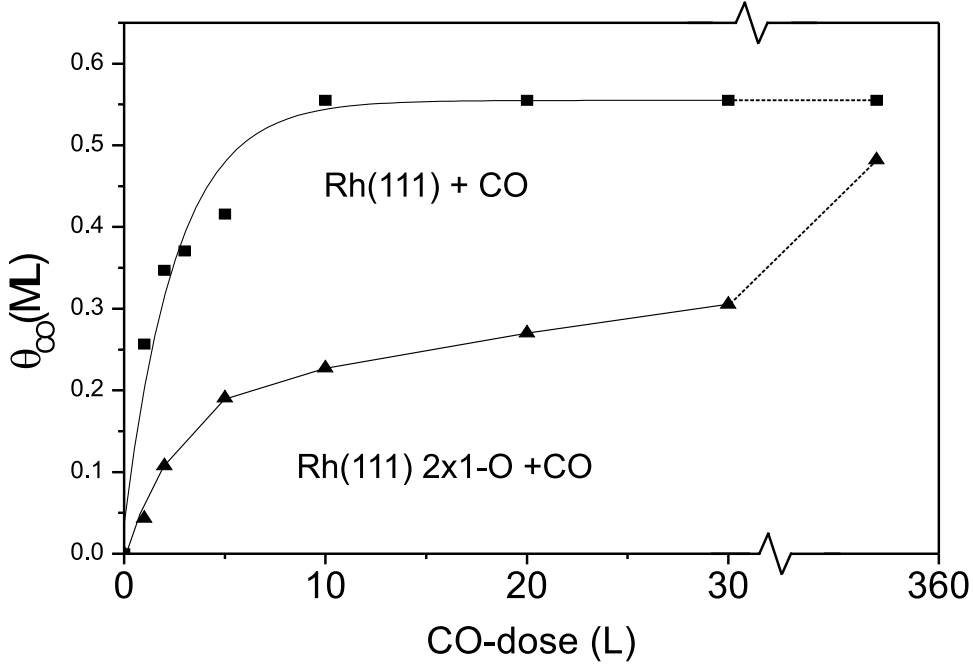


**Figure 3.23:** Comparison of the total CO uptake curves on the clean Rh(111) and the Rh(111)2x1-O surfaces.

with CO,  $O_{ADS} + CO = CO_2$ , which desorbs into the gas phase. The initial, relatively fast uptake of the on-top CO on the  $(2 \times 1)$ -O surface (see figure 3.22) may be the result of the incorporation of  $CO_{on-top}$  into the  $(2 \times 2) - 2O + CO$  structure, which has been proposed by Jaworowski et al. [34]. This latter structure, with  $\theta_O = 0.5$  ML and  $\theta_{CO} = 0.25$  ML, is obtained from the  $(2 \times 1) - O$  structure by shifting every other oxygen into an adjacent hollow site and adsorbing CO at the resulting free on-top Rh site [34]. We suggest that this structure may be a precursor phase for the CO oxidation reaction at  $\sim 300$ - $320$  K, as observed here.

The O+CO clean-off reaction is confirmed by the valence band spectra of figure 3.25. These spectra have been recorded with a photon energy  $h\nu = 125$  eV, which is at the Cooper minimum of the Rh 4d photoionisation cross section, to emphasise the adsorbate features. The lower spectrum of figure 3.25 has been recorded from the Rh(111)2x1-O surface: the O 2p structure of the chemisorbed oxygen at  $\sim 6$  eV is the prominent feature in the valence band, and the O 2s emission is seen at  $\sim 21$  eV.

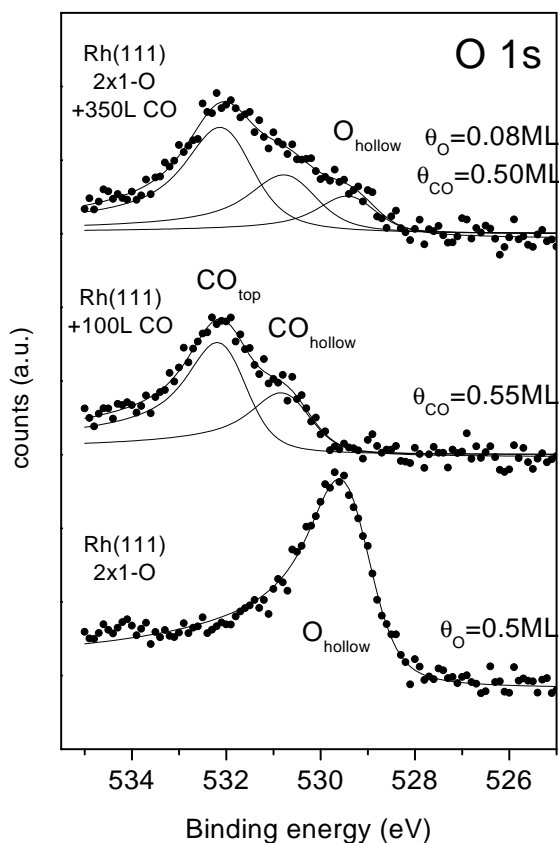


**Figure 3.24:** *O 1s* XPS spectra, excited by Mg  $K\alpha$  radiation ( $h\nu = 1253.6 \text{ eV}$ ), of the Rh(111)2x1-O surface, of clean Rh(111) exposed to 100L CO at room temperature, and of the Rh(111)2x1-O surface exposed to 350L CO at room temperature. The spectra have been normalised to the background intensity at 526 eV. The curves below the data points are the spectral components of chemisorbed oxygen ( $O_{\text{hollow}}$ ) and of CO in on-top and hollow sites.

After exposure to 350L CO at room temperature (upper spectrum) both O 2p and O 2s emissions are strongly reduced in intensity and the well-known CO derived  $5\sigma/1\pi$  ( $\sim 7.5 \text{ eV}$ ) and  $4\sigma$  ( $\sim 11 \text{ eV}$ ) valence orbital emissions dominate the spectrum. Most of the chemisorbed O has thus been removed by the clean-off reaction.

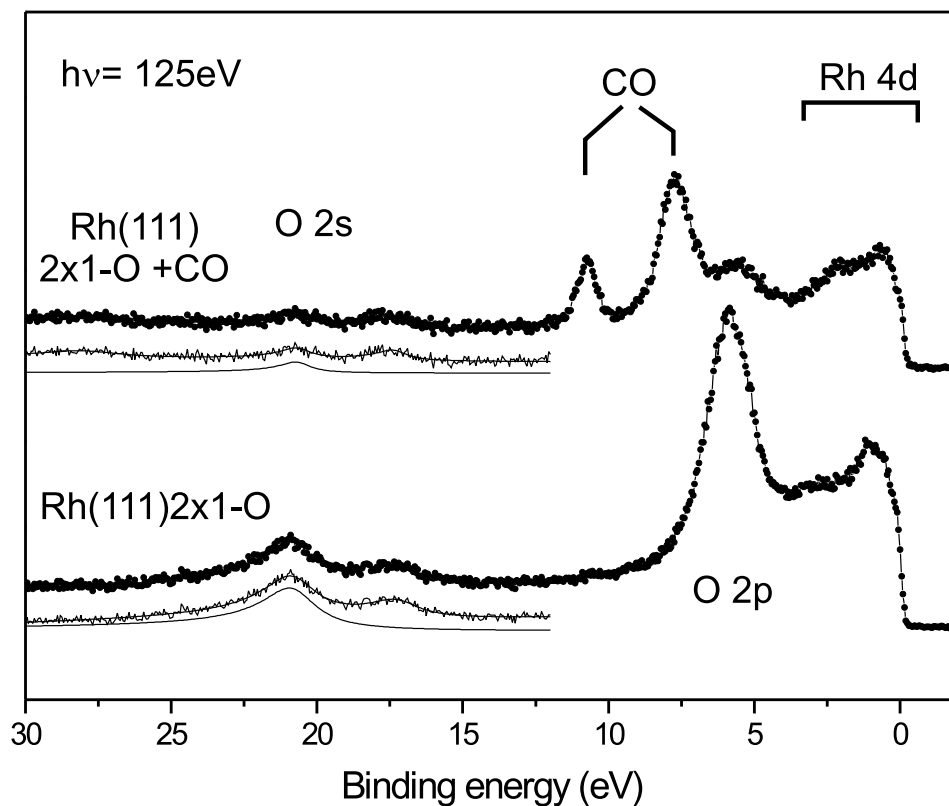


**Figure 3.25:** Valence band photoemission spectra of the pristine Rh(111) 2x1-O surface (bottom) and after exposure of this surface to 350L CO at room temperature (top). The spectra have been normalised to the background at 15 eV.

### 3.3.3 Adsorption of CO on ceria-Rh(111) surfaces

The adsorption of CO on ceria-Rh(111) inverse catalyst surfaces is illustrated in figures 3.26 to 3.29. Figure 3.26 shows a set of C 1s XPS spectra of CO adsorbed at room temperature on a  $\sim 0.5$  MLE ceria-Rh(111) surface as a function of exposure. For low CO doses the single C 1s peak at 286.2 eV binding energy indicates that the on-top Rh adsorption sites are populated first as on bare Rh(111), but the appearance of the second peak at 285.5 eV for higher exposures ( $\sim 10$  L) shows that the three-fold hollow Rh sites become populated as well, albeit delayed.

There are no indications of CO adsorption on the oxide surface at room temperature

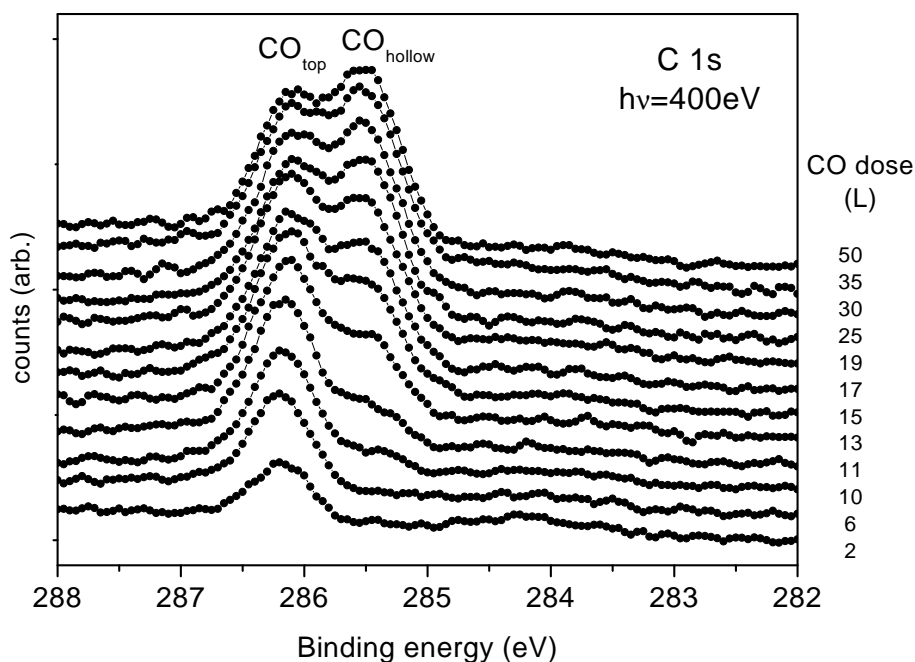


**Figure 3.26:** *C 1s* core level spectra of CO on a 0.5 MLE ceria-Rh(111) surface as a function of exposure at room temperature; spectra normalised at 282 eV.

or lower temperatures, with an expected C 1s binding energy of 290-291 eV [47]. This is illustrated by the wide range C1s spectra in figure 3.27. The weak emission intensity at around 284 eV in the low-exposure spectrum in figure 3.26 is due to adventitious carbon contamination of the initial surface. The fact that the intensity in this region does not grow and remains constant during CO dosing indicates that CO does not dissociate on the ceria-Rh(111) inverse catalyst surface.

A qualitative inspection of figures 3.26 and 3.21 reveals that the balance of adsorption sites is different on the ceria-Rh(111) as compared to the O-precovered Rh(111) surface, with a relative preference for the hollow sites in the former case.

Figure 3.28 gives a quantitative measure of this behaviour on ceria-Rh(111) in the form of the uptake curves of the total CO coverage versus exposure and of the CO coverage in on-top and hollow sites. We notice that the occupation of hollow sites is delayed until the on-top sites are nearly saturated ( $\sim 10$  L), but that the ratio  $CO_{on-top}/CO_{hollow}$  becomes  $\sim 1$  at saturation (we recall that this ratio is 2 on the O-precovered Rh surface - see

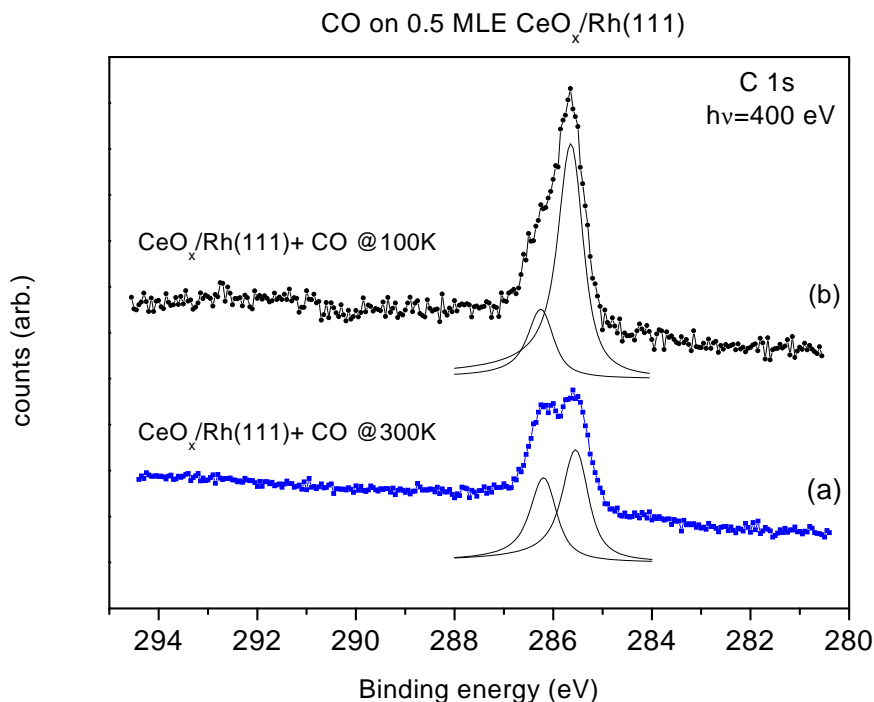


**Figure 3.27:** Wide-range  $C\ 1s$  core level spectra of CO on a 0.5 ML ceria-Rh(111) surface; a) CO saturation at room temperature; b) CO saturation at 100K

section 3.3.2). The total CO saturation coverage on this particular ceria-Rh(111) surface is 0.32 ML, which agrees well with the corresponding ceria-free surface suggested from the ceria coverage estimated from the evaporation rate during preparation.

Figure 3.29 compares the total CO uptake curves on the ceria-Rh(111) and Rh(111)2x1-O surfaces. The ceria-Rh(111) surface reaches CO saturation after a dose of  $\sim 35$  L, whereas the  $(2 \times 1)$ -O surface is still not saturated with CO after offering 10 times more CO (350 L). The initial sticking coefficient of CO on the ceria-Rh(111) surface is  $S_0 \approx 0.5$  as referenced to the available Rh sites, which is about twice the value on the Rh(111)2x1-O surface. These results clearly indicate that the  $O+CO$  clean-off reaction is significantly promoted on the ceria-Rh(111) surface.

The exposure of the ceria-Rh(111) surface to CO results in a partial reduction of the  $CeO_2$  layer. Figure 3.30 displays valence band spectra of the pristine 0.5 MLE ceria-Rh(111) surface and after exposure to 50 L CO at room temperature. The valence band spectrum of the pristine ceria-Rh surface (bottom curve) shows the emission of the Rh 4d



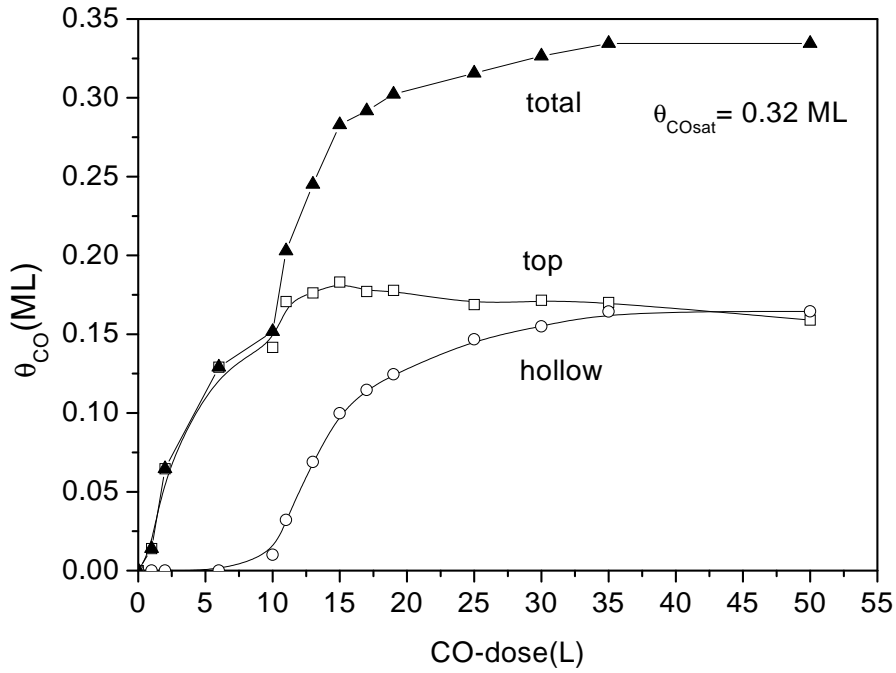


**Figure 3.28:** CO uptake curves on 0.5 MLE ceria-Rh(111) for the total CO coverage and for the CO coverage in on-top and hollow adsorption positions, derived from the respective C 1s components.

states from the Fermi level to 2.5 eV below  $E_F$  and the characteristic O 2p double-peak structure of  $CeO_2$  in the range 2.5-8 eV (see section 3.1.2). The Ce 5p and O 2s emissions occur in the region 15-25 eV. After CO exposure (top curve) a feature at  $\sim 1.5$  eV below  $E_F$  has appeared which is associated with the emission from the Ce  $4f^1$  states of  $Ce^{3+}$  species, indicating the partial reduction of the ceria. The spectra of figure 3.30 have been recorded with a photon energy of 125 eV, i.e. at the giant 4d-4f resonance of Ce atoms [50]: the emission from the Ce 4f states is thus resonantly enhanced and a low degree of reduction becomes detectable. The partial reduction of the oxide is also apparent in some changes in the region of the O 2p structure.

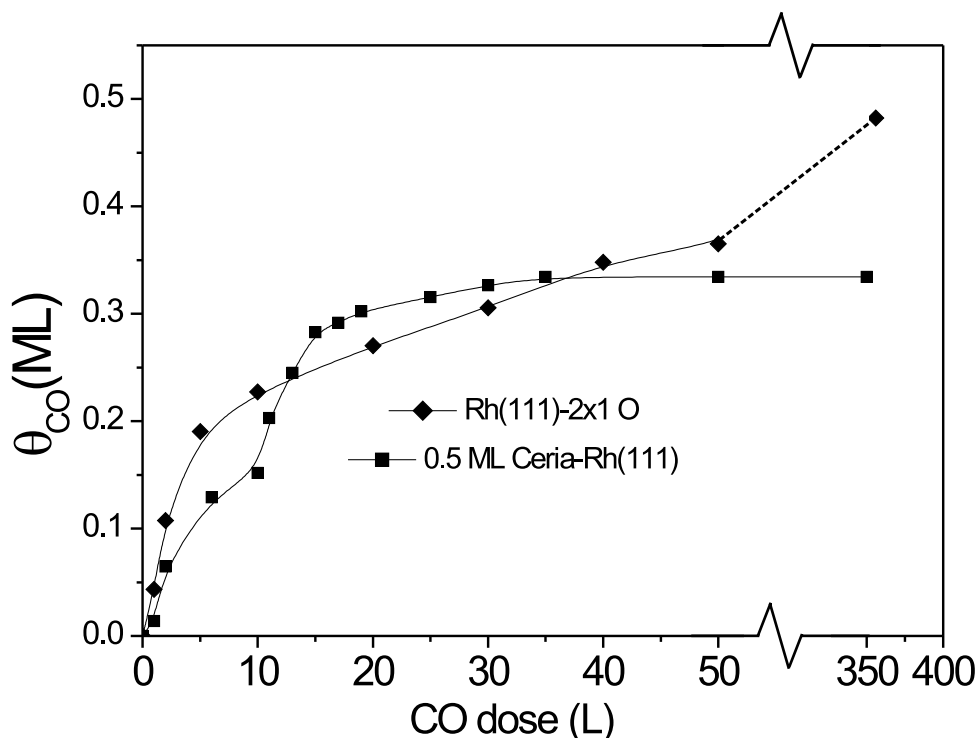


**Figure 3.29:** Comparison of the total CO uptake curves on the 0.5 MLE ceria-Rh(111) and on the Rh(111)2x1-O surfaces.

### 3.3.4 Adsorption of CO on (partially) reduced ceria-Rh(111) surfaces

Annealing of ceria-Rh(111) inverse catalyst surfaces in ultrahigh vacuum leads to a partial reduction of the ceria overlayer, but the balance of CO adsorption sites (on-top vs. hollow) is only slightly modified (see figure 3.31 a and b). On the Ce-Rh alloy surface, however, formed after annealing to  $>1100$  K, CO adsorption occurs almost exclusively in the hollow adsorption sites and the saturation coverage is reduced as compared to the clean Rh(111) surface (fig. 3.31c).

We notice a small C 1s emission peak at  $\sim 284$  eV on the alloy surface (top curve of figure 3.31, which is due to surface carbide and could indicate a small amount of CO dissociation (see below). Figure 3.32 summarises the analysis of the C 1s spectra in terms of CO coverages and also includes the percentage of  $Ce^{3+}$ , i.e. the degree of ceria

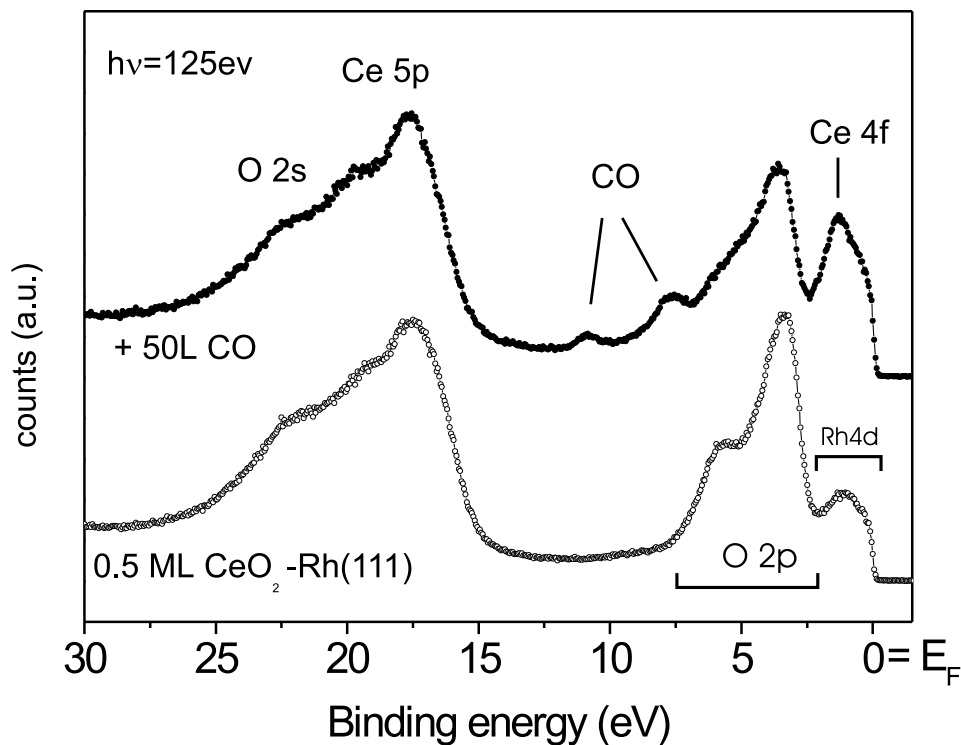


**Figure 3.30:** Resonant valence band photoemission spectra of the 0.5 MLE ceria-Rh(111) surface (bottom) and after exposure of this surface to 50 L CO at room temperature (top). The spectra have been normalised at 13 eV.

reduction, on the respective surfaces as deduced from Ce 3d XPS spectra 3.2.

On as-prepared ceria-Rh surfaces some  $Ce^{3+}$  species have always been detected in the Ce 3d XPS spectra for coverages less than several monolayers, and in section 3.2.2 it has been argued that these are located at the Ce-Rh interface [8]. On the 950 K annealed surface the  $Ce^{3+}$  content of the oxide layer has increased to  $\sim 50\%$ , and this is associated with the formation of oxygen vacancies at the oxide surface [21].

The ratio  $CO_{top}/CO_{hollow}$  is still close to one, but significantly there are no indications of CO dissociation on this reduced ceria-Rh(111) surface (no C 1s signal of surface carbide). This is in contrast to what has been reported by Mullins and Overbury on Rh particles supported on reduced ceria surfaces [47], where the observed dissociation of CO has been ascribed to the reduced state of the ceria. After annealing to  $>1000$  K

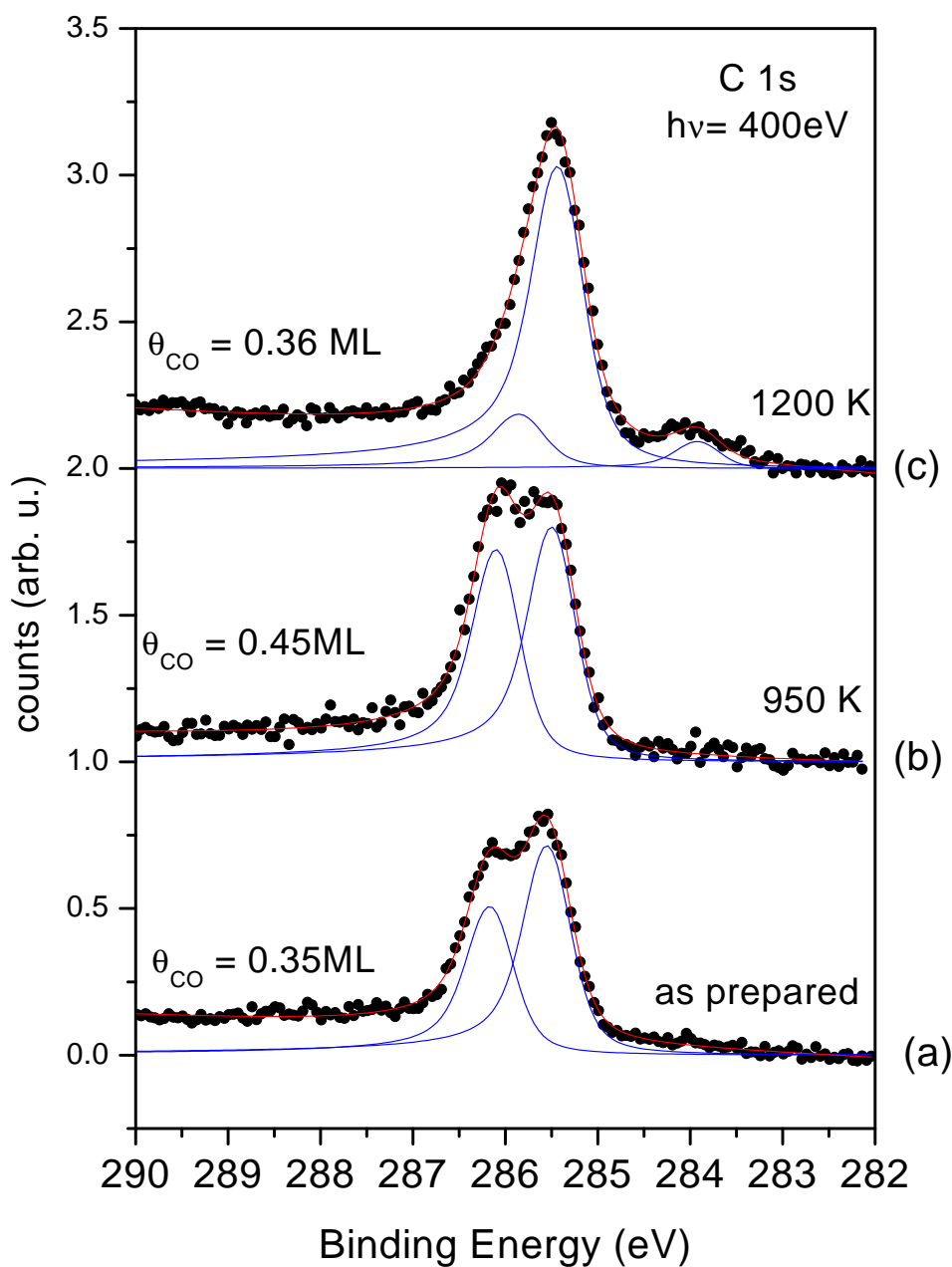


**Figure 3.31:** C 1s core level spectra of CO (50 L room temperature exposure) on 0.45 MLE ceria-Rh(111) in the as-prepared state (bottom spectrum), on the reduced ceria-Rh surface obtained after annealing to 950 K (middle spectrum), and on the ceria-Rh alloy surface after annealing to 1200 K. The curves below the data points show the spectral components after the fitting analysis.

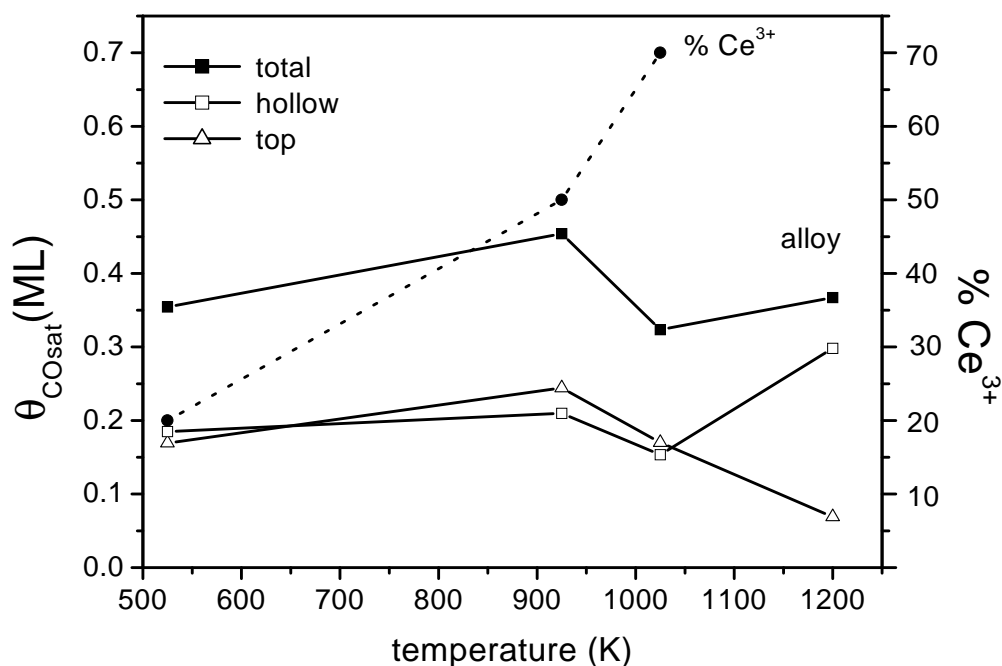


**Figure 3.32:** CO coverages on the as-prepared and annealed surfaces and the percentage of  $\text{Ce}^{3+}$  species at the surface, as derived from Ce 3d XPS spectra

progressive oxide decomposition and alloy formation characterise the surfaces, and the CO adsorption occurs with reduced saturation coverage but predominantly in the hollow sites. Most of the  $\text{Ce}^{4+}$  species of the oxide have been replaced by the  $\text{Ce}^{3+}$  of the alloy on this surface.

Annealing of 1 MLE ceria on Rh(111) at 1200 K produces an ordered  $\text{CeRh}_3$  alloy surface with a  $(2 \times 2)$  LEED structure [27]. The adsorption of CO on this surface is illustrated in figure 3.33. The insert shows a set of C 1s spectra as a function of exposure and the main panel gives the corresponding total CO uptake curve. The C 1s peak is observed at 285.3 eV binding energy for low coverage and shifts slightly to 285.5 eV upon saturation, which is typical within the range of density effects in adsorbate layers. This major C 1s peak is associated with CO in hollow adsorption sites on the alloy surface, with a somewhat modified binding energy with respect to the corresponding sites on the Rh(111) surface as a result of the different alloy surface potential. A minor spectral component at 285.9 eV is necessary for a good fit of the saturation C 1s spectrum (see

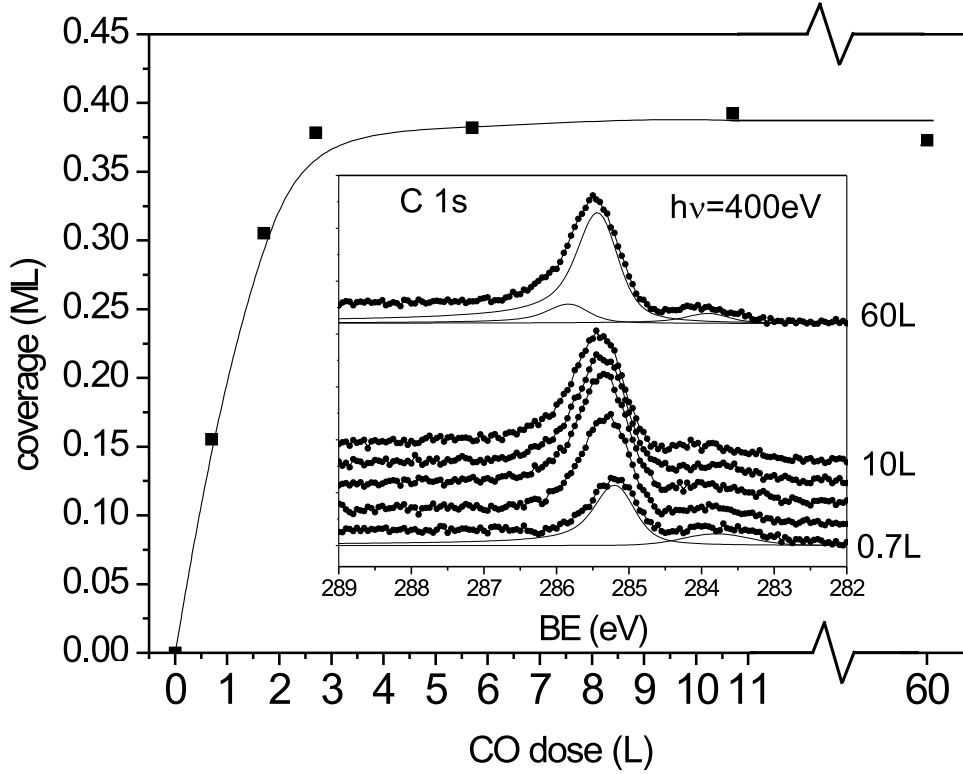


**Figure 3.33:** Total CO uptake curve on a  $(2 \times 2)$   $\text{CeRh}_3$  alloy surface. The insert shows the normalised C 1s spectra as a function of CO exposure at room temperature.

also figure 3.31c), and it is ascribed to CO minority species in on-top sites. The C 1s emission intensity at 283.9 eV is due to the presence of surface carbon and suggests a small amount of CO dissociation on the alloy surface. The coverage of this surface carbon in the saturation C 1s spectrum (top curve of insert) is estimated to 0.03 ML. The adsorption of CO on the alloy surface is fast, with an initial sticking coefficient  $S_0 \approx 0.7$ , but the saturation adsorption coverage of  $\sim 0.37$  ML at room temperature is smaller than on the clean Rh(111) surface (0.55 ML). This is similar to what has been observed on other alloy surfaces, e.g. on V-Pd [51].

**Summary: CO adsorption experiments**

The adsorption of CO on the Rh(111)2x1-O surface is followed by the O+CO oxidation reaction at room temperature or slightly above, which removes the preadsorbed oxygen from the surface. The initial fast uptake of CO into on-top adsorption sites suggests that the  $(2 \times 2)2\text{O}+\text{CO}$  structure, in which CO adsorption can take place in on-top positions after a rearrangement of the chemisorbed oxygen atoms [34], may be a precursor phase for the oxidation reaction. After removal of  $\sim 0.25$  ML oxygen the threefold hollow sites become also available for CO chemisorption, as observed in figure 3.23. On the ceria-Rh(111) surface a similar mechanism is possible in principle, however the CO uptake is much faster on this surface. The initial abundance of  $\text{CO}_{\text{on-top}}$  may also be understood by the incorporation into the  $(2 \times 2)2\text{O}$  structure, but the faster uptake indicates that the clean-off reaction, i.e. the CO oxidation, is enhanced. It is most natural to associate the promotion of the CO oxidation reaction with adsorption sites close to the ceria-Rh interface, i.e. with sites at the boundaries of the ceria island structures.

A different balance of CO adsorption sites on the Rh(111) areas in the presence of the ceria nanostructures has indeed been established (see figure 3.28), with a coverage ratio  $\text{CO}_{\text{top}}/\text{CO}_{\text{hollow}} \approx 1$ . However, the experimental XPS spectra indicate only that CO species with a binding energy similar to CO in hollow sites are preferentially present on the ceria-Rh(111) surface. It is reasonable to associate at least part of these CO species with particular sites at the metal-oxide phase boundaries (they need not necessarily be hollow sites), but the present XPS results do not allow us to specify their exact coordination. The delayed detection of these CO species at the surface may then also be due to the fact that they are more efficiently removed as  $\text{CO}_2$  in the vicinity of the oxide-metal interface during the initial stages of the adsorption/reaction process. Some participation of oxygen from the periphery of the ceria islands in the CO oxidation reaction may also be indicated by the partial reduction of the ceria overlayer, but this reaction path appears to be less important at the relatively low temperatures of the present experiments than reported at higher temperatures [45].

Dissociative adsorption of CO has been reported in the literature on ceria supported Rh model catalyst surfaces [47]. On the Rh(111) supported ceria inverse catalyst surfaces no dissociation of CO has been detected here after room temperature exposure, and even after significant reduction of the ceria island surfaces only molecular CO adsorption has

been identified. This is significant since the reduction of the ceria has been invoked as an important factor for the dissociation of CO on the Rh particles [47]. The present results demonstrate that the morphology of the Rh particles, with their low-coordinated Rh sites, are most likely to play a decisive role in the dissociation process.

The energy balance of CO adsorption sites on Ce-Rh alloy surfaces is different from that on the Rh(111) surface. The hollow sites constitute clearly the lowest energy sites for CO adsorption, they are almost exclusively populated at room temperature, but the lower saturation coverage of CO indicates that the global adsorption energy is smaller on the alloy than on Rh(111). Recently, a similar preference for the population of hollow CO adsorption sites has been found experimentally on a V-Pd alloy surface [51], where the relative stability of the hollow adsorption sites has also been predicted theoretically by density functional theory calculations [52]. A reduction of the CO adsorption energy on the V-Pd alloy surface as compared to Pd(111) has also been calculated in this latter work, in close agreement with the experimental findings. The results obtained here are in line with these observations and suggest that this trend is more general for the adsorption of CO on alloy surfaces. The weak dissociation activity observed on the Ce-Rh alloy surface is probably a defect induced effect.



### 3.4 Summary

#### Growth and thermal reduction of ultrathin $CeO_{2-x}$ films on Rh(111)

Ultrathin layers of cerium oxide have been deposited on a Rh(111) surface and their growth morphology, structure, and thermal stability have been investigated by LEED, STM, XPS, and valence band resonant photoemission. STM and LEED indicate that the ceria grows epitaxially in form of ordered  $CeO_2$  islands at elevated substrate temperature (250-300°C), with (111) faces parallel and orientationally aligned to the main azimuthal directions of the substrate.

The ultrathin ceria films contain significant amounts of reduced  $Ce^{3+}$  species, which appear to be located predominantly at the ceria-Rh interface. For thicker films (>6 equivalent monolayers) stoichiometric  $CeO_2$  is detected in XPS. Vacuum annealing produces morphologically well-defined hexagonal islands, accompanied by partial reduction and the formation of oxygen vacancies at the ceria surface.

The thermal stability and the degree of reduction is a function of the oxide layer thickness, with thinner layers being thermally less stable. At temperatures >800°C, the ceria decomposes and Ce-Rh alloy phases are identified.

#### CO-adsorption experiments on $CeO_x/Rh(111)$ surfaces

The adsorption of CO and the reaction of CO with preadsorbed oxygen has been investigated by comparing the Rh(111)2x1-O surface and ceria decorated Rh(111) inverse model catalyst surfaces using C 1s and O 1s core level and valence band photoelectron spectroscopy with synchrotron radiation.

The adsorption of CO on the oxygen precovered Rh(111)2x1-O surface was found to proceed slower than on the clean Rh(111) surface, as a result of the kinetic constraints imposed by the O+CO oxidation reaction, which removes the adsorbed oxygen as  $CO_2$  in a clean-off reaction at 300-320K. On the ceria-Rh(111) surfaces the O+CO oxidation reaction is much faster than on the Rh(111)2x1-O surface and a catalytically active role of the ceria-Rh interface is suggested; the latter may be promoted by CO adsorption sites near the metal-ceria island phase boundaries. The XPS results support the notion that these CO sites close to the periphery of ceria islands are of the threefold hollow type.

No dissociation of CO has been detected on the Rh(111) supported ceria inverse catalyst

surfaces, but a small amount of CO dissociation is seen on  $CeRh_3$  alloy surfaces; the latter have been prepared by thermal decomposition of the ceria in UHV at high temperature. On the  $CeRh_3$  alloy surface the hollow-type CO adsorption sites are energetically favoured, but the global adsorption energy is lower than on Rh(111), as indicated by the reduced CO saturation coverage.

# Chapter 4

## The

## Manganese-oxide-Palladium(111)

## interface

### 4.1 Introduction

#### Properties of Mn and its oxides

Mn is a group VII metal with the atomic number 25 and a simple cubic crystal structure. The stable manganese oxidation states at room temperature are given in table 4.1. Furthermore, this table gives the electronic ground state configuration for each oxidation state and the melting / decomposition temperatures to monitor their thermal stability as bulk oxides.

The interesting magnetic properties of manganese and its oxides originate from the half filled Mn 3d-band. A sketch of the d-orbitals is presented in figure 4.1.

For MnO the 3d orbitals are split into  $t_{2g}$  and  $e_g$  states, which are separated by a crystal field splitting of 1.8 eV [53]. This crystal field splitting of MnO is illustrated in figure 4.2.

The crystal field splitting theory is an ionic theory which is an offshoot of electrostatic theory. It ignores all covalent bonding effects. It was developed by Hans Bethe in 1929 by applying group theory and quantum mechanics to electrostatic theory. It was further developed by physicists during the 1930s and 1940s. It can be used to predict chemical

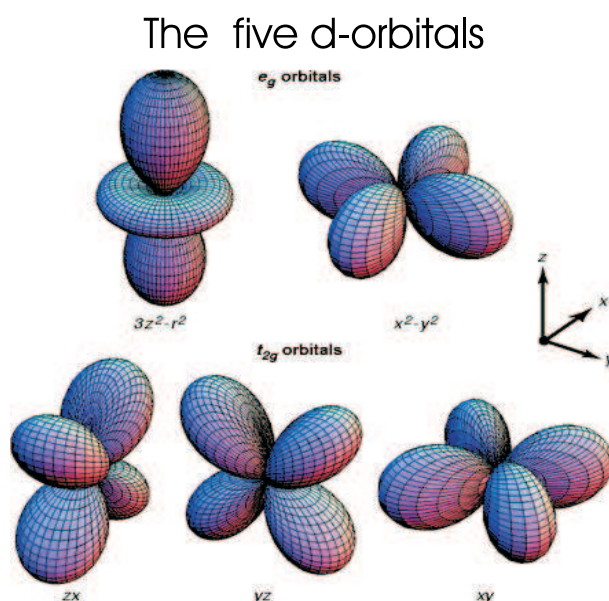


**Figure 4.1:** Sketch of the orbitals for the d-electrons

properties, kinetic properties, reaction mechanisms, magnetic and spectral properties, and thermodynamic data. It cannot, however, be applied to sulfides, since sulfides form mainly covalent bonds. A splitting of the energy levels ("crystal field splitting") occurs because the orientation of the d orbital wave functions will increase an electron's energy when the orbital is located in a region of high electron density, and lower it when the reverse is true.

Manganese oxides			
Oxide	formal oxidation state	ground state configuration	melting /decomposition temp.
Mn		[Ar] $3d^5 4s^2$	1246°C (m.)
MnO	2+	[Ar] $3d^5$	1785°C, 1840°C (m.)
$Mn_2O_3$	3+	[Ar] $3d^4$	940°C, 1080°C (d.)
$Mn_3O_4$	2+/3+	[Ar] $3d^5/3d^4$	1590°C (m.)
$MnO_2$	4+	[Ar] $3d^3$	535°C (d.)
$Mn_2O_7$	7+	[Ar]	6°C (liquid at RT!)

**Table 4.1:** Properties of manganese and its oxides: electronic configurations and melting / decomposition temperatures

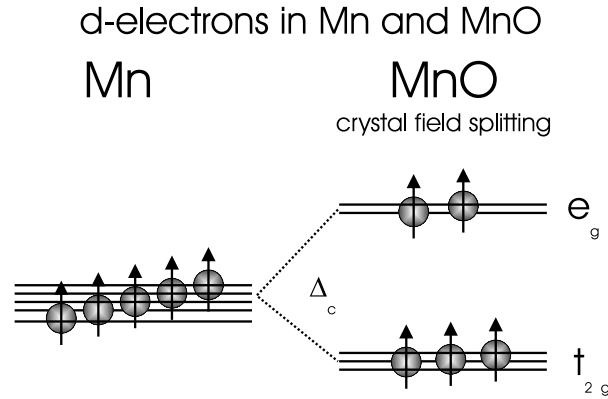


**Figure 4.2:** Crystal field splitting for MnO (sketch)

In the MnO bulk crystal (NaCl structure, thus cubic), the  $d_{xy}$ ,  $d_{xz}$ ,  $d_{yz}$ ,  $d_{z^2}$  and  $d_{x^2-y^2}$  orbitals split up, due to the coordination of the cation. The total energy splitting  $\Delta_c$  (c stands for cubic) is called the crystal field stabilisation energy.  $\Delta_c$  may be estimated from

$$\Delta_c \approx \frac{\langle r^4 \rangle}{R^5}$$

where  $r$  is the radius of the d-orbital and  $R$  is the metal-ligand inter-nuclear distance. Generally, a large crystal field splitting energy is provided by ligands with high negative charge and small radius, and by metal cations with a large oxidation number. In the case of MnO the electrons in the  $e_g$  states are coupled spin-wise with the electrons in the adjacent oxygen orbitals. In that way the oxygen electrons synchronise the spin orientation of the Mn 3d electrons, which leads to a magnetic interaction.

### The importance of manganese and its oxides

Manganese and its compounds are important in many applications. Mn is a component of many alloy systems, especially in the various steels, and is used in the production of steel. Alloying with manganese can improve the strength and ductility of the alloy. Manganese compounds have many important applications, such as the use of manganese oxides in batteries, and in catalytic systems. Other applications include glass bleaching and colouring, the preparation of oxygen and chlorine and the production of fertilisers, pesticides and fungicides [54].

In recent years there has been a steadily increasing interest in the growth of ultra-thin films, that is, films with thicknesses of just a few atomic layers. In this respect,

thin magnetic films deposited on non-magnetic substrates constitute one of the most important types of systems [55]. MnO bulk crystals, for instance, undergo a first order paramagnetic to anti-ferromagnetic phase transition at 118 K. Furthermore, a recent theoretical study predicts that nanoparticles of MnO would have ferromagnetic behaviour [56, and references therein].

Apart from the importance of manganese thin films due to their magnetic properties, i.e. in electronic devices, they are important due to their catalytic properties.  $MnO_x$  is known to be an excellent catalyst for oxidation reactions because it may act as an oxygen reservoir. Palladium, on the other hand, is a metal with a high thermal stability and a high activity under excess of oxygen and Pd has proven to be a good catalyst, e.g. for the oxidation of CO to  $CO_2$  [57].

In the introduction to their investigations of adsorption and reactions on the Pd(100)-Mn-c(2x2) surface alloy Sandell et al. emphasised the role of Mn and Pd in heterogeneous catalysis [58]. In a study of Pd-based catalyst particles containing manganese supported on silica it was found that such particles are more active towards reduction of NO by CO than pure Pd [57]. One possible reason for this is the high tendency for Mn to dissociate NO. Consequently  $MnO_x$  could play an important role for the enhanced activity of the Pd-Mn system [58, and references therein], because it is likely that the Mn becomes oxidised under reaction conditions.

In this chapter the controlled growth of manganese oxide films on a palladium(111) single crystal surface under ultra high vacuum conditions will be investigated with XPS, UPS, LEED and STM. The preparation conditions to achieve ordered manganese oxide films on Pd(111) will be presented in the sections 4.1.1, 4.2.4 and 4.2.9. In the sections 4.2.1, 4.2.2 and 4.2.5 XPS and UPS investigations will prove that the films achieved by reactive evaporation and post-oxidation of Mn on Pd(111) at elevated temperatures are manganese oxides in the chemical state of  $Mn^{2+}$ , i.e. MnO.

The sections 4.2.6 (XPS), 4.2.7 (UPS) and 4.4.2 (STM) will discuss the growth mode of the MnO films on Pd(111). The thermal stability of the MnO/Pd(111) surfaces and the formation of a Pd-Mn surface alloy (of as yet unknown stoichiometry) will be presented in sections 4.2.10 (XPS), 4.3.2 (XPS), 4.3.3 (UPS), 4.3.4 (XPS, UPS) and 4.4.3 (STM). Summaries of the photoemission and scanning tunnelling microscopy results are given in 4.3.6 and 4.4.4, respectively.

### 4.1.1 Preparation of thin oxidised manganese films

For the preparation of ordered oxide films several approaches are commonly used. For ordered ceria films on Rh(111) the so-called reactive evaporation has been used, i.e. the cerium metal has been evaporated in an oxygen background pressure onto the substrate at an elevated temperature. In case of ceria an oxygen pressure of  $2 \times 10^{-7}$  mbar and a substrate temperature of 250°C led to well ordered cerium oxide films in their highest oxidation state. Lower oxygen pressures led to lower oxidation states of the films, lower temperatures led to lower ordering of the films, i.e. no diffraction spots in LEED [20].

Mueller et al. presented epitaxial films of MnO grown on Ag(001) at room temperature. They achieved ordered MnO films on Ag(001) via reactive evaporation in oxygen pressures between  $1 \times 10^{-8}$  and  $5 \times 10^{-7}$  mbar at room temperature and improved the film ordering by subsequent annealing temperatures between 400 and 500°C [59].

Tian et al. reported epitaxy of MnO on Cu(001) by first depositing 2 to 3 layer equivalents of Mn on the Cu (001) surface, then exposing the surface to considerably high pressures of oxygen ( $10^{-5}$  mbar) for 30 minutes and finally annealing at 475°C for 5min [60].

Rizzi et al. published epitaxial growth of MnO on Pt(111) by reactive deposition of  $Mn_2(CO)_{10}$ .  $Mn_2(CO)_{10}$  and  $H_2O$  vapours ( $8 \times 10^{-7}$  mbar background pressure) were dosed in close sequence while the Pt(111) substrate was kept at 200°C [56].

For the presented work both reactive evaporation and post-oxidation were investigated in order to find the best conditions to prepare ordered manganese oxide films on Pd(111). For the evaporation of manganese a directly heated tungsten coil evaporator and an two different e-beam evaporators have been used. The experimenter was confronted with the same stability problems during manganese evaporation that were mentioned by Mueller et al. [59]. Due to the high vapour pressure of Mn, the evaporators had to be operated at their lowest limit, otherwise the Mn flakes evaporated at a single burst. Comparing a tungsten coil evaporator, a not coolable Caburn e-beam evaporator and a water cooled Omicron e-beam evaporator the best controllable deposition rate was achieved with the Omicron evaporator, where a single Mn piece (diameter 5 mm, length 1cm) was pressed into a molybdenum crucible.

## 4.2 Thick films (>3 MLE) of MnO on Pd(111): XPS, UPS and LEED

### 4.2.1 Mn 2p XPS

Mn 2p, the strongest feature in XPS, has been used in many publications (e.g. in the standard handbook of X-ray photo electron spectroscopy [61]) as a monitor for the oxidation state of manganese. Mn 2p XP-spectra have been reported in the literature for both metallic and oxidised manganese bulk crystals and thin films. Much effort has been invested to characterise the satellite structure of MnO, that had been observed in both core-level and valence band photo-emission spectra [62, 56, 63, 64, 65, 66, 67].

A complete table of XPS core level data for the oxidation states from MnO to  $MnO_2$  is given by A. Audi et al. [54]. In this publication the authors compare their own measured data with a variety of other publications. Table 4.2 gives an overview of some published Mn 2p binding energies for the various oxidation states.

Rizzi et al. [56] interpreted the Mn 2p spectra observed in high resolution XPS and published by other groups [67, 63] that they assigned two components plus a satellite line to the complex Mn  $2p_{3/2}$  peaks of their spectra. The two main components were estimated to be 1.9 eV apart.

Mn $2p_{3/2}$ binding energies in eV					
eV	[61]	[54]	[56]	[68]	this work
Mn	639.0	638.8			638.6
MnO	640.5	641.1	640.6	640.7	640.7
$Mn_2O_3$	641.5	641.7			
$Mn_3O_4$	641.5	641.4		641.4	
$MnO_2$	642.1	642.3			

**Table 4.2:** Mn  $2p_{3/2}$  binding energies (eV) found in the literature; the last column shows the values obtained on 12 ML Mn deposited onto Pd(111) in UHV and post-oxidised in  $2 \times 10^{-7}$  mbar  $O_2$  at 250 °C



Taguchi et al. [66] show even more than three major contributions to both  $2p_{3/2}$  and  $2p_{1/2}$  in the figure that represents their calculations of the Mn2p line shapes, but in the text they mention only "two main peaks which correspond to the  $2p_{3/2}$  and  $2p_{1/2}$  core levels and the satellites about 6 eV above the main peaks".

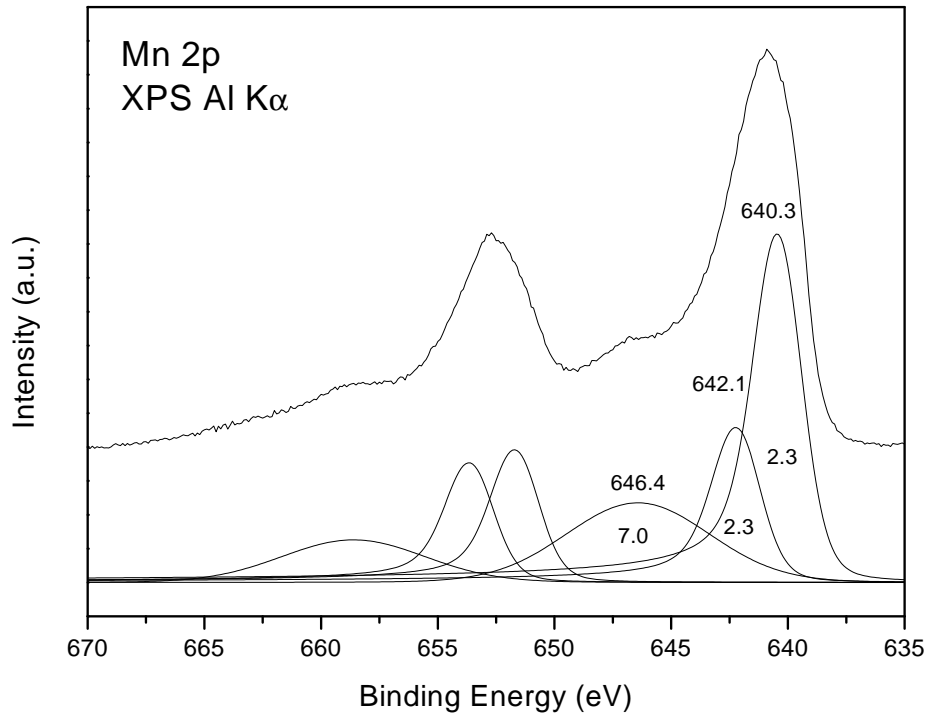


**Figure 4.3:** Mn2p spectrum of 12 ML Mn evaporated at RT and post-oxidised in  $2 \times 10^{-7}$  mbar  $O_2$  at 300°C. Below: fit with 6 components

Fig. 4.3 shows a spectrum taken after oxidising 12 ML of Mn in  $2 \times 10^{-7}$  mbar  $O_2$  at 300°C. Below the spectrum a fit with 6 components is shown. Best agreement with the measured spectrum has been found with the two main Mn  $2p_{3/2}$  components at 640.3 and 642.1 eV (Gauss FWHM= 2.3 eV for both) and the satellite at 646.4 eV with a Gauss-FWHM of 7 eV. These fit results closely resemble those published by Rizzi et. al. for MnO thin films on Pt(111)[56], where the main contributions to the Mn  $2p_{3/2}$  were found at 640.6 and 642.5 eV binding energy. Unfortunately no other fit parameters are given in this publication.

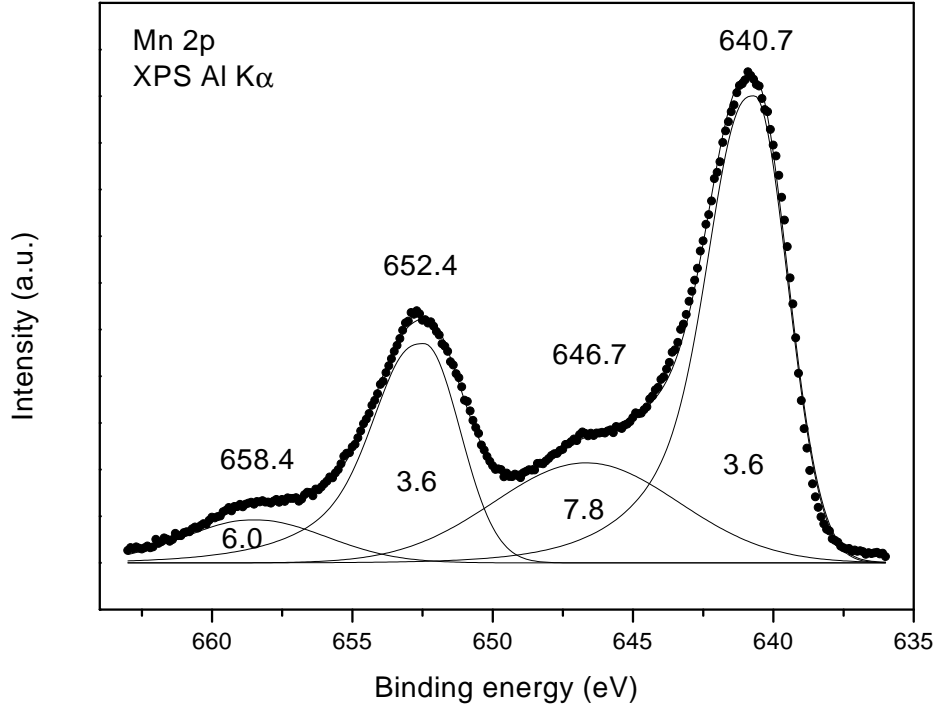


**Figure 4.4:** *Mn2p spectrum of 12 ML Mn evaporated at RT and post-oxidised in  $2 \times 10^{-7}$  mbar  $O_2$  at 300° C. Below: fit with 4 components*

Oku et al. have reported a chemical shift of only 0.2 eV between bulk MnO and  $Mn_2O_3$  [63]. This small shift and the similarity of the reported spectral profiles for MnO and  $Mn_2O_3$  complicates the interpretation of Mn2p spectra. This might be the reason why most published Mn2p spectra, especially those obtained with a standard (non-monochromatised) Al K $\alpha$  source only refer to one main Mn  $2p_{3/2}$  component and a satellite separated 5 to 6 eV from the main line.

For the spectra presented in this work, a standard Al K $\alpha$  source has been used. Because no monochromator was equipped, the total line width of analyser and source was dominated by the 0.85 eV line width of the source. Due to these limitations of the resolution, a fit with three components per spin-orbit split line was not sensible. Most of the spectra shown in this work have therefore been fit in the way shown in Fig. 4.4. Since the x-ray line width was estimated to be the major contribution to the broadening, Gaussian

line shapes have been used to fit both main lines and satellites. Above the spectra the obtained binding energies have been given in electron volts (eV) and inside the peaks their FWHM have been labelled. Thus for this preparation the  $Mn2p_{3/2}$  position was at 640.7 eV and its satellite was found at 6.0 eV higher binding energy.

### 4.2.2 Mn 3s XPS

Apart from using the binding energy of the Mn  $2p_{3/2}$  core level, the Mn 3s core lines are often used to determine the Mn oxidation state [62, 67, 54, 56]. Core-level photoemission always produces a final state with spin and angular momentum. If the system under investigation has an open valence-state configuration  $l^n$ , with corresponding spin and orbital momenta, the coupling with the core-hole orbital and angular momentum leads to a number of different final states. A particularly simple situation arises if the core level is an  $s^2$ -state resulting in a net spin of  $s = 1/2$  for the photo-hole. This spin can couple parallel or anti-parallel to the spin  $S$  of the valence-shell configuration. This then leads to an exchange splitting  $\Delta E_s$

$$\Delta E_s = \left( \frac{2S + 1}{2l + 1} \right) \times G^l(s, l) \quad (4.1)$$

where  $G^l(s, l)$  is the exchange integral.

This exchange splitting is also referred to as *core polarisation*. Apart from this core polarisation Gweon et al. found contributions of intra-shell electron correlation and final state screening (charge transfer satellite) effects to the Mn 3s satellite structure [69]. Mueller et al. compiled a table of literature data of Mn 3s splitting for metallic Mn and for several Mn oxides in their publication on the growth of MnO on Ag(001) [56], and give an intensity ratio of 1.45 to 1 for the main and satellite Mn 3s features of their bulk MnO crystal.

Table 4.3 compiles the values found in the literature for the Mn 3s splitting together with the values obtained for 24 ML Mn on Pd after deposition in UHV and post-oxidation in  $2 \times 10^{-7}$  mbar  $O_2$  at 250°C.

Fig. 4.6 shows the Al  $K\alpha$  excited photoemission spectra from the Fermi level to  $\sim 100$  eV BE. In the substrate spectrum shown at the bottom, the shallow Pd core levels Pd 4s and Pd 4p can be assigned at 87.5 and 51.6 eV, respectively. In the top part of figure 4.6 the corresponding spectrum is shown for a considerably thick MnO layer of

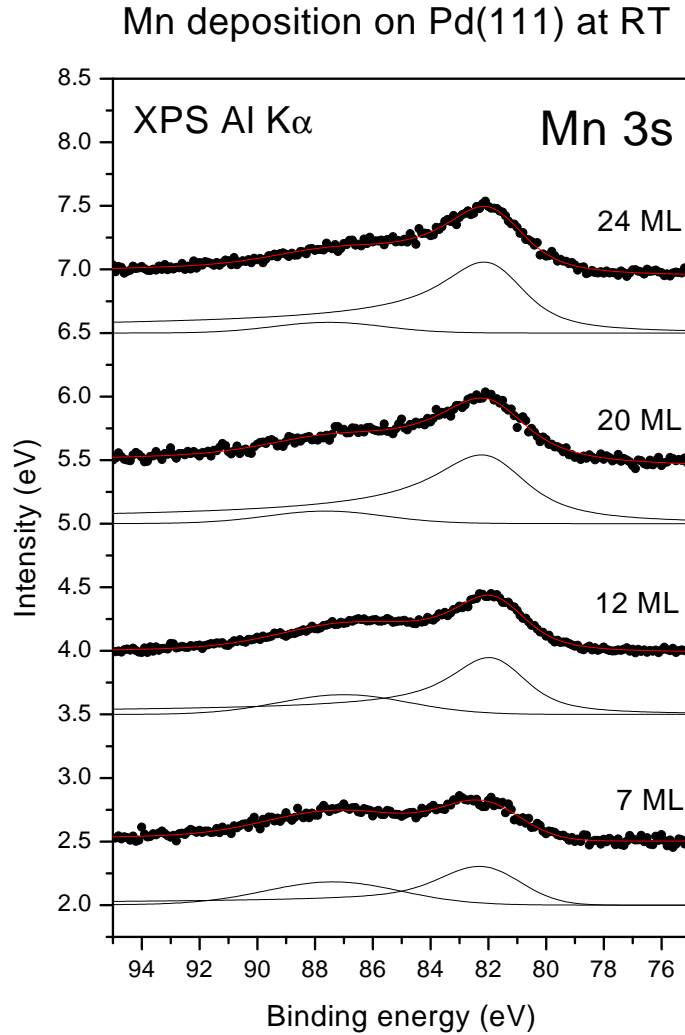


**Figure 4.5:** Al K $\alpha$  excited Mn 3s spectra: thick layers of metallic Mn on Pd(111)

7 MLE, post-oxidised in  $2 \times 10^{-7}$  mbar  $O_2$  at 250°C. Mn 3p emission of this surface is found at 47.6 eV binding energy, the Mn 3s main peak and satellite at 82.7 and 88.3 eV, respectively.

Fig 4.5 shows the Mn 3s spectra for depositions higher than 7 ML. All metallic Mn depositions show the Mn 3s main line at 81.8 eV ( $\pm 0.1$  eV) with a FWHM of 4.3 eV. The satellite line of metallic Mn 3s is measured at 87.5 eV ( $\pm 0.1$  eV), thus the split energy is about 5.7 eV. This split energy does not agree with the 4.1 to 4.7 eV published for bulk

Mn 3s split energies					
ref.	[69]	[54]	[56]	[70]	this work
Mn	-	-	3.6 - 4.1	-	5.7
MnO	6.1	5.89	5.8 - 6.15	5.8	6.3
$Mn_2O_3$	-	5.43	5.2 - 5.7	5.2	
$Mn_3O_4$	-	5.35	4.6 - 5.3	5.3	
$MnO_2$	-	4.86	4.5 - 4.7	4.7	

**Table 4.3:** Mn 3s split energies found in the literature; last column: the values obtained for 24 ML Mn on Pd after deposition in UHV and post-oxidation in  $2 \times 10^{-7}$  mbar  $O_2$  at 250° C.

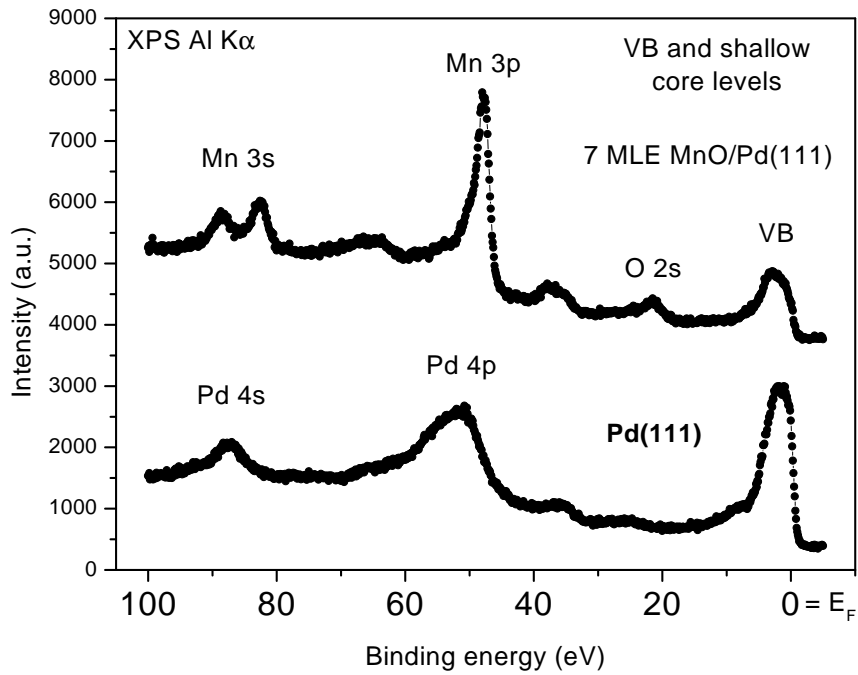


**Figure 4.6:** XPS valence band and shallow core level spectra; bottom: clean Pd(111); top: 24 MLE MnO/Pd(111)

Mn metal [56]. The Mn 3s split measured for Mn deposited on Pd(111) resembles more the one published by Huefner for Mn in the gas-phase [62]. Huefner found that MnO and  $MnF_2$  have identical 3s splittings as atomic Mn (in the gas-phase). His explanation was that atomic manganese has a  $d^5$  configuration which is not changed by the core level photo-emission process. Therefore the 3s splitting reflects the core polarisation of the 3s hole with that  $d^5$  configuration.

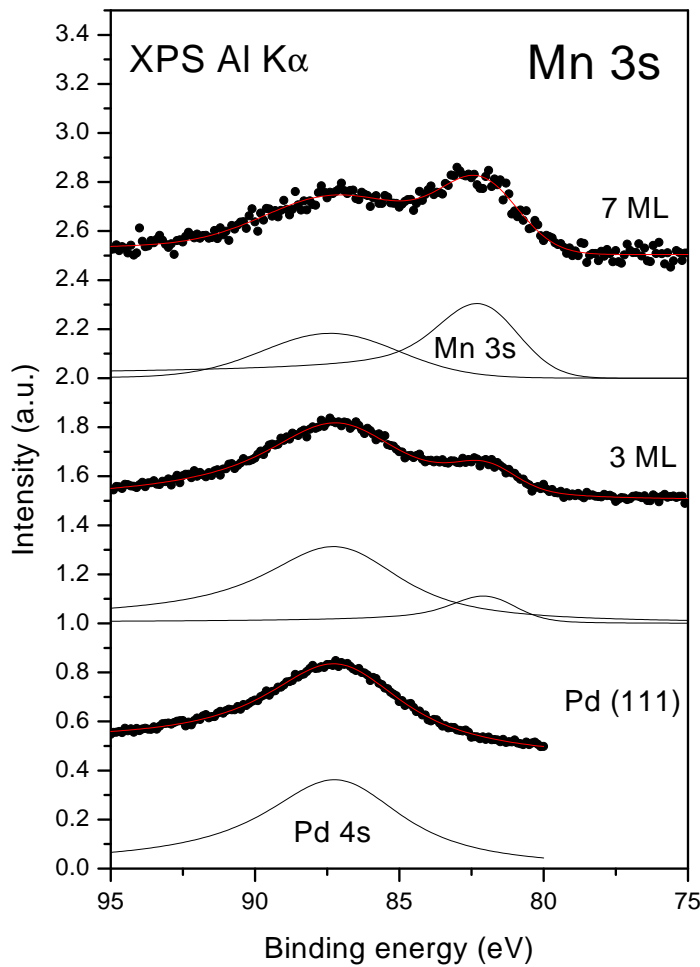


**Figure 4.7:** Uptake of metallic Mn on Pd(111): Mn 3s spectra

In section 4.2.4 it will be shown that the Mn 3s splitting for oxidised Mn surfaces is

0.6 eV larger than the one measured for the metallic surfaces. The Mn 3s main line for oxidised Mn films was found at 0.6 eV higher binding energy with respect to the metallic Mn films. Furthermore, the spectral characteristics of the Mn 3s satellites for metallic and oxidised Mn differ drastically. In summary, thick layers of Mn and MnO can be clearly distinguished by laboratory source-XPS using the Mn2p, Mn3s and O1s spectra.

Taking the overlap of the Mn 3s and Pd 4d photoemission peaks into account, it is obvious that for lower coverages the Mn 3s splitting can not be determined unambiguously. This is illustrated in figure 4.7, where the spectra and fits for two thinner layers of metallic Mn are shown together with the Pd 4s spectrum. The Mn 3s satellite line, which is expected at 87.5 eV (see 4.5 on page 96), overlaps with the Pd 4s line measured at 87.0 eV.

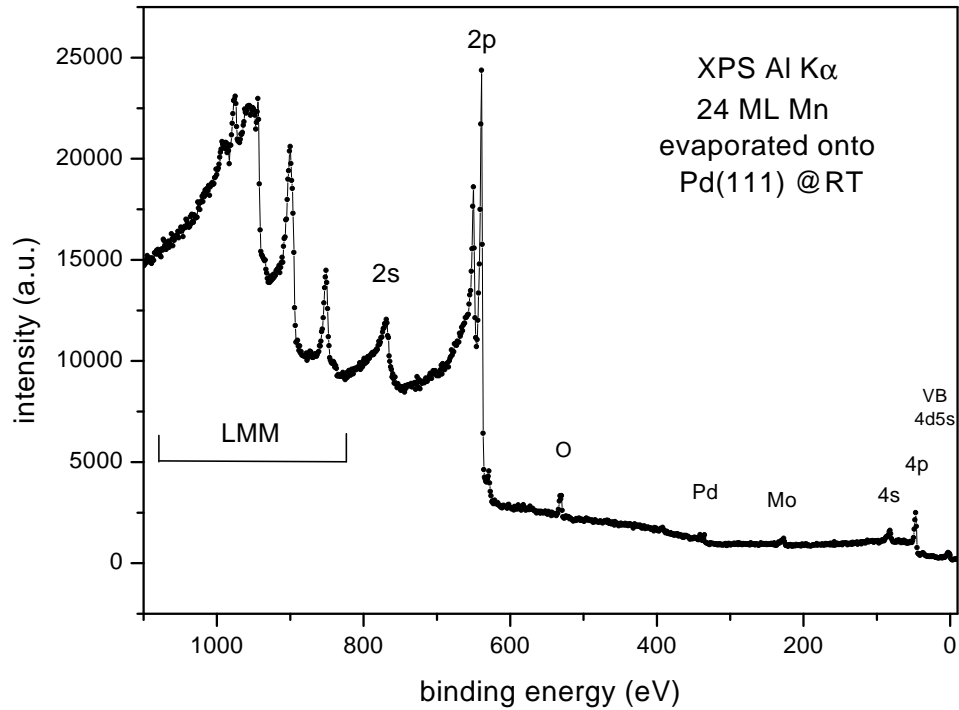
### 4.2.3 Mn metal deposition as studied with XPS

Fig 4.8 shows a wide-range XP spectrum of 24 mono-layers of manganese evaporated onto the Pd single crystal at room temperature in ultra high vacuum. The main XPS features of Mn are labelled as well as small amounts of detected contaminants. The small amount of oxygen derives either from reaction of the deposited metal with the background pressure ( $\text{CO}$ ,  $\text{O}_2$ ) or - more likely - from oxidation of the Mn material inside the evaporator due to previous oxygen treatments in the preparation chamber.

The small Pd signal detected shows that the film thickness of 24 ML is not quite sufficient to completely suppress photo-emitted electrons from the substrate underneath. The small Mo signal in the spectrum shown derives from the sample plate onto which the Pd crystal was mounted. This signal could be excluded in later spectra by changing to a narrower detection window in the ESCA 300 software (see Scienta manual in appendix A).

Figure 4.9 shows the development of the total Mn 2p and Pd 3d signals versus the nominal coverage. It shows that at 35 ML nominal Mn coverage the film thickness has exceeded the probing depth of Al-K $\alpha$  excited XPS, thus no more Pd signal can be detected. In figure 4.10 Mn 2p spectra of various depositions at room temperature are shown together for comparison. All spectra have been taken with the same analyser and x-ray source settings.

The last spectrum of the uptake series in figure 4.10 on page 102 is presented again



**Figure 4.8:** Wide range XP spectrum of 24 mono-layers of manganese evaporated onto the Pd single crystal at room temperature in UHV

in figure 4.11 together with calculated fit curves underneath. The Mn  $2p_{3/2}$  component of this Mn film shows a binding energy of 638.6 eV, which is in good agreement with the reported binding energy for bulk Mn [61, 54]. The analyser resolution was set to 0.1 eV (pass energy 300, slit curved 0.8 mm) which is considerably below the resolution of the x-ray source and resulted in reasonably good statistics in 10 minutes measurement time.

The spin - orbit split contributions and their binding energies are labelled in fig 4.11, assuming only one single peak for each component. The Mn 2p satellite structure was taken into account by allowing a strong asymmetry to higher binding energies in the fits. All spectra in figure 4.10 have been fit using the same parameters and the resulting change in the Mn  $2p_{3/2}$  binding energy is shown in the figure 4.12.

Interestingly, the thinner layers with a coverage below 2 ML showed a 1 eV higher Mn  $2p_{3/2}$  binding energy of 638.9 eV and a different shape than the thick layers above 5



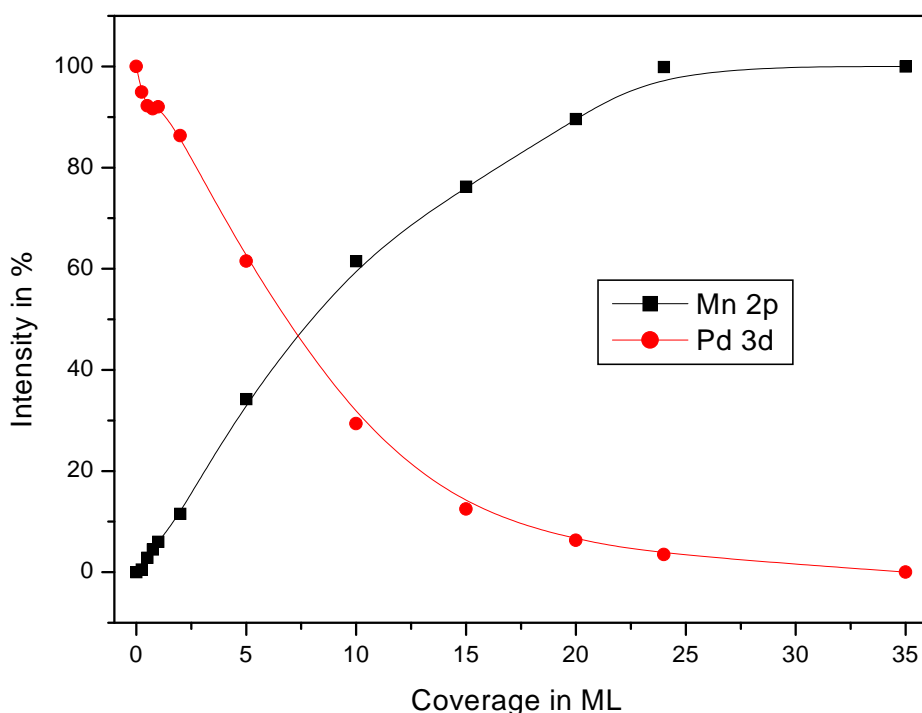


**Figure 4.9:** Uptake of metallic Mn on Pd(111): total signal of Mn 2p vs. Pd 3d in percent, normalised to the respective starting and saturation intensities

ML. This result can be explained either by a contribution of a small amount of MnO in the thin layers or by a different binding energy due to the Mn-Pd bond at the interface. For the last spectrum of the uptake curve, the O contamination of the metallic surface was measured by comparing the O 1s signal at the same coverage after full oxidation at 250°C. The O1s signal of the 24 ML metallic surface was less than 10 percent of the 24 MLE MnO surface, for lower coverages of metallic Mn the O 1s signal was below the detection limit. The absence of a measurable O 1s signal in the XP spectra suggests that the changes in the Mn 2p binding energy for the lower coverages can be attributed to the Mn-Pd bond.

Another effect of the Mn-Pd bond can be seen in the Pd 3d spectra of the substrate, as shown in figure 4.13. With increasing Mn coverage the measured Pd  $3d_{5/2}$  signal shifted to higher binding energies by 0.2 eV.

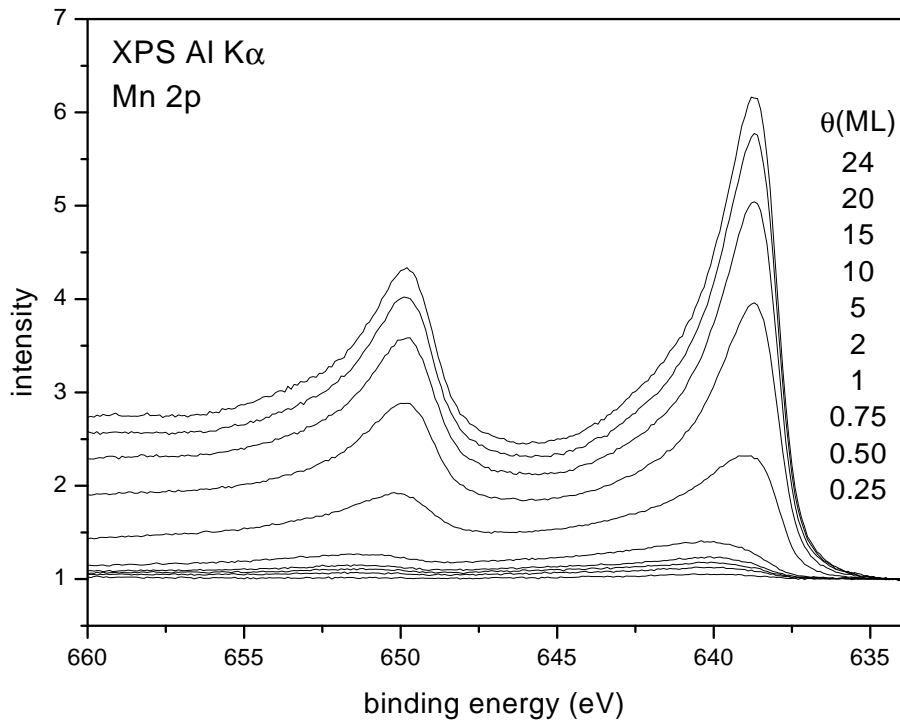


**Figure 4.10:** Uptake of metallic Mn on Pd(111): Mn 2p spectra

For the formation of a Mn mono-layer on Pd(100) Sandell et al. found a Pd  $3d_{5/2}$  interface component that was shifted by 0.8 eV to higher binding energies with respect to the Pd bulk component in their high resolution Pd 3d spectra [55]. After the completion of the mono-layer the Pd 3d HR-XPS did not change upon further deposition. Considering the higher resolution as well as the more open Pd(100) substrate, the change in our Pd 3d binding energy can be interpreted as the formation of a complete layer of Mn on Pd(111). The fact that the Pd  $3d_{5/2}$  binding energy shift saturates at 5 ML and not at 1 ML, as observed by Sandell et al. [55], could be interpreted by an island growth mode, however the low surface sensitivity of Al  $K\alpha$  XPS as compared to the 400eV-excited HR-XPS dilutes that argument. The fact that the changes in Mn 2p and Pd 3d spectra saturate at the same coverage confirms that the changes in the Mn 2p spectra for the lower coverages can be attributed to the Mn-Pd bond, and that the Mn layer grows presumably in an island growth mode.

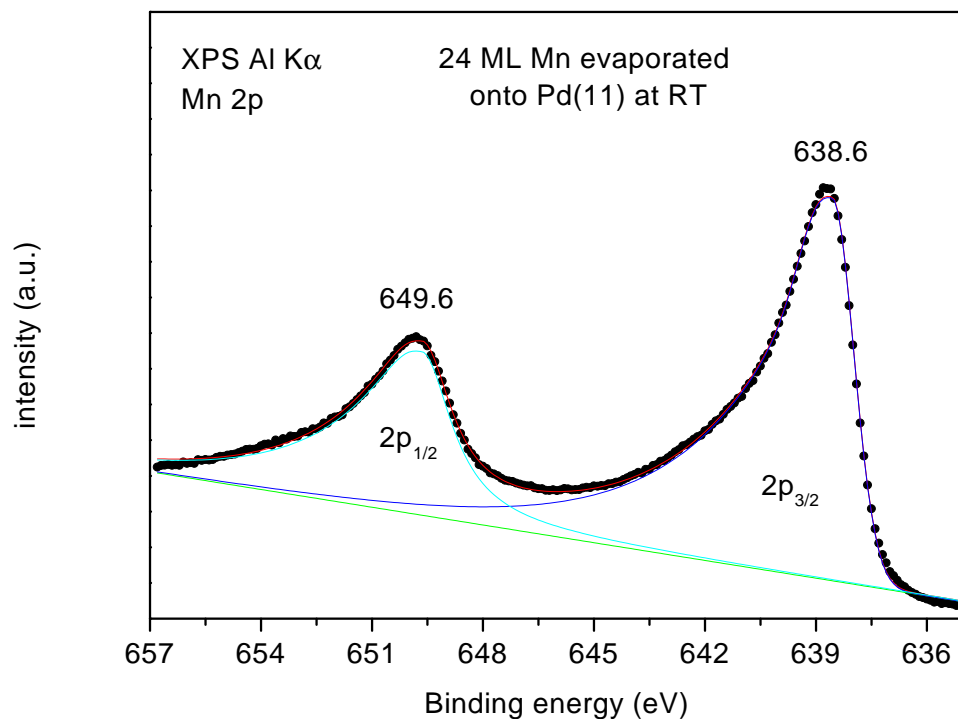


**Figure 4.11:** Mn 2p spectrum of 24 ML Mn evaporated onto the Pd single crystal at room temperature in UHV. Dots represent the measured spectrum, lines the fits

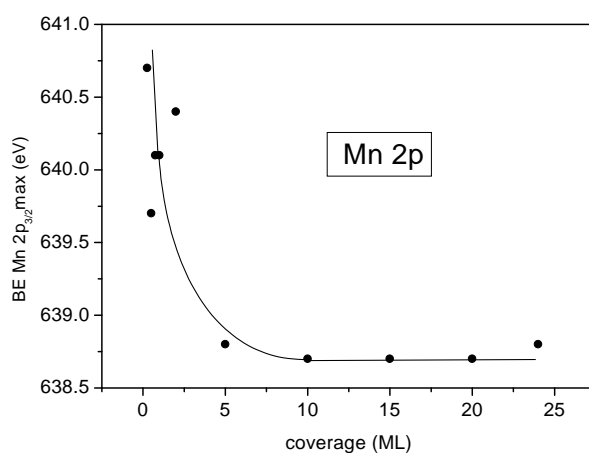


**Figure 4.12:** Uptake of metallic Mn on Pd(111) - Pd  $3d_{5/2}$  binding energy vs. Mn coverage

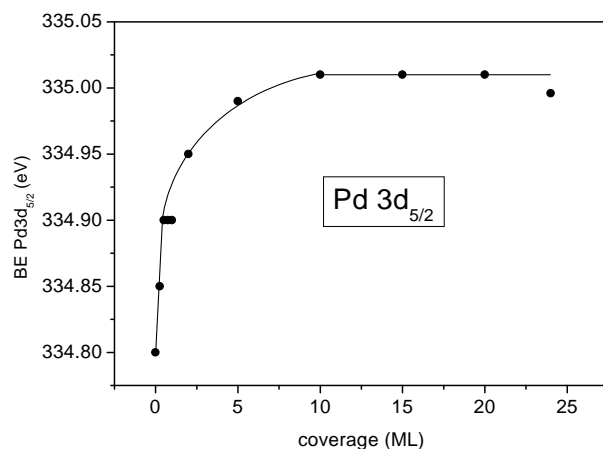


**Figure 4.13:** Uptake of metallic Mn on Pd(111) - Mn 2p<sub>3/2</sub> binding energy vs. Mn coverage

#### 4.2.4 Oxidation of thick manganese films on Pd(111)

The last surface of the uptake series of Mn on Pd(111) at RT (24 ML) shown in figure 4.10 (page 102) was then exposed to oxygen. In Figure 4.14 the area of the O 1s signal is plotted against the exposure at room temperature. Between 200 and 500 Langmuir oxygen at room temperature, a saturation of the O 1s signal was reached. After that saturation the surface was subsequently exposed to  $2.5 \times 10^{-7}$  mbar oxygen at elevated substrate temperatures for 10 minutes.

The exposures at 250, 300 and 400°C resulted in higher oxygen signals with respect to the room temperature saturation and a new saturation level was reached for 300°C. This result can be interpreted by a passivation towards oxidation of the deeper Mn layer by the oxide overlayer at room temperature, that can be overcome by increasing the mobility. The second saturation level indicates that the whole manganese layer in the XPS detection region has been oxidised.

This passivation behaviour during the room temperature oxidation is confirmed by the Mn 2p spectra and corresponding fits shown in Fig. 4.15. The bottom spectrum shows the as-laid metallic Mn surface before the oxygen dosing series. The Mn 2p<sub>3/2</sub> can be fit by one single component at 638.6 eV with a FWHM of 3.0 eV and an asymmetry factor of 0.5. The top spectrum shows the same Mn coverage after oxidation in  $2.5 \times 10^{-7}$  mbar O<sub>2</sub> at 300°C. Its Mn 2p<sub>3/2</sub> part had to be fit by a main component at 640.7 eV

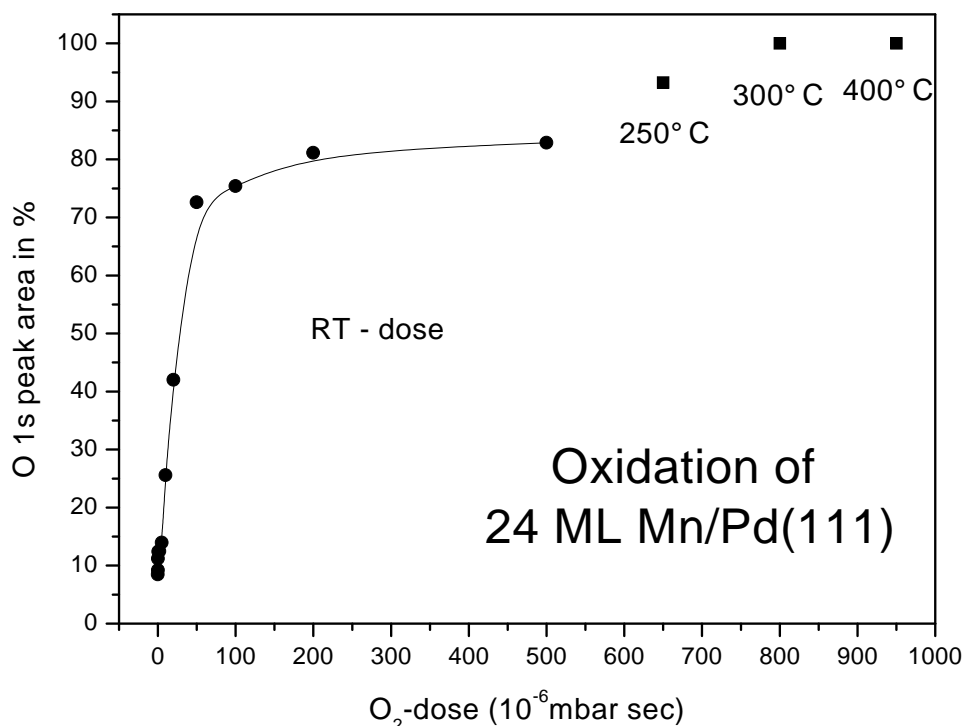


**Figure 4.14:** Oxidation of 24 ML/Pd(111) at room - and elevated temperature

(FWHM 3.6 eV; asymmetry 0.28) and a satellite component at 646.9 eV (FWHM 6 eV, no asymmetry). These results correspond to those found for bulk MnO in the literature (see table 4.2 on page 92).

The Mn 2p spectrum recorded after room temperature O<sub>2</sub> saturation is shown in the middle spectrum of figure 4.15. This spectrum shows a small component of metallic Mn visible as a shoulder at the lower binding energy side of Mn 2p<sub>3/2</sub>. The total Mn 2p spectrum can be well fit by a combination of MnO and Mn fit parameters used in the other two spectra.

In figure 4.16 the Mn 3s XP-spectra of several coverages of MnO are compared. In the spectrum of the lowest coverage (3 MLE) the Pd 4s still overlaps the Mn 3s satellite, but for the higher coverage the Pd emission was sufficiently suppressed to fit the satellite unambiguously. For these higher coverages the Mn 3s main peak is always found at 82.4 eV ( $\pm 0.05$  eV). The Mn 3s satellites has a binding energy of 88.6 eV, which results in a

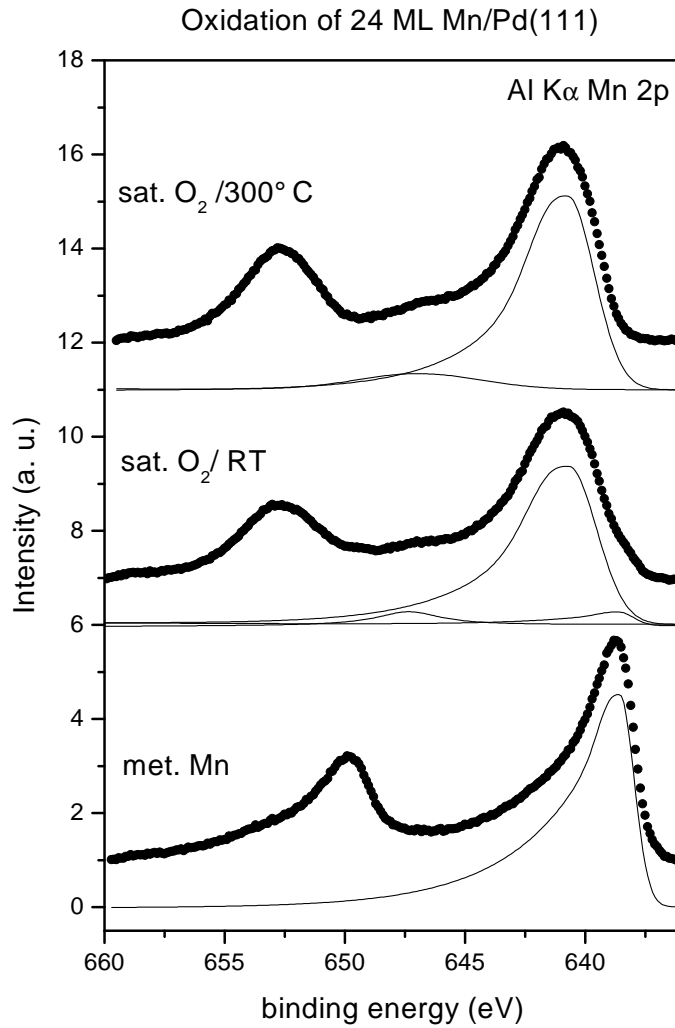


**Figure 4.15:** *Mn 2p spectra of 24 ML Mn/Pd(111) before and after oxygen treatments, for details see text*

separation energy of 6.3 eV. From the Mn 3s table on page 97 one can extract that MnO has the highest Mn 3s splitting of all manganese oxides. The measured value of 6.3 eV agrees with the highest reported value of 6.15 eV within the experimental error of  $\pm 5\%$ .

The Mn 2p, Mn 3s and O 1s measurements all show that manganese thin films up to 24 ML can be fully oxidised by 10 minutes exposure to  $2 \times 10^{-7}$  mbar oxygen at 250-300°C. The Mn2p and Mn3s spectra of these films suggest that the resulting oxidation state of

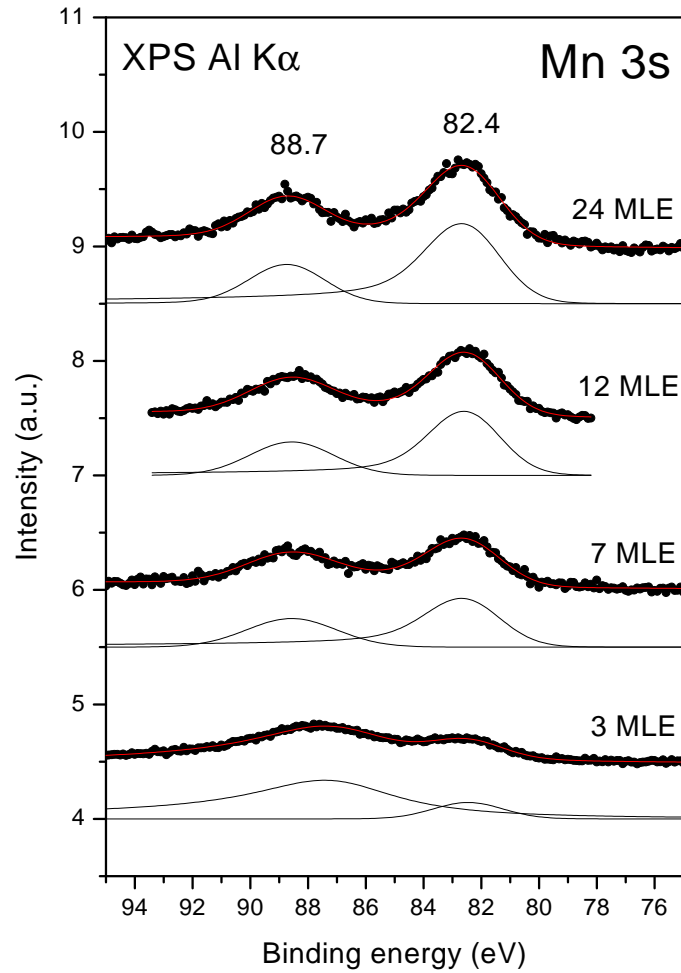


**Figure 4.16:** Mn 3p spectra and corresponding fits of various coverages of Mn deposited at RT and oxidised in  $2 \times 10^{-7}$  mbar  $O_2$  at  $250^\circ C$

the manganese films is  $Mn^{2+}$ . LEED experiments on these manganese films before and after oxidation did not show any diffraction spots that could be attributed to ordered manganese structures.

### 4.2.5 UPS of manganese oxide films

#### Pd substrate and thick MnO films

In section 4.2.4 it has been shown that manganese thin films up to 24 ML could be fully oxidised by an exposure of  $\sim 10$  minutes to  $2 \times 10^{-7}$  mbar oxygen at 250-300°C. Mn 2p and Mn 3s spectra of these films suggest that the resulting stoichiometry of the manganese oxide films is MnO. For UPS investigations of thin manganese films on Pd(111) the valence band features of the clean Pd(111) substrate and of a thick oxide film had to be characterised. UPS spectra of the clean Pd(111) substrate taken with He and He II are presented in figure 4.17. The spectra show the Pd 4d-derived valence band features as described in detail by Leisenberger et. al. [16].

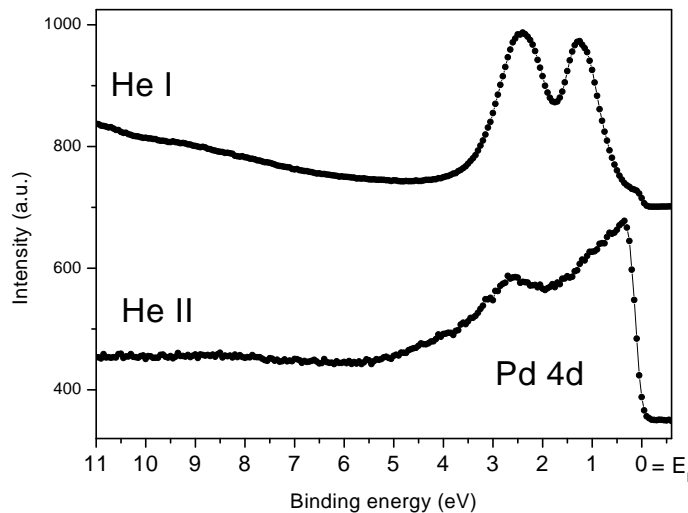


**Figure 4.17:** He I and He II - excited photoemission spectra of the clean Pd(111) surface. The spectra are displayed to show the same size.

He I and He II spectra of cleaved MnO(100) crystals have been published in 1988 by Heinrich et al. [71]. Together with the spectra, they presented the valence band structure predicted by band theory and cluster calculations. Due to the insulating nature of bulk MnO and the resulting charging problems in photoemission they could not determine the position of the Fermi level. Therefore, their presented valence band spectra were referenced in energy to the valence band maximum, which was labelled as  $t_{2g\uparrow}({}^5T_2)$ . According



to this publication the Mn density of states (DOS) consists of a  $\sim 3$  eV wide Mn 3d band with a sharp maximum on the higher binding energy side and a second maximum at 1.8 eV lower binding energy. The Mn 3d band overlaps on its higher binding energy side with the  $\sim 4$  eV wide O 2p band. The O 2p band again consists of 2 components arising from  $\sigma$  and  $\pi$  states. The resulting maximum in the valence band was interpreted as an overlap of the lower binding energy maximum of the Mn3d states with the higher binding energy maximum of the O 2p states (see [71, fig 1]).

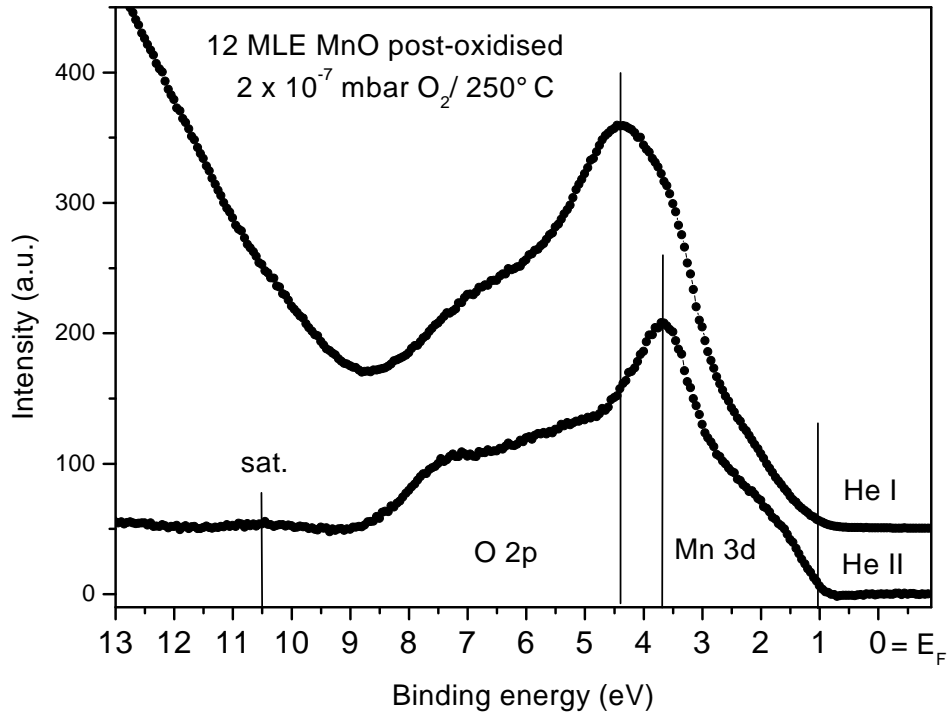


**Figure 4.18:** Valence band spectra of 12 MLE MnO excited with He I and He II in normal emission. The spectra are displayed to show the same size.

The valence band spectra of the 12 MLE post-oxidised MnO film on Pd(111) (figure 4.18) show the same spectral characteristics as the spectra of the cleaved MnO (100) surfaces([71, fig 1]). However, having a metallic substrate solves the charging problem due to secondary electrons created in the substrate underneath the insulating oxide layer and the Fermi edge can be assigned unambiguously.

For thick MnO films the Pd derived states at the Fermi level are suppressed and the

band gap of MnO dominates. During the MnO/Pd(111) valence band experiments, checks of the energy calibration, i.e. the determination of the correct Fermi level position, were performed every time the substrate Fermi level states were suppressed. These checks were performed on a polycrystalline gold sample mounted underneath the Pd single crystal in the same geometry as the Pd crystal.

The MnO valence band edge is 1 eV below the Fermi level. The valence band of MnO shows states between 1 and 9 eV below the Fermi level; the maximum is found at 3.7 eV binding energy in the case of He I excitation and at 4.4 eV for He II excitation. This shift suggests that the Mn 3d states become dominant at 40.8 eV (He II) whereas the O 2p states dominate at 21.2 eV (He I) excitation energy. This can be explained by changes in photo-ionization cross-section and surface sensitivity and by band structure effects. The biggest influence is probably the change in the photoemission cross section. Table 4.4 gives the values reported for O2p and Mn 3d in the standard nuclear data tables [28]. For the O 2p states the cross section decreases when going from He I to He II, whereas for the Mn 3d states it rises.

Atomic photo-ionization cross sections		
$\Gamma$	He I (21.2 eV)	He II (40.8eV)
O 2p	10.6	6.8
Mn 3d	5.3	8.4

**Table 4.4:** Atomic photo-ionization cross sections for O2p and Mn 3d states at He I and He II excitation.

The changes in the surface sensitivity could change the valence band features in a similar way, provided that the MnO film is not purely oxygen terminated - as suggested by XPS measurements (see section 4.3.2). For He I the O 2p states have a kinetic energy of 15 eV and are therefore less surface sensitive by a factor of 2 than the He II excited states at KE 34 eV (see [72, page100]). Although a resonance behaviour of the Mn3d states is reported by Heinrich et al. (see [73]), it is not considered strong enough to generate the observed change in the valence band maximum.

The satellite observed in the He II spectrum at 10.5 eV binding energy, i.e. 6 eV below the valence band maximum, is another subject of a publication by Heinrich et al. [73]. The evolution of this satellite has been studied on cleaved MnO crystals with

synchrotron-, He II- and  $AlK\alpha$ -excited photoemission. The intensity of the satellite was found to depend strongly on the way in which the MnO crystal surfaces were treated. The intensity of the satellite decreased upon argon bombardment, compared to the cleaved surface, while it regained intensity upon annealing in UHV. The satellite disappeared after exposure to 1 L oxygen at 340°C (see [73, fig. 4]). In contrast to the high surface sensitivity of the satellite in the valence band spectrum, the 2p core level spectra for bulk MnO remained unchanged even after the surface was bombarded with argon ions. Heinrich therefore concluded that the satellite is a surface-related feature that does not originate from the electronic bulk structure of MnO but is associated with point defects on the surface. Interestingly, theoretical work on models of several transition metal oxides has suggested that these defects in MnO tend to be localised on the metal sites [73, and references therein], in contrast to the cerium oxides whose defects are mainly associated with oxygen vacancies [21].

### 4.2.6 MnO uptake - XPS

As for the bimetallic Mn-Pd surfaces, the development of the Mn 2p, O1s and Pd 3d spectra has been investigated also for the post-oxidised and reactively oxidised MnO/Pd(111) surfaces with increasing coverage. The uptake of the total Mn2p and the decrease of the Pd3d signals is plotted versus the amount of MnO deposited (figure 4.19). The uptake of the Mn signal does not show any significant kinks. Indeed, both Mn 2p increase and Pd 3d decrease can be fit by exponential curves, as expected for island growth [74, page 115]. However, the low surface sensitivity of XPS and the difficulties in obtaining stable evaporation rates made it difficult to determine the growth mode for the first 2 layers.

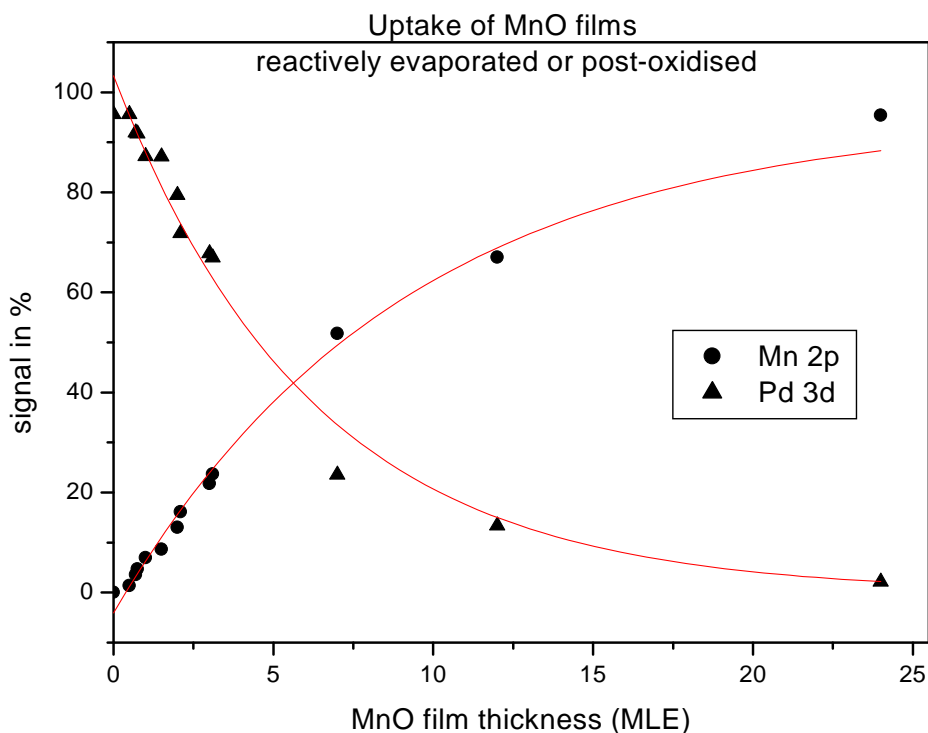


**Figure 4.19:** Mn 2p and Pd 3d peak area (normalised to signal saturation) vs. MnO film thickness in MLE;; points show measured data, lines represent fits with exponential decay

The Mn2p spectra as a function of coverage are shown in figure 4.20. All post-oxidised and reactively evaporated manganese oxide surfaces show Mn 2p spectra with the characteristics of MnO, as described in section 4.2.1. The binding energies of the Mn  $2p_{3/2}$

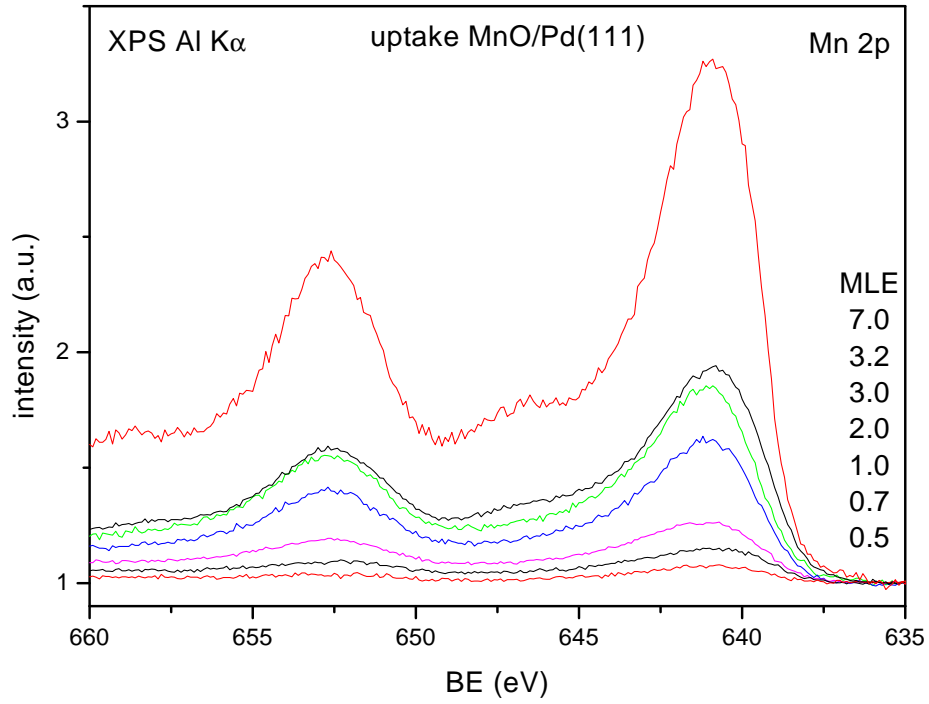


**Figure 4.20:** Mn 2p spectra of post-oxidised manganese thin films, thicknesses 0.5 to 7 MLE

components were consistently measured at 640.70 eV within an experimental error of  $\pm 0.05$  eV. The only significant change in the Mn2p spectra with coverage is the onset of the 6 eV satellites on the high binding energy side of the main Mn 2p components. The satellite can not be distinguished for coverages below 2 MLE MnO. This satellite is explained by Coulomb and exchange interactions between the 2p core hole and the five 3d electrons in the outer shell. A correlation between that satellite and the crystal structure and/or growth mode is however not trivial [67, 66].

The Pd spectra for the different MnO coverages are shown in figure 4.21. The Pd  $3d_{5/2}$  binding energy remained unchanged at  $334.85 \text{ eV} \pm 0.5 \text{ eV}$ .

As for the Pd 3d and Mn 2p regions, the development of the O1s signal was monitored with increasing MnO coverage. The corresponding spectra are displayed in figure 4.22. The O1s spectra of the low coverages overlap with the Pd  $3p_{3/2}$  photo emission of the substrate. For the investigation of the O1s signal development with increasing coverage both Pd  $3p_{3/2}$  and O1s signals had to be fit. The fit parameters for the clean Pd  $3p_{3/2}$  and

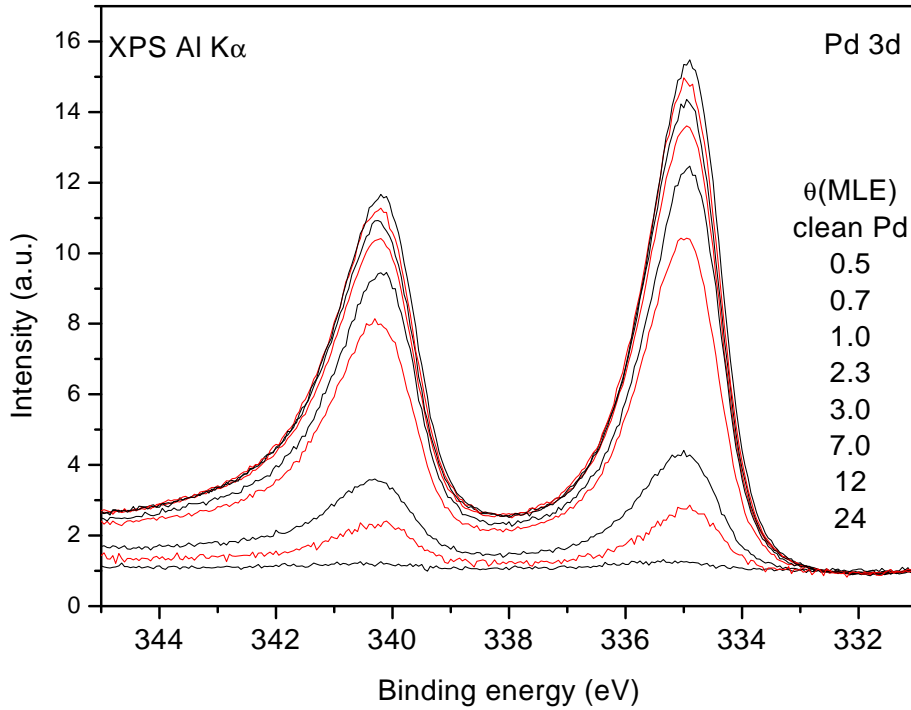


**Figure 4.21:** *Pd 3d spectra vs. MnO coverage*

the 24 ML MnO - O 1s signals have been used to fit the intermediate coverages, leaving only intensities and binding energies variable. The O1s binding energies that have been obtained by these fits are plotted against the MnO coverage in the insert to figure 4.22.

Interestingly, the O1s binding energies determined by the fits undergo a shift from 529.5 eV for layers thicker than 7 MLE to 529.2 eV for layers around 2-3 MLE and further down to 529.0 eV for the coverages below 2 MLE. In a recent publication of Audi et al. [54] a compilation of photoemission data on manganese and its oxides is given. This compilation includes O 1s binding energies of bulk manganese oxides. For the bulk oxides the O1s binding energy shifted to lower binding energies with increased oxidation state. The O 1s binding energy between bulk MnO ( $Mn^{2+}$ ) and  $Mn_2O_3$  ( $Mn^{3+}$ ) changed from 530.0 to 529.55 eV, for bulk  $MnO_2$  ( $Mn^{4+}$ ) the reported O 1s binding energy was 529.14 eV. A shift of the O 1s to lower binding energies with increasing oxidation state has also been reported for the vanadium oxides [75]. The observed O 1s shift to higher binding energies for lower coverages can therefore be interpreted as a interfacial oxide with

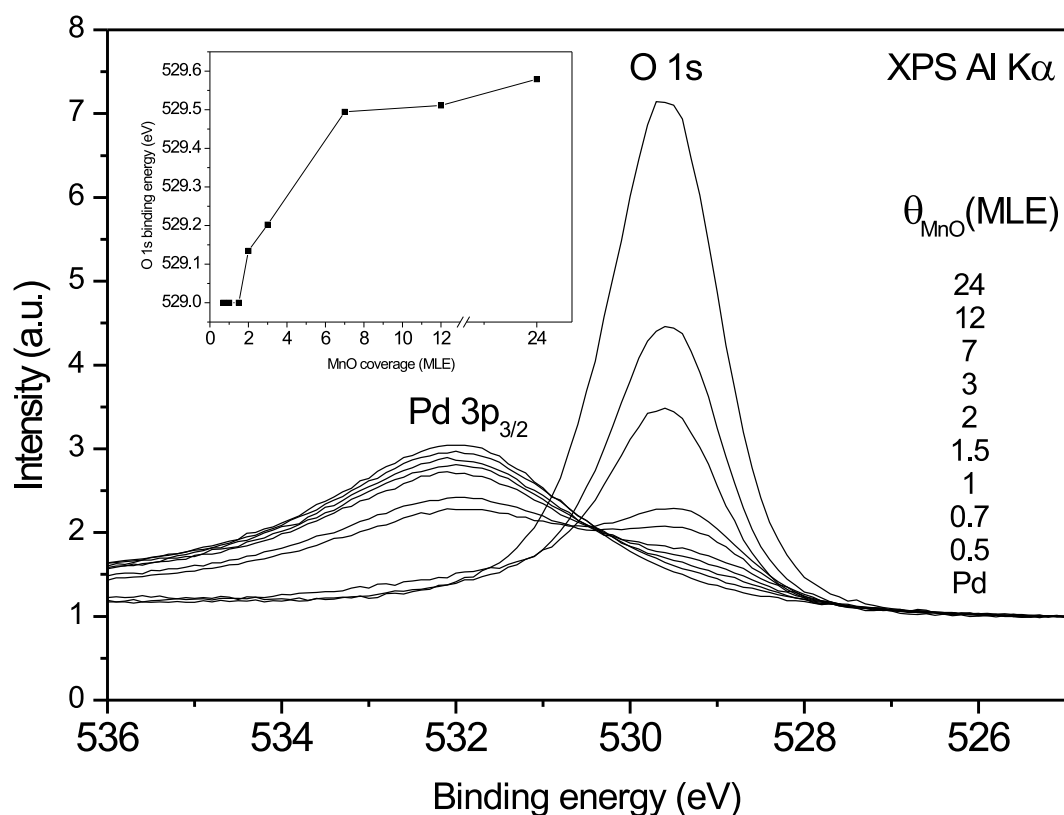


**Figure 4.22:** Pd 3p<sub>3/2</sub> and O1s spectra for various MnO coverages; insert: O1s binding energy vs. MnO coverage

a higher oxidation state as compared to the thicker oxide layers. However the overlap of the O 1s with the Pd3p<sub>3/2</sub>) signal renders the O1s curve fits inaccurate for low manganese oxide coverages. Since the Mn 2p and Pd 3d spectra showed no significant changes and because interfacial oxides generally tend to show lower rather than higher oxidation states [8] due to the metal-metal bonding, the observed shift in the O 1s binding energy is judged as an artifact of the fitting procedure.

For 0.5 MLE no reasonably high O1s signal could be detected. Although the thin layers of metallic Mn show a higher binding energy than the thick ones, one can still clearly distinguish them from the thin post-oxidised manganese films, because these show almost the same Mn 2p binding energy as the thick MnO films. This is illustrated by

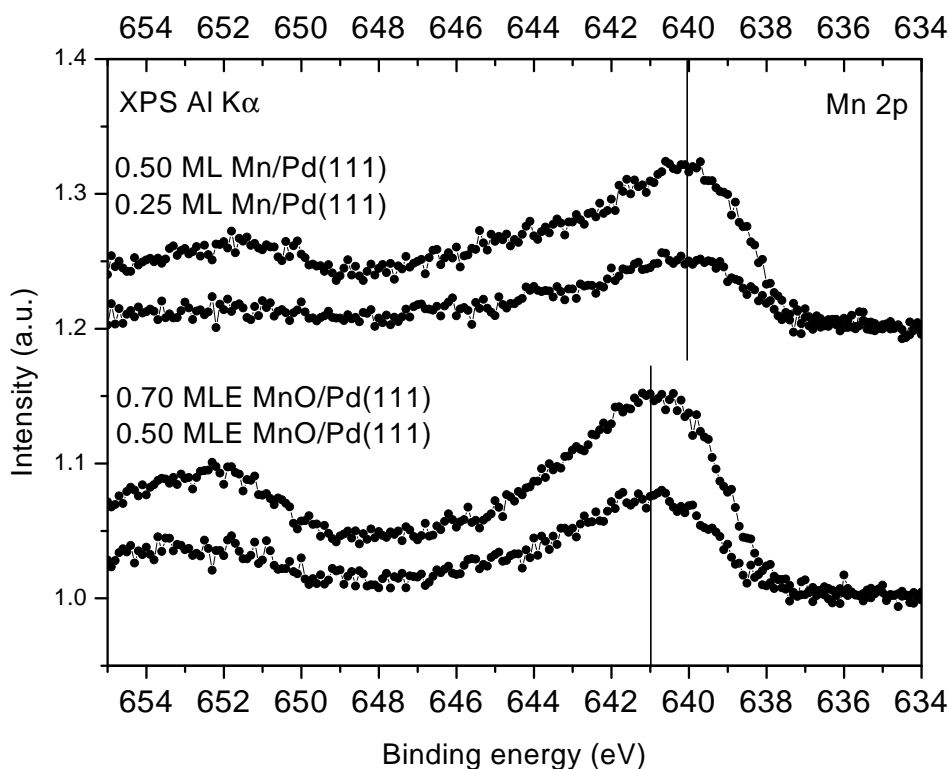


**Figure 4.23:** Comparison of the Mn2p spectra of sub-monolayer Mn and MnO

figure 4.23, where the Mn2p spectra of 4 sub-monolayer coverages were put together in one graph. In that way two coverages of metallic Mn deposition can be compared with two similar coverages of post-oxidised Mn. At the top of the figure the Mn2p spectra of 0.25 and 0.5 ML Mn show the maximum of the Mn2p<sub>3/2</sub> emission at  $\sim 640$  eV. At the bottom, the Mn 2p spectra of 0.5 and 0.7 MLE post-oxidised Mn show the maximum of the Mn2p<sub>3/2</sub> emission at  $\sim 641$  eV. Thick Mn layers on Pd(111) showed their Mn 2p<sub>3/2</sub> maximum at 638.6 eV, thick MnO layers on Pd(111) showed the maximum at 640.7 eV (see sections 4.2.3 and 4.2.1).



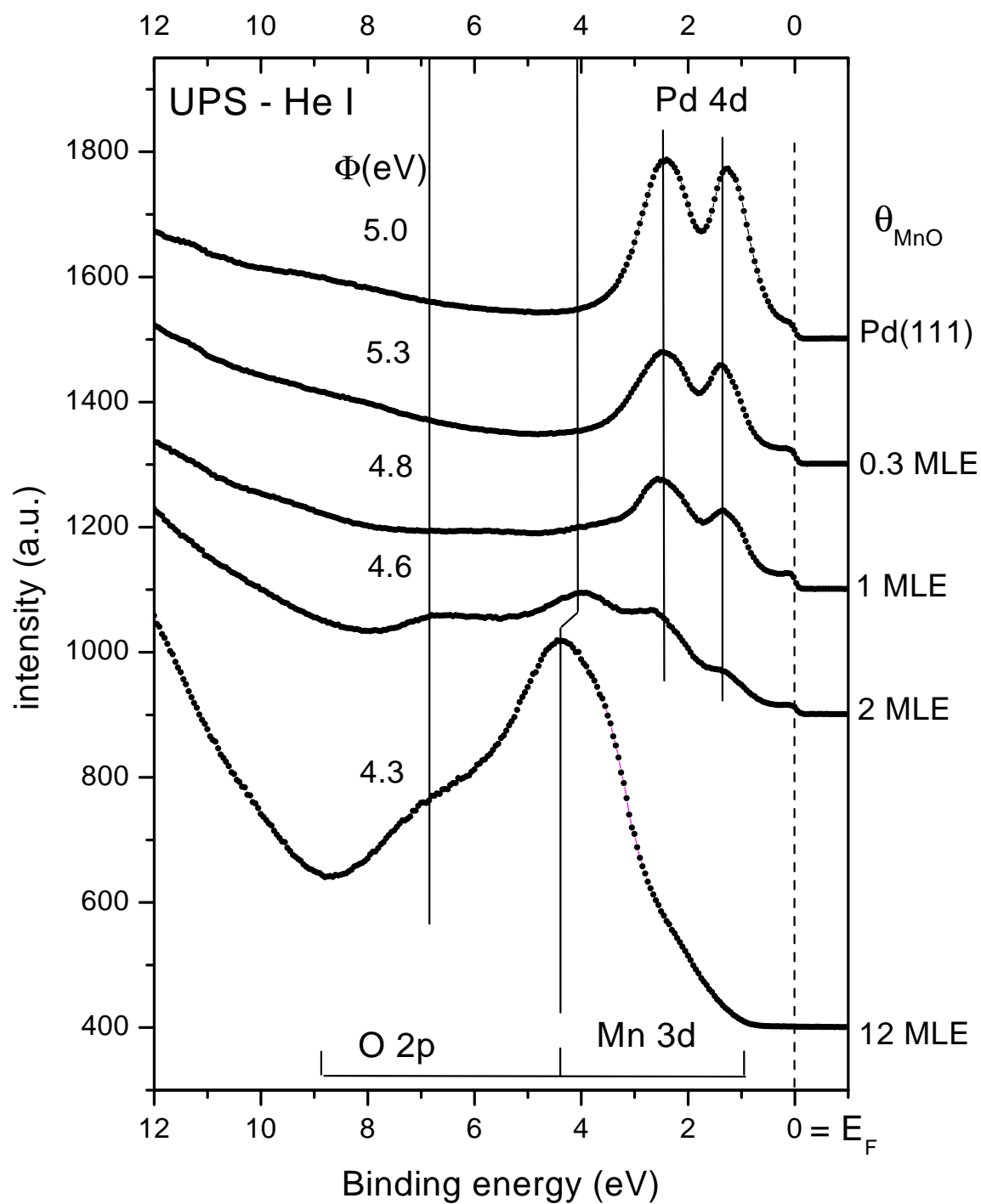
### 4.2.7 MnO uptake - UPS

Figure 4.24 shows the He I spectra of Pd(111) covered with different MnO films. The top most spectrum is from the Pd(111) substrate, the lowest spectrum shows the 12 MLE MnO/Pd(111) discussed before. The surfaces for 0.3, 1, 2 and 3 MLE all refer to MnO coverages prepared by post-oxidation at 250°C; the corresponding LEED patterns and XPS spectra are described in sections 4.2.6 and 4.2.9. Together with the He I experiments the work-function has been measured using the Fermi edge and the secondary electron cut-off, as described in the author's diploma thesis [20, section 2.4]. The resulting work-functions ( $\Phi$ ) are given above the corresponding valence band spectra in figure 4.24.

Increasing the MnO coverage from 0 to 2 MLE, the Pd 4d substrate features become gradually suppressed while the Mn 3d-O2p features of MnO increase. The 2 MLE spectrum is a clear superposition of the Pd valence band and the MnO valence band.

The He II - excited UP-spectra show the same tendency between 0.3 and 2 MLE MnO coverage: the Pd d-band between Fermi edge and 4 eV binding energy decreases and the O2p/Mn3d photo emission between 1 and 9 eV binding energy increases. Apart from the Pd and MnO features the 0.3 MLE valence band spectrum shows two maxima at 10.9 and 8.1 eV. These maxima can be attributed to CO  $4\sigma$  and  $5\sigma/1\pi$  orbitals, due to CO which adventitiously adsorbed from the background gas. He II spectra of CO adsorbed on clean Pd(111) at room temperature showed maxima at the same binding energies (see figure 4.27 D) and ref. [16]). In the case of He I excitation the CO orbitals are hardly distinguishable, they tend to disappear in the secondary electron tail (see [20, 16]).

The results of the work-function measurements on clean Pd, Pd after CO-saturation at room temperature and the results for the MnO films are all included in figure 4.26. On the clean Pd single crystal a work function of 5.0 eV was measured. Adsorption of CO on the Pd(111) surface gradually increases the work-function until a saturation value of 5.9 eV is reached. The resulting He II and He I spectra were identical to the ones published by Leisenberger [16] and the increase in the work-function is comparable to the one measured on Rh(111) [20]. Deposition of manganese oxide onto the Pd(111) substrate gradually decreased the work-function down to a saturation value of 4.3 eV. The work-function of the 0.3 MLE MnO/Pd(111) surface is 0.3 eV higher than the one of the clean substrate. This increase of the work-function for the sub-monolayer MnO deposition can be attributed to the adsorption of CO from the residual gas, as indicated



**Figure 4.24:** He I excited UPS spectra of different MnO/Pd(111) coverages; all surfaces are prepared by post-oxidation at 250° C; the corresponding work-functions are given on top of each spectrum ( $\Phi$  in eV).

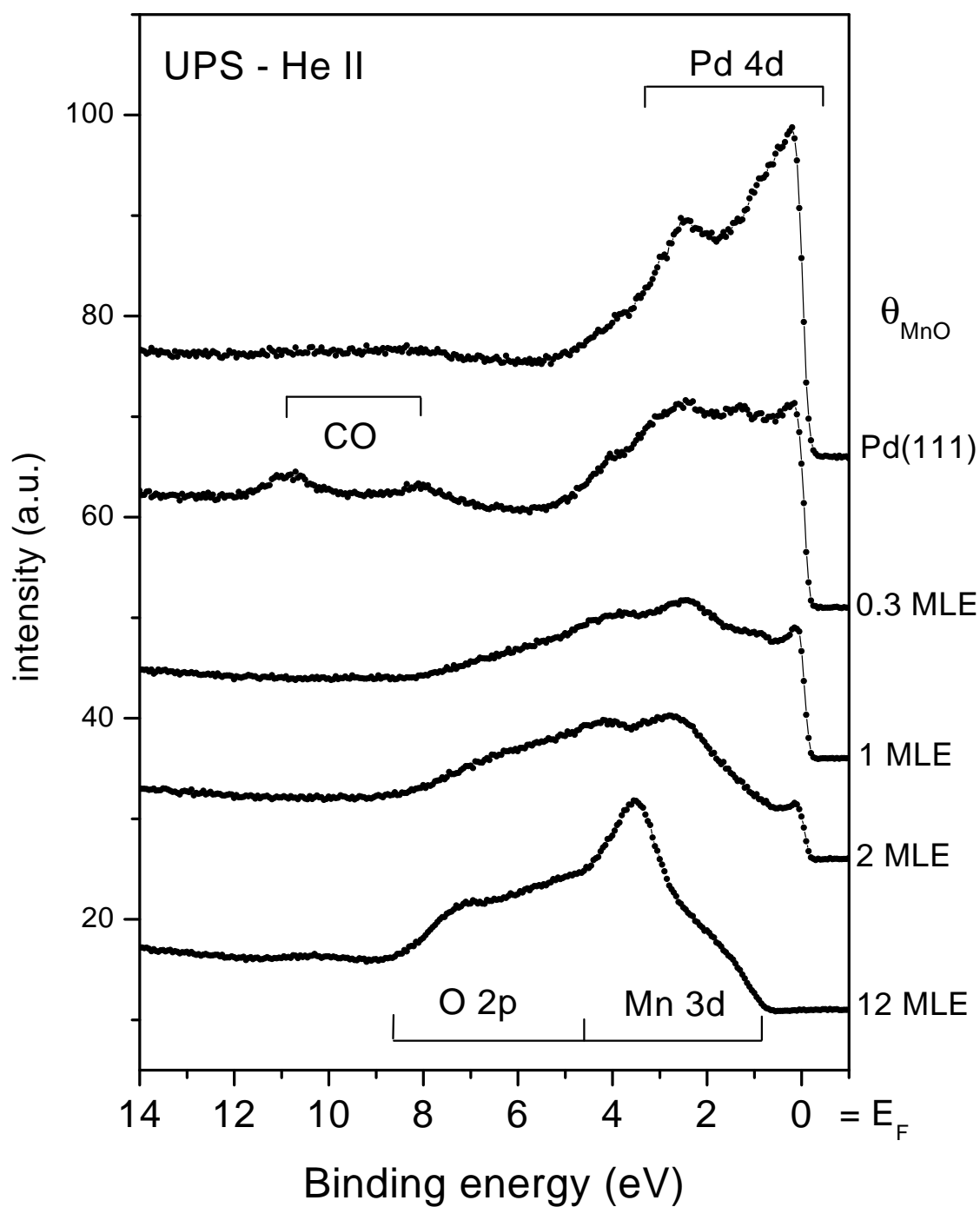


**Figure 4.25:** He II excited UPS spectra of different MnO/Pd(111) coverages; all surfaces are prepared by post-oxidation at 250° C

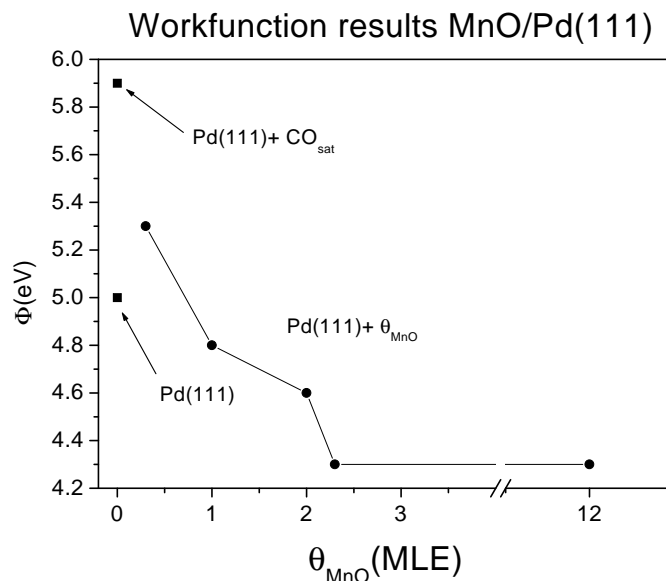


**Figure 4.26:** Results of work-function measurements on different MnO/Pd(111) surfaces and on clean and CO-saturated Pd(111)

by the characteristic CO orbitals in the He II spectrum.

#### 4.2.8 CO adsorption experiments with UPS

The UPS uptake in section 4.2.7, the 0.3 MLE surface showed some CO adsorbed from the residual gas, but for coverages higher than 1 MLE no CO molecular orbitals were detected. For the cerium oxides on Rh(111) it has been proved that CO adsorbs exclusively on the free Rh sites for sub-monolayer  $\text{CeO}_{2-x}$  coverages. Therefore, CO titration experiments were a useful means to determine the amount of free metal sites.

For an unambiguous interpretation of CO titration results, Co adsorption had to be investigated on the pure metal and oxide surfaces. The results of room temperature CO adsorption on clean Pd(111), Mn metal and Mn-oxide surfaces are presented in figure 4.27.

UPS of CO saturation on Pd(111) at room temperature (fig. 4.27-C) shows two molecular orbitals at 8.1 and 10.9 eV in addition to the known Pd-derived d-band structure that is found 0-5 eV below the Fermi edge. In agreement with previous investigations the 8.1 eV peak can be assigned as the unresolved CO  $5\sigma/1\pi$  orbitals and the 10.9 eV peak as the CO  $4\sigma$  orbital of on-top-bonded CO on Pd(111) ([16], [58]).

Lad et al. published He II spectra of cleaved MnO(100) single crystals that have been exposed to high doses ( $10^6$  Langmuir) of  $O_2$ , CO and  $H_2O$  at room temperature. Although the presented He II spectra show no evidence of CO orbitals, Lad et al. claim that difference spectra reveal the growth of two peaks in the valence band which may correspond to the  $4\sigma$  and the unresolved  $5\sigma, 1\pi$  [53]. However, the high CO doses and the undetectability of distinct molecular CO orbitals in the valence band suggest that CO adsorption on MnO can be neglected in CO - titration experiments. This is in agreement with the CO titration on thick MnO films on Pd(111) where no changes in the valence band and no changes in the work function of the surfaces can be detected after a dose of 50 L CO at RT (spectra E and F in figure 4.27).

UPS measurements of the CO orbitals are not as sensitive as HR-XPS measurements of C 1s with synchrotron radiation. Therefore a determination, to which extent the metal surface is covered by the oxide, is not as accurate with UPS as with HR-XPS; for comparison see references [20] and [76]. Despite that fact, the absence of detectable CO orbitals in the UPS curve of 1 MLE MnO after exposure to CO (Fig. 4.27E) indicates that the metallic substrate is covered by at least one complete oxide layer.

An analysis of the CO photo-emission peak areas for CO saturation on Pd(111) and on 0.3 MLE MnO/Pd(111) results in 55% free Pd sites for the 0.3 MLE surface; i.e. the CO peak area for the 0.3 MLE is 55% of the saturation area on bare Pd(111). A linear extrapolation of this value - assuming a layer growth mode in this coverage regime - results in a complete manganese oxide layer at  $\theta_{MnO} = 0.66$  MLE. The spectrum 4.27E proves that no CO adsorbs on 1 MLE MnO, i.e. the surface is fully covered with oxide.

The spectrum in figure 4.27A indicates that carbon monoxide adsorbs on metallic Mn at room temperature. The peak at 11 eV binding energy can be assigned to the CO  $4\sigma$  orbital, but the CO  $5\sigma, 1\pi$  orbitals overlap with a valence band emission at 6.5 eV that could be O2p-derived emissions from chemisorbed oxygen. In section 4.2.3 it has already been mentioned that there was always some small oxygen XPS signal detectable after the deposition of thick manganese layers in UHV. The small amount of oxygen derives either from reaction of the deposited metal with the background pressure (CO,  $O_2$ ) or - more likely - from oxidation of the Mn material inside the evaporator due to previous oxygen treatments in the preparation chamber.

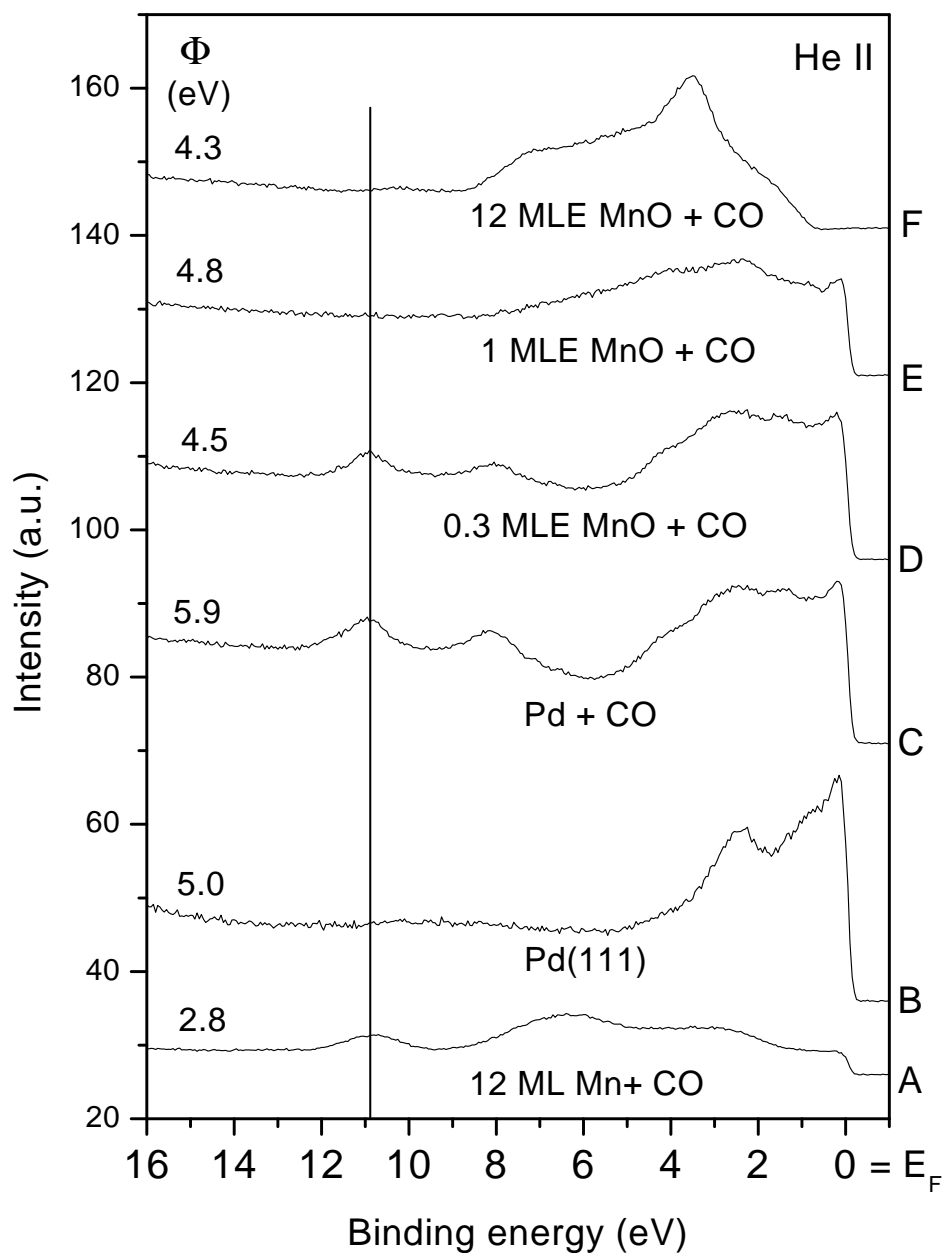


**Figure 4.27:** Work function results ( $\Phi$ ) and He II UPS spectra: A) 12 ML Mn deposited on Pd(111) at RT + 50L CO; B) clean Pd(111); C) Pd(111) + saturation dose of CO at RT; D) 0.3 MLE + saturation dose of CO at RT; E) 1 MLE post-oxidised MnO/Pd(111)+ 50 L CO at RT; F) 12 MLE post-oxidised MnO/Pd(111)+ 50 L CO at RT

### 4.2.9 MnO/Pd(111) LEED phase diagram

One of the aims of the investigation of manganese films on Pd(111) was to create well defined, i.e. well ordered oxide structures on a known substrate. The appearance of diffraction spots in LEED indicates long range ordering of the surface. Therefore, the preparation conditions have been varied in order to find LEED spots on the oxide covered Pd(111) surfaces, i.e. ordered oxide structures. A "LEED phase diagram" is given in figure 4.28, i.e. the observed LEED patterns are presented in a diagram with the MnO coverage on the abscissa and the annealing temperature on the ordinate.

The surfaces have been prepared by post-oxidation at 250-300°C and subsequently heated ( $\sim 10$  min) to the displayed temperature in UHV. The LEED pattern has been observed after cooling the single crystal below 100°C. For the ordered structures the resulting LEED images are shown in figure 4.29; the different patterns will be described along with the corresponding phase in the following section. For the LEED images presented in figure 4.29 the azimuthal orientation of the Pd(111) crystal is always the same. The energies, at which the presented LEED images were taken, vary between 100 and 12 eV which was necessary to obtain a good contrast. Therefore, the spot distances of two different images in figure 4.29 cannot be used for a direct comparison of the reciprocal unit cell vectors.

The LEED pattern of the clean Pd(111) substrate is shown in figure 4.29A. At room temperature the post-oxidised surfaces show no other LEED spots, that can be assigned to ordered MnO islands (phase I). With increasing MnO coverage the LEED pattern of the substrate loses intensity with respect to the LEED background

For coverages above  $\sim 1.5$  MLE MnO (2 ML Mn in the case of metallic Mn deposition), the Pd(111) diffraction spots vanish completely, showing only a bright LEED screen without diffraction spots (phase II). This indicates that at these coverage the well-ordered Pd(111) substrate is covered by several layers of disordered MnO. The disappearance of the substrate spots is correlated with the thickness of the covering films via the electron effective attenuation length. For MnO stoichiometry and an electron energy of  $\approx 100$  eV (normal emission) the electron attenuation length according to calculations available in the NIST database is  $\approx 6$  Å. This also corresponds to the values given in the "universal curve" of the electron escape length versus electron energy, given in [72, page 100].)

To achieve an ordered LEED pattern from the manganese-oxide covered Pd(111) the

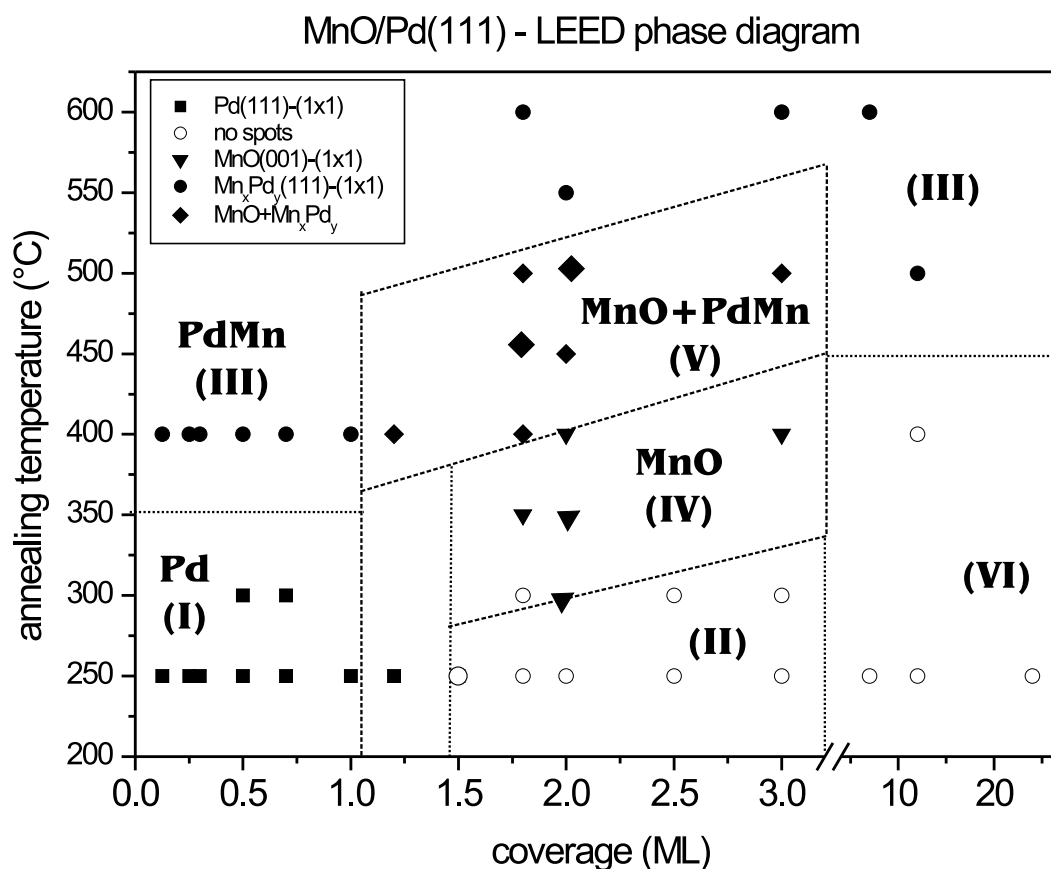


**Figure 4.28:** Phase diagram of LEED structures found for MnO films post-oxidised on Pd(111) as-laid (lowest temperature points) and annealed in UHV

surfaces (which were prepared by post-oxidation) have to be annealed in UHV. For MnO coverages below 1 MLE the annealing results in Pd(111) spots that grow in intensity with respect to the background. At 400°C the LEED spots are as sharp as the ones for the clean Pd(111) substrate, i.e. the diffuse background has disappeared (phase III). XPS on these surfaces shows Mn 2p spectra with metallic characteristics and no detectable O 1s signal. The total Mn signal has decreased with respect to the as-laid MnO film, indicating Mn diffusion into the Pd bulk. Thus, XPS indicates that MnO coverages below 1 MLE turn into a Pd-Mn surface alloy upon annealing to 400°C in UHV. Careful analysis of the LEED patterns of the clean Pd(111) and the well ordered Pd-Mn surface alloy show



the same orientation of the hexagonal unit cells and the same reciprocal lattice vector for both surfaces. The fact that the two unit cells of Pd(111) and the Pd-Mn surface alloy are rotationally aligned can be seen in figures 4.29 A (clean Pd) and 4.29 D (Pd-Mn alloy). Since the stoichiometry of the Pd-Mn surface alloy is not known, it is assigned as  $Pd_xMn_y$  in the figure.

For coverages between 1.5 and 3.5 MLE MnO, there is no ordered LEED pattern after reactive evaporation or post-oxidation at 250-300°C. Annealing these surfaces in UHV to about 300°C still shows no ordering in LEED. Depending on the initial loading, annealing to temperatures slightly above 350°C in UHV results in a new LEED pattern (phase IV) which is presented in figure 4.29 B. Since XPS of these surfaces still shows the characteristics of MnO, these new LEED spots can be attributed to ordered MnO structures on the surface. For low energies LEED shows 12 diffraction spots on a circle around the zero order spot, each rotated by 30 degrees with respect to the next. This LEED pattern is very similar to the one published by Nishimura et al. for MnO on Rh(100) [77]. Nishimura et al. attributed this LEED pattern to hexagonal MnO domains. Measuring the distances between 2 inner opposite spots and comparing them with the diameter of the hexagonal Pd(111) substrate spots leads to an atomic spacing of 3.1 to 3.2 Å for the superstructure, a distance that fits the known  $a_0=3.14\text{Å}$  of MnO(111). However, going to slightly higher energies in LEED shows an outer ring of 12 diffraction spots that is rotated by 30° with respect to the inner ring. These spots can not be simulated by a hexagonal LEED pattern.

Bulk MnO has the NaCl-type crystal structure which is shown in 4.30. This figure illustrates that MnO has a face-centred bulk structure with Mn on the cube corner and O face-centred on the planes or vice versa. In the same figure the (001) plane is shown on the right hand side. Indeed, simulating 3 domains of MnO(001), which has a square unit cell with  $a_0=3.14\text{Å}$ , results in exactly the same LEED pattern as observed in phase IV. The MnO spots of this phase are usually diffuse and show a distortion towards a ring, sometimes the 12 inner and outer spots resemble two concentric rings rather than distinct diffraction spots. This distortion of the LEED pattern indicates some rotational disorder of the domains. The ordering of these surfaces can be improved by longer annealing at the same temperature ( $>10$  min). The best ordered LEED pattern has been observed on a surface that was oxidised step by step, i.e. 3 steps of  $\sim 0.75$  MLE Mn have been

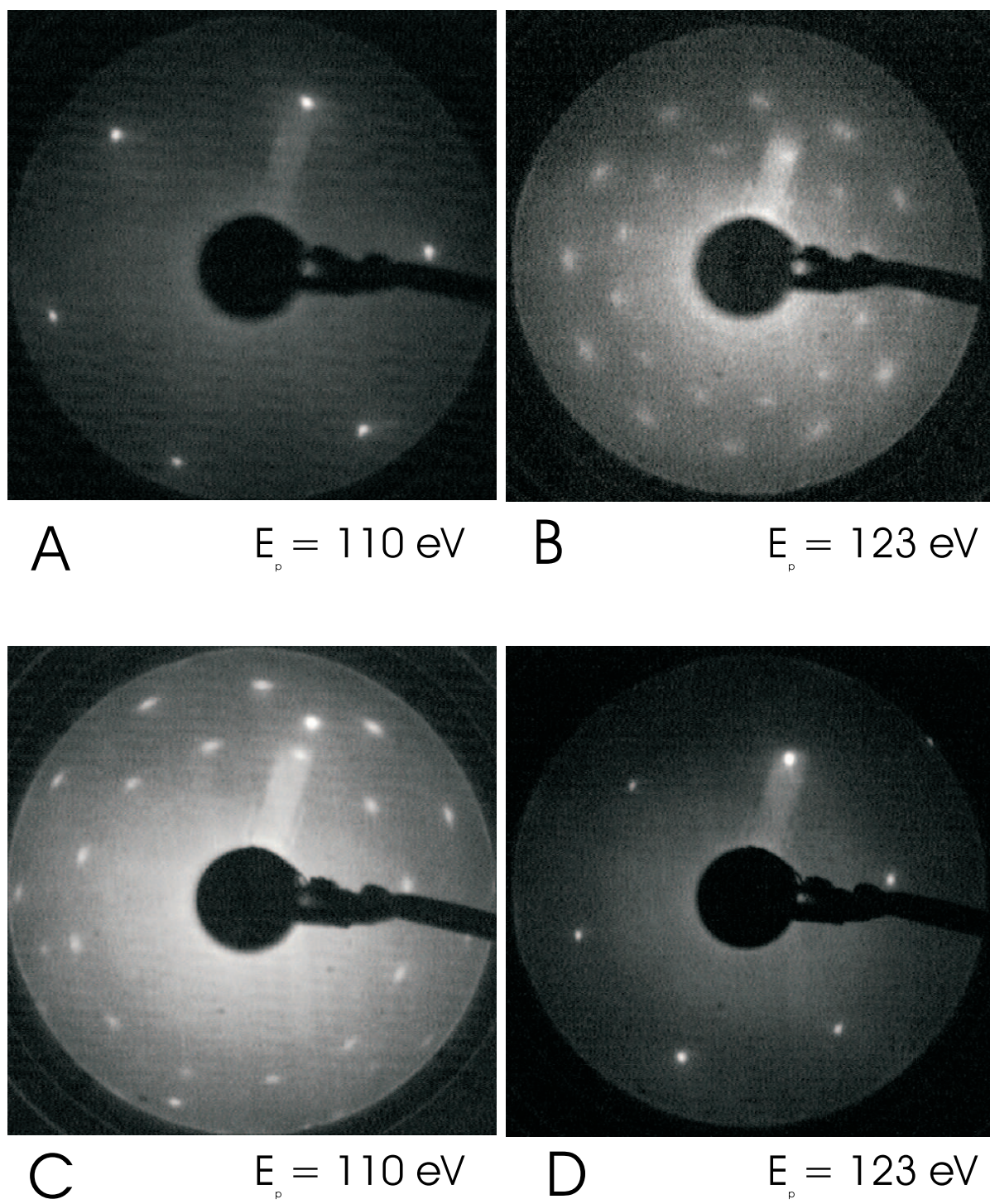


**Figure 4.29:** LEED images of various surfaces A)  $\text{Pd}(111)-(1 \times 1)$ ; B)  $\text{MnO}(001)-(1 \times 1)R120^\circ$ ; C)  $\text{MnO}(001)-(1 \times 1)R120^\circ + \text{Pd}_x\text{Mn}_y(111)-(1 \times 1)$ ; D)  $\text{Pd}_x\text{Mn}_y(111)-(1 \times 1)$

deposited and post-oxidised at 250°C and the final 2.3 MLE MnO film was annealed in UHV to 350°C.

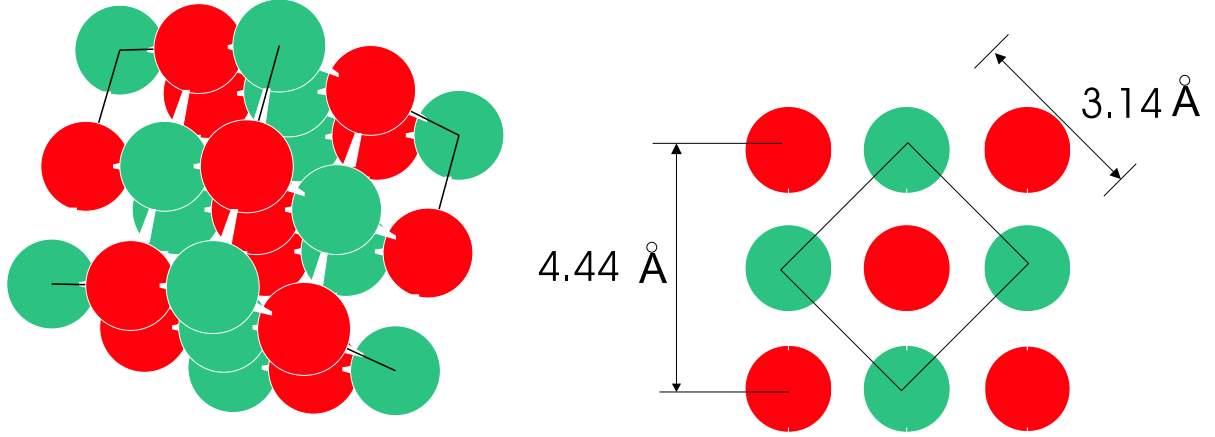


**Figure 4.30:** NaCl-type crystal structure of bulk MnO and the 001-plane

Further annealing of 2-3 MLE MnO/Pd(111) surfaces above 400°C results in a superposition of the phase IV pattern with additional spots that can unambiguously be assigned to the hexagonal (1x1) pattern found for clean Pd(111) and the  $Mn_xPd_y$  surface alloy (phase V). Figure 4.31 presents a comparison of the simulated LEED pattern with the LEED image of the 2.2 MLE step by step evaporated MnO surface after annealing to 500°C. The simulation has been calculated for an incommensurate superposition of the hexagonal Pd(111)-(1x1) pattern with 3 domains of MnO(001)-(1x1) rotated by 120° with respect to each other. Palladium- and MnO derived diffraction spots and unit cells are indicated in figure 4.31.

After annealing MnO surfaces in the 2-3 MLE coverage regime to 600°C the MnO disappears and only the hexagonal  $Mn_xPd_y$  surface alloy pattern remains (phase III). Fig. 4.29D shows the LEED pattern of 3 MLE MnO annealed to 600°C in UHV.

Surprisingly, post-oxidised and reactively evaporated MnO films above 4 MLE do not give rise to the square MnO LEED pattern, but the surfaces remain disordered up to 400°C (phase VI). E.g., 12 MLE MnO post-oxidised at 250°C and subsequently annealed in UHV shows no diffraction spots up to 400°C but directly reveals the  $Mn_xPd_y$ -(111) pattern after annealing to 500°.

In summary, phase IV, where the MnO/Pd(111) surfaces show only reflexes of ordered

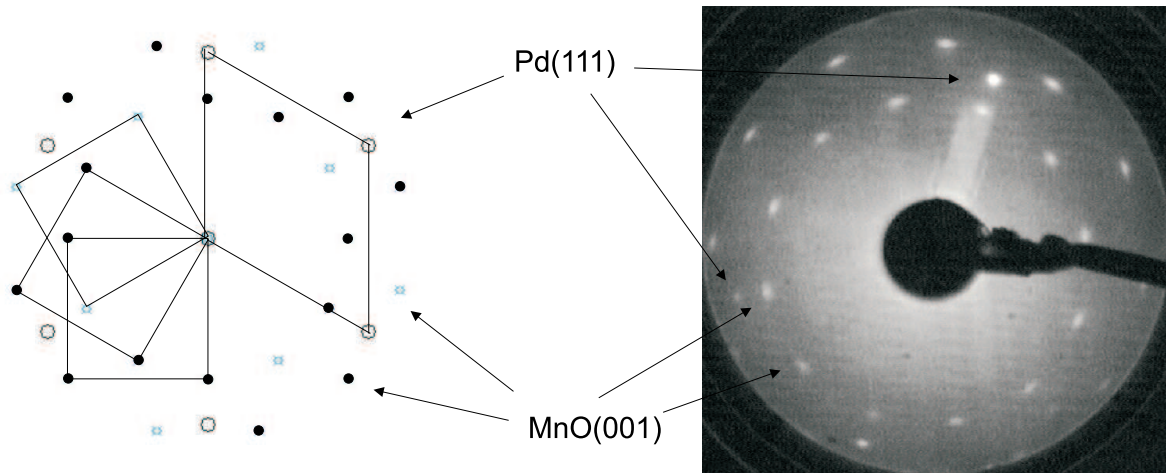


**Figure 4.31:**  $\text{MnO}(001)-(1 \times 1)R120^\circ + \text{Pd}_x\text{Mn}_y(111)-(1 \times 1)$ ; left: simulated LEED pattern of  $\text{Pd}(111) + 3 \text{MnO}(001)$  domains rotated by  $120^\circ$ , showing the unit cells of  $\text{Pd}(111)$  and the three  $\text{MnO}$  domains; right: the observed LEED pattern at 110 eV.

$\text{MnO}$  without an overlap with alloy reflexes is considerably narrow in coverage (2-3 MLE) and temperature (350-400°C). Therefore, a stable evaporation rate of Mn and a good temperature calibration are necessary to reproduce this LEED structure. In the case of the photo-emission experiments a chromel alumel thermocouple was spot welded onto the  $\text{Pd}(111)$  crystal to guarantee exact temperature measurements. In the case of the STM measurements, which will be presented later in this work, the sample had to be transferred by a mechanism that did not allow a fixed thermocouple. Therefore the temperature calibration had to be done carefully to obtain reproducible results.

#### 4.2.10 Annealing thick $\text{MnO}$ layers in UHV

In section 4.2.4 it has been shown that thick Mn films on  $\text{Pd}(111)$  can be fully oxidised to  $\text{MnO}$  by exposure to oxygen at elevated temperatures. In this section the annealing behaviour of a 7 MLE thick  $\text{MnO}$  film on  $\text{Pd}(111)$  will be discussed representatively for the higher coverage regime. The 7 MLE have been post-oxidised at 250°C and subsequently annealed in UHV in steps of 50 and 100 degrees. During the annealing sequences, the  $\text{Pd}(111)$  crystal has been annealed to the indicated temperature and then held at this temperature in UHV for 3 to 5 minutes.  $AlK\alpha$ -excited photo-emission signals have been measured in the  $\text{Mn}2p$ ,  $\text{O}1s$ ,  $\text{Pd}3d$  and  $\text{Pd}3p_{3/2}$  regions and the spectra have been

normalised, a linear background has been subtracted and the peak areas have been evaluated. The resulting Mn 2p and O1s/Pd3p<sub>3/2</sub> spectra are presented in figures 4.32 and 4.33, respectively.

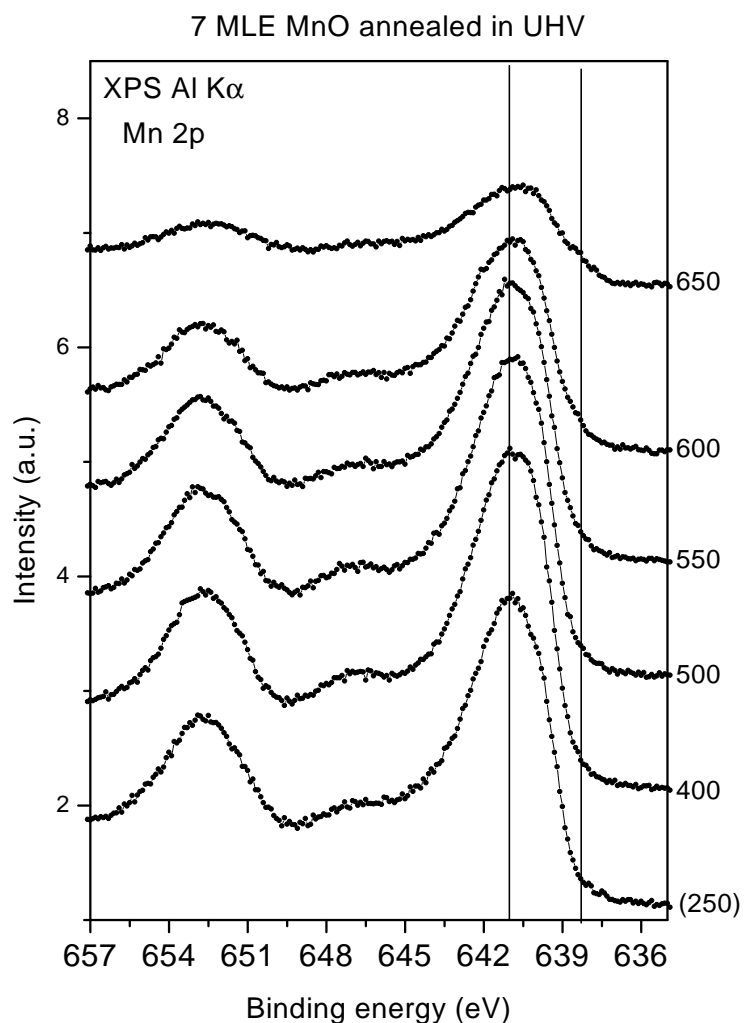


**Figure 4.32:** AlK $\alpha$ -excited Mn 2p spectra of 7 MLE MnO post-oxidised and annealed in UHV

The Pd 3p<sub>3/2</sub> signal overlaps the O 1s signal; the Pd 3p<sub>3/2</sub> and O 1s signal areas can therefore be determined in one spectrum ranging from 526 to 536 eV binding energy. The Pd 3d and Pd 3p represent the substrate equivalently, thus the Pd 3d spectra are not needed to show the development of the XPS substrate features in this section. Figure

4.34 shows the substrate and MnO signal area versus annealing temperature. The Mn 2p and O 1s signal areas were referenced to their initial values after post-oxidation (set to "100%"), the Pd signal is referenced to the value obtained after the final annealing step of 650°C.

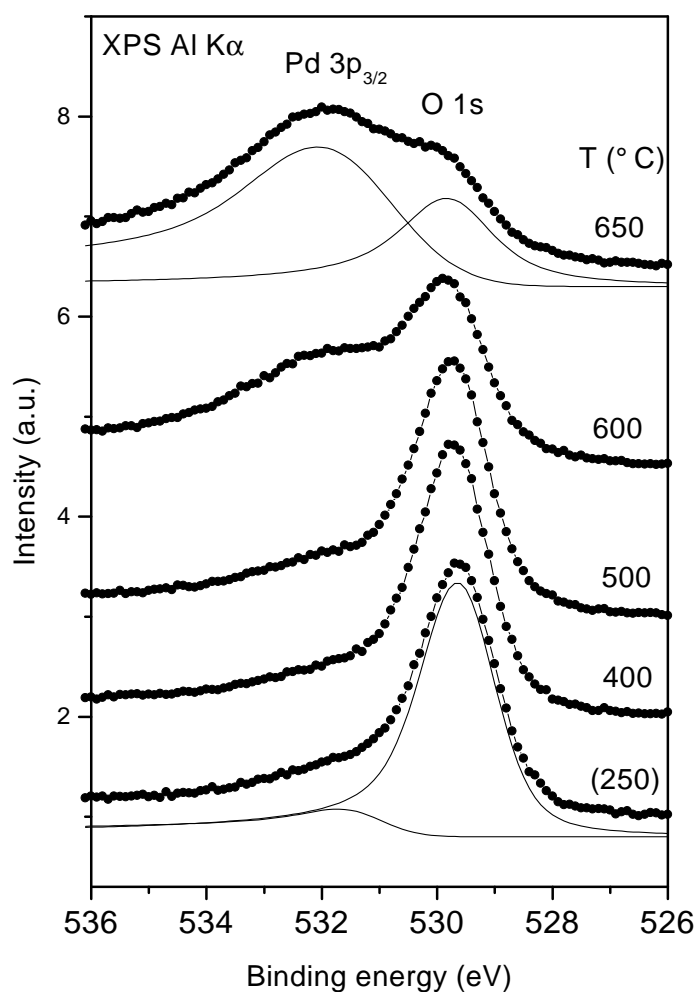


**Figure 4.33:** AlK $\alpha$ - excited O 1s/ and Pd 3p<sub>3/2</sub> spectra of 7 MLE MnO post-oxidised and annealed in UHV. For the first and last annealing step the curve fits are given below the spectra.

Annealing the 7 MLE thick MnO film up to 400°C in UHV has no effect on the manganese, oxygen and palladium signal areas. The Mn 2p spectra of the post-oxidised 7

MLE (at the bottom of fig. 4.32) shows the typical spectral shape which can be attributed to MnO (see section 4.2.1) with the maximum at 641 eV and a characteristic satellite at 6 eV higher binding energy. The Pd  $3p_{3/2}$  signal is almost completely suppressed and can only be distinguished as a shoulder on the high binding energy side of the O 1s signal, which is found at 529.6 eV (figure 4.33, at the bottom).

After annealing to 500°C the Mn 2p total signal has dropped by  $\sim 10\%$ , the O 1s peak area has lost  $\sim 5\%$  and the Pd signal has slightly grown. The Mn 2p spectrum does not show any significant change; the maximum remains at 641 eV and the satellite remains at the same height and position. Annealing to 550°C further decreases the total Mn and oxygen signals and raises the Pd signal. At this annealing temperature the Mn 2p signal shows a shoulder on the lower binding energy side, where the metallic Mn 2p maximum is expected (see section 4.2.1), and the satellite at 647 eV has lost intensity. The trend of losing oxygen and manganese and gaining palladium signal strength continues upon annealing to higher temperatures.

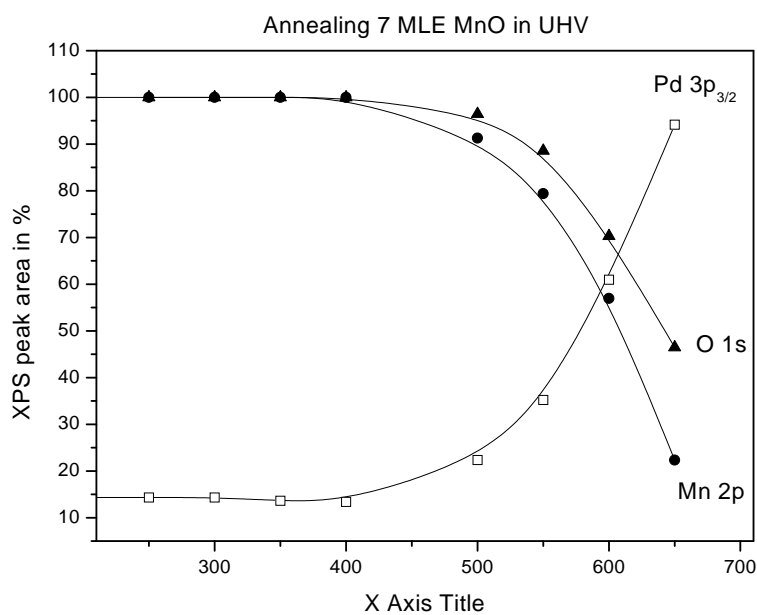


**Figure 4.34:** Pd  $3p_{3/2}$ , O 1s and Mn 2p signal area in % measured on 7 MLE MnO post-oxidised and annealed in UHV

The significant drop of the O1s signal at 600°C together with the loss of manganese signal and the rise of the palladium emissions from the surface indicate the formation of

a Pd-Mn surface alloy. This interpretation is also supported by the metallic component in the Mn 2p spectrum that arises upon annealing. The loss of the manganese and oxygen signals upon annealing in UHV can be explained by a break of the manganese-oxygen bond, desorption of the oxygen and the formation of a metallic Mn-Pd bond, i.e. alloying. The fact that the maximum of the Mn 2p emission remains at 641 eV and the O 1s signal is still visible after an anneal to 650°C suggests MnO and metallic Mn in the alloy coexist in the XPS detection region. This indicates that the Mn-Pd alloying occurs at the MnO-Pd interface whereas the top MnO layers remain in the oxidised state.

Figure 4.35 shows measured curves of the Mn2p total signals versus annealing temperature for several MnO coverages. The development of the total Mn 2p signal is always referenced to the initial signal after evaporation and post-oxidation. To avoid deeper penetration of the manganese into the substrate, some coverages were only annealed up to 500°C.

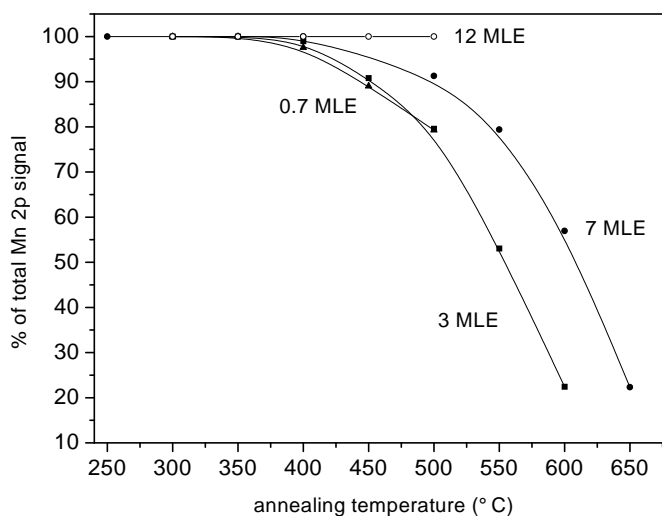


**Figure 4.35:** Mn 2p signal area for different MnO coverages post-oxidised and annealed in UHV

The smallest coverage, 0.7 MLE MnO, shows the same behaviour as the 3 MLE coverage (discussed in detail in section 4.3.2), i.e. upon annealing to 500°C the total signal dropped by 20%. The thickest coverage in this graph, 12 MLE MnO, does not show any drop in the total signal after annealing to 500°C and the intermediate coverage of 7 MLE shows the same drop of 20% after annealing to 550°C. The loss of the manganese signal by



annealing in UHV is therefore strongly dependent on the initial loading of the manganese material. A similar thickness dependent reduction and alloying behaviour has already been observed for cerium oxide films on rhodium [20].

### 4.3 Thin films ( $\leq 3$ MLE) of MnO on Pd(111): XPS, UPS and LEED

#### 4.3.1 1 MLE MnO on Pd(111) - different preparations

Figure 4.36 shows on the left hand side Mn 2p spectra of 1 MLE Mn post-oxidised and reactively evaporated at different temperatures. On the right hand side the O 1s fits of are shown, that have been obtained after deconvoluting the Pd  $3p_{3/2}$ -O 1s photo-emission spectra.

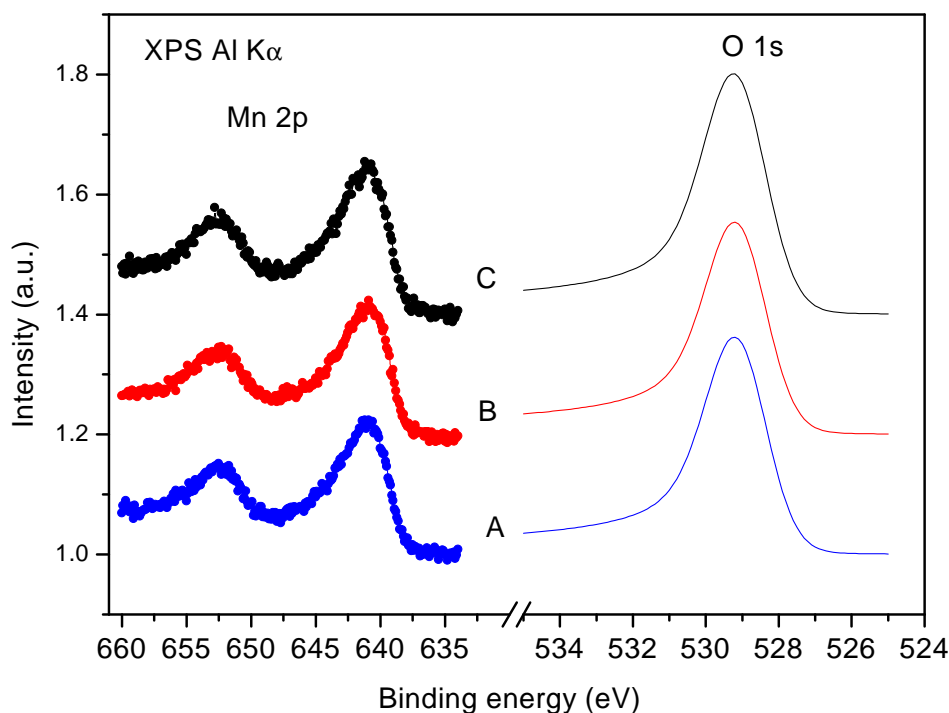


**Figure 4.36:** Mn 2p spectra and O 1s fits of 1 MLE Mn deposited on Pd(111) A)post-ox.  $2 \times 10^{-7}/400^\circ\text{C}$ ; B)post-ox  $2 \times 10^{-7}/250^\circ\text{C}$ ; C)reactively ox.  $/2 \times 10^{-7}/250^\circ\text{C}$

This figure illustrates that there were no obvious differences in the Mn 2p spectra of post-oxidised and reactively evaporated thin layers, in this case 1 MLE of Mn. Post-oxidation and reactive evaporation at oxygen pressures between  $5 \times 10^{-8}$  and  $1 \times 10^{-6}$  mbar and at temperatures between 250 and  $400^\circ\text{C}$  showed the same Mn 2p spectra and LEED

patterns. For both preparations the sample was cooled in the oxygen pressure below  $100^\circ\text{C}$ . Oxygen pressures below  $5 \times 10^{-8}$  mbar  $\text{O}_2$  lead to residual metallic features in Mn2p and lower O 1s signals. Temperatures above  $400^\circ\text{C}$  lead to a total loss of the Mn 2p signal with respect to the same amount of metal deposited at RT. Furthermore, these temperatures led to the development of metallic features in Mn 2p, which can be explained by the manganese alloying with Pd and penetrating into the bulk of the substrate.

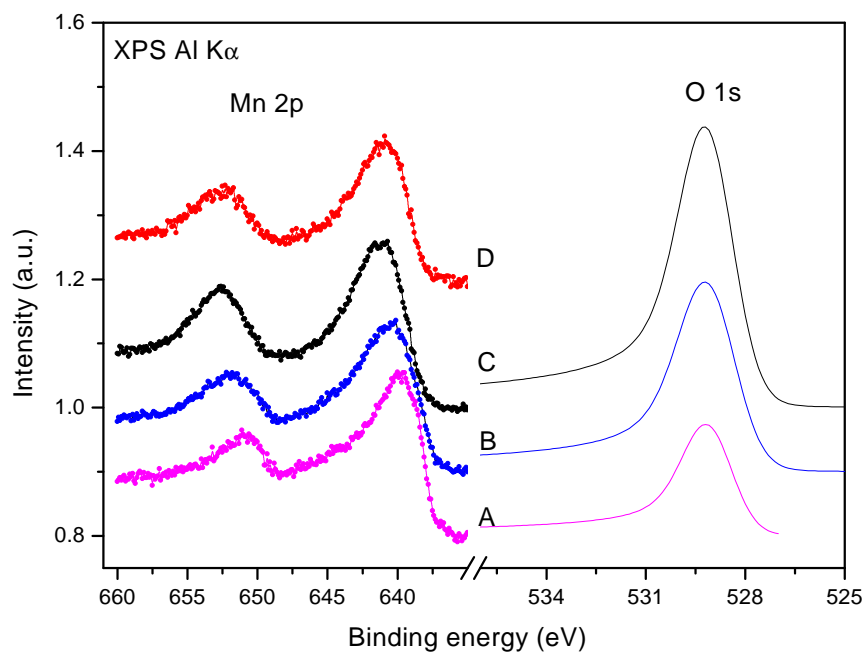


**Figure 4.37:** Mn 2p spectra and O 1s fits of 1 MLE Mn A) deposited on Pd(111) and annealed at  $300^\circ\text{C}$  in UHV; B) after 500L  $\text{O}_2$  dose at RT; C) after oxidation in  $1 \times 10^{-6}$  mbar  $\text{O}_2$  at  $400^\circ\text{C}$ ; D) 1 MLE Mn post-oxidised in  $2 \times 10^{-7}$  mbar  $\text{O}_2$  at  $250^\circ\text{C}$ ;

Figure 4.37 shows Mn 2p spectra and de-convoluted O 1s spectra for a mono-layer equivalent of Mn that has been annealed to  $300^\circ\text{C}$  between room temperature deposition and oxidation. 1 MLE Mn has been deposited at RT (not shown), then annealed to  $300^\circ\text{C}$  (4.37 A), then oxidised at room temperature (4.37 B), and afterwards oxidised at higher oxygen pressure and temperature (4.37 C); The  $\text{Mn}2p_{3/2}$  spectrum in figure 4.37A shows two components; the expected metallic  $\text{Mn}2p_{3/2}$  component at  $\sim 639$  eV BE overlaps with an MnO component, thus during the evaporation and subsequent annealing

to 300°C the Mn film has already reacted with the background gas. If the metallic Mn is deposited or subsequently treated at moderate temperatures ( $\geq 300^\circ\text{C}$ ) it already forms a Pd-Mn surface alloy. Thus, the oxidation at room temperature can not fully oxidise the manganese film any more - there is still a remaining metallic  $Mn2p_{3/2}$  component at 639eV, as seen in spectrum 4.37. To fully oxidise this low temperature Pd-Mn alloy an activation barrier has to be overcome by oxidation at elevated temperature. After oxidation at  $T \geq 250^\circ\text{C}$  (here  $400^\circ\text{C}$  has been used) the Mn 2p spectrum contains no more metallic component, thus the film is fully oxidised and the spectrum is similar to the one obtained on 1 MLE post-oxidised at the "standard conditions", which is shown in figure (4.37 D).

### 4.3.2 Annealing thin MnO films in UHV - XPS and LEED

It has already been mentioned in section 4.2.9 that the post-oxidised and reactively evaporated MnO films above 1.5 MLE coverage only showed a LEED pattern after they had been annealed in UHV. To learn something about the oxidation state of the ordered manganese oxide films, several MnO coverages were annealed in UHV in steps of  $50^\circ$  and  $100^\circ\text{C}$ . The changes in XPS and LEED were recorded simultaneously. To represent the coverage regime where the square LEED pattern of MnO has been observed (phase IV in figure 4.28), the results for 3 MLE of post-oxidised MnO are presented in figure 4.38.

The total Mn 2p, O 1s and Pd 3d signals have been plotted against the applied annealing temperature and the observed LEED patterns have been included in the figure. The total Mn, Pd and O 1s signals do not change significantly when the surface is annealed to  $400^\circ\text{C}$ , where the ordered MnO domains are observed in LEED. Annealing to  $500^\circ\text{C}$  leads to the appearance of the hexagonal  $Mn_xPd_y-(1 \times 1)$  LEED pattern in addition to the MnO domains, this LEED pattern has been described in detail in section 4.2.9. Concomitant with the new LEED pattern, an evident drop of the Mn and O 1s signals and a rise of the Pd signal are observed. The drop is about 20% of the initial value for Mn 2p and O1s; the Pd signal has increased by approximately 15%.

After further annealing to  $600^\circ\text{C}$  the O 1s signal vanishes, the total Mn 2p signal drops further to 25% of the original value and the Pd signal has increased to 140% of the original value. To illustrate the changes in the oxidation state of Mn, the Mn 2p spectra are displayed in figure 4.39. The Mn 2p maximum stays at the same value as obtained for

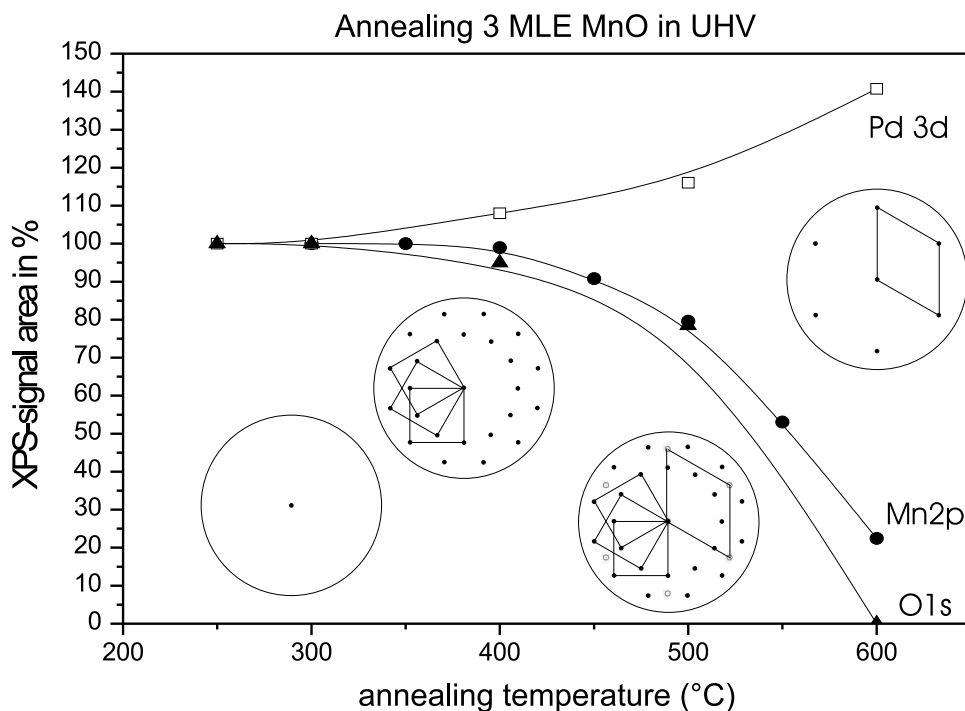


**Figure 4.38:** XPS signals and sketches of the LEED structures that have been observed for 3MLE MnO post-oxidised and annealed in UHV

thicker MnO films ( $\approx 640.7$  eV) when annealed up to  $400^\circ\text{C}$ . Further annealing to  $500^\circ\text{C}$  shifts the maximum by about 0.6 eV to 640.1 eV binding energy. Upon annealing to  $600^\circ\text{C}$  in UHV the Mn 2p spectrum shows a change in shape that can be fit by 2 maxima at 638.7 and 640.1 eV.

The measured binding energies together with the total photoemission signals prove that the deposited manganese oxide remains in the same oxidation state (MnO) upon ordering, i.e. annealing in UHV to  $\sim 400^\circ\text{C}$ . The LEED pattern explained by three domains with square unit cells (see section 4.2.9) can therefore be attributed to ordered domains of MnO on the surface. The disappearance of the O 1s signal at  $600^\circ\text{C}$  together with the loss of manganese signal and the rise of the palladium emissions from the surface indicate the formation of a Pd-Mn surface alloy. The remaining MnO-like Mn 2p feature suggests that there is still some amount of MnO left, but it must be considerably small compared to the initial MnO coverage because the O 1s signal has sunk below the detection

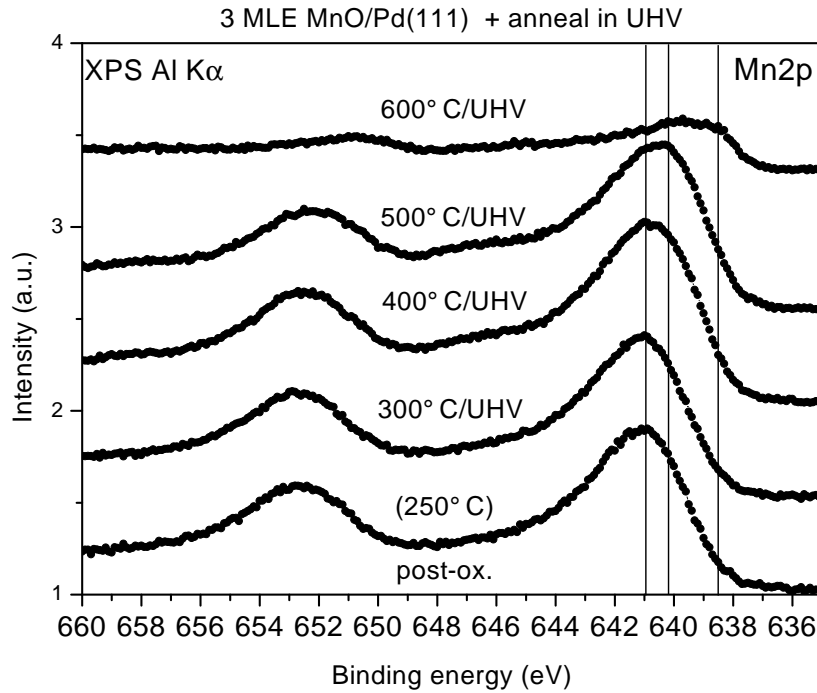


**Figure 4.39:** *Mn 2p spectra of 3MLE Mn post-oxidised and annealed in UHV*

limit. The hexagonal LEED pattern observed at these temperatures thus arises from a  $Pd_xMn_y$  surface alloy with the same periodicity as the clean Pd(111) crystal.

The incommensurate superposition of the hexagonal  $Pd_xMn_y$ -(1x1) LEED pattern with the square MnO pattern at 500°C annealing temperature corresponds to the superposition of  $Pd_xMn_y$  and MnO photoemission features, i.e. at this temperature the thin MnO films start alloying with the substrate.

### Changing the emission angle in XPS

It has already been mentioned that  $AlK\alpha$  excited XPS is intrinsically not very surface sensitive due to the high kinetic energy of the photoelectrons emitted. To gain a bit more surface sensitivity with the same excitation source, a change in geometry can be used. The photon energy of  $Al K\alpha$  x-rays is  $\approx 1480\text{eV}$ , the binding energy of O 1s is  $\sim 530\text{eV}$ , i.e. the kinetic energy of the detected photoelectrons is  $\sim 950\text{eV}$ . According to the universal curve [72, page 100], this kinetic energy corresponds to an electron escape length of more than 15 Å. In normal emission  $AlK\alpha$  excited O 1s photoelectrons that leave the surface

are generated up to a depth of  $\sim 15\text{\AA}$  below the surface.

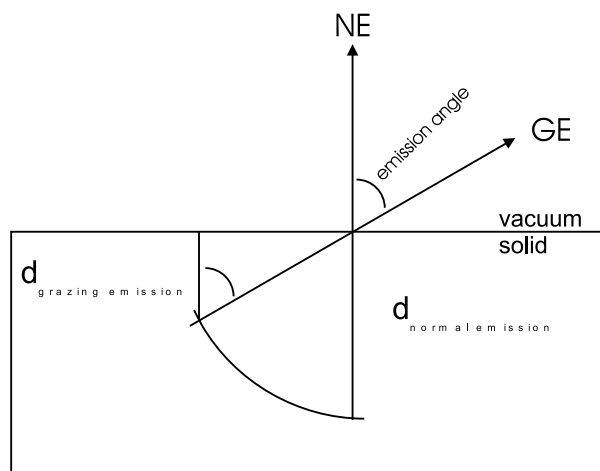


**Figure 4.40:** Sketch to correlate grazing and normal emission spectra via the emission angle

If the emission angle is defined as sketched in figure 4.40, the grazing emission depth  $d_{\text{grazing emission}}$  for the same photoelectrons is related to the emission angle via

$$d_{\text{grazing emission}} = d_{\text{normal emission}} \times \cos(\text{emission angle}) \quad (4.2)$$

e.g. for an emission angle of  $60^\circ$  the detected O 1s photoelectrons originate from half the normal emission depth. The total O 1s and Mn 2p signals measured in an XPS experiment depend on the amount of oxygen and Mn in this detection region, on the photoelectron cross sections for O 1s and Mn 2p at the  $Al - K\alpha$  excitation energy and on the sensitivity factors of the analyser due to the analyser transmission function. Unfortunately, the sensitivity factors are different for each electron analyser and the SCIENZA producers did not give any values for the SES-200 analyser, which was used for the presented experiments. For quantitative analysis of every photoemission peak the sensitivity factors must be measured with known excitation sources, geometry and test samples.

Furthermore, especially in ordered surface structures, photoelectron diffraction effects can complicate the interpretation of XPS data when changes of the emission angle are applied. Since the laboratory x-ray source does not deliver polarised light, the change in the incidence angle upon turning the sample in front of the source can be considered negligible to first approximation. However, qualitative information about the surface stoichiometry can still be gained by comparing the changes in the photoemission peaks when going from normal to grazing emission geometry.

Grazing and normal emission Mn 2p spectra of 2.2 MLE MnO before and after annealing to 500°C are presented in figure 4.41. The LEED pattern of the annealed surface show the typical superposition of the square MnO pattern and the hexagonal  $Pd_xMn_y$  spots (see figure 4.29C) . The next figure (4.42) shows the corresponding O 1s and Pd  $3p_{3/2}$  spectra.

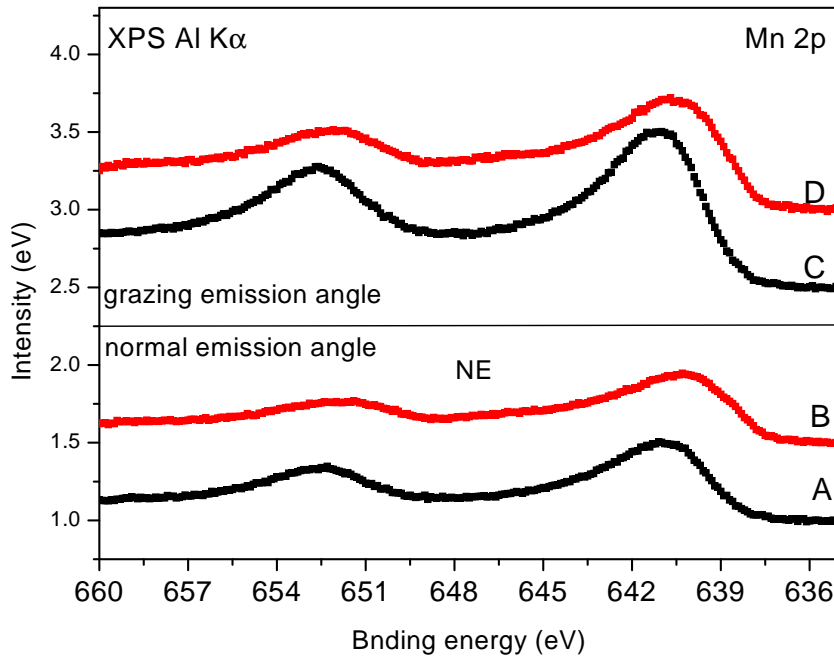


**Figure 4.41:** Grazing (emission angle 70°) and normal emission Mn 2p spectra; A) 2.2 MLE MnO post-oxidised, NE ; B) 2.2 MLE MnO annealed to 500°C, NE; C) 2.2 MLE MnO post-oxidised, GE; D) 2.2 MLE MnO annealed to 500°C, GE

If the oxide surface were oxygen terminated one would expect a higher O 1s to Mn 2p ratio in grazing emission than in normal emission. For comparison of the signals in normal and grazing emission, O1s, Pd  $3p_{2/3}$  and Mn 2p spectra have been normalised to the same number of scans and linear backgrounds have been subtracted. The resulting peak areas for two different MnO surfaces are presented in table 4.5.

For the post oxidised surface the measured signal ratios for normal emission are

$$\frac{O1s}{Mn2p}(post - ox.) = 0.37 \text{ and } \frac{O1s}{Mn2p}(annealed) = 0.23.$$



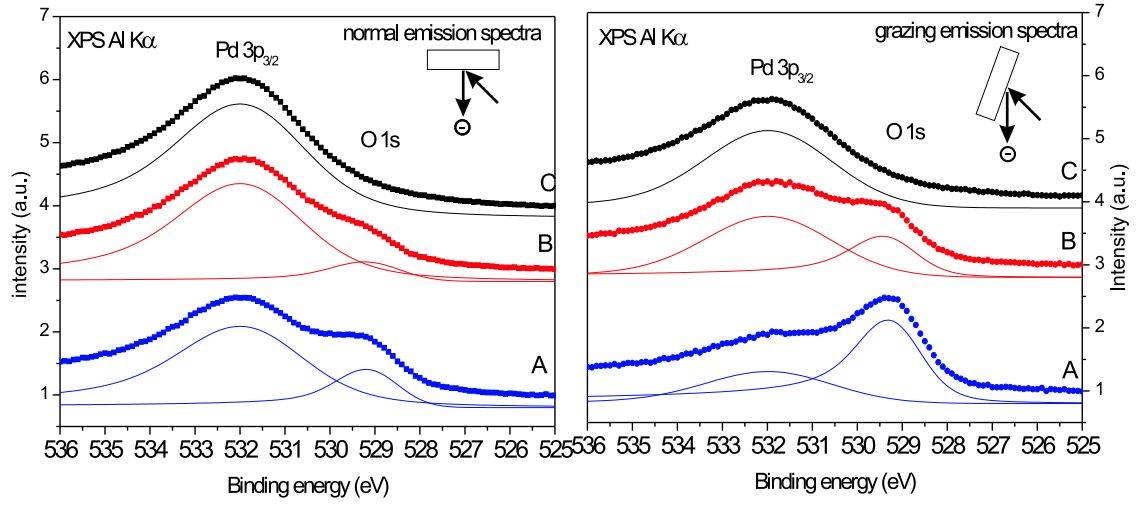


**Figure 4.42:** Al-K $\alpha$  excited Pd3p $_{3/2}$  and O 1s spectra taken at normal and grazing emission geometry (emission angle 70°); A) 2.3 MLE MnO after post-oxidation; B) 2.3 MLE MnO annealed to 500° C in UHV; C) clean Pd(111)

XP-signal areas measured in grazing and normal emission			
surface	O 1s	Pd 3p $_{3/2}$	Mn 2p
2.2 MLE MnO post-oxidised, NE	1.28	3.82	3.41
2.2 MLE MnO post-oxidised, GE	2.92	1.65	9.54
2.2 MLE MnO annealed to 500°C, NE	0.70	4.59	3.00
2.2 MLE MnO annealed to 500°C, NE	1.47	3.18	6.94

**Table 4.5:** XPS signal areas in grazing and normal emission, measured after normalisation and linear background subtraction

$$\frac{Mn2p}{Pd3p}(post - ox.) = 0.98 \text{ and } \frac{Mn2p}{Pd2p}(annealed) = 0.65.$$

For grazing emission the ratios

$$\frac{O1s}{Mn2p}(post - ox.) = 0.31 \text{ and } \frac{O1s}{Mn2p}(annealed) = 0.21$$

$$\frac{Mn2p}{Pd3p}(post - ox.) = 5.78 \text{ and } \frac{Mn2p}{Pd2p}(annealed) = 2.18.$$

were evaluated. For grazing emission the  $\frac{Mn2p}{Pd3p}$  ratios are higher than for normal emission,

i.e. grazing emission is indeed more surface sensitive. For the annealed surface the grazing emission  $\frac{Mn2p}{Pd3p}$  value is more than 2 times lower than for the non-annealed surface, which is another indication for Mn segregation into the Pd bulk at this MnO coverage and annealing temperature. Within the experimental error grazing and normal emission showed the same  $\frac{O1s}{Mn2p}$  ratios for both as-laid and annealed surfaces. This result indicates that both annealed and non-annealed MnO films are not purely oxygen terminated. On the other hand metal terminated interfaces between the oxide and the vacuum generally form polar surfaces, which are energetically less favourable [78]. A possible explanation of this result is a structure where oxygen and metal alternate in the topmost layer. This is the case for the MnO(001) plane sketched in figure 4.30 on page 127 where the oxygen and manganese atoms form a chequerboard structure.

### 4.3.3 Annealing thin MnO films in UHV - UPS and LEED

For comparison of the UPS spectra of disordered and ordered MnO overlayers, 2 monolayers of Mn have been evaporated and post-oxidised under standard conditions. The resulting 2 MLE MnO surface shows no LEED diffraction spots after post-oxidation. The surface has been annealed in UHV in steps of 50°C. UPS spectra and work-function measurements have been recorded with He I and He II excitation and the resulting LEED patterns have been observed after each annealing step. Furthermore, after each annealing step the surface has been cooled to room temperature and exposed to 50 L of CO. The He I and He II excited UPS spectra prior to CO exposure are presented in the figures 4.44 and 4.43, respectively.

Figure 4.43 shows sketches of the LEED patterns recorded after each annealing step together with the corresponding temperature and valence band spectrum excited with He II. Figure 4.44 shows the corresponding He I spectra.

Upon annealing to 300°C the LEED shows a square MnO(001)-R120° pattern that is diffuse and distorted towards a ring, as described in section 4.2.9. The square MnO pattern becomes sharper and loses the distortion after further annealing steps of 350 and 400°C. At 450 °C the hexagonal  $Pd_xMn_y$  LEED pattern arises and is superimposed on the sharp square MnO pattern. The corresponding pattern has been explained in section 4.2.9 (see also figure 4.31). Annealing to 500°C increases the intensity of the hexagonal  $Pd_xMn_y$  LEED spots and decreases the intensity of the square MnO(001)-R120° pattern.

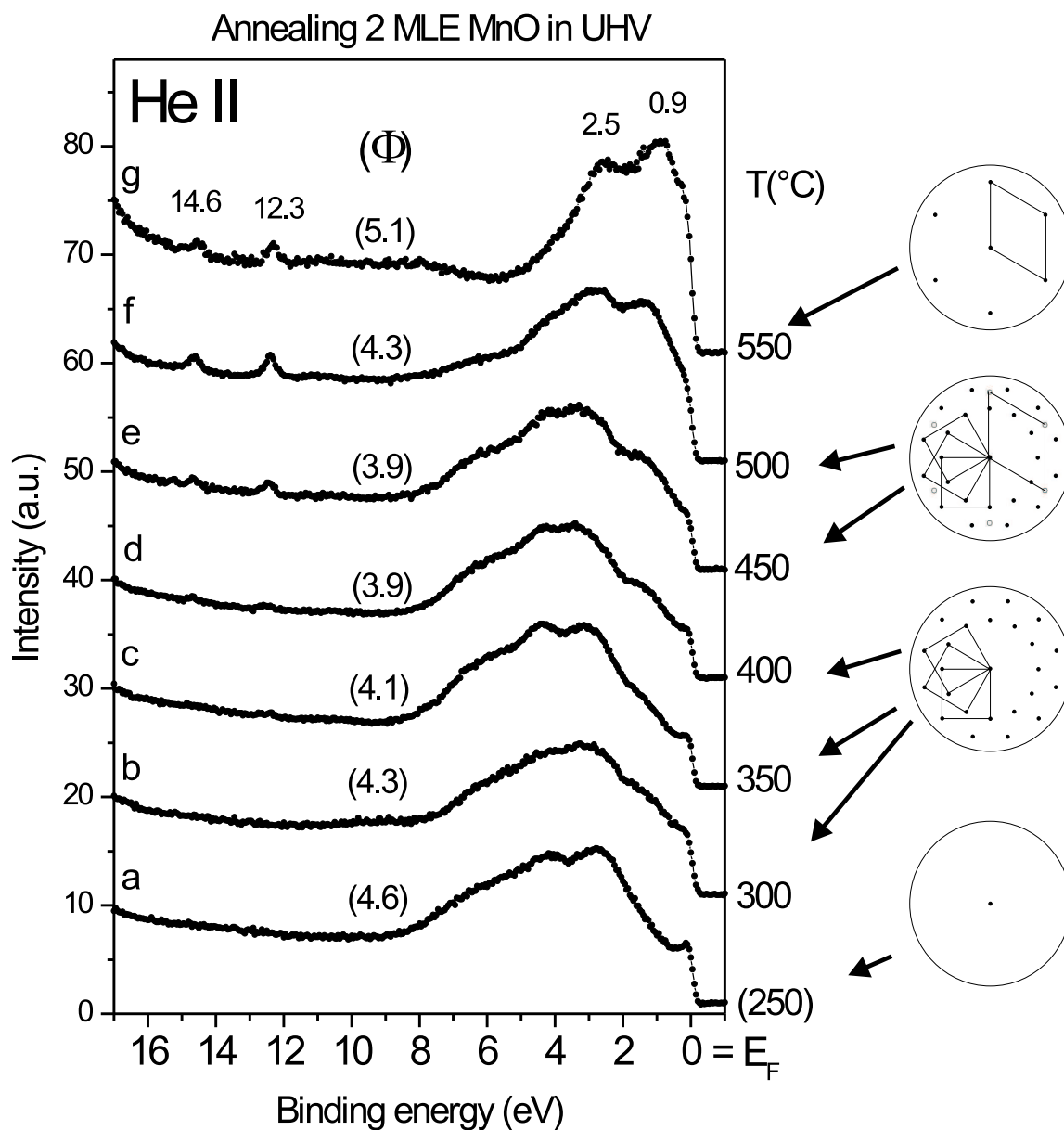


**Figure 4.43:** He II excited UPS spectra of 2 MLE MnO post-oxidised and annealed in UHV. The observed LEED patterns are sketched on the side of the corresponding spectra; The work function of each surface is given on top of the corresponding spectrum in eV.

At 550°C the square MnO(001)-R120° has disappeared, leaving only the a sharp hexagonal  $Pd_xMn_y(111)$ -(1x1) pattern.

The valence band spectra of the post-oxidised 2 MLE surface (figures 4.44a and 4.43a) are identical with the ones presented in the UPS uptake in section 4.2.7. The valence band of the post-oxidised surface consists of an overlap of the Mn 3d band structure with the Pd 4d band on the lower binding energy side and the O 2p band on the higher binding energy side.

Both He I and He II excited valence band spectra of the post-oxidised MnO/Pd(111) surface (fig. 4.44a and 4.43a) show emission from occupied states at the Fermi-level, i.e. the Fermi edge is clearly visible. In He I (fig. 4.44a) the Pd-derived photo-emission maxima are measured at 1.2 and 2.5 eV binding energy; in He II (fig. 4.43a) the maxima are found at 0.9 and 2.5 eV. Furthermore, He I shows two distinct MnO-derived maxima at 4.4 and 6.9 eV binding energy, whereas in the He II spectrum only one maximum is found at 4.4 eV BE with a shoulder to higher BE.

After annealing to 300°C He I (fig.4.44b) shows a Mn 3d band and a broadened O 2p band which both decreased with respect to the Palladium d band. The He II spectrum (fig.4.43b) shows O 2p-Mn 3d emissions which can no longer be separated from the Pd d-band.

Further ordering of the surface by annealing to 350°C brings the sharpness of the O 2p band back and the Mn 3d/O 2p overlap shows a sharp maximum at 4.4 eV that has gained intensity with respect to the substrate d-band (fig.4.44c) . This maximum corresponds to the  $t_{2g\uparrow}({}^5T_2)$  states (notation according to ref. [71]) found in the bulk MnO spectra and the UPS spectra of a thick MnO film, presented in section 4.2.5. The He II spectra show a clear maximum at the same binding energy and the O 2p shoulder becomes more pronounced (fig.4.43c) . At 400°C the valence band maxima are at the same positions as found for 350°C, but the Pd d-band emissions gained with respect to the MnO emissions (figs.4.44d and 4.43d). This gain of the substrate emissions which occurs simultaneously with the appearance of the hexagonal LEED pattern indicates the onset of Mn-Pd alloy formation for this MnO coverage and temperature. Further alloying by heating to 500°C induces a drastic change in the He I spectrum. The palladium d-band dominates the spectrum whereas the  $t_{2g\uparrow}({}^5T_2)$  and O 2p bands have almost disappeared (figs.4.44e and 4.43e).

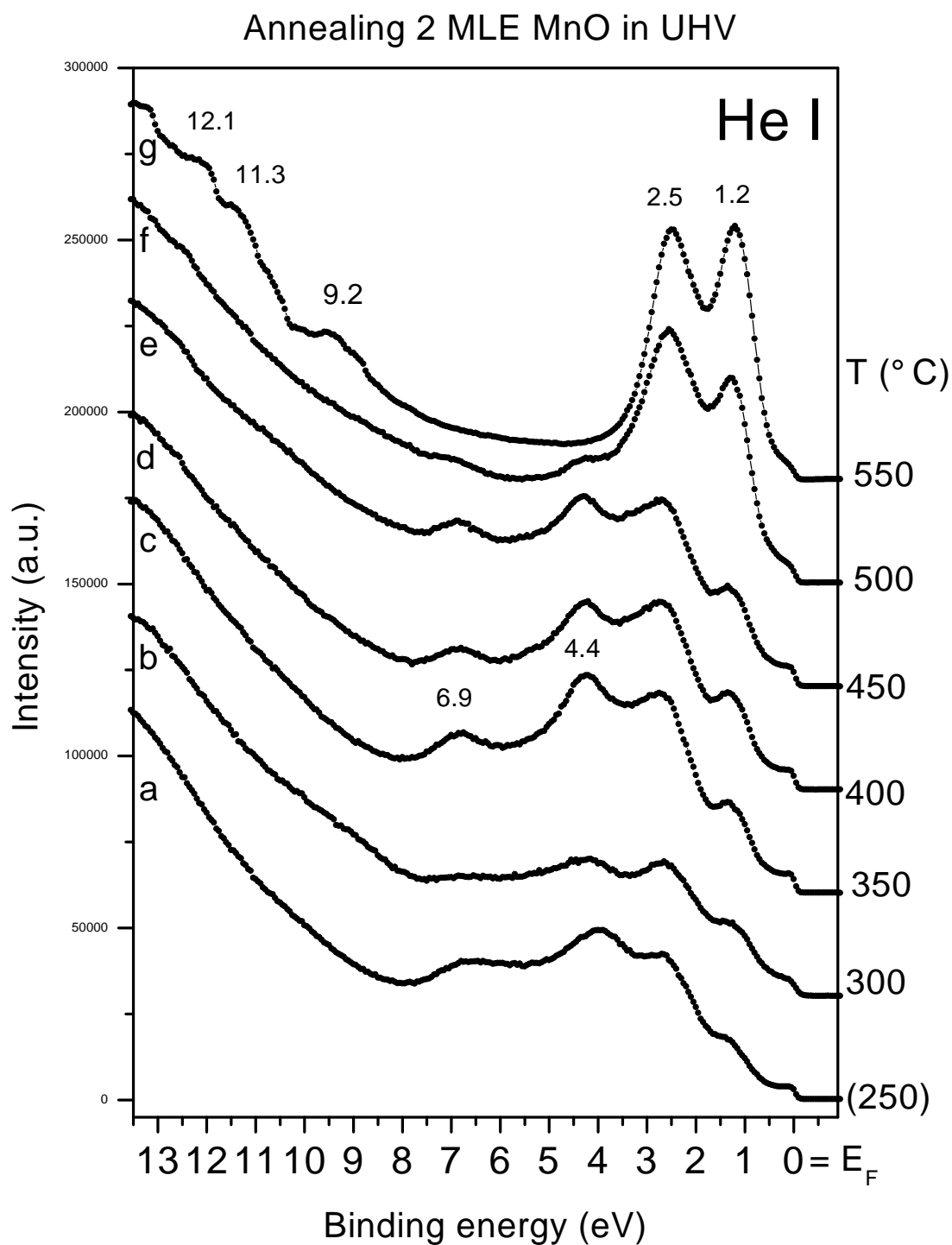


**Figure 4.44:** He I excited UPS spectra of 2 MLE MnO post-oxidised and annealed in UHV; the binding energies of some prominent maxima are given above the spectra.

Further annealing of 2 MLE MnO to 550°C results in valence band spectra without any maxima that can be assigned to O 2p or Mn 3d states (figs.4.44f and 4.43f), the Pd d-band strongly resembles the valence band of the clean substrate (fig. 4.17 on page 108). In fact the only difference between the d-band of the alloy and the one of Pd(111) is the lower emission from the occupied states around the Fermi level. Furthermore the He II spectrum of the alloy displays the sharp low-intensity maxima at 12.3 and 14.6 eV and the He I spectrum shows strangely shaped maxima at and below 9.32 eV binding energy. The strange shapes are probably due to the overlap with the secondary electrons.

Figure 4.45 shows the He I and He II excited spectra of the post-oxidised surface ("MnO disordered", and the spectra after annealing to 350 ("MnO ordered") and 550°C ("Mn-Pd alloy"). The spectra are displayed on the same binding energy axis to illustrate the changes between He I and He II.

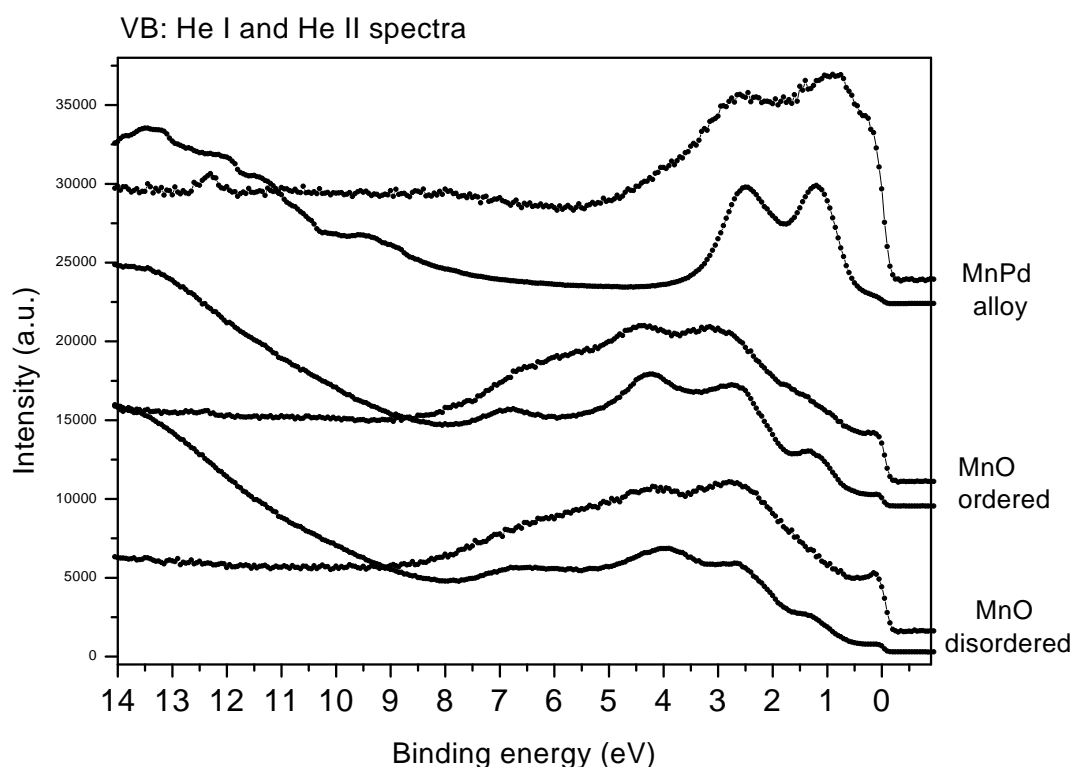


**Figure 4.45:** Comparison of the valence band spectra taken with He I and He II excitation. The spectra of the post-oxidised disordered MnO surface, the ordered MnO surface obtained after anneal to 350° C and the Pd-Mn alloy surface obtained after anneal to 550° C are shown.

A comparison of the He I and the He II excited VB-spectra of this 500°C-surface leads to two interesting results:

A) the changes in the He II band, i.e. the gain of the Pd d-band with respect to the MnO valence band structures, are weaker than in the He I spectrum. Taking the LEED pattern and cross-section and surface sensitivity effects into account this points at a Pd-Mn surface alloy covered by a probably incomplete mono-layer of MnO .

B) two new distinct maxima appeared in the He II spectra at 12.3 and 14.6 eV binding energy. These emissions are very low in intensity, that is why they are probably buried in the secondary electron tail of the He I spectrum. Although the two maxima are surprisingly sharp for valence band emissions, they can not be simply explained by spectrometer derived artifacts like counting errors. These emissions have been reproduced two times on 2.0 and a 2.2 MLE MnO coverages and have not been found in any other valence band spectra. A careful XPS analysis showed no other elements than Pd, Mn and O on the surfaces where these valence band emissions were recorded.

The last He II spectrum of the annealing series suggests that the low-intensity maxima at 12.3 and 14.6 eV are somehow related to the formation of the Pd-Mn surface alloy that shows the sharp hexagonal LEED pattern. However, a close look at the spectra c and d in the annealing series (figure 4.43) shows that the emissions at 12.3 and 14.6 eV already arise after the annealing to 350 and 400°C, where XPS shows no indication for alloying, i.e. where the manganese film is ordered MnO.

In figure 4.46 the UPS spectra of the same annealing sequence are shown after the surfaces had been cooled to room temperature and exposed to 50 Langmuirs of CO. The peaks at 12.3 and 14.6 eV did not increase upon (further) CO dose at room temperature. The valence band spectra of the surfaces annealed to 500 and 550°C show additional peaks at 8.1 and 10.9 eV that can be attributed to the characteristic CO  $4\sigma$  and  $5\sigma, 1\pi$  orbitals of CO adsorbed on Pd.

Sandell et al. investigated reactions of CO,  $O_2$  and  $CO_2$  on the Pd(100)-Mn-c(2x2) surface alloy ([58]) using synchrotron excited C1s and Pd 3d spectra in addition to He II excited valence band spectra. The valence band that was reached after dosing 1 L  $O_2$  at 150 K on the Pd(100)-Mn-c(2x2) surface and subsequently dosing 20 L CO at 120 K shows discernible features at 8.5, 10.5, 11.5 and 14.4 eV. All these features were attributed to adsorbates on the Pd-Mn alloy. Upon heating to 270 K features at 8.5 and

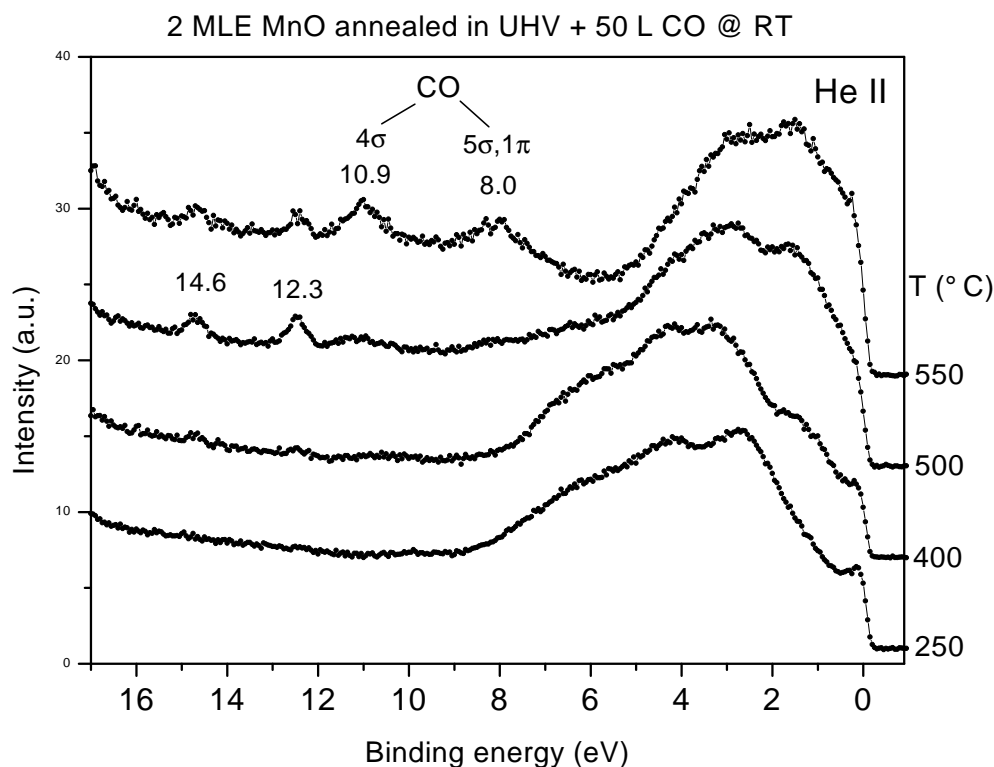


**Figure 4.46:** He II excited valence band spectra of 2 MLE MnO post-oxidised and annealed in UHV (to the temperatures labelled on the right side) and subsequently exposed to 50 L CO at RT.

11.5 eV disappeared, which was attributed to desorption of CO on-top-bonded to Pd. A combination with C 1s spectra connected the valence band features at 8.9, 11.9 and 14.4 eV with a C 1s peak at 291.5 eV. From combinations with EELS data ([79]) and  $CO_2$  adsorption experiments at low temperatures, Sandell et al. attributed these features to  $CO_2$  which is formed on the Pd-Mn surface alloy at 120 K through a reaction between CO and pre-adsorbed atomic O. However this  $CO_2$  species was found to desorb upon heating to 170 K. Furthermore, the valence band features at 6.0, 10.5 and 12.8 eV were associated with a C 1s peak at 290 eV. Comparison with the core and valence levels found for adsorbed  $CO_3^{2-}/Na/Pd(111)$  suggested that a carbonate species ( $CO_3^{\delta-}$ ) forms on the oxygen-modified Pd-Mn surface alloy by a reaction between CO and oxygen. This  $CO_3^{\delta-}$  species was found to be stable up to temperatures between RT and 200°C ([58]).

The alloy obtained after annealing 2 MLE post-oxidised MnO/Pd(111) to 550°C shows



a hexagonal LEED pattern with the same unit cell vectors as the Pd(111) substrate and has therefore a different stoichiometry than the Pd(100)-Mn-c(2x2) surface alloy obtained after depositing 2 ML Mn on Pd(001) and annealing to 300°C in UHV. A  $CO_2$  species which is stable at room temperature on the surfaces is unfavourable and has not been reported on Pd and Pd-Mn alloy surfaces([58], [80]). Therefore, the peaks at 14.6 and 12.3 are most likely to derive from an adsorbed carbonate(  $CO_3^{\delta-}$ ) species similar to the one found on the oxygen pre-treated Pd(100)-Mn-c(2x2) surface alloy. The difference in the binding energies can be attributed to the different stoichiometry of the Pd-Mn-O surfaces.

The fact that the features appear after temperature treatments, where XPS shows no indication for surface alloying, and the absence of the CO ( $4\sigma$  and  $5\pi, 1\sigma$ ) orbitals that can be attributed to CO adsorption on Pd, indicate that this carbonate originates from reaction of CO (from the residual gas) with the ordered MnO film at 400°C and with residual Mn and oxygen on the alloy surface at 500 and 550°C.

The results of work function measurements that have been performed simultaneously with the UPS experiments are given above the corresponding spectra in figure 4.43. The work function of the disordered 2 MLE surface is 4.6 eV. Interestingly, the work function changes upon ordering to the value obtained for thick layers on MnO, 4.3 eV(section 4.2.7). The results of the uptake curve show a work function which gradually decreased with increasing MnO coverage from 5.0 eV for clean Pd(111) to 4.3 eV for the thick layer. The work function drop upon ordering can then be interpreted in the following way: The MnO islands after deposition at room temperature and post-oxidation at 250°C are disordered (no LEED pattern!). Adding mobility via annealing in UHV causes the MnO islands to coalesce and form a uniform and ordered MnO layer (LEED diffraction spots!). The higher work function of the post-oxidised surface in this coverage regime can be due the contribution of some bare Pd sites to the total work function, e.g. as holes in the MnO ad-layer. These holes might not be big enough to adsorb CO on the Pd sites (no CO orbitals in UPS) but they might be frequent enough to raise the total work function of the surface.

#### 4.3.4 UPS and XPS of 1 MLE MnO post-oxidised and annealed in UHV

CO titration experiments have been used on cerium-oxide/rhodium surfaces to monitor the amount of free rhodium before and after temperature treatments in UHV (see section copaper and ref. [20]). In this section CO titration results will be presented, which have been obtained on a 1MLE MnO/Pd(111) surface before and after annealing in UHV. 1 MLE of Mn has been post-oxidised at 250°C and subsequently annealed in steps up to 500°C in UHV. After each annealing step the surface was cooled and exposed to 50 L CO at room temperature. The LEED patterns observed on these surfaces are fcc(111)-(1x1) patterns that only gain in sharpness upon annealing. This finding is consistent with the phases I and III in the LEED phase diagram (section 4.2.9).

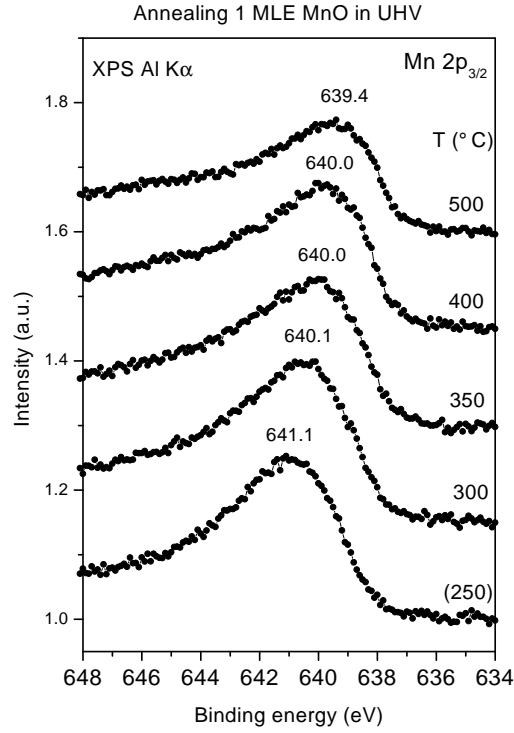
$AlK\alpha$ -excited Mn 2p spectra for the various annealing steps (figure 4.47) show a shift of the Mn  $2p_{3/2}$  maximum and a loss in the total Mn 2p signal upon annealing. The shift from 641.1 eV to 639.4 eV is interpreted as a change of the chemical state of Mn from MnO to  $Mn_xPd_y$  (see section 4.2.1), i.e. the thin manganese film changes from oxide with MnO stoichiometry to a Pd-Mn surface alloy upon annealing.

Figure 4.48 summarises the XPS results obtained on the 1 MLE MnO film after post-oxidation and annealing in UHV. The results agree with the XPS and LEED results obtained with the 3 MLE coverage in section 4.3.2 and the coverage dependent alloying behaviour examined in section 4.2.10.

He II spectra before the CO dose are presented in figure 4.49. Dosing CO onto the post-oxidised surface does not induce any changes in the work-function or the valence band. The work-function and UPS spectrum of the 1 MLE surface after post-oxidation and exposure to CO are identical to those presented in figure 4.25 on page 119, thus no CO adsorbs on the surface.

After annealing to 300°C in UHV the work-function has changed from 4.8 eV to 4.3 eV and the MnO valence band features with a maximum at 4.3 eV binding energy become more distinct. After exposing the 300°C-annealed surface to 50 L CO a satellite arises at 10 eV, but no distinct CO orbitals are visible (see fig. 4.50).

Further annealing to 350°C does not change the work-function but the Mn 3d/O 2p-derived valence band emission at 4.3 eV BE drop significantly. Furthermore the emission from the Pd-derived states near the Fermi edge decrease. Between 6 and 12 eV binding



**Figure 4.47:** XPS AlK $\alpha$ -excited Mn 2p<sub>3/2</sub> spectra of 1 MLE MnO post-oxidised (bottom spectrum) and annealed in UHV; the maxima positions are given in the graph above each spectrum.

energy, the spectrum obtained after annealing to 350°C and CO titration consists of a superposition of the satellite at 10 eV and CO orbitals at 11 and 8 eV ; the satellite prohibits a quantification of the CO orbitals. Furthermore, the CO adsorption has blurred the two Pd d-band maxima at 1.0 and 2.5 eV BE.

The 400°C-tempered surface shows a new peak at 8.6 eV, whereas the work-function remains at 4.3 eV. The Pd-derived band-structure between the Fermi edge and 3.5 eV has again changed its characteristics, now displaying a maximum at 1.1 eV. The spectrum after CO titration now displays two distinct CO-derived maxima at 8 and 11 eV, probably overlapping the 10 eV satellite. The work-function has slightly increased upon CO adsorption from 4.3 eV to 4.4 eV.

Finally, after annealing to 500°C the maximum at 8.5 eV has almost vanished and the d-band features are very similar to the ones obtained on the clean Pd(111) surface,

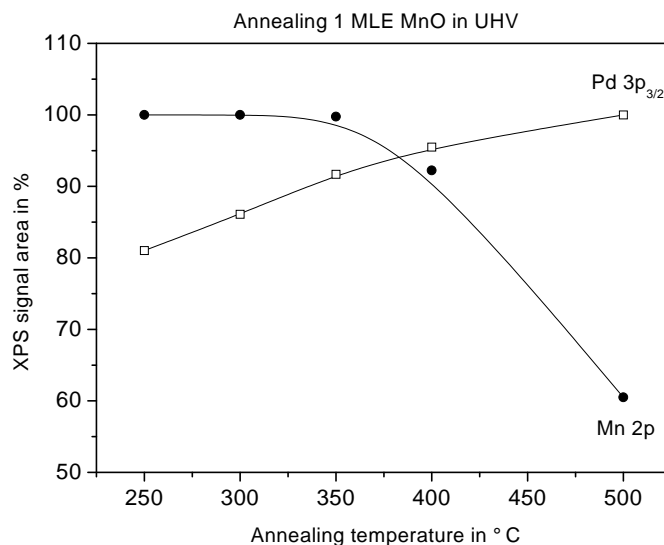


**Figure 4.48:** *Mn 2p and Pd 3p<sub>3/2</sub> peak areas evaluated from XPS data obtained on 1 MLE MnO after post-oxidation and annealing in UHV.*

displaying two maxima at 0.7 and 2.4 eV binding energy. After CO titration the CO orbitals appear almost as distinct as on the clean Pd(111) as illustrated in figure 4.51. Within the experimental error the CO orbitals show the same binding energies as on the Pd(111) substrate. After annealing to 400°C and 500°C, the measured CO area for CO deposition corresponds to 34% and 70% of the Pd(111) saturation value, respectively.

On the post-oxidised 1MLE MnO/Pd(111) surface no CO adsorption was found, thus the Pd surface was fully covered by a disordered MnO film. After annealing the MnO film to 350°C and subsequent exposure to CO a small amount of CO orbitals is visible in the UV spectrum (middle spectrum in figure 4.50). This result suggests that the disordered MnO islands coalesce upon ordering, leaving some free Pd sites behind. The adsorption results for the higher annealing steps can be explained with adsorption on bare Pd and on the Mn-Pd alloy that starts its formation at these temperatures.

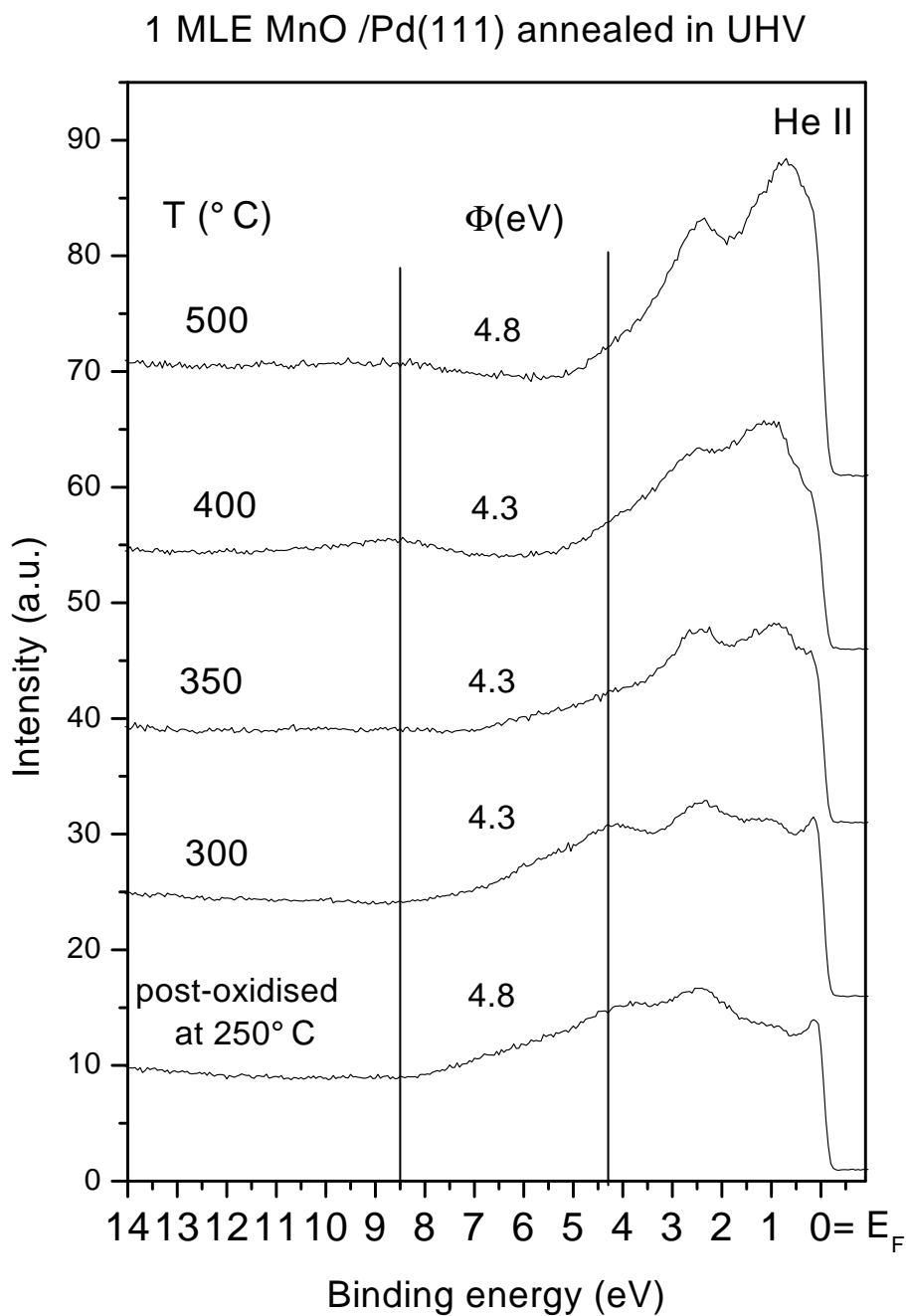


**Figure 4.49:** He II spectra and work-function measurements of 1 MLE MnO post-oxidised and subsequently annealed in UHV; the measured work-functions are labelled above each spectrum.

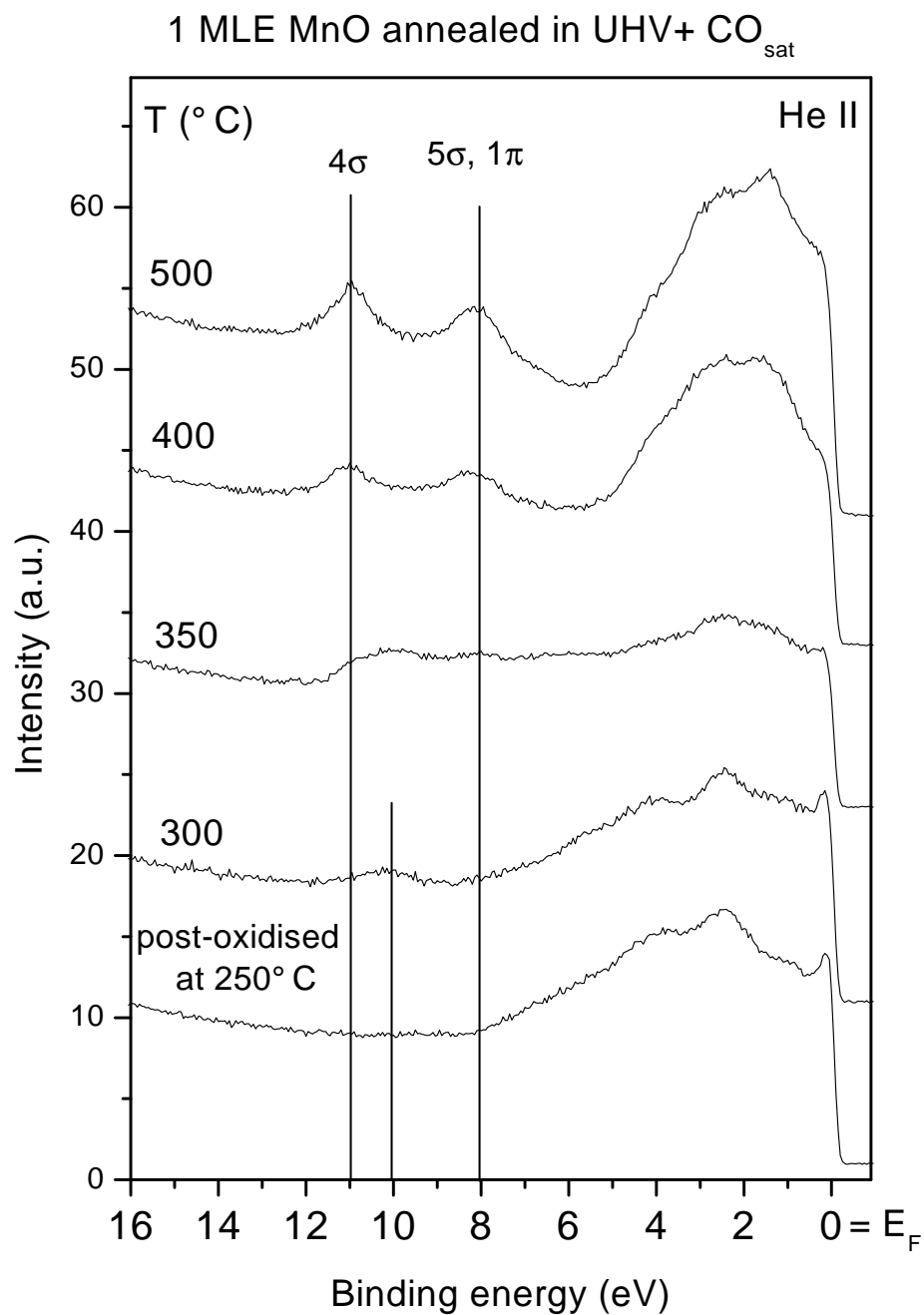


**Figure 4.50:** He II spectra of 1 MLE MnO post-oxidised, subsequently annealed in UHV to the displayed temperatures, cooled to room temperature and exposed to 50 L CO.

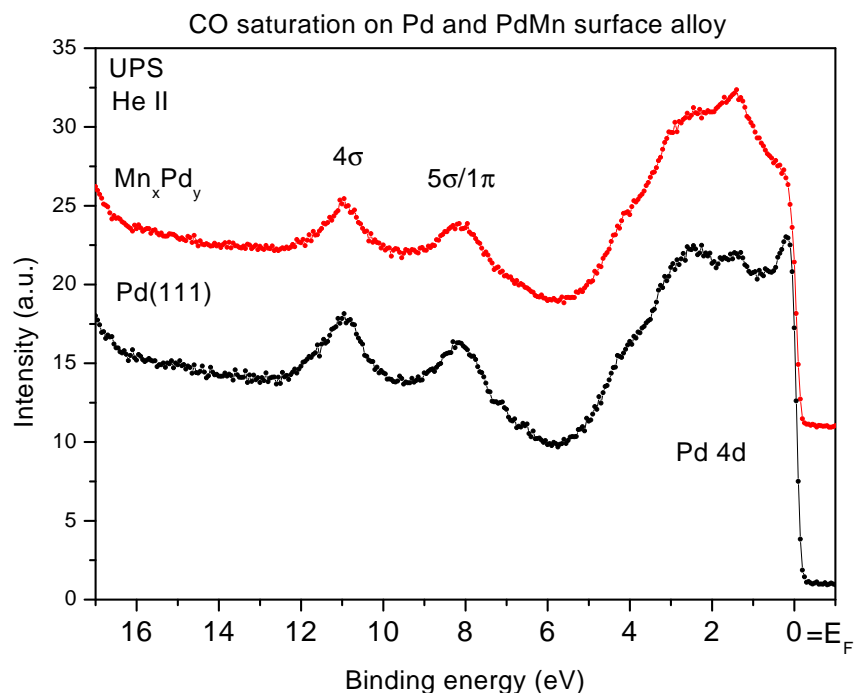


**Figure 4.51:** He II spectra of clean Pd(111) and the PdMn surface alloy (obtained after annealing 1 MLE MnO to 500°C) exposed to 50 L CO at RT.

### 4.3.5 Re-oxidation of the $Pd_xMn_y$ alloy surfaces after annealing in UHV

One of the possibilities to achieve ordered oxide structures on a single crystal is to oxidise a known surface alloy. Sandell et al. found a (4x4) surface alloy reconstruction [55, 81] for 1 ML Mn on Pd(100) at temperatures between 300 and 400°C. In section 4.3.1 it has been shown that one mono-layer of Mn annealed to 300°C can be fully oxidised to MnO by exposure to oxygen at elevated temperatures ( $\geq 250^\circ\text{C}$ ).

Oxidation-reduction cycles are of interest for catalytic systems, e.g. the water gas shift reaction involving ceria as oxygen donor and acceptor. In UHV systems, annealing in the hydrogen dominated background pressure is very often sufficient to reduce the oxide surfaces [20]. Oxidation and re-oxidation of these reduced oxide surfaces is then achieved by offering atomic or molecular oxygen to the surface. This can simply be done by dosing molecular oxygen through a gas inlet in the UHV chamber.

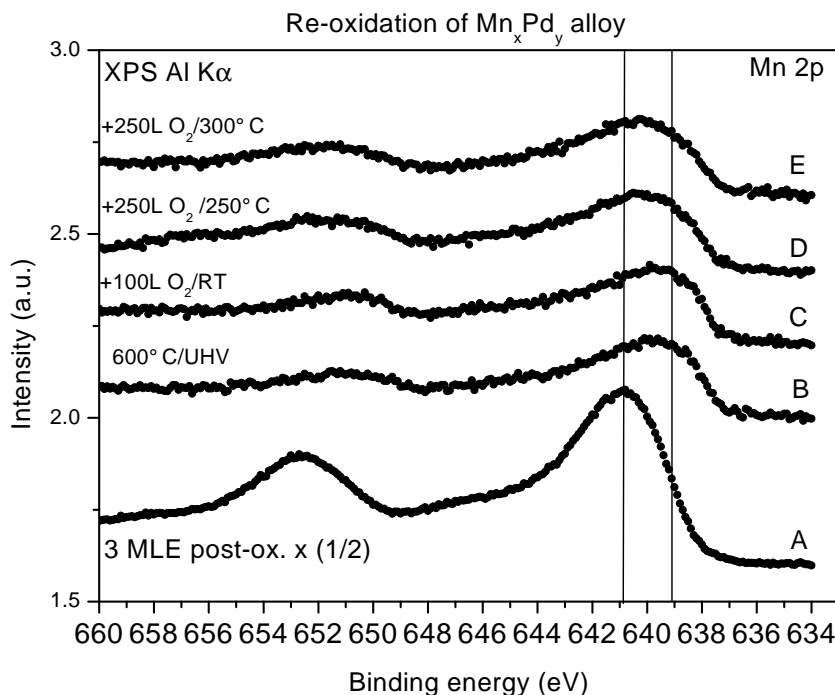


**Figure 4.52:**  $AlK\alpha$  excited  $Mn\ 2p$  spectra of A) 3 MLE  $Mn$  post-oxidised at  $2 \times 10^{-7} mbar O_2 / 250^\circ C$ ; B) after anneal to  $600^\circ C$  in UHV; C) ...+100L  $O_2$  at RT; D) ...re-oxidised in  $2 \times 10^{-7} mbar O_2$  at  $250^\circ C$ ; E) ...re-oxidised in  $2 \times 10^{-7} mbar O_2$  at  $300^\circ C$

In the case of manganese on  $Pd(111)$  it has been shown in section 4.3.2 that annealing in UHV above  $500^\circ C$  reduces the  $MnO$  films via decomposition of the oxide and alloying of the manganese material with the palladium substrate. The resulting surfaces after annealing to temperatures above  $600^\circ C$  show hexagonal  $(1 \times 1)$  LEED patterns, no detectable  $O\ 1s$  emission and a  $Mn\ 2p$  maximum that consists of two components at 638.7 and 640.1 eV, respectively. For a coverage of 3 MLE, the post oxidised  $MnO$  and the  $Pd_xMn_y$  alloy spectra are shown in figure 4.52 A and B, respectively. For better comparison of the spectra, the initial  $MnO$  intensity has been halved. After the anneal the surface shows the known sharp hexagonal  $(1 \times 1)$  LEED structure (see section 4.2.9) and the  $Mn2p$  signal has dropped to 22% of the initial value.

Figure 4.52C shows the spectrum obtained after applying 100L of  $O_2$  to the alloy surface (4.52B) at room temperature. The total signal remains at 22% of the initial  $MnO$  surface, the  $Mn\ 2p$  component at 640.1eV component has marginally risen. The



spectra 4.52C and D show the influence of 10 minutes  $2 \times 10^{-7}$  mbar  $O_2$  at 250 and 300°C and further 10 minutes cooling in the same oxygen pressure, respectively. The signal intensity remains unchanged but a slight shift towards higher binding energies can be detected. Comparing the Mn 2p spectrum 4.52D with post-oxidised 0.7 and 1 MLE MnO, its intensity is similar as a coverage of 0.8 MLE, but the spectrum still shows a metallic component at 639 eV binding energy, that is not observed in the post-oxidised MnO surfaces. The LEED of 4.52C and D does not reveal any new structure, but shows only a diffuse hexagonal (1x1) pattern with the Pd(111) periodicity, thus the re-oxidation does not lead to any new ordered structure.

The O 1s/Pd  $3p_{3/2}$  spectra corresponding to the spectra 4.52 B and C show no detectable O1s signals, the ones corresponding to 4.52 D and E show a shoulder on the  $Pd3p_{3/2}$  that could be attributed to O1s, but the signal is not strong enough to apply reasonable curve fittings.

In summary, XPS shows that the  $Pd_xMn_y$  alloy surfaces obtained after annealing a MnO surface to above 600°C in UHV can not be re-oxidised to MnO surfaces. The Mn 2p intensity loss upon annealing above 600°C, which is attributed to manganese diffusion into the Pd bulk, is irreversible by oxygen treatments involving  $O_2$  pressures up to  $1 \times 10^{-6}$  mbar and temperatures up to 300°C.  $AlK\alpha$ - excited Mn 2p and O 1s spectra suggest that only the topmost layer of the  $Pd_xMn_y$  alloy is oxidised to MnO, which leads to an overlap of MnO- and  $Pd_xMn_y$ -derived Mn 2p maxima. The LEED results suggest that the oxidised topmost layer is disordered because it introduced a higher background to the the well ordered hexagonal  $Pd_xMn_y$  diffraction pattern.

### 4.3.6 Summary of MnO/Pd(111) photo-emission experiments

#### Metallic Mn layers on Pd(111)

Chemically clean Manganese films can be grown on Pd(111) via electron beam evaporation in UHV. Thick Mn films evaporated onto Pd(111) at room temperature (RT) are disordered, i.e. no LEED diffraction spots can be detected. The Mn films show no contamination other than small amounts of oxygen, which are either due to oxidation of the evaporated films by the residual gas or by oxidation of the evaporant in the evaporator during preliminary oxygen treatments in the preparation chamber.

Mn layers above 5 mono-layers (ML), i.e.  $5 \times 13.9 \approx 70$  units on the quartz microbalance (see definition in section 2.4), show the same XPS Mn 2p binding energy and Mn 3s split energy as reported for bulk Mn in the literature (sections 4.2.1 and 4.2.2). Mn layers below 5 ML show a 0.3 eV higher Mn 2p binding energy than thicker layers and the Palladium 3d peaks shift by 0.2 eV to higher binding energies (the Pd  $3d_{5/2}$  binding energy shifts from 334.8 to 335.0 eV). These shifts are attributed to the formation of a bimetallic Mn-Pd interface layer that is completed after a deposition of 5 ML Mn (section 4.2.3), thus the film becomes continuous at this coverage.

#### Thick (>3 MLE) MnO films on Pd(111)

Thick manganese films deposited on Pd(111) at room temperature can be fully oxidised to MnO by exposure to  $2 \times 10^{-7}$  mbar  $O_2$  at 250°C (section 4.2.4). The XPS and UPS spectra obtained from these surfaces are equivalent to those published for bulk MnO samples (sections 4.2.4 and 4.2.5). Carbon monoxide (CO) adsorption experiments showed that CO does not adsorb on thick MnO films at room temperature. Work function measurements resulted in a work function of 4.3 eV for thick MnO films and work functions of 5.0 eV and 5.9 eV for the clean and CO-saturated Pd(111) substrate, respectively.

Annealing thick MnO layers in UHV results in a gradual decomposition of the oxide and the formation of a Pd-Mn alloy. The onset temperature for the oxide decomposition and the alloying is thickness dependent. MnO films with thicknesses above 2-3 MLE do not show any decomposition, i.e. no changes in XPS, when they are annealed up to 350°C in UHV. Further annealing in UHV shows a gradual loss of oxygen and manganese in the XPS detection depth and increasing palladium signals, i.e. oxide decomposition

and alloying. Furthermore, the Mn  $2p_{3/2}$  shifts from the MnO value of 640.7 eV to lower binding energies until the value of metallic Mn (638.6 eV) dominates.

The Mn-Pd alloy obtained by annealing in UHV above 600°C shows no detectable O 1s signal, a Pd 3d signal equivalent to the clean Pd(111) value and an Mn 2p signal equivalent to the one obtained for thick metallic layers. The LEED structure of this surface alloy is equivalent to the one of the clean Pd(111) surface.

The decomposition of MnO and the segregation of Mn into the Pd(111) bulk by annealing in UHV is irreversible, i.e. the Pd-Mn alloy obtained by annealing to 600°C can not be re-oxidised to MnO (section 4.3.5).

### Thin ( $<3$ MLE) MnO films on Pd(111)

MnO films with coverages below 3 MLE show the same XPS, UPS and LEED characteristics, whether they were reactively oxidised, post-oxidised at room temperature or post-oxidised at 250°C (section 4.1.1). The Mn  $2p_{3/2}$  binding energy of post-oxidised films with thicknesses from 0.5 to 24 mono-layer-equivalents (see MLE definition in section 2.4) was always 640.7 eV which is in agreement with the values published for bulk MnO. Therefore, the chemical state of the post-oxidised manganese films can unambiguously be assigned as  $Mn^{2+}$  (section 4.2.1).

Thin layers of MnO show the same Mn 2p binding energies as thick layers. For metallic Mn deposited on Pd(111) the Pd 3d spectra show a thickness dependent binding energy shift which is attributed to the formation of a bimetallic interface layer, i.e. a surface alloy which already forms at room temperature. For the MnO/Pd(111) surfaces no such shift is observed in the Pd 3d spectra, thus a different interface layer is expected.

The valence band of the thin layers shows a superposition of the Mn 3d- and O 2p-derived MnO valence band with the Pd 4d derived substrate valence band (section 4.2.7). CO titration experiments suggest that the substrate is fully oxide covered for coverages  $\geq 0.7$  MLE (section 4.2.8). LEED experiments show no MnO derived diffraction spots on the post-oxidised MnO surfaces. The Pd substrate spots become gradually weakened with increasing thickness of the MnO film and disappear at a MnO coverage of  $\sim 1.5$  MLE.

Annealing the disordered MnO films in UHV up to 350-400°C (thickness dependent) results in ordering of the MnO films without changes in the chemical states, as demon-

strated simultaneously by LEED, XPS (section 4.3.2) and UPS (section 4.43) experiments. The ordered MnO films show a LEED pattern that has been identified as domains with a square unit cell and a unit cell vector of  $\sim 3.1$  Å. Three square domains are rotated by  $120^\circ$  with respect to each other and one unit cell vector of each domain is rotationally aligned with a Pd(111) unit cell vector. These MnO LEED patterns are assigned as MnO(001)-(1x1)R120° due to the observed chemical state and the similarity of the unit cell with the square unit cell of bulk MnO(001).

Annealing to temperatures above  $400^\circ\text{C}$  in UHV leads to a gradual decomposition of the oxide and the formation of a Mn-Pd inter-facial alloy, as concluded from XPS and UPS measurements.

LEED experiments show that after annealing at  $450^\circ\text{C}$  an incommensurate superposition of the MnO(001)-(1x1)R120° pattern with a hexagonal fcc(111)-(1x1) pattern occurs; the latter is identical with the LEED pattern of the Pd(111) substrate. After annealing thin MnO layers to  $600^\circ\text{C}$  in UHV only the hexagonal fcc(111)-(1x1) pattern remains. In agreement with the XPS results, this pattern is attributed to a  $Pd_xMn_y$  surface alloy which has the same unit cell vectors as the Pd(111) substrate. (section 4.2.9).

A comparison of XPS in normal and grazing emission angle geometry suggests that neither the disordered post-oxidised nor the ordered MnO(001)-(1x1)R120° surfaces are purely oxygen terminated (section 4.3.2), thus a topmost layer with alternating oxygen and manganese atoms is suggested.

CO titration experiments on 1 MLE MnO post-oxidised and annealed in UHV indicate that the disordered MnO oxide islands coalesce upon annealing to  $350^\circ\text{C}$ , i.e. upon ordering (section 4.3.4). He II excited UPS spectra of 2 MLE MnO annealed in UHV above  $400^\circ\text{C}$  show peaks at 12.3 and 14.6 eV in addition to the Mn 3d, O2p and Pd 4d derived valence band, that are interpreted as the formation of a carbonate species ( $CO_3^{\delta-}$ ) through a reaction of CO from the residual gas with the ordered MnO film. CO adsorption on the fcc(111)- $Mn_xPd_y$  alloy obtained after annealing 2 MLE MnO above  $500^\circ\text{C}$  in UHV showed additional peaks at 8.0 and 10.9 eV that are attributed to CO  $5\sigma$ ,  $1\pi$  and  $4\sigma$  orbitals originating from CO which is bonded to the fcc(111)- $Mn_xPd_y$  surface alloy (section 4.43).

## 4.4 STM of manganese oxide on Pd(111)

In this section the author presents the preliminary STM experiments that have been performed to investigate the growth of manganese oxide films on Pd(111). The experiments were performed in a three chamber UHV system which is described in detail by C. Castellarin-Cudia [21, chapter 3]. This system was set up for combined LEED / STM measurements in UHV. For the evaporation of Mn a water-cooled e-beam evaporator (fabricated by OMICRON) was used and the film thicknesses were measured with a quartz-micro-balance, as described in section 2.4. The measured corrugations given in the following section are generally bias dependent (see [21, fig.4.17]), however with comparable bias voltages they can be taken as an indication of height.

### 4.4.1 STM characterisation of the ordered MnO phase

The first aim of the STM measurements was to get a real-space picture of the square MnO(001)-(1x1)R120° LEED pattern, which was obtained for MnO coverages around 2 MLE and annealing temperatures around 400°C (phase IV in the LEED phase diagram in section 4.2.9).

The best MnO-derived LEED pattern was obtained when the Mn oxidation was done in two or three steps. First, a low coverage (0.7 to 1 ML) of Mn was deposited on the Pd(111) crystal at RT, then it was post-oxidised ( $2 \times 10^{-7}$  mbar  $O_2$  at 250°C for 10 min), then another 0.7 to 1 ML was deposited and post-oxidised and so on. After the last deposition and post-oxidation step the sample was gradually annealed in UHV in steps of 50°C in front of the LEED apparatus and the LEED pattern was recorded after every annealing step. In that way a LEED pattern with sharp rectangular MnO spots without any hexagonal spots and without a bright background was obtained for MnO coverages between 2 and 3.5 MLE, which were post-oxidised in 2 to 4 steps and annealed to temperatures between 350 and 400°C. XPS showed the same spectral characteristics for the step-by-step post-oxidised and annealed surface as for the reactively oxidised or in one-step post-oxidised surfaces, but the LEED pattern was considerably sharper for the step-by-step oxidised MnO surfaces. This indicates that a better long-range order of the MnO films is achieved by the step-by-step oxidation.

2 MLE MnO, two-step post-oxidised and annealed to 350°C in UHV, displayed a sharp

## 2 MLE MnO evaporated and post-oxidised in 2 steps and subsequently annealed to 350°C

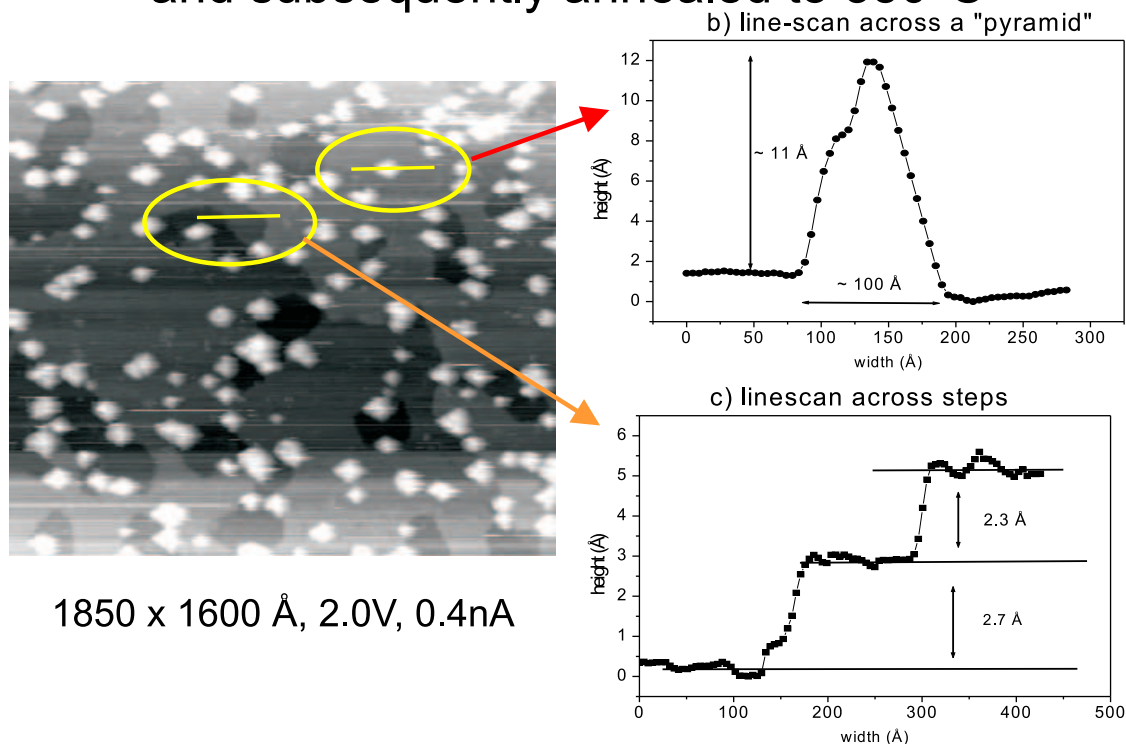


**Figure 4.53:** Topographic STM image of 2 MLE MnO deposited and post-oxidised in two steps and subsequently annealed to 350°C in UHV; the surface showed a sharp square LEED pattern similar to the one shown in figure 4.29B. The image size and tunnelling conditions are given below the image, representative line-scans are presented on the right side.

square MnO LEED pattern as shown in section 4.2.9. This surface was transferred to the STM and topographic STM images were recorded using a sample bias of around 2 V and the lowest possible tunnelling current (0.4 nA). One of these images is shown in Figure 4.53.

The topographic STM images show a surface which consists of three different phases. The most prominent phase is formed by islands with a pyramidal shape. These islands cover about 20 % of the surface, their basal diameters vary between 50 and 200 Å and their heights between 10 and 15 Å. To demonstrate the dimensions of these pyramids, figure 4.53 b) shows a line-scan across one "pyramid"; the top-right bright line in the STM image shows which pyramid has been taken. The basis planes of these pyramids

tend to show triangular shapes. Since the pyramids are considerably small and randomly distributed over the surface it can be assumed that they do not contribute to the observed LEED pattern.

The second phase formed consists of a uniform layer which covers 85 % of the surface and consists of at least two stacked layers. The third phase can be described as holes in the uniform oxide layer. A line-scan across two steps is indicated by another bright line in the STM image and the line profile is plotted in figure 4.53 c). The measured step heights of the phase-two layers vary between 2 and 3 Å. Since the LEED did not show any hexagonal pattern and the XPS of these surfaces shows MnO stoichiometry, this phase can be considered as the MnO layers that give rise to the observed square LEED pattern. The holes that represent the remaining 15 % of the surface can then either be interpreted as free Palladium sites or as another Manganese-Palladium interface layer.

Unfortunately the morphology of this surface impeded a closer investigation. To achieve atomic resolution in STM one has to approach the tip closer to the surface by lowering the sample bias and increasing the tunnelling current. Due to the density of the pyramids the tip then tended to interfere with the islands or to pick up atoms from the pyramids, hence changing its tunnelling performance. Therefore, atomic resolution could neither be achieved on the pyramidal islands nor on the MnO layers in between the islands.

#### 4.4.2 STM of sub-mono-layer MnO/Pd(111) surfaces

The reproduction of the square MnO LEED pattern and characterisation of these surfaces with STM showed surfaces with three dimensional islands that made atomic resolution STM images on the MnO islands very difficult. Although sharp phase IV and phase V LEED patterns (see section 4.2.9) have been obtained by step-by step oxidation the surfaces were considerably rough as imaged STM. It appears that ordered LEED structures do not guarantee well ordered surfaces in STM, probably due to a discrepancy between long range order (reflected by a sharp LEED pattern) and short range order (imaged by STM). Due to time limitations the growth mode investigations - presented in the following section - are far from being complete and the presented results should be understood as a starting point for future investigations.

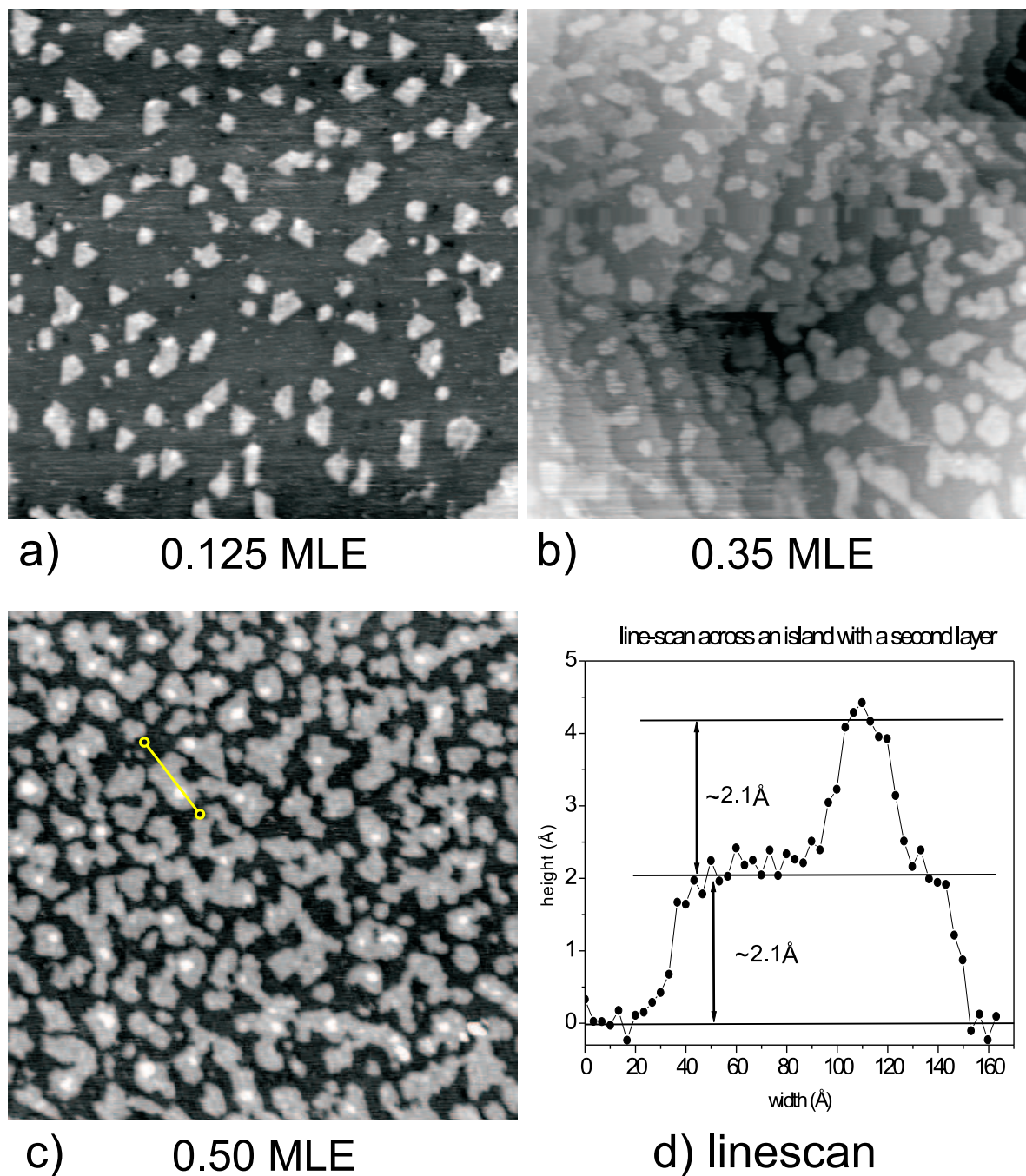
In Figure 4.54 topographic STM images of three different MnO-coverages on Pd(111) are presented. The preparation conditions for these surfaces were the same as for the XPS, UPS and LEED experiments described before, i.e. Mn was deposited on Pd(111) at RT in UHV and post-oxidised in  $2 \times 10^{-7}$  mbar  $O_2$  at 250°C. The lowest coverage investigated with STM was one eighth of a mono layer equivalent (MLE), i.e. 1.7 units Mn- as measured on the quartz-micro-balance - were deposited on the clean Pd(111) single crystal and subsequently oxidised under the conditions given above. Large scale STM images ( $\geq 1000\text{\AA}$ ) show the Pd(111) surface covered by about 20 % with randomly distributed islands. Due to the XPS results these islands are attributed to MnO. The MnO islands in image 4.54a) show diameters between 20 and 100Å. The island heights measured at +2.5V bias and 0.4 nA tunnelling current were  $1.8\text{\AA} \pm 0.1\text{\AA}$ . The island shapes are dominated by triangular shapes with straight edges.

Figure 4.54b) shows the STM image of 0.35 MLE MnO on Pd(111). The MnO islands at 0.35 MLE cover 35% of the Pd(111) surface. The islands have grown in size, now showing diameters between 30 and 200Å with an average height of  $2.2\text{\AA} \pm 0.2\text{\AA}$  (measured with sample bias +2.4 V and tunnelling current 0.4 nA), and it appears that islands have grown together. Thus, going from 0.125 to 0.35 MLE coverage the MnO islands grow in size and coalesce.

At 0.5 MLE (Figure 4.54c), the Pd(111) surface is covered by 55 %; the island sizes now range from  $30\text{\AA} \times 30\text{\AA}$  to  $100\text{\AA} \times 300\text{\AA}$ . In addition to the two-dimensional MnO islands, islands with a second layer can be seen. This new layer can be recognised as



## MnO - growth: 1000 x 100 Å images



**Figure 4.54:**  $1000 \times 1000 \text{ Å}$  topographic STM images of different MnO coverages on Pd(111) after post-oxidation; a) 0.125 MLE MnO,  $U=2.4 \text{ V}$ ,  $I=0.4 \text{ nA}$ ; b) 0.35 MLE MnO,  $U=2.5 \text{ V}$ ,  $I=0.4 \text{ nA}$ ; c) 0.5 MLE MnO,  $U=2.0 \text{ V}$ ,  $I=0.4 \text{ nA}$

bright spots on top of the grey islands in picture 4.54c. Figure 4.54d shows a line-scan across a MnO island with an additional layer. The 2-dimensional MnO islands show again heights of  $2.1 \text{ \AA} \pm 0.1 \text{ \AA}$ , the next layer is also  $2.1 \text{ \AA}$  high (as measured with sample bias  $+2.0 \text{ V}$  and tunnelling current  $0.4 \text{ nA}$ ). A phase analysis large scale STM images of the 0.5 MLE surface with a threshold value of  $2 \text{ \AA}$  height for the 2-dimensional MnO layer results in 45% free palladium area and 50% surface covered with 2-dimensional MnO islands. The remaining 5% are the area covered with 3-dimensional MnO islands on the 0.5 MLE MnO/Pd(111) surface.

MnO uptake experiments with LEED and UPS showed the disappearance of the substrate features at 1.5 MLE in LEED and between 0.7 and 1 MLE according to CO titration experiments in UPS (sections 4.2.9 and 4.2.8). MnO deposition of 1 MLE (STM images not shown) shows the Pd(111) surface fully covered with MnO and a further growth of the 3 dimensional islands. The completion of the first oxide layer in STM thus agrees with the CO titration UPS results.

Free palladium patches are seen as black areas in the STM images of figure 4.54 for all coverages, where the Pd substrate is not completely covered with manganese oxide. There is no hint for oxygen on the free Pd(111) surface although the surface had been exposed to high doses of  $O_2$  both at  $250^\circ\text{C}$  and at room temperature during the post-oxidation procedure. To clarify the role of oxygen on the bare Pd-parts of the MnO sub-monolayer coverages, additional experiments have been performed with XPS and LEED in the SCIENTA system. The clean Pd(111) surface was exposed to  $2 \times 10^{-7} \text{ mbar } O_2$  for 10 minutes at  $250^\circ\text{C}$  and then cooled in the same oxygen pressure to room temperature for 20 minutes. Subsequent LEED and XPS results showed the well known Pd(111)  $-(2 \times 2)\text{-O}$  superstructure in LEED [82] and a very weak O1s signal in XPS. Both XPS and LEED features disappeared after leaving the surface for 15 minutes in the residual gas of  $1.5 \times 10^{-10} \text{ mbar}$ . The major contributions to the residual gas according to a quadrupole mass-spectrometer were  $H_2$  (80%) and CO (10%). The disappearance of the O signals can be explained by a clean-off reaction of the chemisorbed oxygen with the residual gas which appears to occur at room temperature. The SCIENTA and the STM systems showed comparable base pressures during the MnO/Pd(111) experiments, therefore the same clean-off reaction can be expected in both systems. Furthermore, combined HR-XPS and STM measurements of vanadium-oxides on Pd(111) showed a similar clean-off

## 0.5 MLE MnO post-oxidised

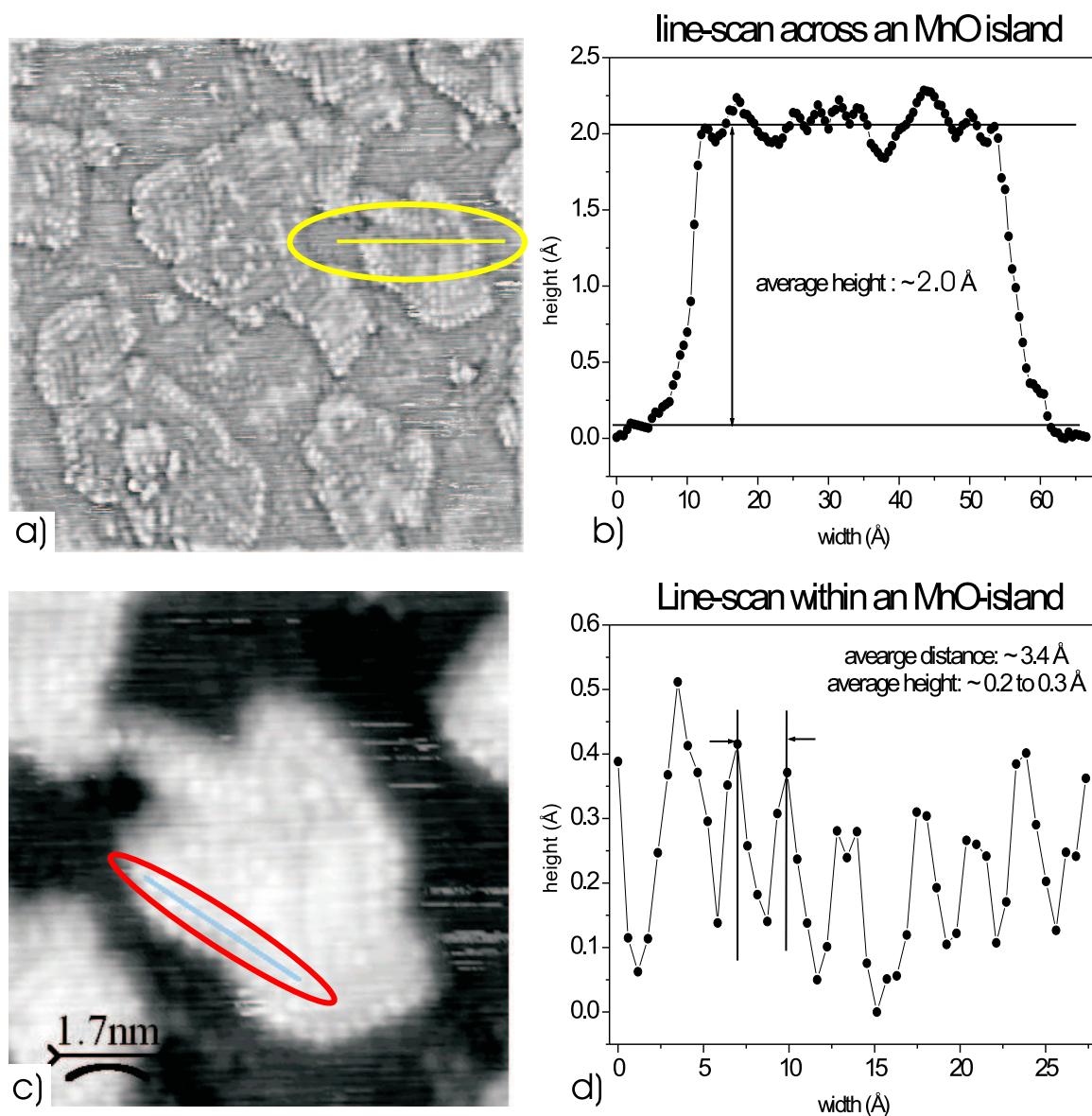


**Figure 4.55:** Atomically resolved STM images of 0.5 MLE post-oxidised MnO and line-scans across and on top of an island. The top STM image is  $200\text{\AA} \times 200\text{\AA}$  (bias =  $-0.6\text{V}$ ; tunnelling current =  $0.4\text{ nA}$ ), the bottom one is a part of the same image magnified for better view of the line-scan on top of the island.

reaction for the chemisorbed oxygen [83, 84].

CO adsorption on the free palladium sites from the residual gas, as seen in UPS, is not visible in the STM due to the high mobility of CO on Pd(111) at room temperature [85].

Three dimensional island growth of post-oxidised MnO starts before the first layer of MnO on Pd(111) is completed, the MnO films thus grow in the Vollmer Weber mode [74, p105 ff.]. The MnO islands after post oxidation of 0.5 ML Mn were considerably wide and flat, that facilitated atomic resolution with STM. With a low sample bias ( $\leq 1V$ ) atomic resolution can be achieved on the MnO islands and the STM images showed no difference whether the bias was positive or negative. Figure 4.55 shows a  $200 \times 200 \text{ \AA}$  STM image taken with -0.6 eV sample bias and 0.4 nA tunnelling current. The STM image shows bright equidistant maxima on top of the MnO island. A line-scan across 8 maxima is indicated by the line in figure 4.55c and the results of the line-scan are presented in 4.55d. The measured average distance between the maxima along this line is  $3.4 \text{ \AA}$ , which is within the experimental error consistent with the  $3.14 \text{ \AA}$  atomic distance for the Mn-Mn (or O-O) distance in the MnO(001) plane.

The assignment whether the maxima are due to manganese or oxygen atoms is not trivial. For an estimation one can use the fact that negative bias imaging is tunnelling out of filled states into the tip. The UPS spectra of MnO/Pd(111) have been presented in section 4.2.7 and they represent the filled density of states. Down to 1eV below the Fermi-level the UPS spectra of sub-monolayer coverages are dominated by the d-band of the palladium substrate, the Mn 3d/O 2p band of MnO is 1 to 9 eV below the Fermi-level. Thus, the maxima seen in STM could be interpreted by tunnelling out of substrate states through the MnO layer, where the measured intensity is modulated by the atomic distances of the MnO overlayer.

The STM maxima on top of the MnO islands show only short range order. On the edge of the oxide islands always two equidistant rows of maxima are visible, however a repeated unit cell with square or hexagonal arrangement can not be assigned. The height of the island with respect to the unresolved Pd(111) substrate is  $2.0 \text{ \AA}$  (figure 4.55b), the corrugation within the island lies between  $0.2$  and  $0.3 \text{ \AA}$  (figure 4.55d).

### 4.4.3 STM of annealed MnO/Pd(111) surfaces

It is known that many surface oxides tend to form uniform layers on metallic single crystal surfaces, when more mobility is added by elevated temperature treatments. For instance, cerium-oxides on Rh(111) [20, 21, 86] and vanadium-oxides on Rh(111) [75, 87] and Pd(111) [16, 88] showed this behaviour. Furthermore, metallic manganese deposited on Pd(100) at room temperature showed island shapes in STM that resembled very much the ones obtained for post-oxidised MnO on Pd(111); for comparison see [81, fig 1a)] and figure 4.54c. Annealing these Mn islands on Pd(100) to 300°C in UHV resulted in a better ordered surface containing fewer, larger islands. Since the square MnO LEED pattern started to form at 350-400°C, this annealing temperature was taken to investigate the influence of annealing on the MnO films.

The different MnO coverages presented in section 4.4.2 have been annealed in UHV at a temperature between 350 and 400°C for 10 minutes. The LEED pattern and STM images were recorded after the sample had cooled down to below 50°C.

The LEED patterns showed no deviation from the LEED phase diagram presented in section 4.2.9. The diffuse hexagonal (1x1) which derives from the Pd(111) substrate covered with disordered MnO turns into a sharp hexagonal (1x1) which can not be distinguished from the substrate (1x1), but which according to XPS is attributed to a  $Mn_xPd_y$  surface alloy.

STM images of 500Å×500Å size are presented in figure 4.56. The left hand side of the figure shows the three different post-oxidised MnO coverages of 0.125, 0.35 and 0.5 MLE prior to annealing. On the right hand side of the figure STM images of the same coverages after annealing in UHV to 400°C are shown. In the top row one can see that the small MnO islands with straight edges and diameters of  $\sim 80\text{\AA}$  turned into fewer, larger islands with diameters between 150 and 350 Å. The island edges after annealing are better oriented along the high symmetry directions of the substrate. This annealing behaviour resembles very much the one observed for Mn islands on Pd(100) [81]. An evaluation of several large scale images showed that the area of the free Pd(111) surface increased from 80% to 90% upon annealing. For 0.35 MLE and 0.5 MLE the trend of forming fewer, larger islands upon annealing continues. The 0.35 MLE coverage shows island diameters between 100 and 400Å after annealing, the 0.5 MLE coverage shows island sizes up to  $200 \times 500\text{\AA}$ . For 0.35 MLE coverage the free Pd(111) area in STM increases from 55%



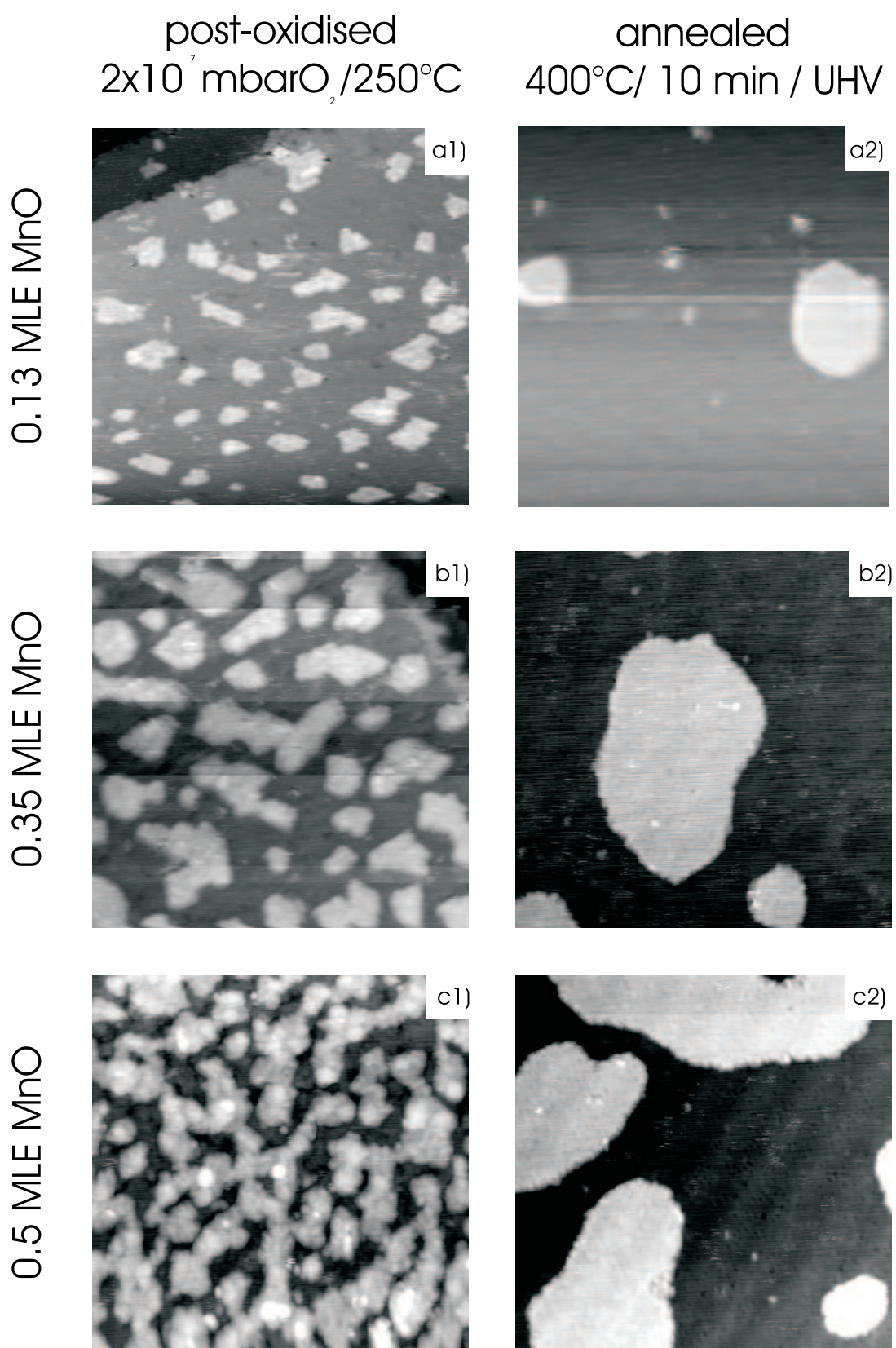


**Figure 4.56:**  $500 \text{ \AA} \times 500 \text{ \AA}$ - STM images of different MnO coverages before and after annealing to  $400^\circ C$  in UHV; sample biases and tunnelling currents: a1)  $2.5V$ ,  $0.4nA$ ; a2)  $2.8V$ ,  $0.4nA$ ; b1)  $2.4V$ ,  $0.6nA$ ; b2)  $2.4V$ ,  $0.4nA$ ; c1)  $1.1V$ ,  $0.4nA$ ; c2)  $0.9V$ ,  $4.5nA$

to 75%; for 0.5 MLE coverage the amount of free Pd on the surface changes from 45% to 66% upon annealing to 400°C in UHV, as evaluated from large scale STM images.

The results for the free Pd area before and after annealing are summarised in a graph in fig.4.57. A linear extrapolation of the points obtained for 0.125, 0.35 and 0.5 MLE post-oxidised MnO (shown as dashed line in the figure) leads to a completion of the first layer at 0.95 MLE MnO coverage, in fact at 1MLE MnO the Pd(111) surface was fully covered, as measured by STM. The square MnO unit cell has a unit cell vector  $a_0 = 3.14\text{\AA}$  and an area of  $9.8\text{\AA}^2$ , the hexagonal Pd(111) unit cell has  $a_0 = 2.79\text{\AA}$  and a unit cell area of  $6.55\text{\AA}^2$ . Therefore, for layer-by-layer growth the free Pd surface would be covered at 0.66 MLE coverage. The fact that more MnO is needed to fully cover the Pd(111) surface originates from the 3 dimensional island growth of MnO which starts at 0.5 MLE MnO coverage. The fact that after annealing the STM images show more free substrate can be interpreted in two ways: either some Mn material leaves the surface upon annealing by diffusion into the bulk or the atomic density in the Mn-Pd alloy islands is higher than the one in the MnO islands.

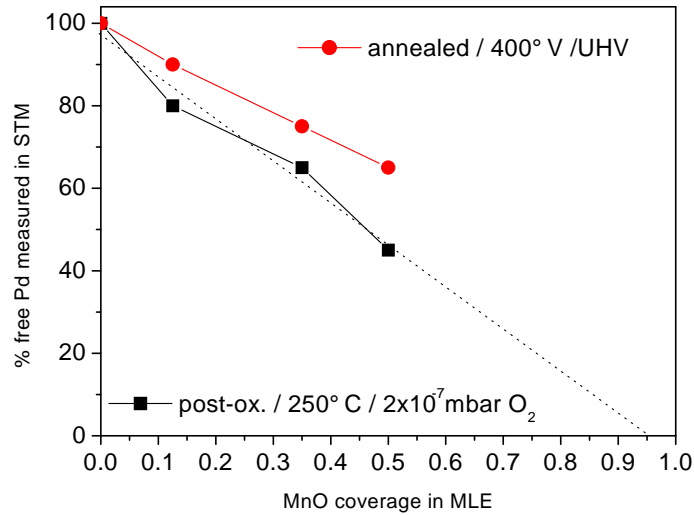


**Figure 4.57:** Free Pd area measured in STM versus MnO coverage in MLE; squares: post-oxidised MnO surfaces; filled circles: Mn-Pd alloy islands after annealing to 400°C in UHV

Figure 4.58 a) and b) show small scale STM images of an island obtained after annealing 0.5 MLE MnO to 400°C. All the islands obtained after annealing were purely

## 0.5 MLE MnO annealed to 400°C

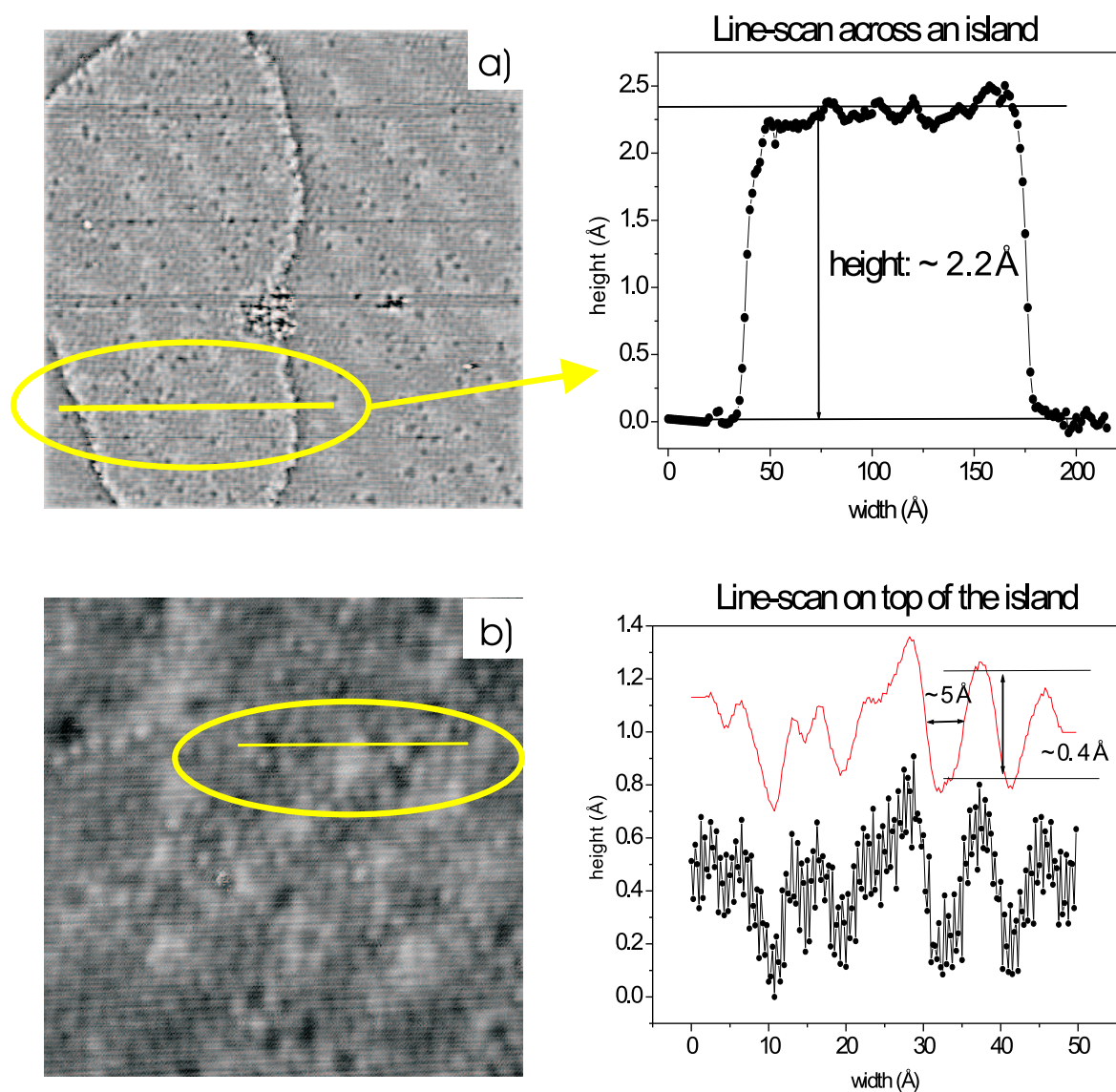


**Figure 4.58:** Atomically resolved STM images of 0.5 MLE MnO annealed to 400°C and line-scans across and on top of an island. The top STM image is 300 Å × 300 Å (bias = -0.6 V; tunnelling current = 0.4 nA), the bottom one is 100 Å × 100 Å (bias = 0.85 V; tunnelling current = 1.6 nA)



two dimensional and the line-scan across these islands show heights between 2.2 and 2.4 Å (for  $U \sim +2\text{V}$  and  $I=0.4\text{nA}$ ). In Figure 4.58a the Mn-Pd island and the flat area which is probably the Pd(111) substrate both show randomly distributed darker imaged point defects. Figure 4.58 b) shows a  $100 \text{ Å} \times 100 \text{ Å}$  STM image taken on top of the island of image 4.58a. A line-scan across 4 point defects is indicated in 4.58b and the result is plotted on the right hand side. The point defects are on average 5 Å wide and 0.4 Å deep. The atomically resolved images obtained from the Pd-Mn islands did not show a distinguishable order, even after performing Fast Fourier Transformation and autocorrelation analysis.

#### 4.4.4 STM on MnO/Pd(111): summary and outline

Topographic STM images of post-oxidised MnO on Pd(111) show a 2 dimensional island growth for coverages below 0.5 MLE. Above 0.5 MLE a second MnO layer starts to form on top of the MnO islands, indicating the Vollmer Weber island growth mode. The measured heights of the two different MnO layers were  $\sim 2\text{\AA}$ . The completion of the first layer, i.e. the coverage where the Pd(111) substrate is fully oxide covered, is found at  $\sim 1$  MLE, which is consistent with the CO-titration experiments. The MnO islands after post-oxidation are randomly distributed over the Pd(111) surface and show straight island edges. Atomic resolution was achieved on the MnO islands with  $U \leq 1\text{V}$  and  $I = 0.4\text{ nA}$ ; no contrast change was observed upon changing the bias polarity. Bright maxima with a corrugation between 0.2 and 0.3  $\text{\AA}$  have been found in STM with distances close to the 3.14  $\text{\AA}$  atomic distance of the MnO(001) unit cell. These maxima are interpreted by tunnelling out of substrate states through the MnO layer, where the measured intensity is modulated by the MnO atomic distance. Thus, they can be attributed either to Mn or to O atoms. The maxima reveal only short range order, which explains the absence of MnO-derived diffraction spots in LEED.

Annealing the MnO islands in UHV at 400°C resulted in fewer and larger islands as compared to the post-oxidised surfaces. Furthermore, the island edges after annealing are better oriented along the high symmetry directions of the substrate. According to previous XPS results these islands are attributed to a Pn-Md surface alloy of unknown stoichiometry. Annealing the MnO islands in UHV increases the amount of the uncovered Pd surface, either due to segregation of Mn into the Pd bulk or due to the morphology changes of the islands including changes of the atomic density within the islands.

The alloy islands are purely 2 dimensional with a measured height of  $\sim 2.2\text{\AA}$ , which is within the experimental error the same value as obtained on the MnO islands. The corrugation within the islands lies below 0.2  $\text{\AA}$ , except for randomly distributed dark imaged point defects that showed depths of around 0.4  $\text{\AA}$  and widths of around 5 $\text{\AA}$ . The atomically resolved images obtained on the Pd-Mn surface alloy islands did not show a distinguishable order, even after performing Fast Fourier Transformation and autocorrelation analysis.

STM images of 2 MLE MnO surfaces, that have been annealed until they showed the square MnO(001)-(1x1) LEED pattern, displayed surfaces which consist of three different

phases. The most prominent phase is formed by MnO islands with a pyramidal shape. These islands cover about 20 % of the surface, their basal diameters vary between 50 and 200 Å and their heights between 10 and 15 Å. The basis planes of these pyramids tend to show triangular shapes. Since the pyramids are considerably small and randomly distributed over the surface it can be assumed that they do not contribute to the observed LEED pattern. The second phase is formed by a uniform layer which covers 85 % of the surface and consists of at least two stacked layers. Since the LEED did not show any hexagonal pattern and XPS of these surfaces showed MnO stoichiometry, this phase is considered as the MnO layers that give rise to the observed square LEED pattern.

The third phase can be described as holes in the uniform oxide layer. These holes represent 15 % of the surface and they can either be interpreted as free palladium sites or as another manganese-palladium interface layer. Unfortunately, the shape of the pyramidal MnO phase and the density of the pyramids impeded a closer investigation by STM.

Due to the density and height of the pyramids the tip tends to interfere with the islands or to pick up atoms from the pyramids, hence changing its tunnelling performance. Therefore, atomic resolution could neither be achieved on the pyramidal islands nor on the MnO layers in between the islands.

Future investigations of the MnO/Pd(111) interface should therefore concentrate on a MnO coverage regime just above 1 MLE, where the first MnO layer is completed and the second layer is not yet forming as high islands as observed on the 2-3 MLE MnO surfaces. Furthermore, the MnO film should be annealed at temperatures around 300°C. For a better ordering of the MnO films longer annealing times should be applied rather than higher annealing temperatures, because for annealing temperatures above 300°C decomposition of the MnO films was found in XPS (for this coverage regime).

The model drawn in figure 4.59 summarises the photoemission (see section 4.3.6), LEED and STM results obtained on MnO films on Pd(111), which have been prepared by post-oxidation. The chequerboard structure for thin MnO films agrees with the square unit cell observed by STM and LEED. Furthermore this structure belongs to a non-polar surface. The positioning of both oxygen and manganese in the surface plane agrees with the grazing emission XPS results, which indicated no purely oxygen terminated surface.

## Model of the MnO/Pd(111) interface structures

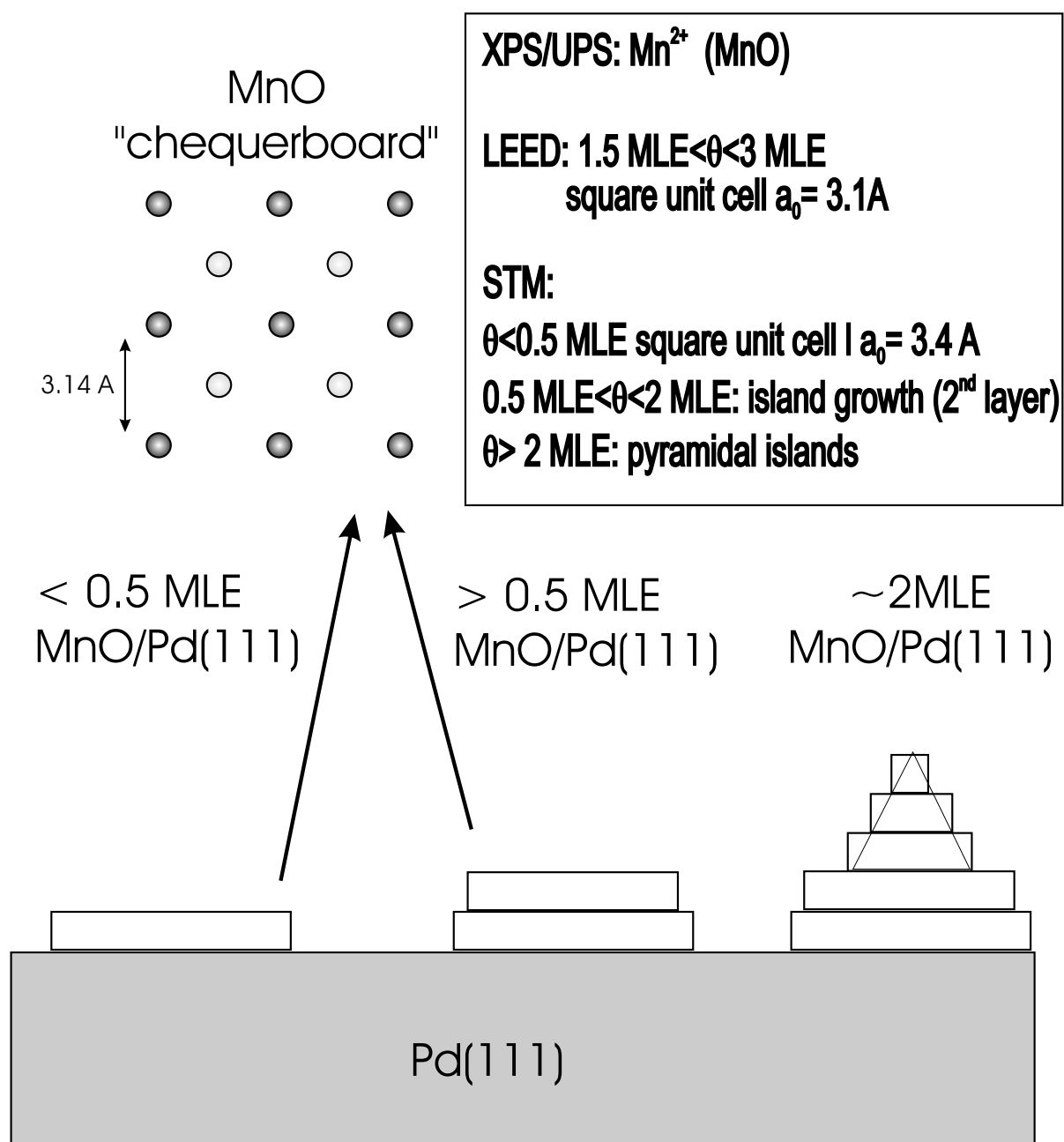


**Figure 4.59:** Model of the MnO/Pd(111) interface derived from XPS, UPS, LEED and STM results

# Bibliography

- [1] R. Franchy, "Growth of thin, crystalline oxide, nitride and oxynitride films on metal and metal alloy surfaces," *Surf Sci. Rep.*, vol. 38, pp. 195–294, 2000.
- [2] S. A. Chambers, "Epitaxial growth and properties of thin film oxides," *Surf Sci. Rep.*, vol. 39, pp. 105 –180, 2000.
- [3] S. C. Street, C. Xu, and D. W. Goodman, "The physical and chemical properties of ultrathin oxide films," *Annu. Rev. Phys.*, vol. 48, p. 43, 1997.
- [4] M. Baeumer and H.-J. Freund, "Metal deposits on well-ordered oxide films," *Prog. Surf. Sci.*, vol. 61, p. 127, 1999.
- [5] D. Goodman, "Catalysis by metals: from extended single crystals to small clusters," *Surf. Rev. Lett.*, vol. 1, p. 449, 1994.
- [6] P. L. J. Gunter, J. W. Niemandsverdriet, and G. A. Somorjai, "New directions of catalysis research," *Catal. Rev. Sci. Eng.*, vol. 39, p. 77, 1997.
- [7] G. A. Somorjai and M. X. Yang, "New directions of catalysis research," *J. Mol. Catal A*, vol. 115, p. 389, 1997.
- [8] F. P. Netzer, "Interfacial oxide layers at the metal-oxide phase boundary," *Surf. Rev. Lett.*, vol. 9, p. 1553, 2002.
- [9] S. J. Tauster, S. C. Fung, R. T. K. Baker, and J. A. Horsley, "Strong interactions in supported-metal catalysts," *Science*, vol. 211, p. 1121, 1981.
- [10] S. J. Tauster, "Strong metal-support interactions," *Acc. Chem. Res.*, vol. 20, p. 389, 1987.

- [11] G. L. Haller and D. E. Resasco, "Metal-support interaction: group VIII metals and reducible oxides," *Adv. Catal.*, vol. 36, p. 173, 1989.
- [12] O. Dulub, W. Hebenstreit, and U. Diebold, "Imaging Cluster Surfaces with Atomic Resolution: The Strong Metal-Support Interaction State of Pt Supported on TiO<sub>2</sub>(110)," *Phys. Rev. Lett.*, vol. 84, p. 3646, 2000.
- [13] E. Ruckenstein and S. H. Lee, "Simulation of the Behavior of Supported Metal Catalysts in Real Reaction Atmosphere by Means of Model Catalysts," *J. Catal.*, vol. 107, p. 23, 1987.
- [14] R. T. K. Baker, E. B. Prestridge, and R. L. Garten *J. Catal.*, vol. 56, p. 390, 1979.
- [15] R. J. Lad, "Interactions at metal/oxide and oxide/oxide interfaces studied by ultra-thin film growth on single crystal oxide substrates," *Surf. Rev. Lett.*, vol. 2, p. 109, 1995.
- [16] F. P. Leisenberger, *Vanadiumoxid auf Palladium (111): Der "Inverse Katalysator"*. Dissertation an der Karl Franzens Universitaet Graz, 1999.
- [17] H. Muraki and G. Zhang, "Design of advanced automotive exhaust catalysts," *Catalysis Today*, vol. 63, pp. 337–345, 2000.
- [18] A. Trovarelli, "Catalytic properties of ceria and CeO<sub>2</sub>-containing materials," *Catal. Rev. Sci. Eng.*, vol. 38, p. 439, 1996.
- [19] A. Boffa, C. Lin, A.T: Bell, and G. Somorjai, "Promotion of CO and CO<sub>2</sub> Hydrogenation over Rh by Metal Oxides: The Influence of Oxide Lewis Acidity and Reducibility," *J. Catal.*, vol. 149, p. 149, 1994.
- [20] S. Eck, *Die Ceroxid/Rhodium(111)Grenzflaeche*. Diplomarbeit an der Karl Franzens Universitaet Graz, 2000.
- [21] C. Castellarin-Cudia, *Atomic scale growth studies of metal and oxide overlayers*. Dissertation an der Karl Franzens Universitaet Graz, Juli 2003.
- [22] N. Martensson and A. Nilsson, "On the origin of core level binding energy shifts," *J. Electr. Spectr. Relat. Phenom.*, vol. 75, pp. 209–223, 1995.

- [23] K. G. Jr., L. Eyring, and S. Huefner, eds., *Handbook on the Physics and Chemistry of the Rare Earths*, vol. 10 of *Chapter 63*. 1984.
- [24] C. Hardacre, G. M. Roe, and R. M. Lambert, "Structure, composition and thermal properties of cerium oxide films," *Surf.Sci.*, vol. 362, pp. 1–10, 1995.
- [25] K. D. Schierbaum, "Ordered ultra-thin cerium oxide overlayers on Pt(111) single crystal surfaces studied by LEED and XPS," *Surf. Sci.*, vol. 399, p. 29, 1998.
- [26] D. Mullins, S. Overbury, and D. Huntley, "Electron spectroscopy of single crystal and polycrystalline cerium oxide surfaces," *Surf. Sci.*, vol. 409, p. 307, 1998.
- [27] E. Napetschnig, C. Konvicka, M. Schmid, and P.Varga, "XPS and STM measurements of Ce deposited on Rh(111)," *Private communication*, 2002.
- [28] J. Yeh and I. Lindau, eds., *Atomic Data and Nuclear Data Tables*, vol. 32 of *Academic Press Inc.* 1985.
- [29] F. Netzer, J. M. in: K.A. Gschneidner Jr., L. Eyring, and S. Huefner, eds., *Handbook on the Physics and Chemistry of the Rare Earths*, vol. 10 of *Chapter 72*. 1984.
- [30] M. E. Dry, "The Fischer-Tropsch process: 1959-2000," *Catalysis Today*, vol. 71, pp. 227–241, 2002.
- [31] O. Björneholm, A. Nilsson, H. Tillborg, P. Bennich, A. Sandell, B. Hernnaes, C. Puglia, and N. Martensson, "Overlayer structure from adsorbate and substrate core level binding energy shifts: CO, CCH<sub>3</sub> and O on Pt(111)," *Surf. Sci.*, vol. 315, pp. 983–989, 1994.
- [32] A. Beutler, E. Lundgren, R. Nyholm, J. Andersen, B.J.Setlik, and D. Heskett, "Coverage- and temperature-dependent site occupancy of carbon monoxide on Rh(111) studied by high-resolution core-level photoemission," *Surf. Sci.*, vol. 396, p. 117, 1998.
- [33] S. Surnev, M. Sock, M. G. Ramsey, F. P. Netzer, M. Wiklund, M. Borg, and J. N. Andersen, "CO adsorption on Pd(111): a high-resolution core level photoemission and electron energy loss spectroscopy study," *Surf. Sci.*, vol. 470, pp. 171–185, 2000.

- [34] A. J. Jaworowski, A. Beutler, F. Strisland, R. Nyholm, B. Setlik, D. Heskett, and J. Andersen, "Adsorption sites in O and CO coadsorption phases on Rh(111) investigated by high-resolution core-level photoemission," *Surf. Sci.*, vol. 431, p. 33, 1999.
- [35] M. Smedh, A. Beutler, T. Ramsvik, R. Nyholm, M. Borg, J. Andersen, R. Duschek, M. Sock, F. Netzer, and M. Ramsey, "Vibrationally resolved C 1s photoemission from CO absorbed on Rh(111): the investigation of a new chemically shifted C 1s component," *Surf. Sci.*, vol. 491, pp. 99–114, 2001.
- [36] S. Schwegmann, H. Over, V. D. Renzi, and G. Ertl, "The atomic geometry of the O and CO + O phases on Rh(111)," *Surf. Sci.*, vol. 375, pp. 91–106, 1997.
- [37] R. Roy, R. Guo, A. Bhala, and L. Cross, "'Oriented film growth" not "epitaxy" in HTSC film growth," *J. Vac. Sci. Technol.*, vol. A 12, p. 269, 1994.
- [38] D. Belton and S. Schmieg, "Low temperature oxidation and reduction of ceria particles on Rh(111)," *J. Vac. Sci. Technol.*, vol. A 11, p. 2330, 1993.
- [39] D. Mullins, S. Overbury, and D. Huntley, "Electron spectroscopy of single crystal and polycrystalline cerium oxide surfaces," *Surf. Sci.*, vol. 409, p. 307, 1998.
- [40] J. P. Warren, X. Zhang, J. E. T. Andersen, and R. M. Lambert, "Growth of Ce on Rh, surface alloy formation and the preparation and properties of Rh/ceria model planar catalysts," *Surf. Sci.*, vol. 287/288, pp. 222 – 227, 1993.
- [41] N. V. Skorodumova, R. Ahuja, S. I. Simak, I. A. Abrikosov, B. Johansson, and B. I. Lundqvist, "Electronic, bonding, and optical properties of  $CeO_2$  and  $Ce_2O_3$  from first principles," *Phys. Rev. B*, vol. 64, p. 115108, 2001.
- [42] U. Berner and K. Schierbaum, "Cerium oxide layers on Pt(111): a scanning tunneling microscopy study," *Thin Solid Films*, vol. 400, p. 46, 2001.
- [43] S. Oh and C. Eickle, " , " *J. Catal.*, vol. 112, p. 543, 1988.
- [44] G. Zafiris and R. Gorte, "Evidence for a Second CO Oxidation Mechanism on Rh/Ceria," *J. Catal.*, vol. 143, p. 86, 1993.



- [45] T. Bunluesin, H. Cordatos, and R. Gorte, "Study of CO Oxidation Kinetics on Rh/Ceria," *J. Catal.*, vol. 157, p. 222, 1995.
- [46] J. Stubenrauch and J. Vohs, "Interaction of CO with Rh Supported on Stoichiometric and Reduced  $CeO_2(111)$  and  $CeO_2(100)$  Surfaces," *J. Catal.*, vol. 159, p. 50, 1996.
- [47] D. Mullins and S. Overbury, "CO dissociation on Rh deposited on reduced Cerium oxide thin films," *J. Catal.*, vol. 188, p. 340, 1999.
- [48] J. C. in: D.A. King and D. Woodruff, eds., *The chemical physics of solid surfaces and heterogeneous catalysis*. Volume 3, Elsevier, Amsterdam, 1990.
- [49] A. Beutler, E. Lundgren, R. Nyholm, J. Andersen, B.J.Setlik, and D. Heskett, "On the adsorption sites for CO on the Rh(111) single crystal surface," *Surf. Sci.*, vol. 371, p. 381, 1997.
- [50] M. Campagne, F. H. in: K.A. Gschneidner Jr., L. Eyring, and S. Huefner, eds., *Handbook on the Physics and Chemistry of the Rare Earths*, vol. 10 of *Chapter 63*. 1984.
- [51] S. Surnev, M. Sock, M. Ramsey, F. Netzer, B. Klötzer, W. Unterberger, and K.Hayek, "Chemical reactivity of the V-Pd(111) subsurface alloy: adsorption of CO," *Surf. Sci.*, vol. 511, p. 392, 2002.
- [52] R. Hirschl and J. Hafner, "First-principles study of Pd-V surface alloys: Chemical reactivity," *Surf. Sci.*, vol. 498, p. 37, 2002.
- [53] R. J. Lad and V. E. Heinrich, "Surface electronic structure and chemisorption properties of MnO(100)," *J. Vac. Sci. Technol.*, vol. A 6, p. 781, 1988.
- [54] A. A. Audi and P. M. Sherwood, "Valence-band x-ray photoelectron spectroscopic studies of manganese and its oxides interpreted by cluster and band structure calculations," *Surface and Interface Analysis*, vol. 33, pp. 274–282, 2002.
- [55] A. Sandell, P. H. Andersson, E. Holmstroem, A. J. Jaworowski, and L. Nordstroem, "Geometric and electronic structure of PdMn bimetallic systems on Pd(100)," *Phys. Rev. B*, vol. 65, p. 035410, 2001.

- [56] G. A. Rizzi, R. Zanoni, S. D. Siro, L. Perriello, and G. Granozzi, "Epitaxial growth of MnO nanoparticles on Pt(111) by reactive deposition of  $Mn_2(CO)_{10}$ ," *Surf. Sci.*, vol. 462, pp. 187–194, 2000.
- [57] D. King and D. Woodruff, eds., *The chemical physics of solid surfaces and heterogeneous catalysis*. Volume 4, Elsevier, Amsterdam, 1984.
- [58] A. Sandell, A. J. Jaworowski, A. Beutler, and M. Wiklund, "Adsorption and reactions on a surface alloy: CO, NO,  $O_2$  and  $CO_2$  on Pd(100)-Mn-c(2x2)," *Surf. Sci.*, vol. 421, pp. 116–134, 1999.
- [59] F. Mueller, R. de Masi, D. Reinicke, P. Steiner, S. Huefner, and K. Stoewe, "Epitaxial growth of MnO/Ag(001) films," *Surf. Sci.*, vol. 520, pp. 158–172, 2002.
- [60] D. Tian, H. Li, S. C. Wu, J. Quinn, Y. S. Li, F. Jona, and P. M. Marcus, "Epitaxy of MnO on Cu(001) films," *Phys. Rev. B*, vol. 46, pp. 7216–7218, 1992.
- [61] M. (editor), *Handbook of X-ray Photoelectron spectroscopy*. Perkin Elmer Corporation, 1995.
- [62] S. Huefner, *Photoelectron Spectroscopy*. Springer Verlag, 1998.
- [63] M. Oku, K. Wagatsuma, and T. Konishi, "Relation between 2p X-ray photoelectron and K- $\alpha$  X-ray emission spectra of manganese and iron oxides," *J. Electron Spectrosc. Relat. Phenom.*, vol. 98-99, pp. 277–285, 1999.
- [64] J. van Elp, R. H. Potze, H. Eskes, R. Berger, and G. A. Sawatzky, "Electronic structure of MnO," *Phys. Rev. B*, vol. 44, pp. 1530 – 1537, 1991.
- [65] A. Fujimori, F. Minami, and S. Suga, "Electronic structure of MnO," *Phys. Rev. B*, vol. 42, pp. 7580–7586, 1990.
- [66] M. Taguchi, T. Uozumi, and A. Kotani, "Theory of X-ray photoemission and X-ray emission spectra in Mn Compounds," *J. of the Physical Society of Japan*, vol. 66, pp. 247–256, 1997.
- [67] F. Parmigiani and L. Sangaletti, "Fine structures in the X-ray photoemission spectra of MnO, FeO, CoO and NiO single crystals," *J. Electron Spectrosc. Relat. Phenom.*, vol. 98-99, pp. 287–302, 1999.

- [68] M. Oku and K. Hirokawa, “X-ray photoelectron spectroscopy of  $Co_3O_4$ ,  $Fe_3O_4$ ,  $Mn_3O_4$  and related compounds,” *J. Electron Spectrosc. Relat. Phenom.*, vol. 8, pp. 475–481, 1976.
- [69] G. H. Gweon, J. G. Park, and S. J. Oh, “Final-state screening effects in the 3s photoemission spectra of Mn and Fe insulating compounds,” *Phys. Rev. B*, vol. 48, pp. 7825–7835, 1993.
- [70] M. Oku, K. Hirokawa, and S. Ikeda, “X-ray photoelectron spectroscopy of manganese - oxygen systems,” *J. Electr. Spec. Relat. Phenom.*, vol. 7, pp. 465–473, 1975.
- [71] R. J. Lad and V. E. Heinrich, “Electronic structure of MnO studied by angle resolved and resonant photoemission,” *Phys. Rev. B*, vol. 38, pp. 10 860–10 869, 1988.
- [72] M. Henzler and W. Goepel, *Oberflaechenphysik des Festkoerpers*. Teubner studienbuecher, 1991.
- [73] S. P. Jeng, R. J. Lad, and V. E. Heinrich, “Satellite structure in the photoemission spectra of MnO(100),” *Phys. Rev. B*, vol. 14, pp. 11971–11977, 1991.
- [74] H. Lueth, *Surfaces and interfaces of solid materials*. Solid State Sciences 82, 1995.
- [75] J. Schoiswohl, *Growth and structure of ultrathin vanadium oxide layers on a Rh(111) single crystal*. Diplomarbeit an der Technischen Universität Graz, 2002.
- [76] S. Eck, C. Castellarin-Cudia, S. Surnev, K. C. Prince, M. G. Ramsey, and F. P. Netzer, “Adsorption and reaction of CO on a ceria-Rh(111) ”inverse model catalyst” surface,” *Surf. Sci.*, vol. 536, pp. 166–176, 2003.
- [77] H. Nishimura, T. Tashiro, T. Fujitani, and J. Nakamura, “Surface structure of MnO/Rh(100) studied by STM and LEED,” *J. Vac. Sci. Technol. A*, vol. 18, pp. 1460–1463, 2000.
- [78] P. W. Tasker, “The stability of ionic crystal surfaces,” *J. Phys. C*, vol. 12, pp. 4977–4984, 1979.
- [79] S.-C. Wu, J.-F. Jia, K. Wu, S.-H. Lu, R.-G. Zhao, and D.-Z. Wang, “Coadsorption of carbon monoxide and oxygen on Pd(001)c(2x2)-Mn: an oxidation pathway for  $CO_2$  formation,” *Surf. Sci.*, vol. 312, pp. 167–173, 1994.

- [80] K. W. Kolasinski, F. Cemic, A. deMeihere, and E. Hasselbrink, "Interactions in co-adsorbed CO + O<sub>2</sub>/Pd(111) layers," *Surf. Sci.*, vol. 334, pp. 19–28, 1995.
- [81] A. J. Jaworowski, S. M. Gray, M. Evans, R. Asmundsson, P. Uvdal, and A. Sandell, "Two- to three dimensional transition during growth and surface alloy formation of Mn on Pd(100)," *Phys. Rev. B*, vol. 63, p. 125401, 2001.
- [82] F. Leisenberger, G. Koller, M. Sock, S. Surnev, M. Ramsey, F. Netzer, B. Klötzer, and K. Hayek, "Surface and subsurface oxygen on Pd(111)," *Surf. Sci.*, vol. 445, pp. 380–393, 2000.
- [83] M. Sock, S. Surnev, M. Ramsey, and F. Netzer, "Adsorption and reaction of CO on vanadium oxide-Pd(111) "inverse" model catalysis: an HREELS study," *Topics in catalysis*, vol. 14, pp. 15–23, 2001.
- [84] S. Surnev, M. Sock, G. Kresse, J. Andersen, M. Ramsey, and F. Netzer, "Unusual CO Adsorption Sites on Vanadium Oxide-Pd(111) "Inverse Model Catalyst" Surfaces ," *J. Phys. Chem. B*, vol. 107, pp. 4777–4785, 2003.
- [85] M. Rose, T. Mitsui, J. Dunphy, A. Borg, D. Ogletree, M. Salmeron, and P. Sautet, "Ordered structures of CO on Pd(111) studied by STM," *Surf. Sci.*, vol. 512, pp. 48–50, 2002.
- [86] S. Eck, C. Castellarin-Cudia, S. Surnev, M. G. Ramsey, and F. P. Netzer, "Growth and thermal properties of ultrathin cerium oxide layers on Rh(111)," *Surf. Sci.*, vol. 520, pp. 173–185, 2002.
- [87] J. Schoiswohl, S. Eck, S. Surnev, M. Ramsey, and F. Netzer, "Electronic structure of ultrathin vanadium oxide films grown on a Rh(111) single crystal surface," *MAX-LAB Activity report*, 2002.
- [88] S. Surnev, G. Kresse, M. Sock, M. Ramsey, and F. Netzer, "Surface structures of ultrathin vanadium oxide films on Pd(111)," *Surf. Sci.*, vol. 495, p. 91, 2001.

# Appendix A

## Curriculum vitae

### Personal



Name: Sven Eck  
Adress: Lichtenfelsgasse 21, A-8010 Graz (Austria)  
Date of birth: 23.10. 1972  
Place of birth: Graz (Austria)  
Marital status: married (Dr. med. Katharina Eck on april 29th, 2000)  
Nationality: Austria (EU)

### Education:

20.06. 1990 Matura "mit gutem Erfolg" in Saalfelden /Austria  
01.10.1990-01.10.1991 Military service (Einj"ahrig Freiwilliger -  
Milizoffiziersausbildung) current rank: "Oberleutnant"  
Aug. 1999 -Apr. 2000 Diploma thesis in surface science, theme: "The Cerium-oxide  
Rhodium(111) interface studied with UPS, XPS and LEED"  
30.05. 2000 Sponson Mag. rer. nat.  
Oct. 2000- Oct. 2003 PhD studies at the Institute of Experimental Physics,  
Karl Franzens University Graz Supervisor: Prof. Dr. F.P. Netzer

**Employments:**

- 04.08.2000-30.01.2002 research assistant ("Vertragsassistent") at the Institute of Experimental Physics, Karl Franzens University Graz
- 01.02.2002-31.08.2003 post graduate research assistant at the FWF-project S8104-Phy "Adsorption on the metal-oxide interface: Local and non-local effects in chemisorption"

**Languages:**

- German: native language
- English: written and spoken fluently
- French: school knowledge (oral final exam "Matura")
- Italian: intermediate knowledge (research in Trieste)

**Technical Experience:**

During the diploma thesis I gained the basic knowledge in building and maintaining Ultra High Vacuum (UHV) equipment and performing experiments in UHV conditions. The main methods were controlled preparation of surfaces by physical vapour deposition and their characterisation with Low Energy Electron Diffraction (LEED), X-ray Photoelectron Spectroscopy (XPS) and Ultra violet Photoelectron Spectroscopy (UPS).

During the research for my PhD I spent 17 Months (2000/2001) at the synchrotron light source ELETTRA in Trieste (Italy). In this period I was in charge of the installation and maintenance of the ultra high vacuum endstation to the Materials Science Beamline (MSB) and the beamline itself. This endstation was equipped with a high-resolution electron spectrometer (Scienta SES 200) to allow high-resolution XPS (X-ray Photoelectron Spectroscopy) and NEXAFS (Near Edge X-ray Absorption Fine Structure) with synchrotron light. After the setup of the endstation I performed the testing and optimisation of both the spectrometer and the beamline (built by the Czech Academy of Sciences). This work resulted in manuals for both beamline and Scienta SES 200 spectrometer dedicated to future users of the Materials Science Beamline (MSB) at ELETTRA.

From October 2001 until January 2002 I investigated Cerium-oxide-Rhodium(111) interfaces with high resolution XPS, NEXAFS and resonant photoemission spectroscopy at the Materials Science Beamline.

From January 2002 until August 2002 I investigated the growth and structure of Vanadium-oxide islands on Rh(111) at the home institute in Graz together with H. Schoiswohl (diploma student). In April 2002 I characterised the V-oxide-Rh(111) interface with high-resolution XPS at the beamline 311 at (MAX II - synchrotron) in Lund, Sweden. From August 2002 until April 2003 I performed experiments on the controlled growth and characterisation of ordered manganese-oxide islands on Pd(111).

### **Conferences, Meetings, Posters and oral Presentations (not including seminars at the home institute)**

#### **1999/2000**

- Sept. 25 – 29<sup>th</sup>, 1999: 25th IUVESTA (International Union for Vacuum Science, Technique and Applications) workshop and Joint-Research-Project "Gas-Surface-Interaction" workshop meeting, Seggau (Austria)  
Participant
- Aug. 8 – 12<sup>th</sup>, 2000: ICES 8 (International Conference on Electronic Spectroscopy and Structure), Berkeley (USA)  
Poster contribution: "A High Resolution NEXAFS Study of an azimuthal oriented molecule: Bithiophene on Ni(110)-S Cu (110)-O surfaces"  
(G.Koller, R.I.R. Blyth, S.Eck, F.P.Netzer, M.G. Ramsey)
- Sept. 25 – 29<sup>th</sup>, 2000: "OPG ("Osterreichische Physikalische Gesellschaft) conference, Graz (Austria)  
Participant
- Oct. 22 – 25<sup>th</sup>, 2000: Joint-Research-Project "Gas-Surface-Interaction" workshop meeting, Aggsbach-Dorf (Austria)  
Oral presentation: "First Investigations of the Ceriumoxide/Rh(111) Interface with XPS, UPS and LEED"

**2001**

- Jan. 12 – 19<sup>th</sup>, 2001: IWOX II, Taos, New Mexico, USA  
 Poster contribution: "Growth and structure of ultra-thin Cerium Oxide Layers on Rh(111)"  
 (C. Castellarin-Cudia, S. Eck, S. Surnev, M.G. Ramsey, F.P. Netzer)
- Jul. 23 – 27<sup>th</sup>, 2001 VUV XIII (13th International Conference on Vacuum Ultraviolet Radiation Physics), Trieste, Italy  
 Poster contribution: "High resolution core level spectroscopy of "inverse catalyst" surfaces: Probing the metal-oxide interface"  
 (S.Surnev, M.Sock, S.Eck, M.G.Ramsey, F.P.Netzer)
- Nov. 18 – 21<sup>st</sup>, 2001: Joint-Research-Project "Gas-Surface-Interaction" Stainz (Austria).  
 Oral presentation: "Adsorption of CO on Cerium-oxide/Rh(111) surfaces - first results of synchrotron investigations"

**2002**

- May 22 – 25<sup>th</sup>, 2002: Joint-Research-Project, Schloss Seggau (Austria)  
 Participant
- Sept. 23 – 26<sup>th</sup>, 2002: OPG (Oesterreichische Physikalische Gesellschaft) conference, Leoben (Austria)  
 Poster contribution: "Interface mediated defect formation in ultrathin cerium oxide films"  
 (C. Castellarin-Cudia, S. Eck, S. Surnev, M.G.Ramsey, F.P. Netzer)  
 Poster contribution: "CO adsorption studies on O and  $CeO_x$  modified Rh(111) surfaces"  
 (S. Eck, C. Castellarin-Cudia, M.G.Ramsey, K.C.Prince, F.P. Netzer)
- Nov. 3 – 8<sup>th</sup>, 2002: 49th AVS (American Vacuum Society) Symposium, Denver, Colorado, USA  
 Poster contribution: "Interface mediated defect formation in ultrathin cerium oxide films"  
 (C. Castellarin-Cudia, S. Eck, S. Surnev, M.G. Ramsey, F.P. Netzer)



**2003**

Jan. 27 – 31<sup>st</sup>, 2003: IWOX III, Sapporo (Japan)

Poster contribution: "Modification of metal reactivity by cerium oxide overlayers on Rh(111): adsorption of CO"

(S. Eck, C. Castellarin-Cudia, M.G.Ramsey, K.C.Prince, F.P. Netzer)

Sept. 7 – 22<sup>nd</sup>, 2003 ECOS 22 (European Conference On Surface Science),  
Praha (Czech rep.)

3 Poster contributions:

"Reactivity of Vanadium decorated Rh(111) Surfaces"

(J.Schoiswohl, S. Surnev, S.Eck, M.G.Ramsey, F.P.Netzer)

"Modification of metal reactivity by cerium oxide overlayers on Rh(111)"

(S. Eck, C. Castellarin-Cudia, S.Surnev, M.G.Ramsey, F.P.Netzer)

"Geometric and Electronic Structure of Sexiphenyl on the  $TiO_2(110)$  surface"

(S. Berkebile, S.Eck, M.G. Ramsey)



# Appendix B

## List of Publications:

### **NEXAFS of Bithiophene: more questions than answers**

G. Koller, R.I.R. Blyth, S. Eck, F.P. Netzer, M.G. Ramsey  
Berliner Elektronenspeicherring - Gesellschaft fuer Synchrotronstrahlung  
BESSY, Jahresbericht 1999, 362-364

### **Growth and thermal properties of ultrathin cerium oxide layers on Rh(111)**

S. Eck, C. Castellarin-Cudia, S. Surnev, M. G. Ramsey and F. P. Netzer  
Surface Science 520 (2002), 173-185

### **Electronic structure of ultrathin vanadium oxide films grown on a Rh(111) single crystal surface**

J. Schoiswohl, S.Eck, S.Surnev, M.G.Ramsey, F.P.Netzer  
Max-lab Activity Report 2002

### **Adsorption and reaction of CO on a ceria-Rh(111) "inverse model catalyst" surface**

S. Eck, C. Castellarin-Cudia, S. Surnev, K. C. Prince, M. G. Ramsey and F. P. Netzer  
Surface Science, 536 (2003) 166-176

### **Growth of ordered bithiophene layers on the p(2x1)O reconstructed Cu (110) surface**

G. Koller, R.I.R. Blyth, S.A. Sardar, S. Eck, F.P. Netzer, M.G. Ramsey  
Surface Science (2003), in press

**Atomic level growth study of vanadium oxide nanostructures on  
Rhodium(111)**

J. Schoiswohl, S. Eck, M. Sock, S. Surnev, M.G. Ramsey, F.P. Netzer  
Surface Science (2003), submitted

# Appendix C

## Manual for SCIENTA SES-200 analyser and ESCA 300 software

- Standard spectra with the SCIENTA SES-200 analyser and ESCA 300 software (p.194)
- Optimization of the countrate by using Scienta "interactive mode" (p.206)
- Lens and software elements changing the countrate and resolution - including theoretical and measured resolution tables (p.211)
- Checklist for valves and pumps settings of the Scienta UHV system for standard procedures (p.216)
- Standard optimization procedure for the Materials Science Beamline at ELETTRA (p.217)
- NEXAFS spectra with the Scienta SES 200, WinESCA and Scienta Analysis (p.222)